

AD-A113 148

PENNSYLVANIA UNIV PHILADELPHIA
SILVER-DOPING EFFECTS AND PHOTOSTRUCTURAL TRANSFORMATION IN EVA--ETC(U)
FEB 82 T J CHEN, J N ZEMEL, I LAUKS

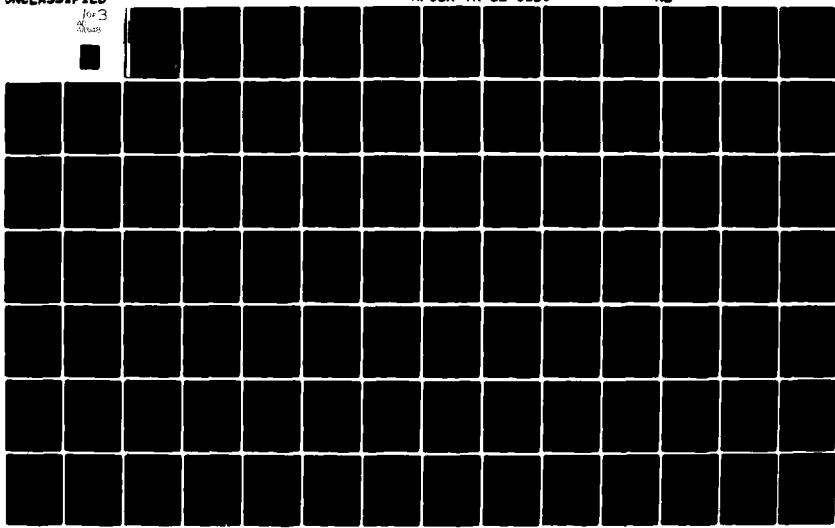
F/0 7/4

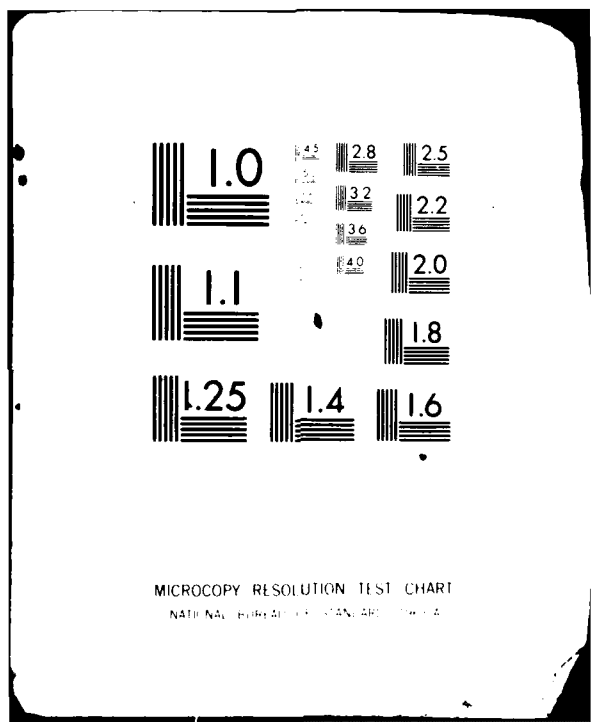
AFOSR-TR-82-0120

NL

UNCLASSIFIED

for 3
years





AFOSR-TR- 82-0120

Silver Noping Effects and Photo-
Structural Transformation in
Evaporated Ag_2S_3 Thin Films.

FINAL

12

REPORT

AD A113148

AFOSR 77-3432

J. N. ZEMEL

Approved for public release;
distribution unlimited.

DTIC FILE COPY

DTIC
ELECTE
APR 6 1982
S D
D

82 04 06 034

Unclassified

REPORT DOCUMENTATION PAGE		FEBRUARY 1982 REPORT OF RESEARCH AND DEVELOPMENT	
1. REPORT NUMBER	AFOSR-TR-32-0120	2. GO	3. DOCUMENT IDENTITY NUMBER
SILVER-DOPING EFFECTS AND PHOTOSTRUCTURAL TRANSFORMATION IN EVAPORATED AS ₂ S ₃ THIN FILMS		5. TYPE OF REPORT (PERFORMING ORGANIZATION)	
		6. FINAL	
		6. PERFORMING ORGANIZATION NUMBER	
7. AUTHOR(s)	Chen, Zemel and Lauks	8. CONTRACT OR GRANT NUMBER	AFOSR-77-3432
9. PERFORMING ORGANIZATION NAME AND ADDRESS	University of Pennsylvania	10. PROGRAM ELEMENT NUMBER, TASK AREA & WORK UNIT NUMBER	61102F
11. CONTROLLING OFFICE NAME AND ADDRESS	Air Force Office of Scientific Research BLDG 410, Bolling Air Force Base Wash. D.C. 20332	12. REPORT DATE	16 FEB 82
13. MONITORING AGENCY NAME & ADDRESS if different from Controlling Office		14. NUMBER OF PAGES	205
15. SECURITY CLASSIFICATION	UNCLASSIFIED	15a. DECLASSIFICATION/DETERMINATION SCHEDULE	
16. DISTRIBUTION STATEMENT (of this Report)	Approved for public release; distribution unlimited.	17. DISTRIBUTION STATEMENT (for the abstract entered in Block 10, if different from Report)	Approved for public release; distribution unlimited.
18. SUPPLEMENTARY NOTES			
19. KEY WORDS (Continue on reverse side if necessary and identify by block number)			
20. ABSTRACT (Cutline on reverse side if necessary and identify by block number)			
The AS ₂ S ₃ thin film undergo photostructural transformation upon bandgap illumination giving rise to differential etch rate between the unexposed portions of the film in an alkaline hydroxide solution and CF ₄ plasma. It is observed that the ultraviolet light and x-ray sensitivity of AS ₂ S ₃ films is poorer than that of conventional organic polymer resists, but that electron-beam exposure sensitivity is better than the typical PMMA resist. However, the contrast in the AS ₂ S ₃ film is poorer than that of PMMA resist. The ultraviolet, x-ray, and electron-beam sensitivity of a modified AgCl-AS ₂ S ₃ composite resist is also			

studied. Not only can the sensitivity be enhanced at least by one order of magnitude, but also the contrast in this composite resist is improved without losing the resolution. The existence of the structural component is examined by x-ray diffraction, IR transmission, and electron diffraction. The results of AS_2S_3 , AS_4S_4 , and S. After band-gap exposure, the as-deposited state is changed into the exposed state being composed of a glassy AS_2S_3 network and arsenic in the form of clusters. The Anderson-Mott theory is employed to explain the microscopic structural transformations in AS_2S_3 and a plausible sequence of events leading to the polymerization of AS_4S_4 molecules into glassy AS_2S_3 network is proposed. The polymerization between AS_4S_4 itself or AS_4S_4 and S-chains can proceed because of the strong electron-phonon coupling in the vicinities of the charged defect centers which in turn causes the switching of local bonds. The properties of AS_2S_3 can be changed both structurally and physically as a result of silver photodoping. The silver ions would be trapped at the negative charged defect center and behave as a negative charged defect killer. In order to obtain more control over the silver dopant concentration, electrochemical injection method is employed. The silver doping level is controlled by varying the current density through the electrochemical cell. It is found that if the injection voltage is below -35 mv, then this process is almost fully reversible in the sense that the Ag injected into the AS_2S_3 film can be removed from the AS_2S_3 into the aqueous solution anodically. If the injection voltage is above -35 mv then the reversibility is decreased. From the experimental data and numerical analysis, it appears that the kinetics of the silver injection process is limited by the interfacial reaction rather than the bulk diffusion. The model also indicates the existence of two phases, one is silver-doped AS_2S_3 and the other undoped, in the AS_2S_3 film. The boundary between these two different phases moves with the extent of silver injection.

Accession For	
NTIS GRA&I	<input checked="" type="checkbox"/>
DTIC TAB	<input type="checkbox"/>
Unannounced	<input type="checkbox"/>
Justification	
By _____	
Distribution/	
Availability Codes	
Dist	Avail and/or Special
F	



Unclassified

**FINAL
REPORT**

AFOSR 77-3432

J. N. ZEMEL

AIR FORCE SYSTEMS COMMAND, AIR FORCE SYSTEMS COMMAND (AFSC)
NOTE
Title _____
Caption _____
Date _____
DRAFTED
MATTHEW J. W.
Chief, Technical Information Division

ACKNOWLEDGEMENTS

I would like to express my sincere appreciation to Professor Jay N. Zemel and Professor Imant Lauks for jointly supervising this dissertation. Their encouragement, enthusiasm, and support are greatly appreciated. Special thanks are extended to my previous advisor, Dr. Mark S. Chang, for his suggestions that resulted in this dissertation.

Drs. H. T. Yuan and C. R. Shaw of Texas Instrument Incorporated are gratefully acknowledged for their support in the electron-beam exposure. Also, to be thanked are present and former colleagues of the Solid State Electronics Laboratory - especially Tom Carroll, Drs. T. W. Hou and S. A. Keneman. Thanks are extended to Dru Spanner for her typing of the manuscript. Also, I would like to express a deep appreciation to my best friend for her love and support during all the years of study.

Finally, the author thanks the National Science Foundation, Air Force Office of Scientific Research, and the Department of Electrical Engineering and Science of the University of Pennsylvania for their continuous financial support during this work.

TABLE OF CONTENTS

ACKNOWLEDGEMENTS	
INDEX	
TABLE OF CONTENTS	
LIST OF FIGURES	
LIST OF TABLES	
BIBLIOGRAPHY	
ABSTRACT	
Chapter 1 INTRODUCTION	1
Chapter 2 THE SENSITIVITIES AND MICROSTRUCTURE APPLICATIONS OF As ₂ S ₃ INORGANIC RESISTS	6
2.1 Preparation of As ₂ S ₃ Thin Films	7
2.2 Basic Definitions	10
2.3 Sensitivity Evaluation of As ₂ S ₃ Films with Respect To Photo-, X-ray, and Electron-beam Exposure	13
2.3.1 Ultraviolet Exposure	13
2.3.2 X-ray Exposure	15
2.3.3. Electron-beam Exposure	15
2.4 Etch Rate Determinations and Diffraction Efficiency of Grating in As ₂ S ₃ Films	19
2.4.1 Etch Rate Determinations in As ₂ S ₃ Films in NaOH Aqueous Solution	19
2.4.2 Diffraction Efficiency of Gratings in As ₂ S ₃ Films in Plasma Etching	21

2.5 Ag-doped As ₂ S ₃ Composite Resists	26
2.5.1 Ag-Doped As ₂ S ₃ Composite Resists	26
2.5.2 The Evaluation of AgCl-As ₂ S ₃ Composite Resists . .	27
2.6 Direct Device Fabrication	34
Chapter 3 PLASMA ETCHING OF As₂S₃ FILMS	40
3.1 Introduction	40
3.2 Basic Chemical and Physical Phenomena in Low Pressure Plasma	44
3.2.1 Chemical Reactions in Plasmas	45
3.2.2 Basic Physical Phenomena in Low Pressure Plasmas .	47
3.3 Plasma Etching System and End Point Detection	50
3.3.1 Plasma Etching System	50
3.3.2 End Point Detection	56
3.4 Experimental Techniques and Results	57
3.4.1 Experimental Techniques	57
3.4.2 Experimental Results	59
3.5 Factors Controlling Plasma Etch Rates	69
3.5.1 Reactor Pressure and RF Power	69
3.5.2 Flow Rate	71
3.6 Etching Mechanisms of As ₂ S ₃ Films in a CF ₄ Plasma . .	72
3.7 The Plasma Oxidation of Amorphous As ₂ S ₃ Films	75
Chapter 4 STRUCTURAL TRANSFORMATIONS IN AMORPHOUS As₂S₃ FILMS . . .	84
4.1 The Structures of Crystalline and Glassy As-S Compounds .	85
4.2 Experimental	89
4.3 Experimental Results	90

4.3.1 X-ray Diffraction	90
4.3.2 Transmission Electron Microscopy (TEM)	95
4.3.3 Infrared Spectroscopy	99
4.3.4 Summary	106
4.4 Photodarkening Effect in Amorphous As ₂ S ₃ Films	107
4.5 Charged Defect Model in Evaporated As ₂ S ₃ Films	111
4.6 Structural Studies of Ag-doped As ₂ S ₃ Films	120
4.6.1 Transmission Electron Microscopy	121
4.6.2 IR Spectroscopy	122
4.6.3 X-ray Diffraction	124
4.7 Morphology of the Heavily Ag-doped As ₂ S ₃ Film	128
4.7.1 Spinodal Decomposition	131
4.8 Ag Impurity States in As ₂ S ₃ Films	136
Chapter 5 THE ELECTROCHEMICAL STUDY OF THE SILVER INJECTION INTO As₂S₃ FILMS IN THE DARK	143
5.1 Voltammetry Studies of The As ₂ S ₃ Films	144
5.1.1 Introduction-General Requirements	144
5.1.2 Description of the Cell for Voltammetry	145
5.2 Experimental	147
5.3 Experimental Results	148
5.4 Discussion of the Voltammetric Results	152
5.4.1 Electrical Properties of The As ₂ S ₃ Electrode/ Electrolyte Interface	156
5.4.2 Electrode Reactions With Charge Transfer By Ag-ion At The As ₂ S ₃ / Electrolyte Interface	159

5.5 The AC Responses Of As ₂ S ₃ Films	170
5.5.1 The Cell For AC Impedance Measurements	170
5.5.2 AC Impedance Measurement Systems	171
(i) AC Bridge Method	171
(ii) Direct Impedance Measurement	174
5.5.3 AC Impedance Responses	176
5.6 The Equivalent Circuit Of The As ₂ S ₃ Electrochemical Cell	176
5.7 Conclusion	182
5.8 Voltammograms Of The Solid Electrochemical Cell Au/As ₂ S ₃ /AgI/Ag	184
5.8.1 The Transport Mechanism of Silver Ions In The Solid Electrolyte	185
5.8.2 Experimental Techniques and Results	185
5.9 Etching Behavior in NaOH Aqueous Solution and Morphology Of The Chemically Processed As ₂ S ₃ Film	187
5.9.1 Etching Behavior Of The Chemically Processed As ₂ S ₃ Film	187
5.9.2 Morphology of The Chemically Processed As ₂ S ₃ Film	190
Chapter 6 CONCLUSIONS AND RECOMMENDATIONS FOR FUTURE RESEARCH . .	194
6.1 Summary of Results	194
6.2 Contributions	203
6.3 Recommendations for Future Research	205

ABSTRACT

SILVER-DOPING EFFECTS AND PHOTOSTRUCTURAL TRANSFORMATIONS IN EVAPORATED As_2S_3 THIN FILMS

Author: Teh-Yi James Chen

Supervisors: Jay N. Zemel and

Imant Lauks

The As_2S_3 thin film undergo photostuctural transformations upon bandgap illumination giving rise to a differential etch rate between the unexposed and exposed portions of the film in an alkaline hydroxide solution and CF_4 plasma. It is observed that the ultraviolet light and x-ray sensitivity of As_2S_3 films is poorer than that of conventional organic polymer resists, but that electron-beam exposure sensitivity is better than the typical PMMA resist. However, the contrast in the As_2S_3 film is poorer than that of PMMA resist. The ultraviolet, x-ray, and electron-beam sensitivity of a modified $\text{AgCl}-\text{As}_2\text{S}_3$ composite resist is also studied. Not only can the sensitivity be enhanced at least by one order of magnitude, but also the contrast in this composite resist is improved without losing the resolution.

The existence of the structural component is examined by x-ray diffraction, IR transmission, and electron diffraction. The results suggest the as-deposited state of As_2S_3 film is a heterogeneous system

of As_2S_3 , As_4S_4 , and S. After band-gap exposure , the as-deposited state is changed into the exposed state being composed of a glassy As_2S_3 network and arsenic in the form of clusters. The Anderson-Mott theory is employed to explain the microscopic structural transformations in As_2S_3 and a plausible sequence of events leading to the polymerization of As_4S_4 molecules into glassy As_2S_3 network is proposed. The polymerization between As_4S_4 itself or As_4S_4 and S-chains can proceed because of the strong electron-phonon coupling in the vicinities of the charged defect centers which in turn causes the switching of local bonds. The properties of As_2S_3 can be changed both structurally and physically as a result of silver photodoping. The silver ions would be trapped at the negative charged defect center and behave as a negative charged defect killer.

In order to obtain more control over the silver dopant concentration, electrochemical injection method is employed. The silver doping level is controlled by varying the current density through the electrochemical cell. It is found that if the injection voltage is below -35 mv, then this process is almost fully reversible in the sense that the Ag injected into the As_2S_3 film can be removed from the As_2S_3 into the aqueous solution anodically. If the injection voltage is above ~35 mv, then the reversibility is decreased. From the experimental data and numerical analysis, it appears that the kinetics of the silver injection process is limited by the interfacial reaction rather than the bulk diffusion. The model also indicates the existence of two phases, one is silver-doped As_2S_3 and the other undoped, in the As_2S_3 film. The

boundary between these two different phases moves with the extent of silver injection.

CHAPTER 1

INTRODUCTION

As the demands for higher resolution and smaller device features grow, it becomes increasingly clear that the traditional UV lithography has its problems. The resolution-limiting diffraction effects in the UV lithography can be reduced or eliminated by using deep UV, X-ray or electron-beam lithography.⁽¹⁻¹⁰⁾ All these new lithographic techniques are resist-dependent. Traditional organic polymer resists tend to have low atomic numbers resulting in low stopping cross section areas for X-rays and electrons. Inorganic resists are far more flexible and are used extensively as additives in organic polymer resists to improve the resist properties.⁽¹¹⁻³⁴⁾

In this dissertation, one of the promising inorganic materials, the evaporated As₂S₃ film, is examined and their applications in micro-fabrications under the use of X-ray and electron-beam to induce the chemical responses are studied in Chapter 2. The compatibilities of As₂S₃ inorganic resists with advanced microfabrication processes, such as plasma etching, are studied in Chapter 3. By using the Ag-doping effect, the sensitivities of As₂S₃ films can be further increased without losing the resolution. However, the fundamental mechanism for the radiation-sensitivity phenomenon is still not well understood despite significant technological progress. The wide variety of reported photo-structural effects in amorphous As₂S₃ and other chalcogenide glass sys-

tems have led to an array of complex and often contradictory mechanisms to account for them.⁽³⁵⁻⁴⁷⁾ In Chapter 4, the structural transformation of the As_2S_3 film upon band-gap illumination is examined.

The experimental data have shown that the as-deposited As_2S_3 films are in an amorphous state, and are a heterogeneous system of As_2S_3 , As_4S_4 and S.⁽⁴⁵⁾ After intense band-gap exposure, the as-deposited state is appeared to be changed into the exposed state being composed of a glassy As_2S_3 network and arsenic in the form of clusters.⁽⁴⁵⁾ A model based on the Anderson's proposal⁽⁴⁸⁻⁴⁹⁾ is employed to explain the microscopic structural transformations in As_2S_3 and a plausible sequence of events leading to the polymerization of As_4S_4 molecules into glassy As_2S_3 network is proposed. The ternary Ag-As-S system can contain as much as 35 at.% of Ag as a result of photodoping. The morphology of Ag-doped As_2S_3 samples was also studied. The silver states and their effects on physical properties in doped As_2S_3 are elaborated in terms of the charged defects model,⁽⁴⁹⁻⁵⁰⁾ and Ag atoms behave as a negative charged defect killer.

Work on the structural, optical and chemical properties of amorphous As_2S_3 films subjected to silver injection process by the electrochemical method will study in Chapter 5.

Chapter 6 summarizes the results of this investigation, followed by recommendations for additional study. The readers, who are interesting on the optical changes of As-S glass systems during band-gap illumination and its applications as an optical storage medium, should refer to works previously done by Keneman⁽⁴⁵⁾ and Hou⁽⁴⁷⁾ at this department.

References to Chapter 1

1. J. Dey, SPIE Vol.135, Developments in Semiconductor Microlithography III, p. 84, (1978).
2. B.J. Lin, J. Vac. Sci. Technol. 12, 1317, (1975).
3. J.D. Cuthbert, Solid State Technol. 20, 59, August, (1977).
4. D.L. Spear, H.I. Smith, Solid State Technol. 15, 21, (1972).
5. M.L. Perlman, E.M. Rowe, R.E. Watson, Phys. Today, 27, 30, (1974).
6. G.L. Vernel, D.F. Spicer, A.C. Roger, J. Vac. Sci. Technol, 10, 1048, (1973).
7. R.L. Seliger, P.A. Sullivan, Electronics, March, (1980).
8. R.L. Laibowitz, A.N. Broers, J.T.C. Yeh, J.M. Viggiano, Appl. Phys. Lett., 35, 891, (1979).
9. A.N. Broers, J.M.E. Harper, W.W. Malzen, Appl. Phys. Lett., 33, 392, (1978).
10. E. Spiller, R. Feder, "X-ray Lithography" in "X-ray Optics" Topics in Appl. Phys., Vol. 22, ed. by H.-J. Queisser, Springer-Verlag, (1977).
11. V.G. Remesnik, Sov. J. Quantum Electron, 7, 353, (1977).
12. K.L. Tai, W.R. Sinclair, R.G. Vadimsky, J.M. Moran, M.J. Rand, J. Vac. Sci. Technol., 16, 1977, (1979).
13. J.I. Masters, G.M. Goldberg, J.M. Lavine, Electron Dev. Lett., EDL -1, No. 4, April, (1980).
14. M.S. Chang, J.T. Chen, Appl. Phys. Lett., 33, 892, (1978).
15. A. Yoshikawa, O. Ochi, Y. Mizushima, Appl. Phys. Lett., 36, 107, (1980).
16. M.S. Chang, T.W. Hou, J.T. Chen, K.D. Kolwicz, J.N. Zemel, J. Vac. Sci. Technol., 16, Nov/Dec, (1979).
17. M.S. Chang, IEEE Conf. Record, Third Biennial University/Industry/Government Microelectronics Symposium, p. 124, (1979).
18. T.W. O'Keefe, R.M. Handy, Solid State Electronics, 11, 261, (1968).
19. B.H. Hill, J. Electrochem. Soc., 116, 668, (1969).

20. E.T. Fitzgibbon, W.H. Hartwig, Abstract 12, p. 38, ECS., Ext. Abst. Spring Meeting, May, (1971).
21. W.R. Sinclair, D.L. Rousseau, J.J. Stancavish, J. Electrochem. Soc., 121, 925, (1974).
22. G.W. Kammolott, W.R. Sinclair, J. Electrochem. Soc., 121, 929, (1974).
23. M.S. Chang, T.W. Hou, Opt. Comm., 24, 220, (1978).
24. M.S. Chang, T.W. Hou, Thin Solid Films, 55, 463, (1978).
25. T.W. Hou, M.S. Chang, Appl. Opt., 18, July, (1979).
26. K.D. Kolwicz, M.S. Chang, J. Electrochem. Soc., 127, 135, (1980).
27. M. Janai, P.S. Rudman, Photogr. Sci. Eng., 20, 234, (1976).
28. M. Janai, S. Oscar, S.G. Lipson, P.S. Rudman, Opt. Lett., 2, 57, (1978).
29. J.S. Berkes, S.W. Ing. Jr., W.J. Hillegas, J. Appl. Phys., 42, 4908, (1971).
30. H. Nagai, A. Yoshikawa, Y. Togoshima, O. Ochi, Y. Mizushima, Appl. Phys. Lett., 28, 145, (1976).
31. A. Yoshikawa, O. Ochi, H. Nagai, Y. Mizushima, Appl. Phys. Lett., 29, 667, (1977).
32. A. Yoshikawa, O. Ochi, H. Nagai, Y. Mizushima, Appl. Phys. Lett., 31, 161, (1977).
33. K.L. Tai, L.F. Johnson, D.W. Murphy, M.S.C. Chung, Abstract 94, Electrochem. Soc. Meeting, Boston, May, (1979).
34. Y. Utsugi, S. Zembutsu, Appl. Phys. Lett., 27, 508, (1975).
35. J.P. deNeufville, in "Optical Properties of Solids- New Development", ed. B.O. Seraphin, Ch. 9, North-Holland, Amsterdam, (1976).
36. J.P. deNeufville, S.C. Moss, S.R. Ovshinsky, J. Non-crystal Solids, 13, 191, (1973).
37. S.A. Solin, G.N. Papatheodorou, Phys. Rev. B 15, 2084, (1976).
38. V. Halpern, Phil. Mag., 34, 331, (1976).
39. R.J. Nemanich, G.A.N. Connel, T.M. Hayes, R.A. Street, Topical Conf. on Atomic Scale Structure of Amorphous Solids, L-11, Yorktown Height. New York, (1978).

40. Y. Utsugi, Y. Mizushima, J. Appl. Phys., 49, 3470, (1978).
41. I. Shimizu, H. Sakuma, H. Kokado, E. Inoue, Photogr. Sci. Eng., 16, 291, (1972).
42. T. Shirakawa, I. Shimizu, H. Kokado, E. Inoue, Photogr. Sci. Eng., 19, 139, (1975).
43. D. Goldschmidt, P.S. Rudman, J. Non-crystal. Solids, 22, 229, (1976).
44. S.A. Keneman, J. Bordogna, J.N. Zemel, J. Appl. Phys., 49, 4663, (1978).
45. S.A. Keneman, Ph.D. Thesis, Univ. of Pennsylvania, (1974).
46. S.A. Keneman, Appl. Phys. Lett., 19, 512, (1971).
47. T.W. Hou, Ph.D. Thesis, Univ. of Pennsylvania, (1979).
48. P.W. Anderson, Phys. Rev. Lett., 34, 953, (1975).
49. N.F. Mott, R.A. Street, Phil. Mag., 36, 33, (1977).
50. M. Kastner, H. Fritzsche, Phil. Mag., 37, 199, (1978).

CHAPTER 2

THE SENSITIVITIES AND MICROSTRUCTURE APPLICATIONS of As_2S_3 INORGANIC RESISTS

In this chapter, the different exposure characteristics of As_2S_3 as an inorganic resist are described. Since As_2S_3 thin films are to be used throughout, their preparation is described in Section 2.1. In Section 2.2 the definitions of basic terms, such as sensitivity and contrast, are given. Next, the sensitivity of the resist for lithographic application is evaluated with an ultraviolet source. Today there is a demand for submicron dimensions in IC technology. For present methods in optical lithography, the resolution is limited by the diffraction of light. Since x-ray and electron-beam exposure systems were established as a viable fabrication technique in the 1970's, the sensitivities of these As_2S_3 resists to x-ray and electron-beam exposure are also examined. In Sec. 2.4, the etch rates of the As_2S_3 thin films are determined by the in situ optical monitoring method. This technique developed by Chang et. al. is briefly described. In order to increase the sensitivity of As_2S_3 with respect to different exposure sources, $\text{AgCl}-\text{As}_2\text{S}_3$ or metallic $\text{Ag}-\text{As}_2\text{S}_3$ composite films were employed. The sensitivity of these composite resists is compared with the pure As_2S_3 thin film. Other techniques to increase the sensitivity are also described in Sec. 2.5. In the last section, various fabrication applications of these novel inorganic resists are

presented.

2.1 PREPARATION OF As₂S₃ THIN FILMS

Two common ways of preparing amorphous solids are (a) by condensation from the vapor as in thermal evaporation, sputtering, glow-discharge decomposition of a gas, or other methods of deposition, or (b) by cooling from a melt. The first method produces thin films while the second yields bulk material. Invariably there are structural differences between the same material prepared by different methods, and these must be considered in any intercomparison of properties with other people's results. Because of the large variety of such chalcogenide glass systems, classification of these materials becomes difficult, particularly in view of the freedom of amorphous systems to depart from stoichiometric proportions of the constituents. However, for any given group of elements it is not normally possible to form glasses for all compositions. The extent of the glass-forming region in As-S is displayed in Fig. 2.1. (1,2) It shows part of system between 55 and 100 at. % S is a glassy region. As₂S₃ thin films with thickness less than a few microns were prepared by vacuum evaporation. The evaporation source was bulk Servofrax^R As₂S₃ glass. The evaporation system is schematically shown in Fig. 2.2. In this system the background pressure was in the 10⁻⁷ torr range before evaporation and about 5 x 10⁻⁶ torr during evaporation. The evaporation rate and film thickness were monitored by a Sloan crystal thickness monitor DTM-4. After deposition of the thin film, the system

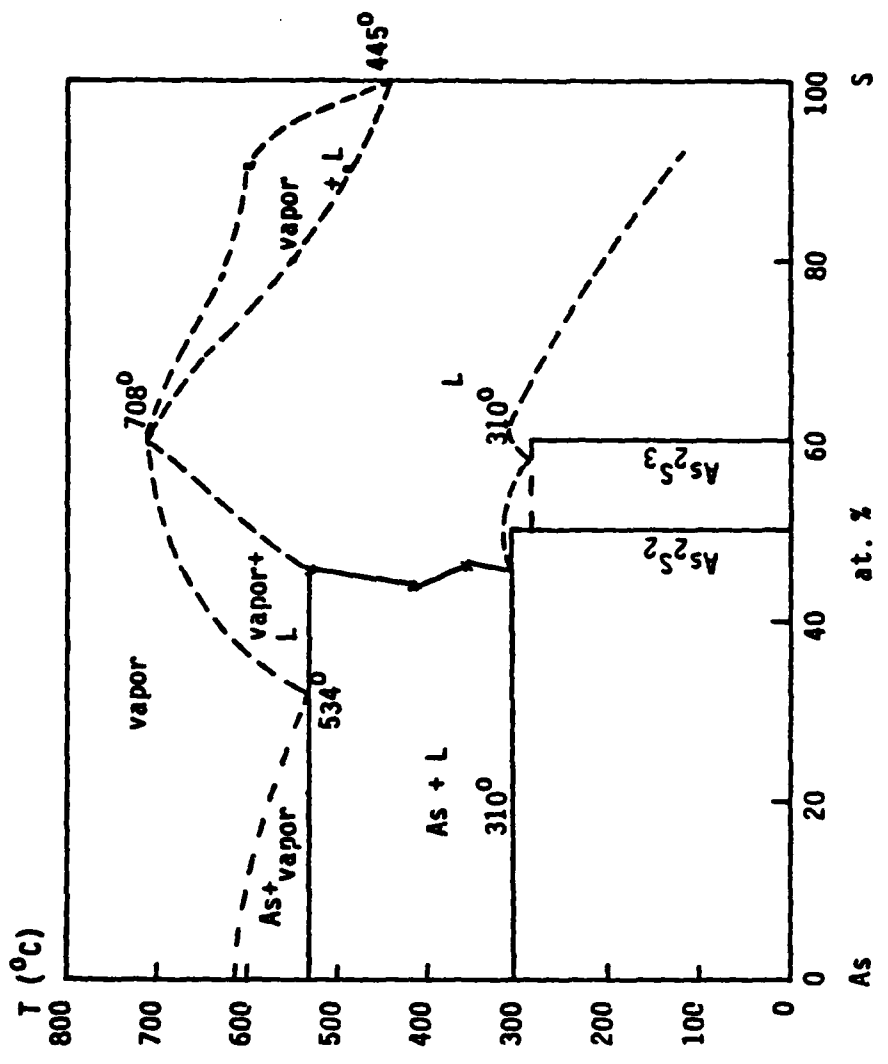


Fig.2.1 Phase diagram of the As-S system. (1,2)

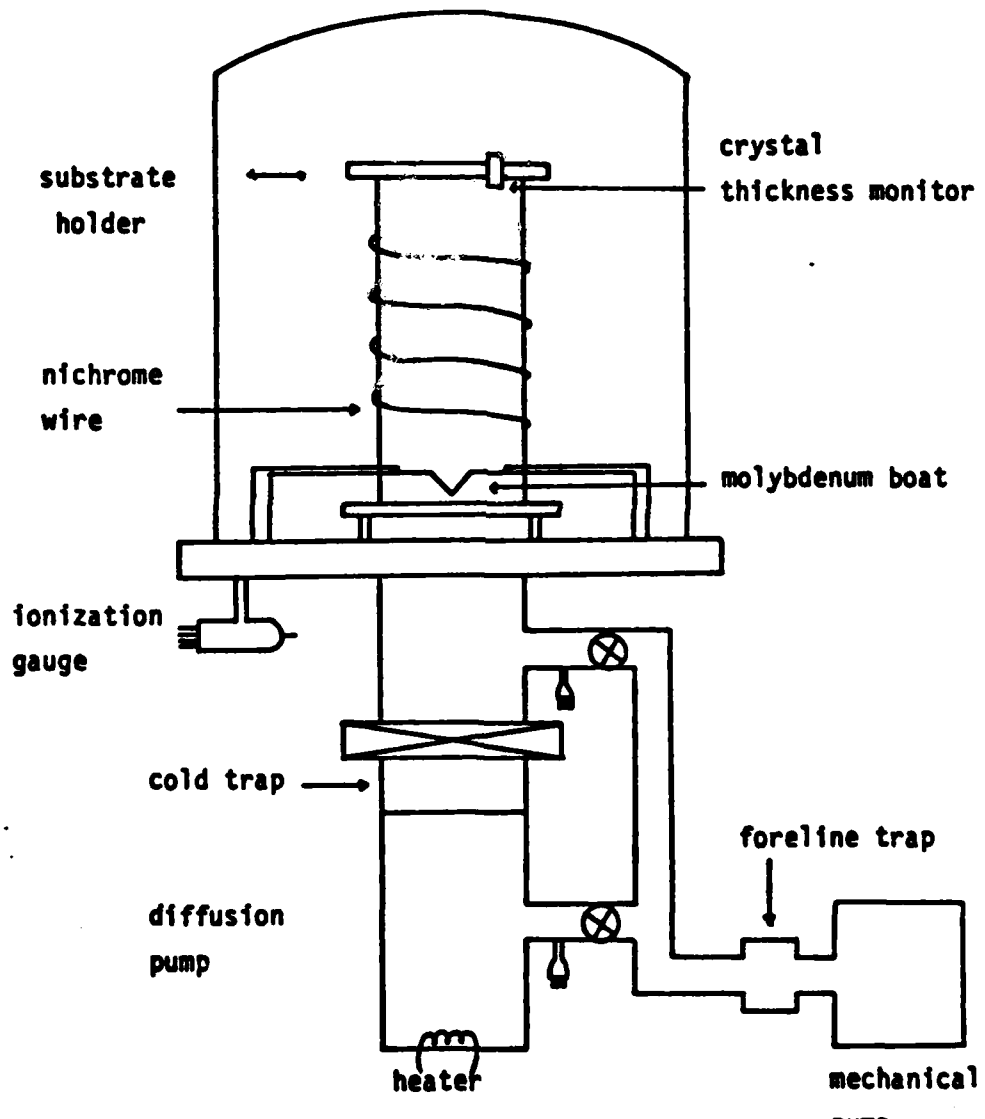


Fig.2.2 Schematic diagram of the vacuum evaporation system.

was normally cooled under high vacuum for 3-4 hours before the samples were taken out. The as-deposited As_2S_3 films are amorphous as determined by x-ray and electron-beam diffraction. A detailed film characterization is presented in a later chapter.

2.2 BASIC DEFINITIONS

Before further discussion of inorganic resists and the effect of radiation, it is necessary to establish some basic definitions that will be used throughout the remainder of this dissertation.

The terms negative and positive photoresists are derived from photographic practice, but in the case of photoresists have the following specific meanings: A positive photoresist on exposure to light undergoes a chemical transformation that increases its solubility in subsequent developing solutions. A negative photoresist on exposure to light reacts to decrease its solubility in developing solutions. The same definition is also applied to x-ray and electron-beam resists. The term sensitivity characterizes a resist's relative reactivity to an exposure source. The sensitivity of a resist is defined as the exposure energy required to achieve the desired degree of chemical reaction in order to produce a lithographically useful image. Sensitivity increases as the required exposure energy or electron dose decreases.

For positive resists the sensitivity is more specifically defined as the exposure energy or electron dose required to produce complete solubility of the exposed region in a solvent while not

affecting or thinning the unexposed region. For negative resist the definition of sensitivity is more complex. In general, we define the exposure energy or electron dose necessary to produce 50% remaining film thickness as the sensitivity for a negative resist. The relative sensitivity and contrast of resist systems on exposure are best illustrated by characteristic curves analogous to the H & D (after Hurter and Driffield) curves of classical photography, which are plots of developed density versus logarithm of exposure energy. The curve for the As_2S_3 resists is obtained by measuring developed resist thickness relative to its coated thickness as a function of total exposure energy or electron dose received. Such characteristic curves for negative resists are illustrated in Fig. 2.3. The contrast, γ , of a resist is defined as the slope of the linear portion of the logarithm of exposure energy or electron dose E versus remaining film thickness curve and is given by

$$\gamma = |\log \frac{E^0}{E^1}|^{-1}$$

E^0 , E^1 are given in Fig. 2.3.

The resolution of a resist is defined as the maximum number of lines per unit length that can be written under the optimum exposure condition. The units are usually given as lines/mm or alternatively the resolution can be quoted as a minimum linewidth in μm . The resolution capability of a resist is related to the contrast.

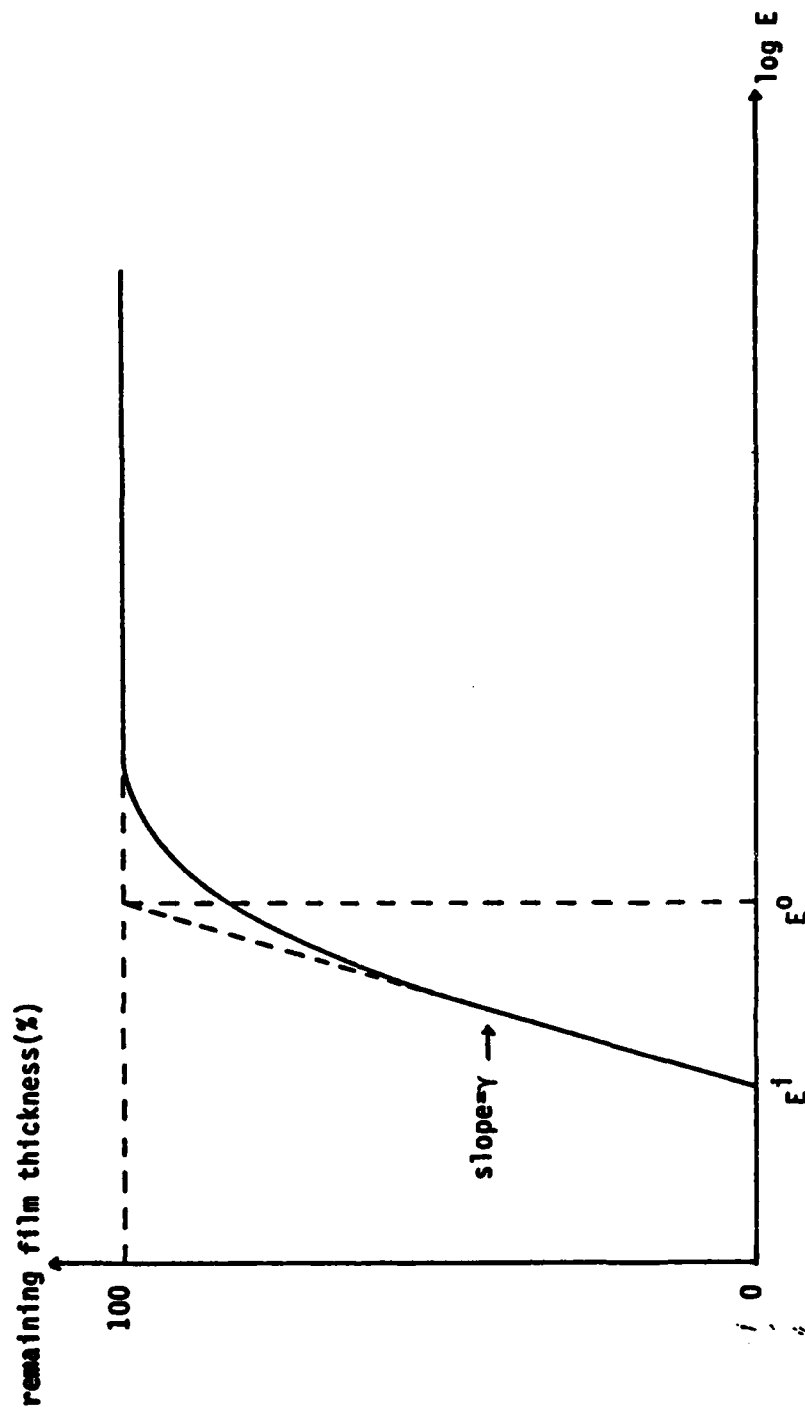


Fig.2.3 Exposure curve for negative resists, and the contrast γ is defined as the slope of the linear portion of the exposure curve.

2.3 SENSITIVITY EVALUATION OF As_2S_3 FILMS WITH RESPECT TO PHOTO-, X-RAY AND ELECTRON-BEAM EXPOSURE

2.3.1 Ultraviolet Exposure

300 nm films of As_2S_3 were used for all of the sensitivity evaluations. For UV exposure, the exposure source was a 200 W high pressure mercury lamp in a Kasper Model 17A mask aligner with a power density of about 90 mw/cm^2 on the sample plane. The samples were exposed for various lengths of time through a quartz mask with a $6 \mu\text{m}$ line width grating and then etched in a 0.03 N NaOH solution. The exposed and unexposed portions of the film etched concurrently but at different etch rates. As_2S_3 behaves as a negative resist since the unexposed portion was etched more quickly. When the unexposed portion was completely removed, the sample was pulled out of the etching solution and rinsed in deionized water. The remaining film thickness in the exposed region was measured with a Sloan Angstrometer. The remaining film thickness versus the logarithm of exposure energy is shown in Fig. 2.4.⁽³⁾ Approximately 30 Joules/ cm^2 is required in order to obtain the maximum of 40% of the initial film thickness. The sensitivity of As_2S_3 is very poor compared to the exposure energy of about 0.2 Joules/ cm^2 or less required for the typical organic polymer resists. For a thinner film, the saturation exposure energy can be reduced. Several other procedures can be employed to improve the sensitivity of the As_2S_3 films. These will be presented in a later section.

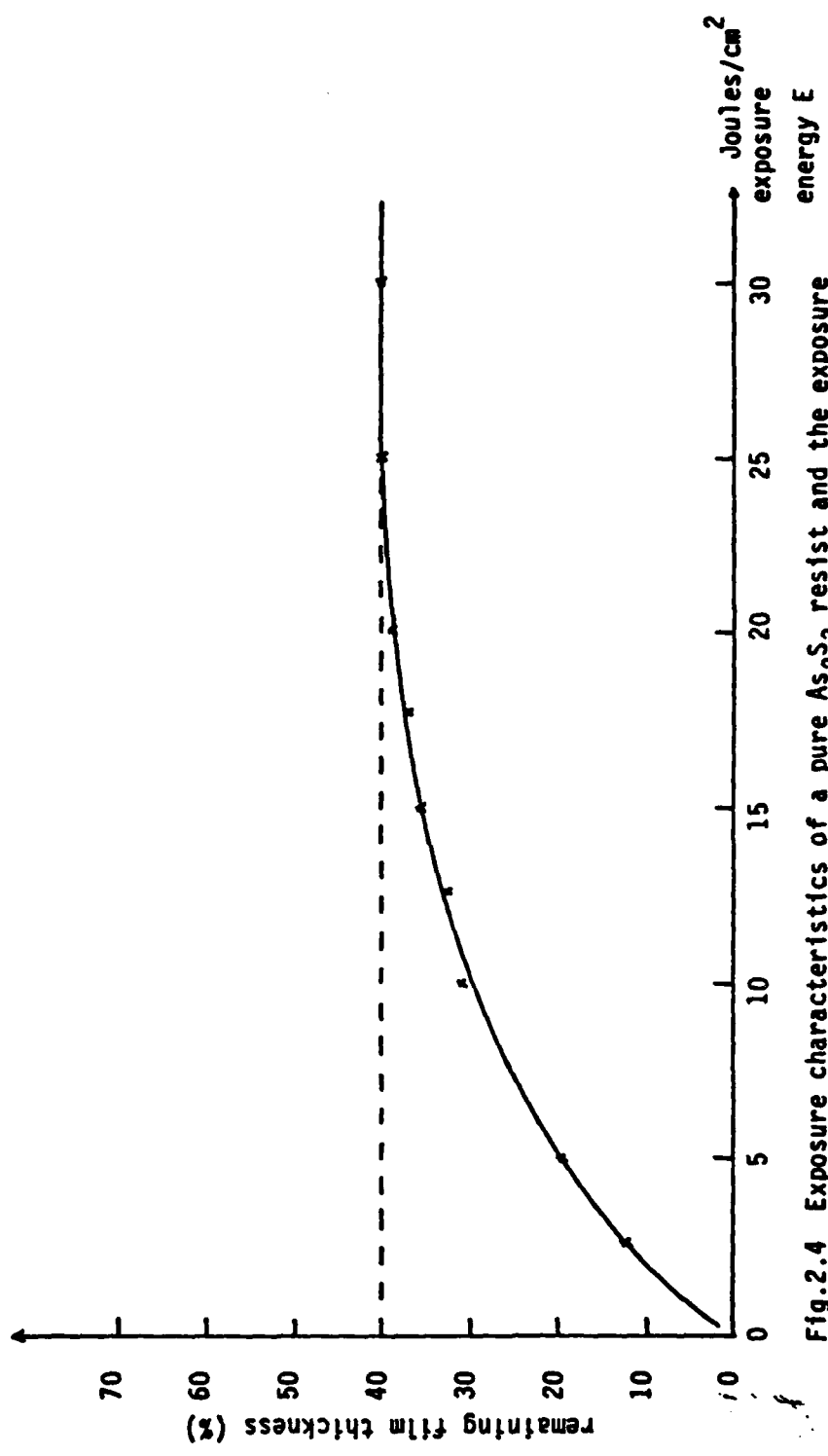


Fig.2.4 Exposure characteristics of a pure As_2S_3 resist and the exposure energy E source is a 200 watts high pressure mercury lamp.

2.3.2 X-Ray Exposure

For x-ray exposure, an x-ray generating system equipped with a 4 kv high voltage supply was used. A schematic of the x-ray exposure system is shown in Fig. 2.5. In this system, high energy electrons are accelerated from a tungsten source and focused by a static magnetic field onto an aluminum target to produce the Al K α x-ray line with wavelength 8.34 Å. The common disadvantage of conventional x-ray sources is the low efficiency. (Efficiency = x-ray power/electron beam power $\leq 10^{-4}$). Today most x-ray generating systems use a rotating anode source⁽⁴⁾ or a synchrotron radiation source⁽⁵⁾. In order to expose a resist selectively, a mask must be used that consists of an x-ray absorbing material, such as gold, patterned on a slightly absorbing substrate. The x-ray mask fabrication technique is described by Kolwicz.⁽⁶⁾ In this work an x-ray mask with a minimum linewidth 0.75 μm , obtained from Hughes Aircraft Incorporated, was used to study the sensitivity and resolution of the As₂S₃ resists. Unfortunately, the sensitivity of As₂S₃ to x-ray radiation is so poor that the image can not be developed even after a 6 hours x-ray exposure. Another reason is the low efficiency of the x-ray generating system. In Sec. 2.5, the x-ray sensitivity of a Ag-As₂S₃ composite resists will be discussed.

2.3.3 Electron-Beam Exposure

Suhara et. al.⁽⁷⁾ have determined that amorphous chalcogenide semiconductor films irradiated by electron beams undergo a change

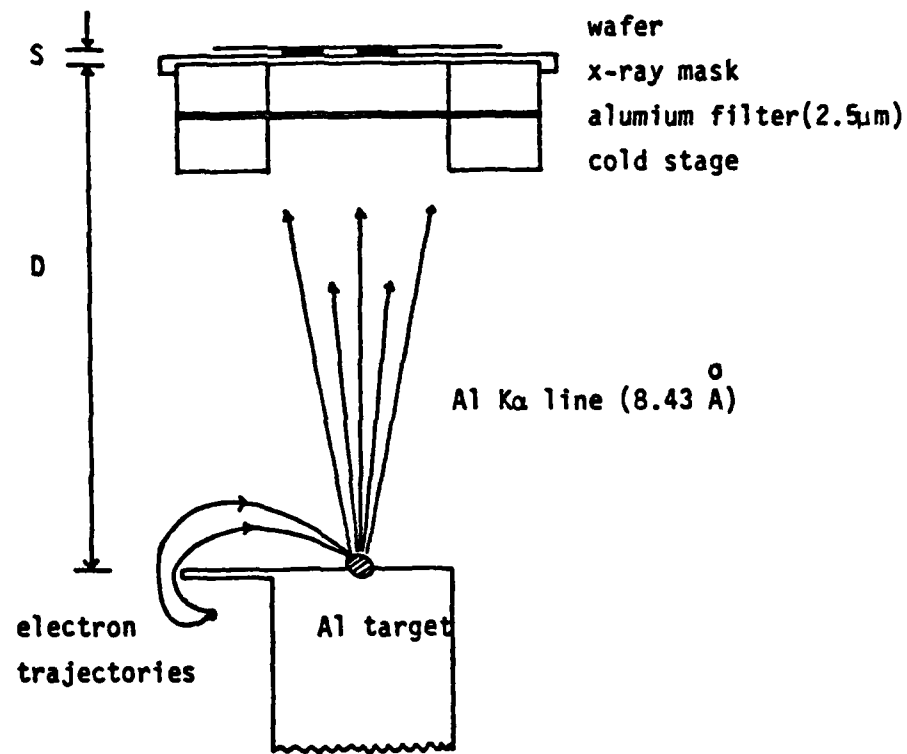
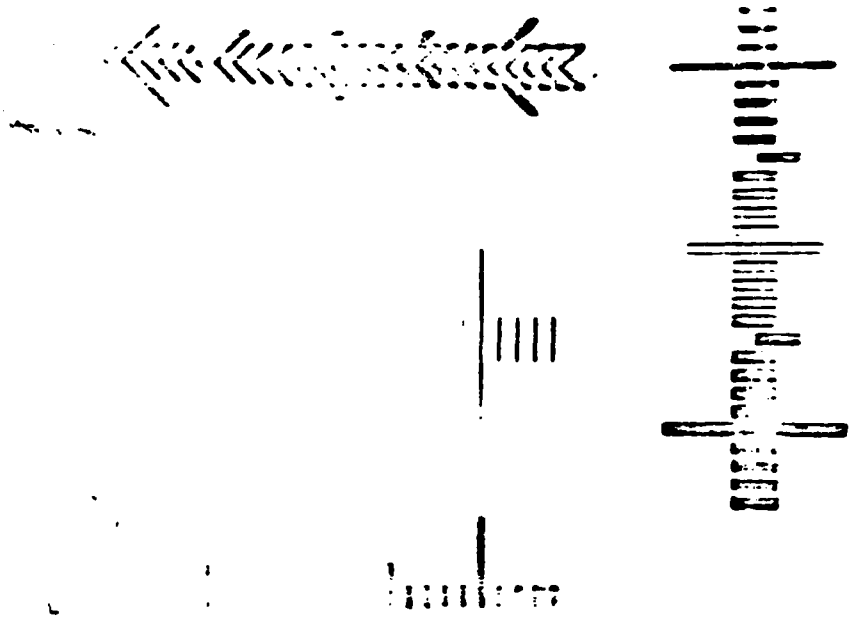


Fig.2.5 Simple x-ray exposure station, where S and D are the mask-wafer and mask-source distances, respectively.

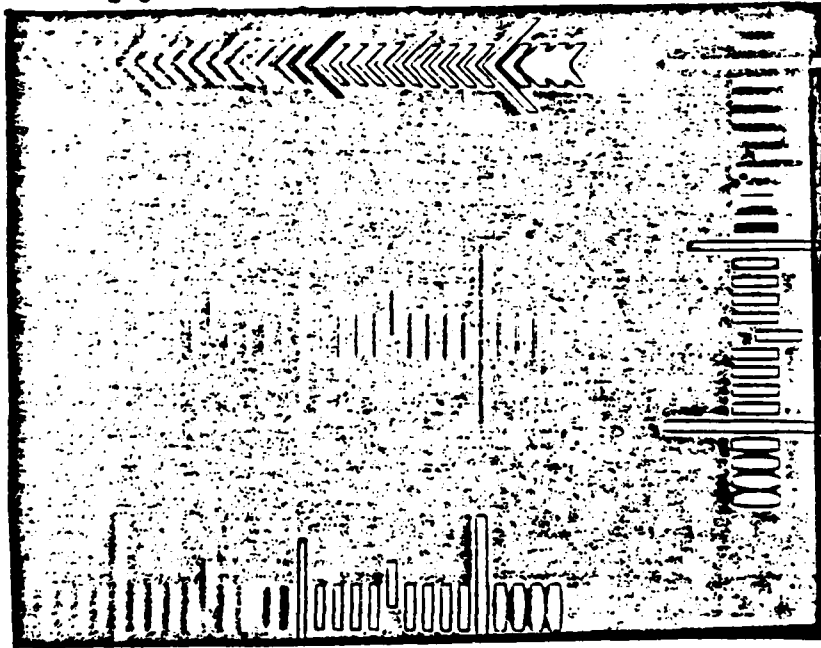
in index of refraction similar to the light-induced refractive index increase. In this section, the effects of electron-beam irradiation and the properties of As_2S_3 based inorganic electron resists are described. Other amorphous arsenic chalcogenide semiconductors, such as Se-Ge, also show the same electron-beam exposure effect. (8-13)

Electron-beam exposure was carried out by Drs. H.T. Yuan and C.H. Shaw of the Central Research Laboratory of Texas Instrument Incorporated. They used a scanning electron system at an accelerating voltage of 20 KV with an electron beam current of $10^{-9} - 10^{-10}$ amperes. The electron dosage ranged from 4×10^{-4} Coul/cm² to 1×10^{-7} Coul/cm². For calibration purposes, one polymethyl methacrylate (PMMA) slice was also exposed on the same electron-beam machine. After exposure, the As_2S_3 films were developed in 0.03 N NaOH aqueous solution to remove the unexposed region. (PMMA was developed in a 40% methyl ethyl ketone in 2-propanol standard solution). In their machine, the electron dosage at optimum PMMA exposure was about 1×10^{-4} coul/cm² with approximately $\pm 5\%$ accuracy. The developed pattern on PMMA is shown in Fig. 2.6. The smallest linewidth in the pattern is about 0.25 μm . The same pattern on As_2S_3 after development is also shown in Fig. 2.6.

The remaining As_2S_3 film thickness versus the logarithm of electron dose was estimated by comparing the remaining As_2S_3 film thickness after development with the calibrated sample having known thickness measured by the Sloan Angstrometer. The results are shown



(a) As_2S_3 film. The minimum linewidth is 0.5 μm .



(b) PMMA resist.

Fig.2.6 Photomicrographs of As_2S_3 (a) and PMMA (b) after electron beam exposure with a beam current of 10^{-10} amp at 20 KV. The As_2S_3 film was developed in 0.03N NaOH for 1 minute.

in Fig. 2.7. One can not directly compare the sensitivity between As_2S_3 and PMMA because PMMA behaves as a positive resist and As_2S_3 as a negative resist under electron beam exposure. However, the As_2S_3 resist has a saturated electron dosage at about 5×10^{-5} Coul/cm² for the maximum of 50% of the initial film thickness. But the contrast in As_2S_3 resists is poorer than PMMA. The same proximity effect is observed in both resists in the higher electron dosage region. The detailed mechanism of the effect is not fully understood at present, however, the most probable interpretation is that the effect may be due to a structural change of the amorphous state under electron beam exposure. No crystallization occurred upon exposure as determined by the scanning electron microscope.

2.4 ETCH RATE DETERMINATIONS AND DIFFRACTION EFFICIENCY OF GRATING IN As_2S_3 FILMS

2.4.1 Etch Rate Determinations in As_2S_3 Films in NaOH Aqueous Solutions

When an As_2S_3 film is etched in a NaOH aqueous solution, using a He-Ne laser at 632.8 nm wavelength as the monitoring beam, the transmitted laser beam intensity will show interference extrema as the film thickness changes. (14-15) If the transmitted beam intensity and the etching time are recorded by a x-t recorder during the etching process, then the etch rate of the film in the solution can be calculated by the formula

$$r = \frac{\lambda \Delta m}{2n_2 \Delta t_e} \quad (2-1)$$

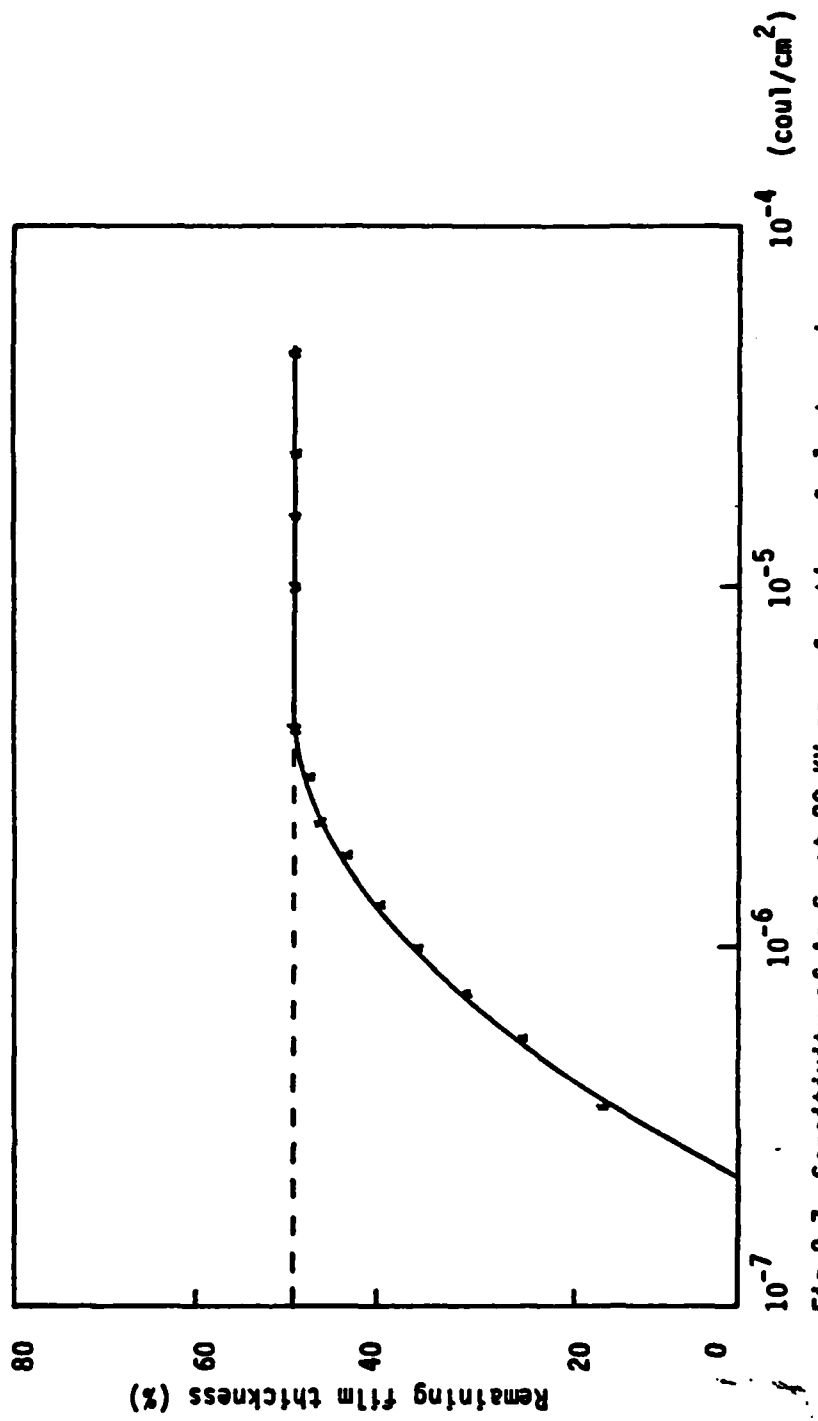


Fig.2.7 Sensitivity of As_2S_3 at 20 kV as a function of electron doses.

provided that the refractive index n_2 of the film is known. Δm is the difference between extrema index and Δt_e is the corresponding etching time. Fig. 2.8 shows the typical observed transmitted light intensity as a function of etching time for an unexposed and an UV exposure-saturated As_2S_3 film 400 nm thick. The etch rates are calculated from Eq. (2-1) to be $r_u = 41 \text{ \AA/sec}$ and $r_s = 25 \text{ \AA/sec}$ for the unexposed and exposure-saturated films at 21°C , respectively. The corresponding refractive index used in the calculation are $n_u = 2.447$ and $n_s = 2.569$, respectively.⁽¹⁶⁾ The etch rate ratio between the unexposed and exposure saturated films is equal to 1.7, giving rise to a maximum of 40% of the initial film thickness remaining. This same technique can also be used to monitor CF_4 plasma etching. This will be described in the next chapter.

2.4.2 Diffraction Efficiency of Gratings in As_2S_3 Films in Plasma Etching

Chang and Hou⁽¹⁷⁾ reported the diffraction efficiency in chalcogenide glass thin films during the liquid-phase chemical etching process. The arrangement of the optical monitoring technique for etching control is shown in Fig. 2.9. A $6 \mu\text{m}$ grating pattern was fabricated by UV exposure through a mask. The first order diffracted beam was monitored by a photodetector. When the 0.03 N NaOH etchant was poured into the cell, the diffraction efficiency as a function of etching time was obtained from a recorder. The diffraction efficiency, n , defined as the ratio of the light intensity diffracted into the

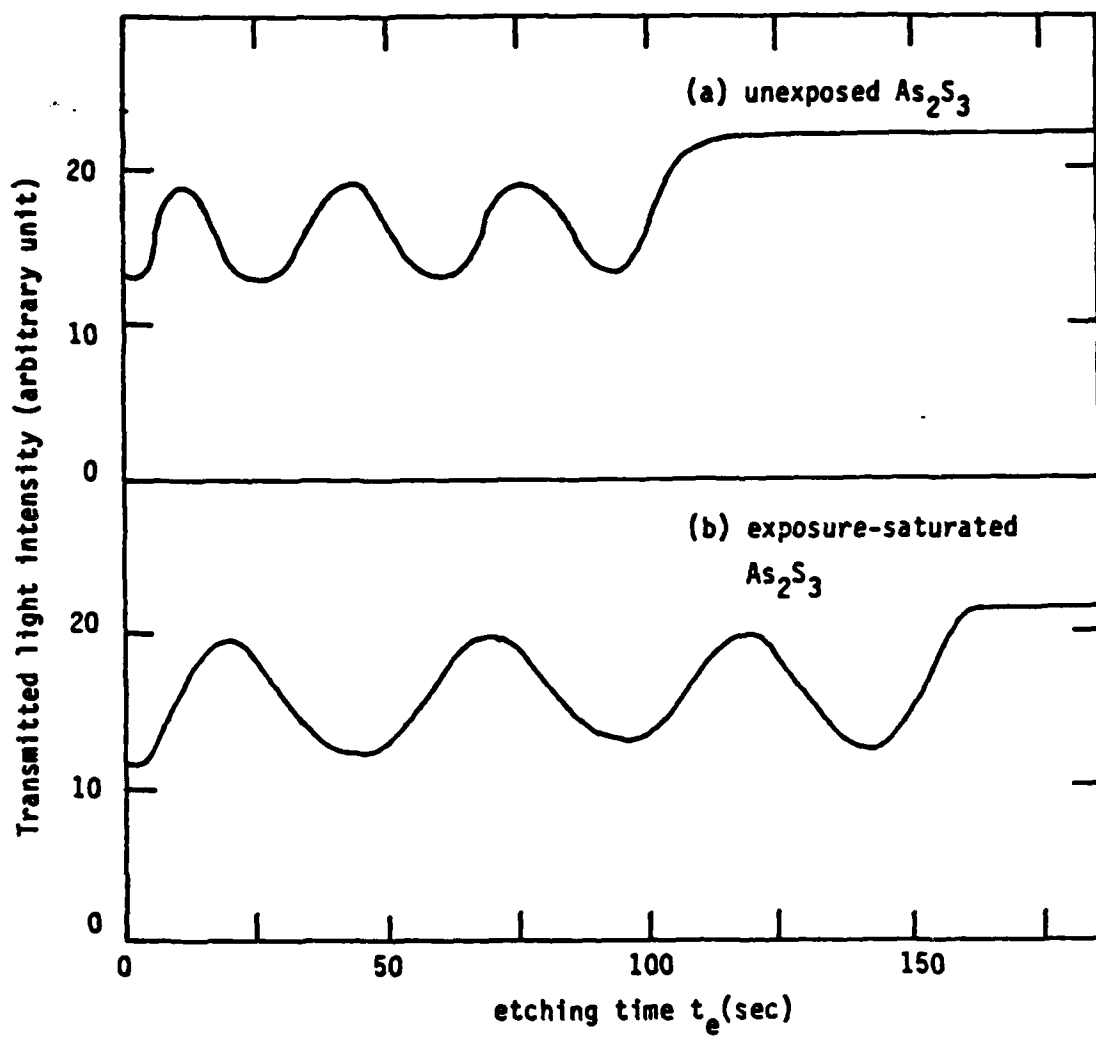


Fig.2.8 The transmitted light intensity as a function of etching time for (a) an exposed As_2S_3 film and (b) an exposure-saturated As_2S_3 film. The exposure source is a mercury lamp at 95 mw/cm^2 and the exposure time is two hours.

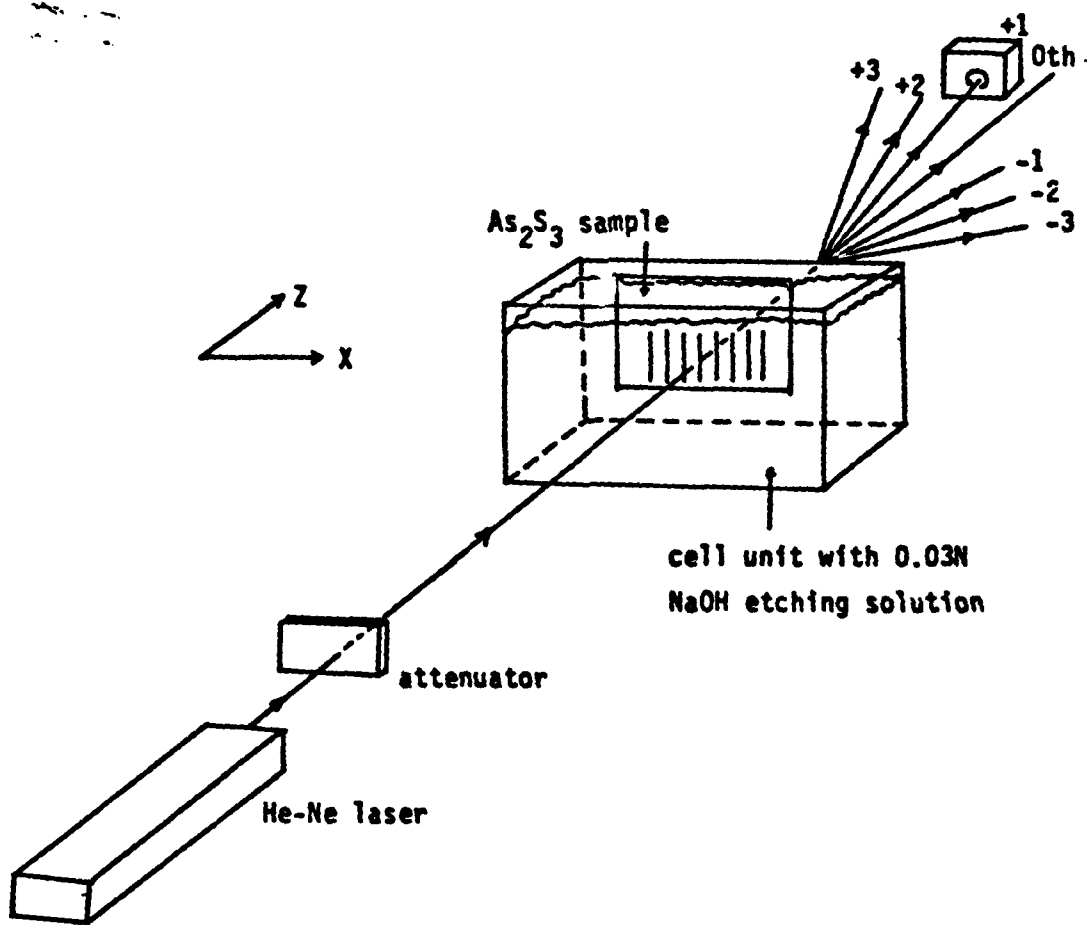


Fig.2.9 Experimental setup for the in-situ optical monitoring of etching process.

first order beam to the light intensity incident on the grating, is equal to⁽¹⁷⁾

$$n(t_e) = | J_1 \left\{ \frac{\pi (n_s - n_1) D(t_e)}{\lambda} \right\}|^2 \quad (2-2)$$

where J_1 is the first order Bessel function, t_e is the etching time, n_1 is the refractive index of etching solution, and D is the peak-to-trough height of the phase grating. For the thin film case etching can be stopped when the diffraction efficiency reaches its maximum and begins to decrease. This maximum diffraction efficiency corresponds to complete removal of the unexposed portion of the film and a clear pattern is delineated. This method is applied to the plasma etching process as well. The CF_4 plasma was used to etch a number of films grown with and without Ag or $AgCl$ overlayers. A $6 \mu m$ -grating was fabricated in these various films. The resulting diffraction efficiencies are given in Fig. 2.10. The detailed experimental conditions are given in the next chapter. The maximum diffraction efficiency η for the Ag-doped As_2S_3 in the composite film structures is much higher than the undoped As_2S_3 sample. The complex appearance of the diffraction efficiency curves is due to the multiple internal reflection resulting from the As_2S_3 film and the substrate interface. In Fig. 2.10 (b), the diffraction efficiency curve does not show the interference effect. That is because the exposed portion on the Ag-overcoated As_2S_3 film is almost unetchable in the CF_4 plasma so that the thickness on the exposed portion remains the same during the etching process.

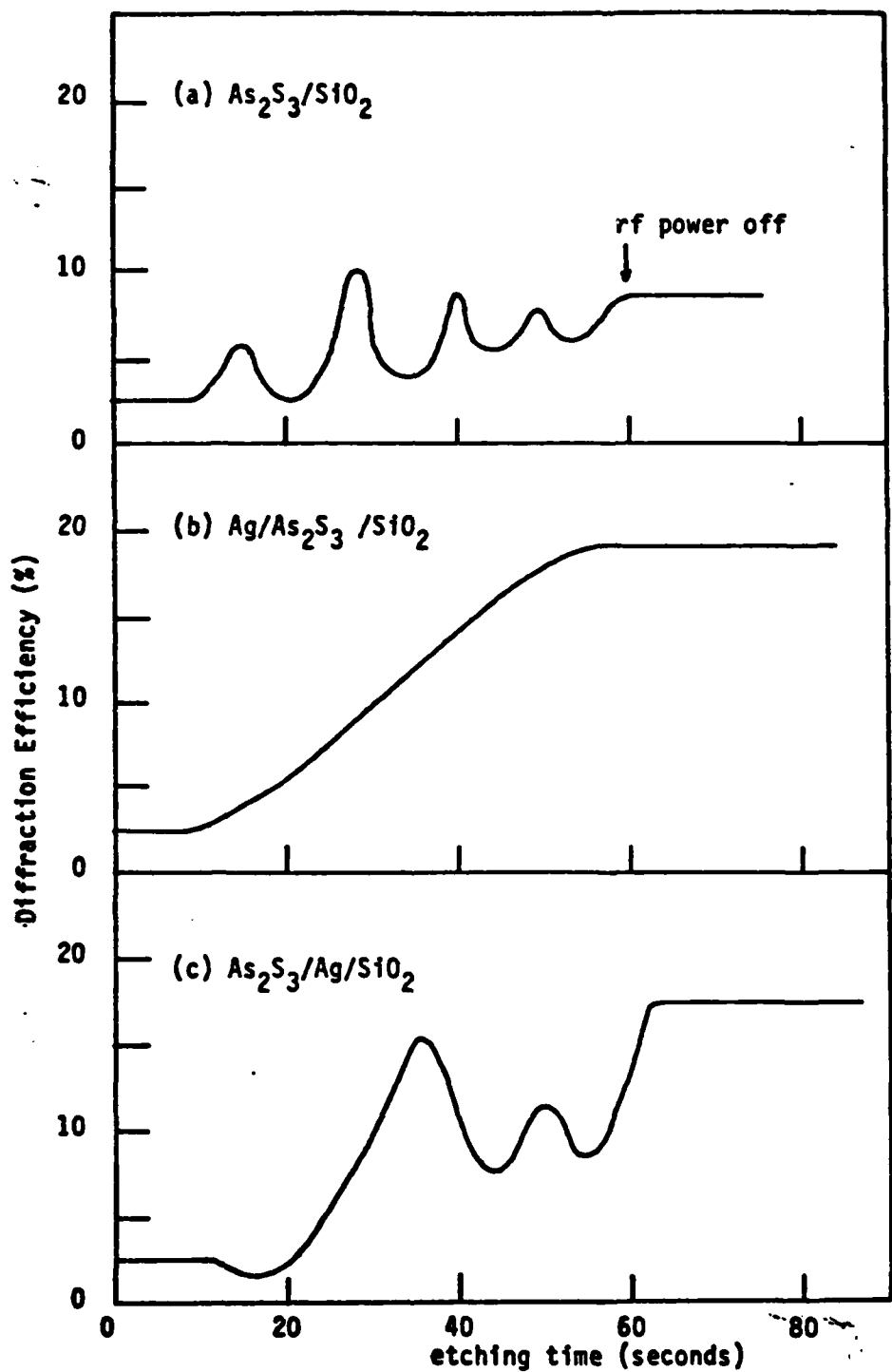


Fig.2.10 The grating diffraction efficiency as a function of etching time in a CF_4 plasma.

2.5 Ag-DOPED As₂S₃ COMPOSITE RESISTS

The observation of Ag photodoping in amorphous chalcogenide glass films goes back at least to 1964. In a study of photodecomposition of PbI₂, Tubb et. al.⁽¹⁸⁾ observed that the electron beam induced a chemical reaction between PbI₂ and an aluminized substrate. In 1966 Kostyshin et. al.⁽¹⁹⁾ extended the study of photodecomposition to many other compounds, such as CuI, CuCl, As₂S₃, Sb₂S₃, PbS, CdS and SbI₃. In their paper, they reported that films of these compounds deposited on metal substrates were capable of giving a visible image during the process of exposure itself, without additional heating. They believed that the photographic sensitivity of these semiconducting films is the consequence of photochemical changes in the substance of the film, including photodissociation of the film material, mutual diffusion of the components of the film and the substrate, and the formation of new compounds. These authors also displayed high-quality optical images from PbI₂-Ag and As₂S₃-Ag systems. This phenomenon is now generally referred to as photodoping and has been exploited by many researchers.⁽²⁰⁻³⁸⁾

2.5.1 Ag-doped As₂S₃ Composite Resists

It was noted above that the sensitivity of As₂S₃ resists is poor compared to that of organic polymer photoresists. Since metallic silver is a fast diffuser in As₂S₃ films upon light exposure, metallic Ag-overcoated As₂S₃ films were first used to increase the

sensitivity for patterning purposes. Although the sensitivity is increased, the problem of silver auto-doping during the metallic silver evaporation process and following steps prevented the use of metallic Ag-As₂S₃ composite resists for microlithographic applications. Recently Kolwicz and Chang⁽³⁹⁾ suggested a composite resist structure for sensitivity enhancement with a layer of AgCl on top of the As₂S₃ film. They found that the sensitivity of the composite film is a factor of ten better than that of the undoped As₂S₃ film under ultraviolet exposure. Hwang et. al.⁽⁴⁰⁾ applied a pulsed electric field during UV exposure and further increased the sensitivity of the AgCl-As₂S₃ composite resist to within the same order of magnitude of that of organic polymer photoresists. In this study no attempt was made to improve the quality of evaporated silver halide films. The details of the preparation of evaporated films of silver halides are reported by Junod et. al.⁽⁴¹⁾ The objective of this section is to study the sensitivities of this AgCl-As₂S₃ composite resists with respect to ultraviolet, x-ray and electron-beam exposure. The techniques developed in the previous sections are applied for the characterization of this composite resist structure.

2.5.2 The Evaluation of AgCl-As₂S₃ Composite Film Resists

Photolithography using an AgCl-As₂S₃ composite resist suggested by Kolwicz and Chang⁽³⁹⁾ is schematically shown in Fig. 2.11 together with that of pure As₂S₃ resists. The thickness of the As₂S₃ film is about 300 nm and the thickness of AgCl is about 20 nm. Both

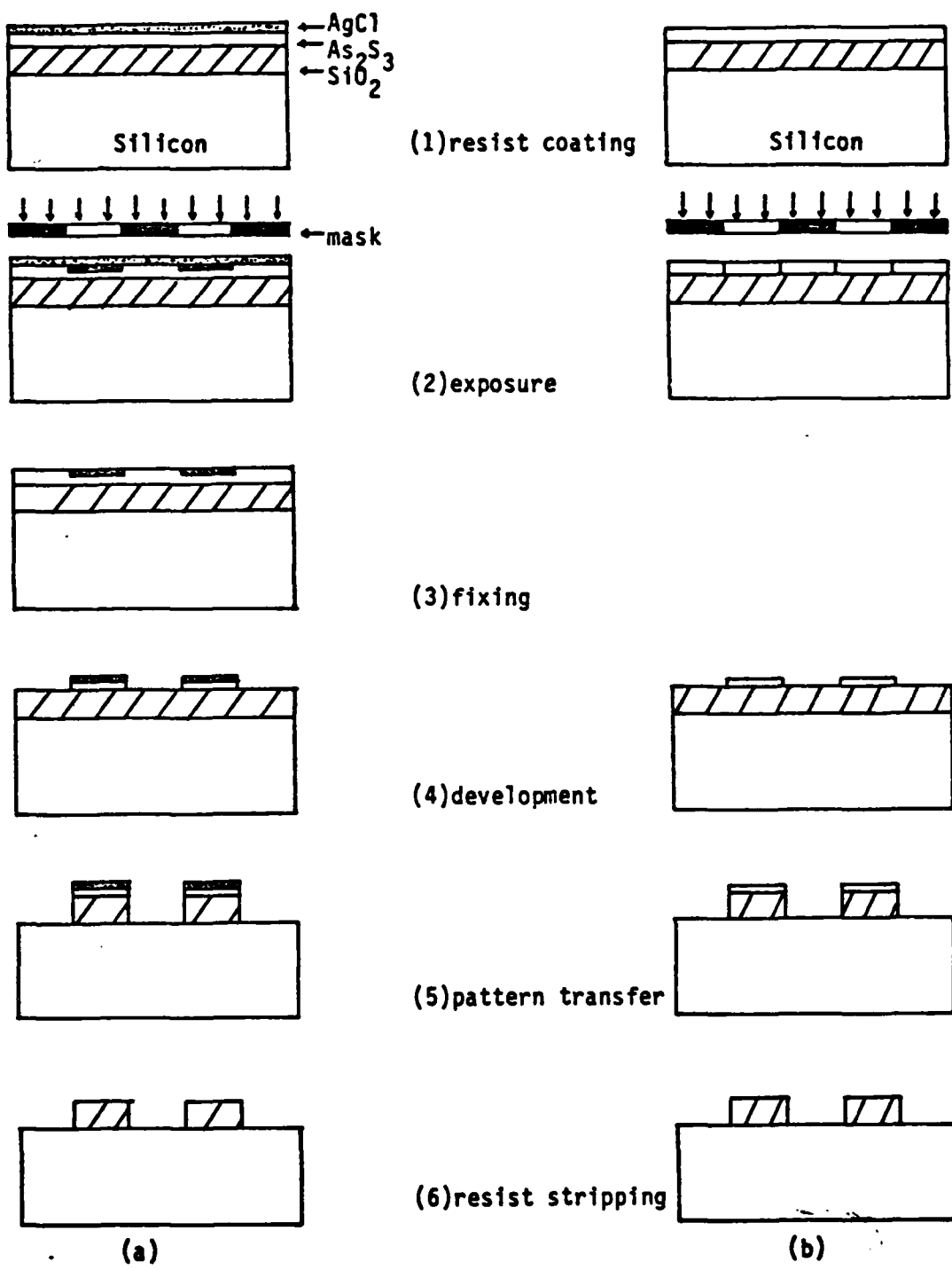
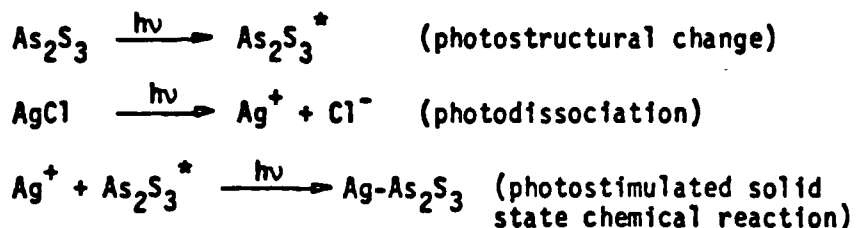


Fig.2.11 Photolithography process of (a)a $\text{AgCl}-\text{As}_2\text{S}_3$ composite photoresist and (b)an As_2S_3 resist.

films were vacuum evaporated. Upon ultraviolet exposure, at least a three-step process is believed to take place: A photostructural change⁽⁴²⁾ in the As_2S_3 film, a photodissociation in silver halide film⁽⁴³⁾, and a photostimulated solid state chemical reaction^(21,44) between the photodissociated silver halide and the photosensitive chalcogenide glass film. This process can be expressed as

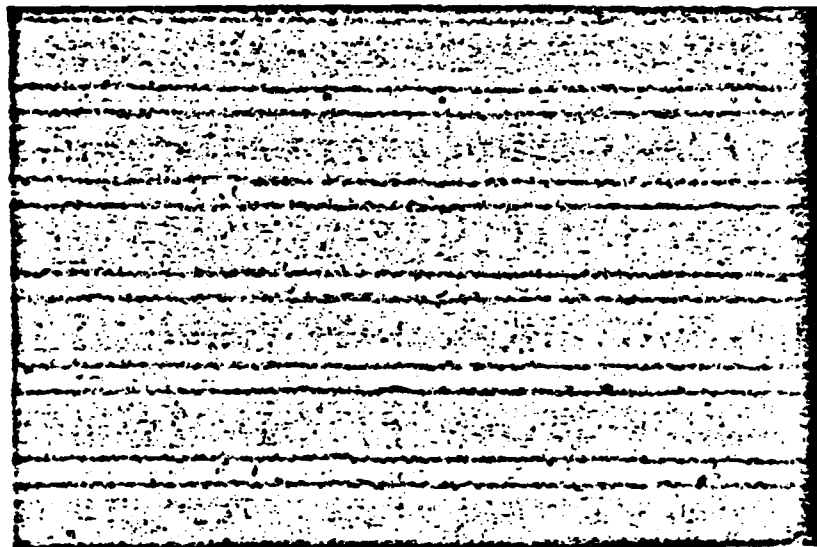


The detailed mechanisms of the photodoping process will be discussed in a later chapter.

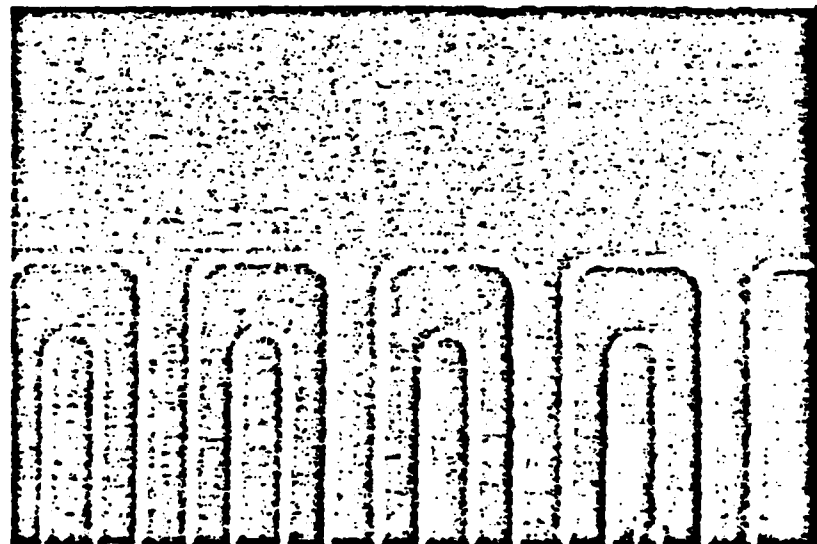
The exposed area thus forms a material that is resistant to the etchant for the chalcogenide glass film. A fixing-step after exposure is required to remove the unexposed AgCl before the development process. Fixing is achieved by dipping the sample into a dilute aqueous solution consisting of 1 part of Kodak Rapid fixer A and 3 parts of deionized water for 5 minutes. A negative image is obtained. The characteristic curve of the remaining thickness of the $\text{AgCl}-\text{As}_2\text{S}_3$ composite resist versus the logarithm of UV exposure energy is shown in Fig. 2.4 together with the characteristic curve for the pure As_2S_3 resist for comparison. A 100% remaining film thickness is obtained at an exposure energy about 3 Joules/cm² which shows that the composite film is much more sensitive than the pure As_2S_3 film. The contrast of

this composite resist is also improved. Hwang et. al.⁽⁴⁰⁾ demonstrated that the sensitivity of $\text{AgCl}-\text{As}_2\text{S}_3$ composite resists can be increased further when a pulsed electric field is applied across the composite resist during light exposure. The sample is placed on an aluminum plate which, together with the high conductivity Si wafer substrate, acts as the bottom electrode. The top electrode is an ultraviolet transparent, electrically conductive tin oxide coated borosilicate glass plate. In order to increase the sensitivity, the top electrode must be at a positive potential with respect to the bottom electrode. Conversely, reversed polarity of the pulsed electric field will reduce the sensitivity. This is understandable if the $\text{AgCl}-\text{As}_2\text{S}_3$ resist sensitivity depends on the speed of silver ion transport and the depth of silver ion penetration into the As_2S_3 . A dc electric field has no effect on the sensitivity of the composite resist. Possibly it is due to the screening of the field by the silver ions in the interface between AgCl and As_2S_3 films that prevents the silver ion going into the As_2S_3 film. Fig. 2.12 shows the patterns defined by UV exposure and developed by dry and wet etching processes, respectively.

The sensitivity of the $\text{AgCl}-\text{As}_2\text{S}_3$ composite resist is also superior to As_2S_3 for x-ray and electron-beam exposure. This study shows that the sensitivities of $\text{AgCl}-\text{As}_2\text{S}_3$ resists to x-ray and electron -beam exposure are at least one order of magnitude better than that of the As_2S_3 films. Fig. 2.13 (a) shows the pattern on the composite resist after x-ray exposure for 2 hours and developing by CF_4 plasma. For the electron-beam exposure the sensitivity of the AgCl -



(a)



(b)

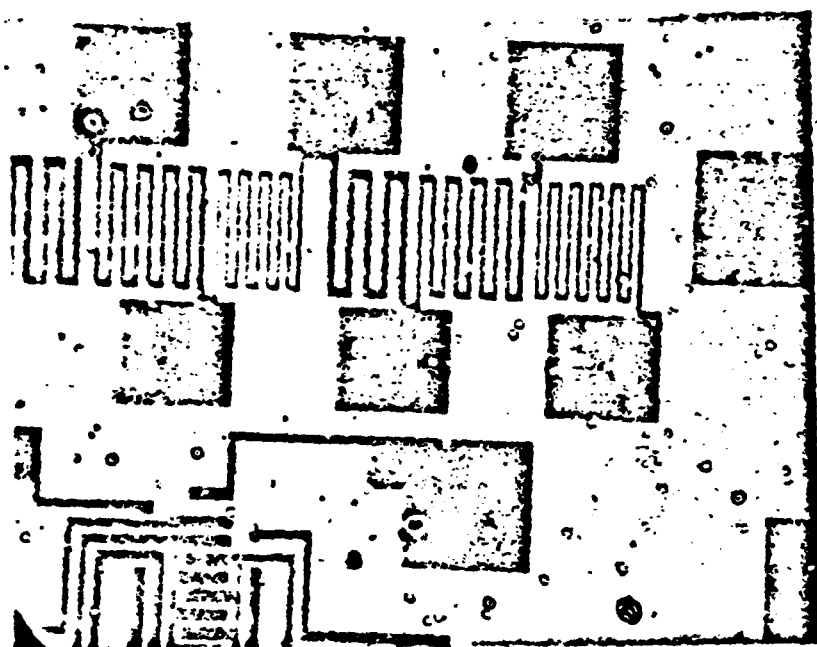
Fig.2.12 UV exposure: AgCl (200 Å)/ As_2S_3 (3000 Å)

(a) 0.03 N NaOH wet etching.

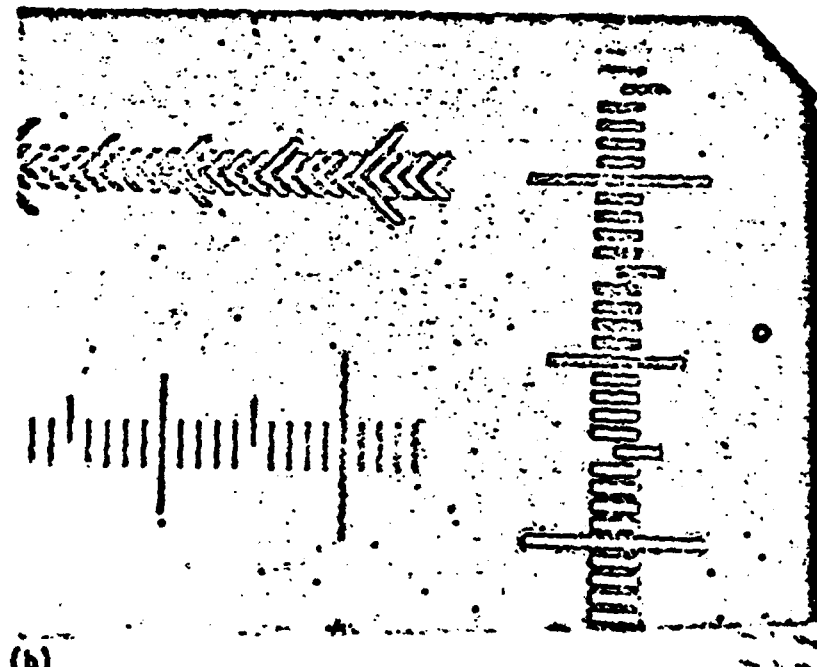
(b) 50 watts, CF_4 plasma etching.

As_2S_3 composite resist is estimated at about 10^{-6} Coul/cm². Fig. 2.13 (b) shows the pattern developed by CF_4 plasma. Upon x-ray and electron-beam exposure, this composite resist not only shows higher sensitivity, but also higher contrast. It is shown that a thin cap of a Ag-doped As_2S_3 layer forming near the surface in the exposed region of the $\text{AgCl}-\text{As}_2\text{S}_3$ resist is sufficient to transfer the pattern into the underlying film. Another advantage of this composite resist is that the resolution available in the amorphous As_2S_3 film is retained in the composite structure.⁽³⁾ A grating pattern with a periodicity of 0.27 μm was fabricated and a minimum linewidth of 0.1 μm was resolved by Hou and Chang.⁽⁴⁵⁾ The high resolution ability of the composite resist is also shown in x-ray and electron-beam exposures. Nagai et. al.⁽⁴⁶⁾ first demonstrated the use of Ag-doped Se-Ge glass films as an inorganic resist and a resolution of better than 30 nm was reported for this resist by Tai et. al.⁽⁴⁷⁾ There is no doubt that a few hundred angstroms linewidth could be resolved in the $\text{AgCl}-\text{As}_2\text{S}_3$ composite resist if more advanced exposure facilities were available in this laboratory.

The $\text{AgCl}-\text{As}_2\text{S}_3$ composite resist has been shown to be a promising structure for pattern generation applications. However, the phenomenon of Ag photodoping in As_2S_3 films and other chalcogenide glass films, such as Ge_2S_3 , As_2Se_3 , etc., is complex. To date there is neither a complete description of this process nor a real understanding of the mechanism. In Chapters 4 and 5, the Ag doping process will be further studied with different characterizing techniques



(a)



(b)

Fig.2.13 AgCl(200 Å)/As₂S₃(3000 Å) composite resist (a) after Al K α x-ray exposure and CF₄ plasma etching. The minimum linewidth is 2 μ m, and (b) after electron beam exposure at 20 KV and CF₄ etching. The minimum linewidth is 0.5 μ m.

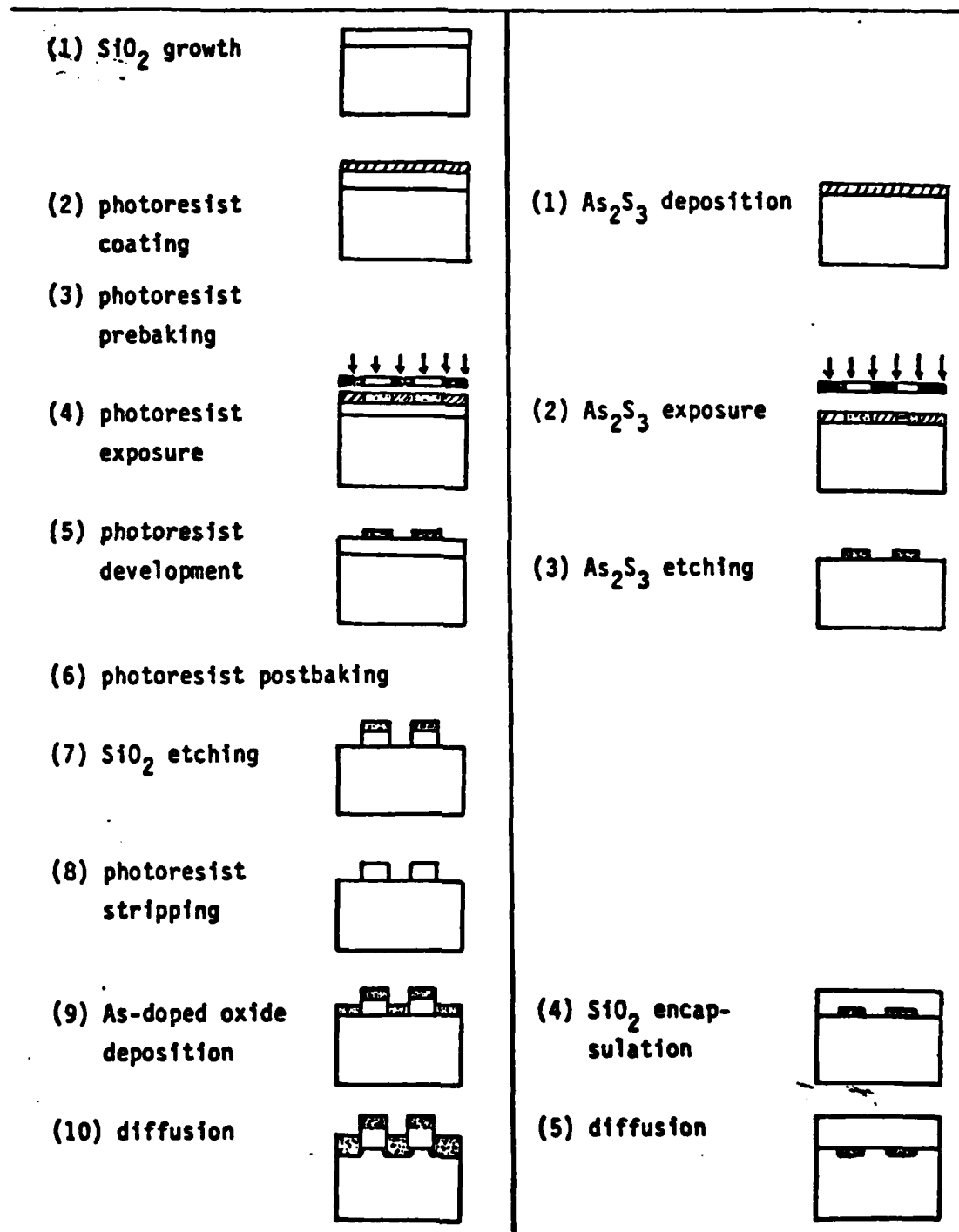
together with the presentation of our interpretation of this complicated process.

2.6 DIRECT DEVICE FABRICATION

Recently, amorphous chalcogenide semiconductors have received increasing attention as promising materials for various novel applications such as an inorganic resist for microlithography, optical integrated circuits and solid state ion-selective sensors in electrochemistry. In this section the potential applications in device fabrication will be briefly discussed.

The As_2S_3 inorganic resist contains arsenic, a dopant for silicon device fabrication. As a photoformable dopant it can be used as a diffusion source after patterning. Thus a considerable simplification in the overall device processing is expected. Fig. 2.14 shows the schematics. A mask aligner can be used for pattern generation. After patterning the remaining As_2S_3 film defines the diffusion region. Since the diffusion source As_2S_3 has a low melting temperature of about 400°C and high vapor pressure above 250°C which are well below the temperature needed in the diffusion process, it is necessary to encapsulate the source with SiO_2 or Si_3N_4 layers of 500 nm thickness produced either by electron-beam sputtering or a low temperature low pressure plasma deposition technique. The S-containing As_2S_3 is not suitable as a direct dopant source since the sulfur vapor will attack the silicon surface at high temperature. One way to avoid the sulfur

Fig.2.14 Comparison of the conventional device fabrication processes and the proposed device fabrication processes using As_2S_3 as a source.



vapor erosion is to convert the remaining As_2S_3 film into As_2O_3 with an oxygen plasma, and then encapsulate the film with a plasma-deposited SiO_2 or Si_3N_4 layer at about 150°C. This will be described in the next chapter. In the low pressure plasma deposition system, the sample temperature can be controlled through a water-cooled silicon-carbide-coated graphite substrate holder and the distance between the sample and the center of the induction coil. The details of the plasma deposition technique is described elsewhere.⁽⁴⁸⁾ The differential etching of As_2S_3 in a CF_4 plasma and the conversion of the As_2S_3 film into As_2O_3 in an O_2 plasma have been demonstrated in this laboratory.^(49,50) A low pressure plasma deposition system has been built and a plasma-deposited Si_3N_4 layer has been prepared by using a mixture of silane and ammonia gas with Ar as a carrier gas. A complete dry processing for device fabrication is thus possible. A simple p-n junction has been fabricated in this way by Chang et. al.⁽⁵⁰⁾

References to Chapter 2

1. N. Kh. Abrifkosov, V.F. Bankina, L.V. Porstskaya, L.Z. Shelimova, E.V. Skudnova, "Semiconducting II-VI, IV-VI, and V-VI Compounds", Plenum Press, N.Y. (1969).
2. N. Hansen, K. Anderko, "Constitution of Binary Alloys", 2nd ed., McGraw-Hill, N.Y., (1958).
3. T.W. Hou, Ph.D. Thesis, University of Pennsylvania, (1979).
4. G. Wardly, E. Munro, R.W. Scott, Intern. Conf. on Microlithography, p. 217, Paris, (1977).
5. C. Kunz, Vacuum Ultraviolet Radiation Physics, ed. by E.E. Koch, R. Haensel, C. Kunz, Vieweg, Braunschweig, p. 753, (1974).
6. K.D. Kolwicz, M.S. Thesis, University of Pennsylvania, (1978).
7. T. Suhara, H. Nishihara, J. Koyama, Jpn. J. Appl. Phys., 14, 1079, (1975).
8. H. Nagai, A. Yoshikawa, Y. Toyoshima, O. Ochi, Y. Mizushima, Appl. Phys. Lett., 28, 145, (1976).
9. H. Nishihara, Y. Handa, T. Shara, J. Koyama, Appl. Opt., 17, 2342, (1978).
10. T. Suhana, Y. Handa, H. Nishihara, J. Koyama, Jpn. J. Appl. Phys., 16, 1877, (1977).
11. A. Yoshikawa, O. Ochi, H. Nagai, Y. Mizushima, Appl. Phys. Lett., 29, 677, (1976).
12. K.Y. Ng, M.S. Thesis, University of Pennsylvania, (1978).
13. H. Nishihara, IOCC'77, 02-4, p. 587, (1977).
14. M. Born, E. Wolf, "Principles of Optics", p. 627, 4th ed., Pergamon Press (1970).
15. E.D. Palik, R.T. Holm, in "Nondestructive Evaluation of Semiconductor Materials and Devices", ed. by J.N. Zemel, NATO Advanced Study Institute, Plenum, (1979).
16. S.A. Keneman, Ph.D. Dissertation, University of Pennsylvania, (1974).

17. M.S. Chang, T.W. Hou, Thin Solid Films, 55, 463, (1978).
18. M.R. Tubbs, A.J. Forty, Brit. J. Appl. Phys., 15, 1553 (1964).
19. M.T. Kostyshin, E.V. Mikhailovskaya, P.F. Romanenko, Sov. Phys. Solid State, 8, 451, (1966).
20. I. Shimizu, H. Sakama, H. Kokado, E. Inoue, Bull. of the Chem. Soc. of Jpn., 44, 1173, (1971).
21. I. Shimizu, H. Sakuma, H. Kokado, E. Inoue, Photogr. Sci. and Eng., 16, 291, (1972).
22. A. Matsuda, M. Kikuchi, Proc. of the 4th Conf. on Solid State Dev., Tokyo, (1972).
23. I. Shimizu, H. Kokado, E. Inoue, Bull. of the Chem. Soc. of Jpn., 46, 3662, (1973).
24. H. Mizuno, K. Tanaka, M. Kikuchi, Solid State Commun., 12, 999, (1973).
25. I. Shimizu, H. Sakuma, H. Kokado, E. Inoue, Bull. of the Chem. Soc. of Jpn., 46, 1291, (1973).
26. A. Matsuda, M. Kikuchi, Solid State Commun., 13, 401, (1973).
27. I. Shimizu, H. Kokado, E. Inoue, Photogr. Sci. and Eng., 19, (1975).
28. I. Shimizu, H. Kokado, E. Inoue, Photogr. Sci. and Eng., 19, 141, (1978).
29. H. Kokado, I. Shimizu, T. Tatsuko, E. Inoue, J. Of Non-Cryst. Solids, 21, 225, (1976).
30. M. Kasai, Y. Hajimoto, J. Appl. Phys., 47, 3894, (1976).
31. D. Goldschmidt, P.S. Rudman, J. of Non-Crystl. Solids, 22, 229, (1976).
32. E. Inoue, H. Yasujima, H. Kokado, Photogr. Sci. and Eng., 21, 142, (1977).
33. K. Chatan, I. Shimizu, H. Kokado, E. Inoue, Jpn. J. Appl. Phys., 16, 389, (1977).
34. A. Buroff, P. Simidchieva, K. Kolev, R. Stoycheva, Int. Conf. on Photogr. Sci., p. 243, (1978).

35. I. Shimizu, T. Ikeda, E. Inoue, *Ibid.*, p. 235, (1978).
36. R. Ishikawa, *Solid State Commun.*, 30, 99, (1979).
37. B.I. Boltaks, T.D. Dzhafarov, V. Kh. Kudoyarova, N.F. Kartenko, R.M. Imamov, A.A. Obraztsov, *Sov. Phys. Semicond.*, 13, 23 (1979).
38. V. Kh. Kudoyarova, T.D. Dzhafarov, M.D. Mikhailov, *Sov. Phys. Semicond.*, 13, 1191, (1979).
39. K.D. Kolwicz, M.S. Chang, *J. Electrochem Soc.*, 127, 135, (1980).
40. M.S. Chang, H.D. Hwang, J.T. Chen, *Extended Abstr. Electrochem. Soc.*, 80-1, 692, (1980).
41. P. Junod, M. Hediger, B. Kilchoy, R. Steiger, *Photogr. Sci. and Eng.*, 23, 266, (1979).
42. J.P. deNeufville, in "Optical Properties of Solid-New Developments", ed. by B.O. Seraphin, North-Holland, Amsterdam, (1976).
43. J.P. Ballantyne, W.C. Nixon, *J. Vac. Sci. Technol.*, 10, 1094, (1973).
44. J. Malinowski, A. Buroff, *Contem. Phys.*, 19, 99, (1978).
45. T.W. Hou, M.S. Chang, *Appl. Optics*, 18, 1753 (1979).
46. H. Nagai, A. Yoshihawa, Y. Toyoshima, O. Ochi, T. Mizushima, *Appl. Phys. Lett.*, 28, 145, (1976).
47. K.L. Tai, L.F. Johnson, D.W. Murphy, M.S.C. Chung, *Extended Abstr. Electrochem. Soc.*, No. 94, May, (1979).
48. C.-E. Morosanu, *Thin Solid Films*, 65, 171, (1980).
49. M.S. Chang, J.T. Chen, *Appl. Phys. Lett.*, 33, 897, (1978).
50. M.S. Chang, T.W. Hou, J.T. Chen, K.D. Kolwicz, J.N. Zemel, *J. Vac. Sci. Technol.*, 16, 1973, (1979).

CHAPTER 3

PLASMA ETCHING OF AS₂S₃ FILMS

Recent developments in lithographic techniques have permitted a reduction in feature size in photo, x-ray, and electron sensitive resist masks into a range where conventional liquid phase chemical etching is no longer a viable means of transfer of the resist pattern into underlying inorganic material. Accordingly, there has been a growing emphasis on the use of gas phase, plasma-assisted etching methods, which offer the potential for very high resolution pattern transfer. This potential is linked to the fact that charged particles from the plasma are directed onto the surface being etched in such a manner that the vertical etch rate can be made to greatly exceed the lateral etch rate (i.e., anisotropic etching).

Under the generic title "Plasma-assisted etching" will be included milling, sputter-etching, reactive ion etching, and plasma etching. Although all of these techniques utilize plasma activated species, the mechanisms involved in the etching processes differ. Ion etching (ion milling or sputter-etching) is a physical process in which high energy (typically several hundred or a few thousand ev) noble gas ions are directed at the film surface and etching occurs by momentum-transfer while plasma etching occurs primarily by chemical reaction. Between these two extremes is a parameter space referred to as reactive ion

etching (RIE). In this mode, reactive gases are used and substrates are exposed to ion energies of several hundred electron volts. Ion energies are sufficient to produce anisotropic etching but are not high enough to produce significant physical sputtering rates. In ion milling, the ions are generated in a plasma far from the substrate and are subsequently accelerated, while in sputter-etching the substrate is an integral part of the cathode in a parallel plate discharge.

Plasma etching employs a glow discharge to generate the active species from a relatively inert molecular gas. The active species are transported to the substrate where they react to produce volatile products. In general, plasma etching is carried out using a higher pressure discharge than is normal for ion etching methods and etching occurs predominantly by direct chemical reaction. Also the plasma etch rate is far higher than in ion milling. Plasma-assisted etching techniques have been intensively developed in the past few years and several review articles have been published.⁽¹⁻¹⁴⁾ A summary of dry etching processes is shown in Table 3.1. The differences between the wet-chemical and dry etching processes is given in Fig. 3.1.

In order to understand the etching mechanism in the plasma discharge will be given in Section 3.2. The plasma etching systems which include barrel-and parallel-plate-type reactors are discussed in detail in Section 3.3. An in-situ double-beam monitoring technique is also described in this section. The details of the plasma etching of As_2S_3 films are presented in Section 3.4. The macroscopic modeling of the

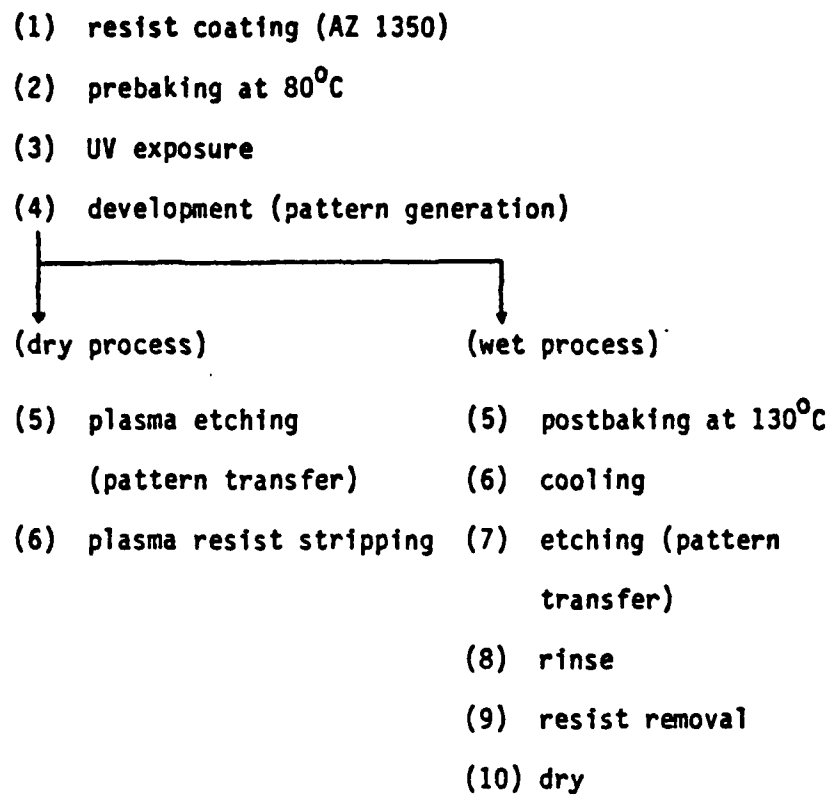


Fig.3.1 Comparison of dry and wet etching processes

Table 3.1 Dry etching processes

dry etch	etch mode	etchant	directionality	system	mechanism
plasma etch	excited etch gas	radical	isotropic	etch tunnel	chemical
	plasma etch	radical	isotropic	barrel	chemical
sputtering etch	reactive ion etch	reactive ion	anisotropic	parallel plate	physical and chemical
	sputtering etch	ion	anisotropic	parallel plate	physical
ion beam etch	reactive ion beam etch	reactive ion	anisotropic	parallel plate	physical and chemical
	ion beam etch	ion	anisotropic	parallel plate	physical

* Source: H.Abe and H.Nakata: Electrochem.Soc. Abstr., no 86, May (1980)

dependence of plasma etch rates on the gas flow rates and pressures together with the tentatively proposed chemical reactions of As_2S_3 thin films in the CF_4 plasma are given in the following section. The plasma oxidation of As_2S_3 films produces crystalline As_2O_3 and a phenomenological explanation is presented in the final section.

3.2 BASIC CHEMICAL AND PHYSICAL PHENOMENA IN LOW PRESSURE PLASMA

A plasma can be loosely defined as an assembly of positively and negatively charged particles which is electrically neutral on a macroscopic scale. The plasma used for semiconductor applications is produced by applying a high-frequency electric field across a body of gas. The discharge is initiated when an electron is released by some means, such as photoionization or field emission, in a gas to which an electric field is applied. The free electrons gain energy from the electric field and lose this energy through collisions with neutral gas molecules. This transfer of energy to the molecules leads to the formation of a variety of new species including metastables, atoms, free radicals, and ions. These products are active chemically and can serve as precursors to the formation of new stable compounds. The reactions of plasma produced species with gaseous or solid materials gives rise to either the deposition (i.e., plasma deposition) or etching (i.e., plasma etching) of thin film. Fundamentals of plasma chemistry and physics related to the plasma etching is given below.

3.2.1 Chemical Reactions in Plasmas

The chemistry which takes place in a plasma is usually quite complex and involves a large number of elementary reactions. In every case, reactions are initiated by collisions between energetic free electrons and gas molecules to form various active species. The nature of the final product is governed by the reactions which these precursors subsequently undergo. The chemical reactions which occur in a plasma, in general, can be divided into the following groups: (i) electron-impact reactions, (ii) inelastic collisions between heavy particles, and (iii) heterogeneous reactions. A brief discussion of these reactions is given below.

(1) Electron-Impact Reactions⁽¹⁵⁻¹⁸⁾

The rate at which active species are produced in a plasma is closely related to the electron density and average energy. The relation between the generation rate r_1 and the electron density and average energy is given by

$$r_1 = k_1 n_e N$$

where n_e is the electron density, N the concentration of a reactant, and k_1 the rate coefficient. The rate coefficient can be expressed as⁽¹⁵⁾

$$k_1 = \int_0^{\infty} \left(\frac{E}{2m_e} \right)^{1/2} \sigma(E) f(E) dE$$

where E is the electron energy, $\sigma(E)$ the reaction cross section, $f(E)$ the electron energy distribution function, and m_e the electron mass.

(ii) Inelastic Collisions between Heavy Particles (19-20)

The species produced by electron-impact reactions can react further either with each other or with molecules of the gas sustaining the plasma to yield a variety of new ionic and free radical species. The rate is given by

$$r_2 = k_2 N_i N_j$$

where N_i, N_j are concentrations of species i, j involved in the reaction, respectively. The rate coefficient, k_2 , depends on the effective temperatures ($k_B T$) of the involved species.

(iii) Heterogeneous Reactions (20)

In addition to participating in homogeneous reactions, the species produced in a plasma can also undergo a wide range of heterogeneous reactions. These types of reactions occur at surfaces in contact with the plasma and are quite important in the processing of semiconductor materials. In particular, if the active species reacting with the material form volatile compounds which are removed from the system by some means, then the etching process occurs (i.e. plasma etching). The reaction rates of heterogeneous reactions depend on the temperature of the reacting surface and the energy and concentration

of the active species. The details of these reactions were described by Carter et. al. (21)

A list of elementary processes occurring in the plasma (i.e., homogeneous reactions) and at the interface between a plasma and a solid surface (i.e., heterogeneous reactions) was given by Bell. (22)

3.2.2 Basic Physical Phenomena in Low Pressure Plasmas

One recognizes that, as a feature is being etched, the surface is subjected to a flux of ions and/or electrons. Therefore all etching characteristics could be very dependent on this radiation effect. (23) Since the energies of charged particles are a function of the potential distribution in the glow discharge, these potentials are discussed below.

There are several potentials of interest in the rf glow discharge system. The first is the plasma potential, ϕ_p . The plasma potential is the potential of the glowing part of the glow discharge and is the most positive potential anywhere in the system. In general it is the reference potential of the glow discharge. The floating potential, ϕ_f , is the potential at which equal numbers of electrons and ions arrive at a surface that is not externally biased or grounded. It is related to the electron temperature (T_e) by the approximate relation (24)

$$-\phi_f = \frac{k_B T_e}{2e} \ln \left(\frac{m_i}{m_e} \right)$$

where m_i is the ion mass. The difference between the plasma and floating potentials determines the maximum energy with which ions collide with an electrically floating surface.

The space immediately adjacent to a solid surface, such as insulated substrates, in which the transition from the plasma potential to the potential on the surface occurs is known as the ion sheath or dark space. This is the region through which positive ions are accelerated toward the surface and electrons and negative ions are accelerated away from the surface. The thickness of the ion sheath is related to the electron mean free path and increases with decreasing gas pressure. The potential distribution $\phi(y)$ (where $y = 0$ is the floating electrode surface) in the sheath, illustrated in Fig. 3.2, can be shown to be⁽¹⁶⁾.

$$\phi(y) = \phi_f e^{-\sqrt{Z} y/\lambda_D}$$

where λ_D is the Debye length. The Debye Length defines the distance over which a charge imbalance can exist. One conclusion from this result is that the spatial extent of the sheath is of the order of the Debye length. In the plasma the concentrations of positive and negative charge carriers are approximately equal. This criterion is satisfied when the dimension of the discharged gas volume are significantly larger than the Debye length⁽¹⁵⁾.

$$\lambda_D = \frac{\epsilon_0 k_B T_e}{n_e e^2}^{1/2}$$

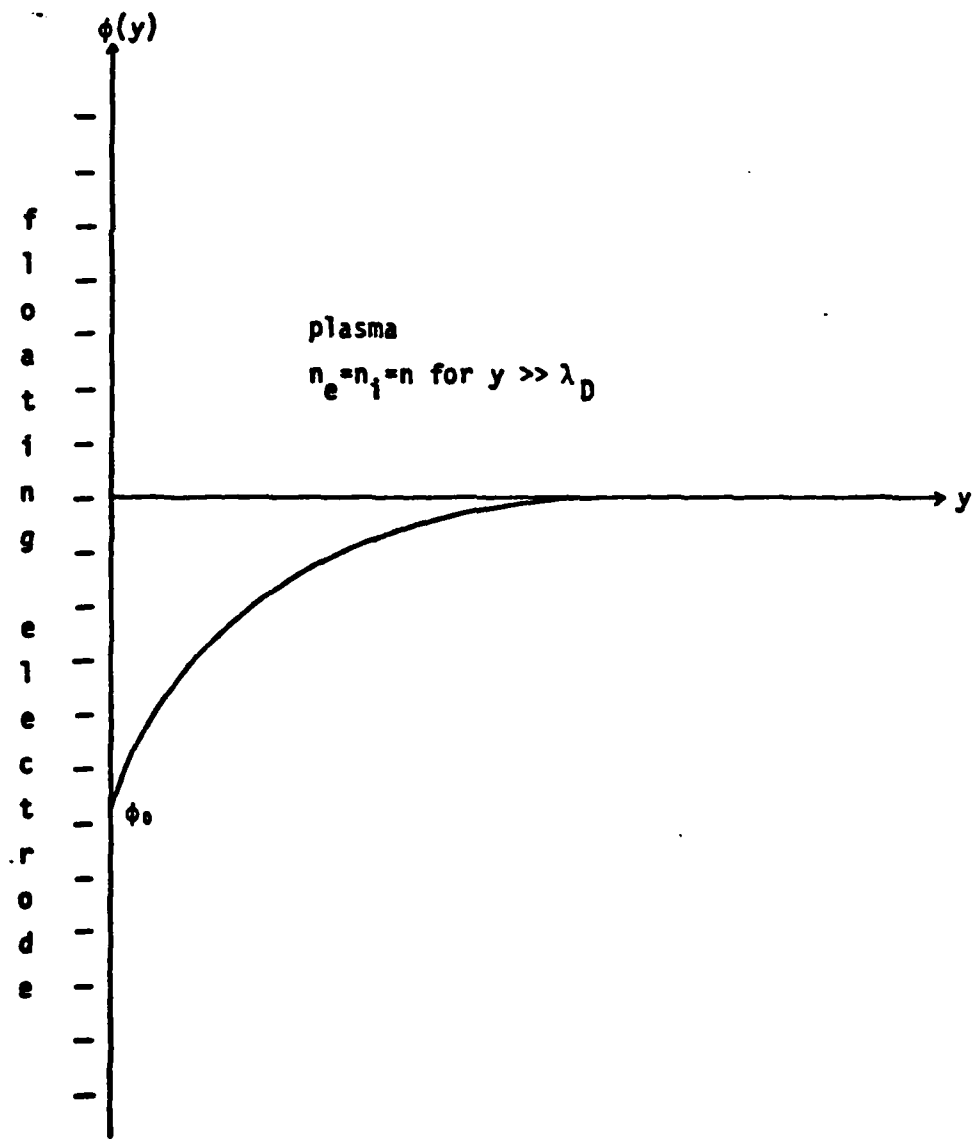


Fig.3.2 The steady-state potential distribution for a floating electrode in contact with a plasma. ϕ_0 is referred as floating potential and λ_D Debye length.

where ϵ_0 is the permittivity of free space, T_e is the effective electron temperature which differs from the gas temperature in general, k_B is the Boltzmann constant, and e is the electron charge.

Reactors used for plasma etching and deposition may be classified broadly as tube and parallel-plate reactors. The details of both reactors will be given in the next section. The average potentials in both reactors are shown in Fig. 3.3. In the tube reactor the potential distribution is symmetric across the tube. In the parallel-plate reactors the largest potential difference is found between the plasma and the capacitively coupled electrode, but significant potential can develop across the plasma and the floating or grounded surfaces in contact with the discharge. The ratio of these potentials has been shown to be area dependent. (25)

3.3 PLASMA ETCHING SYSTEM AND END POINT DETECTION

3.3.1 Plasma Etching System

The essential components of an etching system include a vacuum chamber and pump, a rf power supply, and gas handling equipment to monitor and control the flow of gas to the reactor. A schematic of the plasma etching system is shown in Fig. 3.4. In this study both tube and parallel-plate reactors were used. Fig. 3.5 shows schematically the two most common techniques for coupling rf power into tube reactors. In the capacitively coupled reactor (Fig. 3.5 (a)), the rf power is coupled through the capacitance of the dielectric wall of the tube. In the inductively

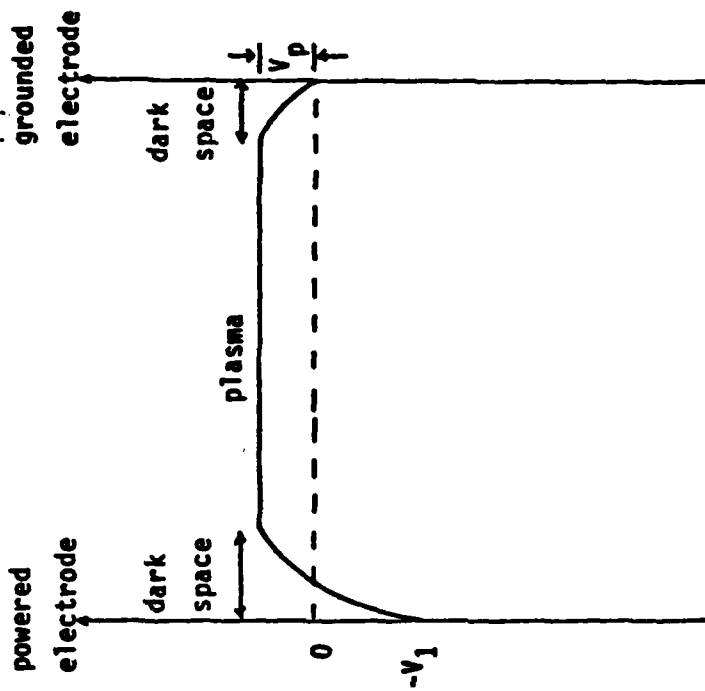
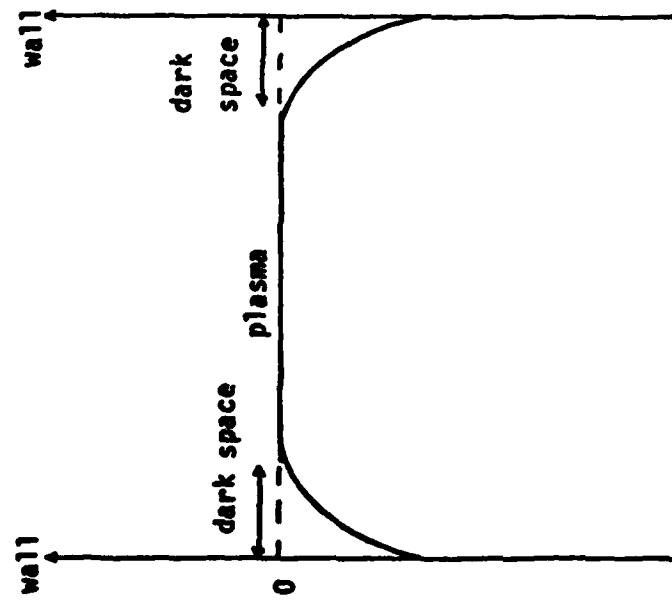


Fig.3.3 The potential distribution in the different type plasma reactor. (a) tube-type reactor and (b) parallel-plate type reactor, where V_p is the plasma potential.

(b) Parallel-plate type reactor
Fig.3.3 The potential distribution in the different type plasma reactor. (a) tube-type reactor and (b) parallel-plate type reactor, where V_p is the plasma potential.

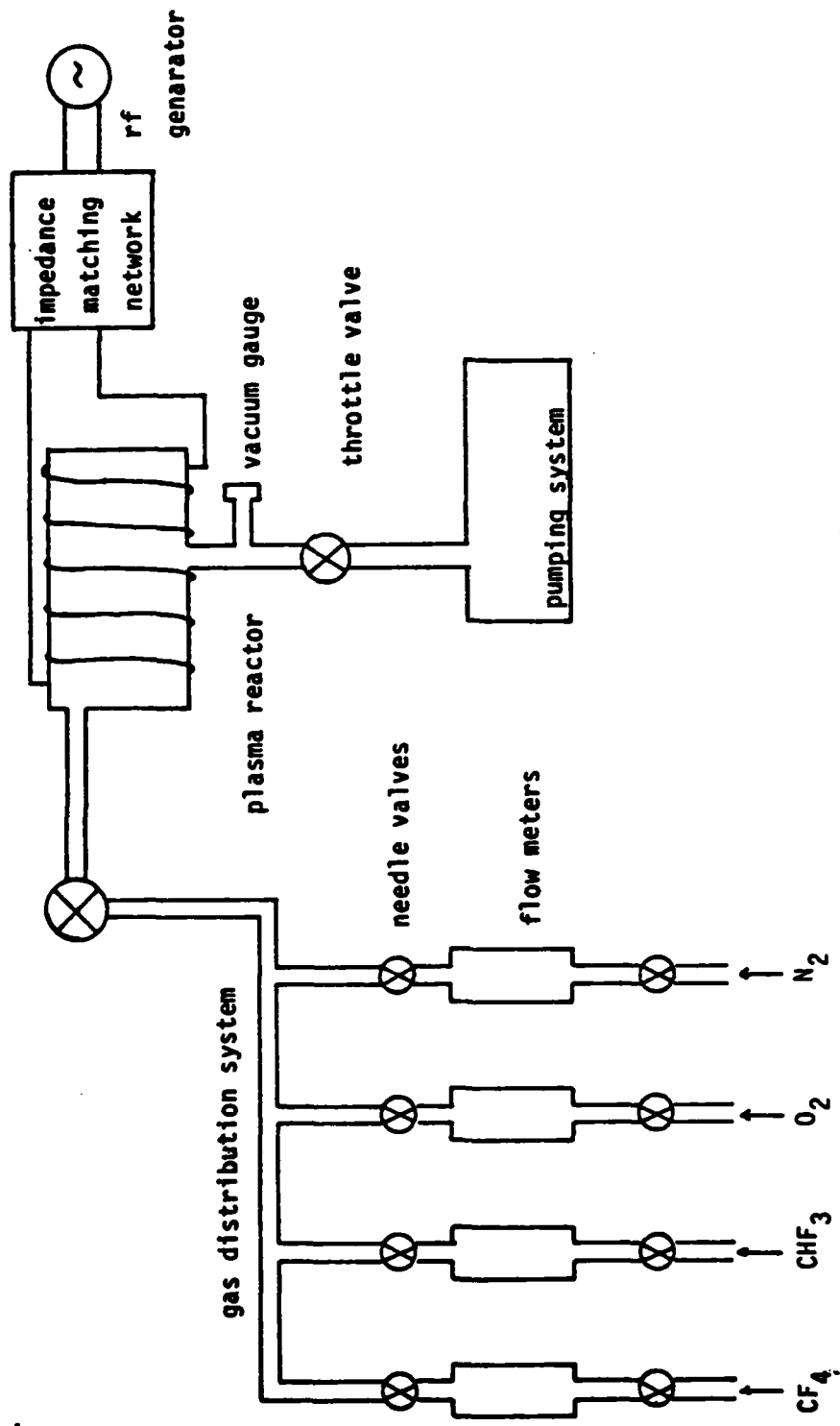
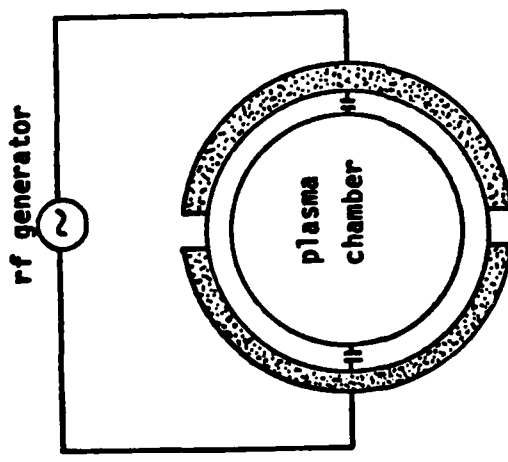
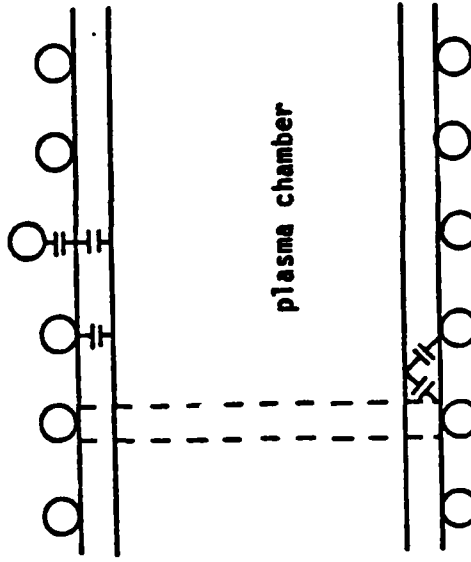


Fig.3.4 The general-purpose plasma etching system consists of four major parts:
 (1) rf generator and matching network,(2) plasma reactor,(3) pumping
 system, and (4) gas distribution system.



(a) capacitively coupled system



(b) inductively coupled system

Fig.3.5 In both techniques, (a) and (b), the rf power is coupled through the capacitance of the dielectric wall of the plasma tube, except that the coupling in (b) is not uniform.

coupled reactor (Fig. 3.5 (b)), the rf power is also coupled capacitively through the wall except that the coupling is nonuniform. The non-uniformity is insignificant if the operating pressure in the reactor is high (> 1 torr).⁽²⁶⁻²⁷⁾ To improve uniformity, most tube reactors employ gas inlet manifolds arranged to provide uniform gas flow over the substrates. In addition to this, the so-called etch-tunnel was introduced to enhance the etching uniformity.⁽²⁹⁻³⁰⁾

Fig. 3.6 shows schematically two basic configurations in parallel-plate reactors. When the substrate rests on a grounded or floating electrode with the rf electrode above, the system can be used either for plasma etching or deposition. If the substrate rests on the rf electrode, it is a conventional rf sputter-etching system and can only be used for a variant of plasma etching known as reactive ion etching (RIE). There are several advantages in this type of reactor. First, the temperature of the substrate can be easily controlled by the use of heating elements or circulating water through a hollow electrode. Second, the concentration of active species can be homogenized through the bulk of the plasma by controlling the flow pattern of the gas⁽³¹⁾ and the uniform electric field in this diode-like structure.

It has been pointed out that all etching anisotropy is caused by positive ions and/or electrons radiation to some degree⁽²³⁾. Anisotropic etching means that the etch rate of the surface is

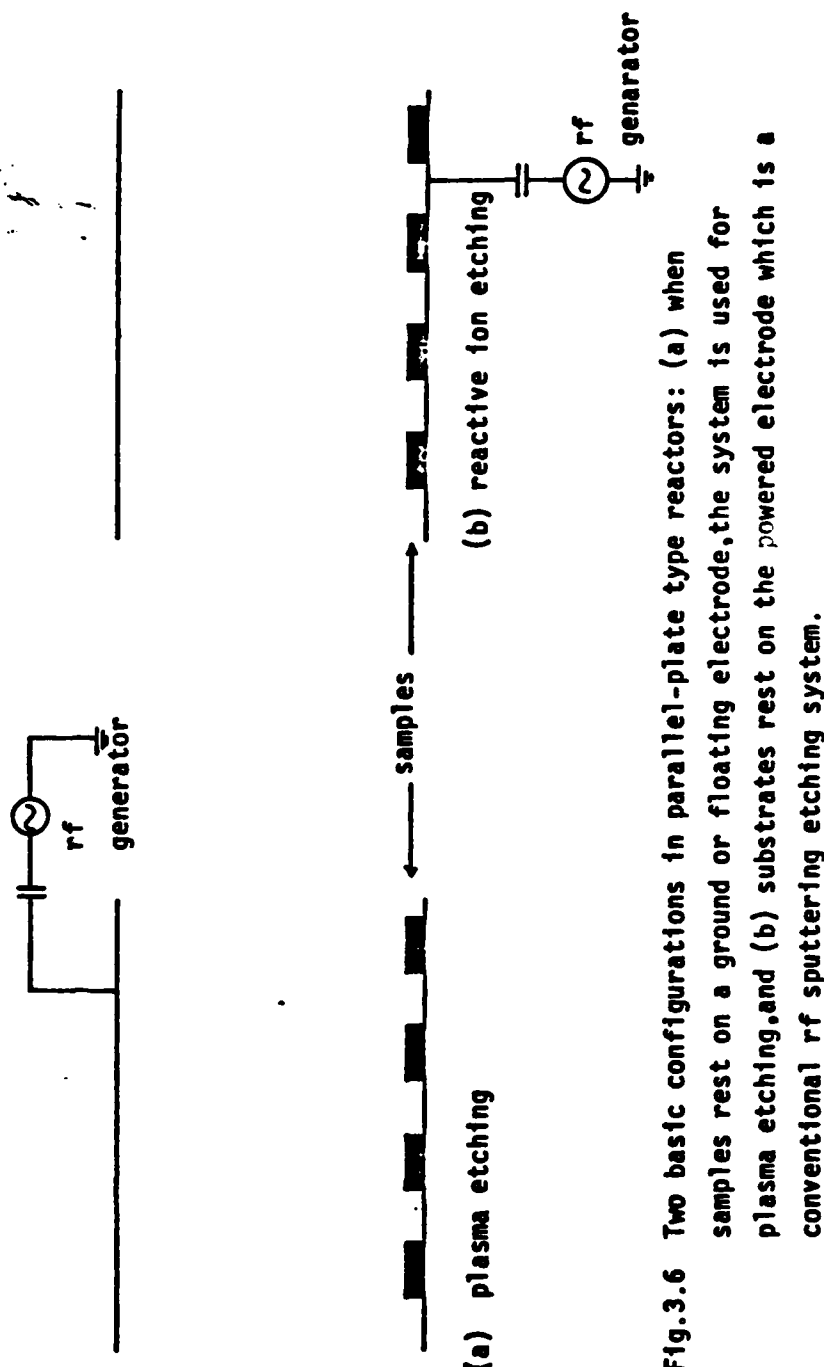


Fig.3.6 Two basic configurations in parallel-plate type reactors: (a) when samples rest on a ground or floating electrode, the system is used for plasma etching, and (b) substrates rest on the powered electrode which is a conventional rf sputtering etching system.

substantially larger than the etch rate of the sidewalls. As a feature is being etched, the surface is subjected to a flux of ions and/or electrons whereas the sidewalls are subjected to a greatly diminished energetic particle flux. Accordingly, better etching directionality and profile control have been reported in parallel-plate system as compared to the barrel system.

3.3.2 End Point Detection

In pattern transfer applications it is desirable to have some means of end point detection, i.e., a method of determining when the etched layer is completely removed and the underlying layer is reached. Currently, there are several methods of end point detection. One is mass spectroscopy⁽³²⁾ and another is optical emission spectroscopy⁽³³⁻³⁵⁾. In both methods, the end point is detected when the amplitude of particularly sensitive etch gas component (for mass spectrometer) or emission lines (for spectrophotometer) changes as the desired layer is etched. For example, in Si and Si₃N₄ etching, monitoring F emission lines from the CF₄-O₂ mixture plasma gas allows the etching end point to be determined easily.⁽³⁶⁾ In addition to these methods, a simple optical interferometric technique has been developed that can be used for both end point determination and in situ etch rate monitoring.⁽³⁷⁻³⁹⁾ In comparison to the two spectroscopic methods described above, the interferometric method is generally easier to set up and uses less expensive equipment.

An in situ optical monitoring technique is schematically shown in Fig. 3.7⁽⁴⁰⁾. The monitoring laser wave-length 6328 Å was obtained from a He-Ne laser. A beam splitter was used. One beam for the freshly prepared As_2S_3 film and the other for the UV exposed As_2S_3 film. This is necessary to maintain identical etching conditions so a true etching difference can be determined. The transmitted light intensities were detected and recorded continuously during plasma etching. This technique established the time dependence of the etch rate. The acquisition of etch rates from the recorded transmitted light intensities was described in the previous chapter.

3.4 EXPERIMENTAL TECHNIQUES AND RESULTS

3.4.1 Experimental Techniques

600 nm thick As_2S_3 films on glass substrates were used throughout the plasma etching experiments. Aside from the pure As_2S_3 layers, two different structures were used for Ag photodoping experiments. They are represented by $\text{Ag}|\text{As}_2\text{S}_3|\text{SiO}_2$ and $\text{As}_2\text{S}_3|\text{Ag}|\text{SiO}_2$, corresponding to Ag overcoating and undercoating, respectively. For the $\text{Ag}|\text{As}_2\text{S}_3|\text{SiO}_2$ structure, the excess Ag on the unexposed portion of the film was removed with dilute nitric acid before the plasma etching process.

A small commercial tube reactor PLASMODTM (Manufactured by Tegal Corp.) was used in the plasma etching experiment. It has a rf power of 0-100 W continuously variable at 13.56 MHz. The inner

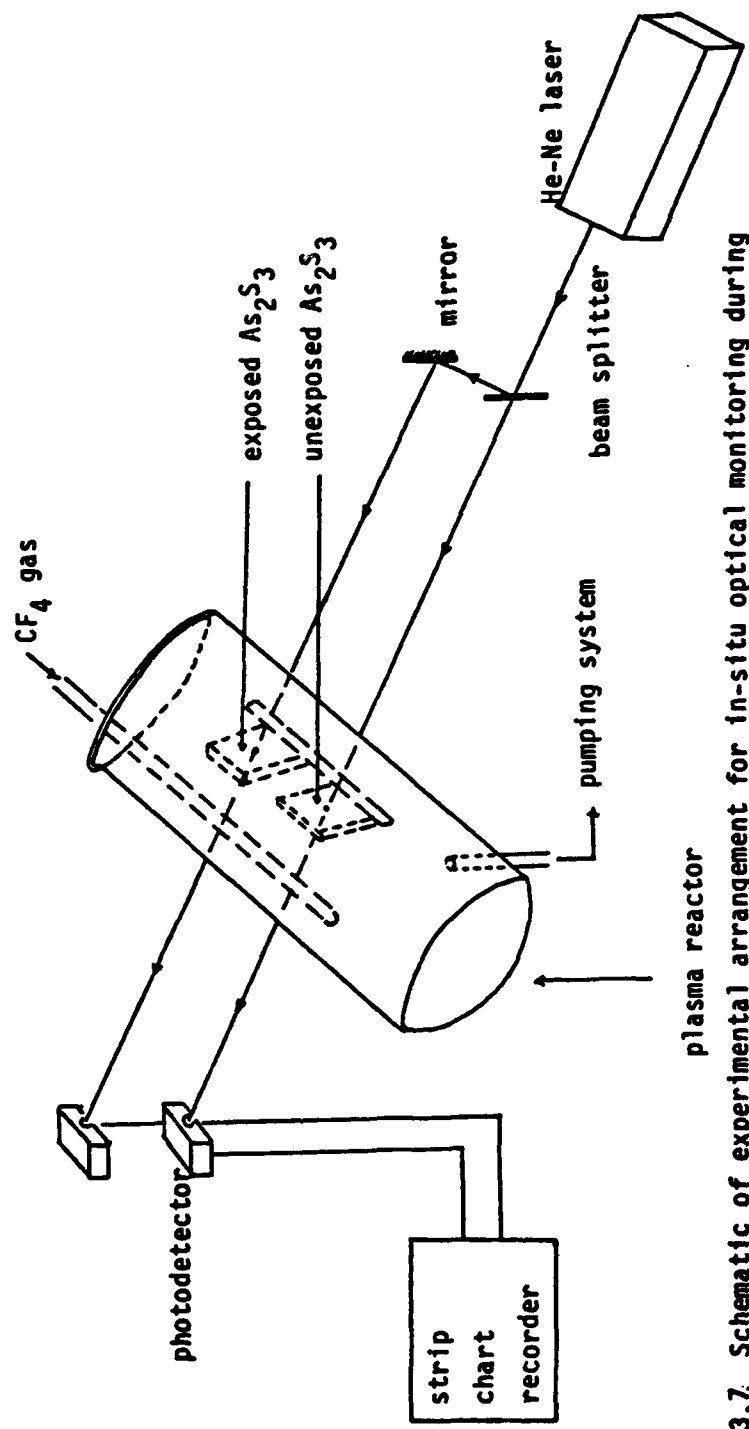


Fig.3.7 Schematic of experimental arrangement for in-situ optical monitoring during
 CF_4 plasma etching

chamber has a diameter of 10.5 cm and height of 15.5 cm. To control the experimental conditions for reproducible results, the following procedure was established. A dummy run of about 20 minutes was performed every time the system was to be used. The purpose was to eliminate water vapor condensed in the inner chamber and to warm up the system. When the sample was loaded, the reaction gas was allowed to flow for a few minutes to establish equilibrium (i.e., uniform distribution of the etching gas) before turn on the rf power. An in situ optical monitoring technique described previously was used in plasma etching experiments.

3.4.2 Experimental Results

The plasma etching results for pure As_2S_3 films, unexposed and UV exposed, are shown in Fig. 3.8 (a) and (b), respectively. The following plasma conditions were used: 0.36 torr reactor pressure, 25 W rf power, and 12×10^{-3} SCCM CF_4 gas flow rate. The time required to completely etch the UV exposed As_2S_3 film (Fig. 3.8 (b)) is longer than for the unexposed As_2S_3 film (Fig. 3.8 (a)) with the same thickness. This indicates that there is a suitable differential etch rate for pattern delineation with As_2S_3 as a negative resist. A noticeable feature in Fig. 3.8 (a) and (b) is the decrease in time between consecutive interference maxima and minima as the etching time increases. This nonuniform etch rate is explained by the plasma heating effect.⁽⁴⁾ This is a striking difference between plasma and wet chemical etching processes (see Fig. 2.8).

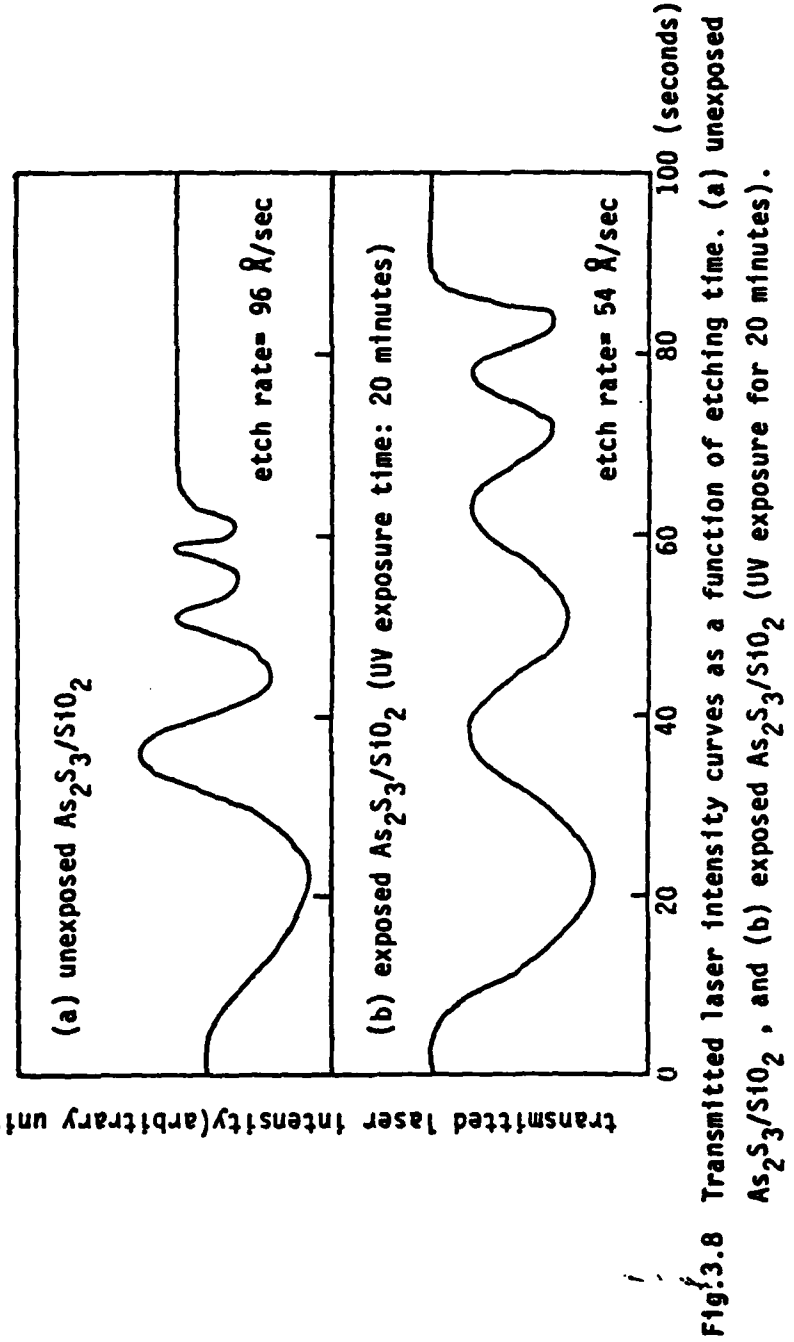


Fig.3.8 Transmitted laser intensity curves as a function of etching time. (a) unexposed $\text{As}_2\text{S}_3/\text{SiO}_2$, and (b) exposed $\text{As}_2\text{S}_3/\text{SiO}_2$ (UV exposure for 20 minutes).

It was found that $\text{Ag}|\text{As}_2\text{S}_3|\text{SiO}_2$ structure etched very slowly in the CF_4 plasma (Fig. 3.9 (a)). It is therefore quite suitable for patterning purpose. Fig. 3.9 (b) shows the etching behavior of the $\text{As}_2\text{S}_3|\text{Ag}|\text{SiO}_2$ sample. Since the doping process occurred at the bottom of the film and proceeded upward, the top portion of the film etched at a faster rate, indicating insufficient Ag photodoping. The Ag-photodoping layer thickness is estimated to be about 100 nm. Applying this result to the $\text{Ag}|\text{As}_2\text{S}_3|\text{SiO}_2$ structure, one found that this 100 nm Ag-photodoped layer is sufficient to protect the As_2S_3 underneath from the CF_4 plasma etching.

Because of the plasma heating effect, the etch rate increases as the etching time increases. It indicates that the etch rate is non-uniform (Fig. 3.8). The etch rate of the As_2S_3 film is determined from the time Δt , it took from the first maximum (or minimum) to the second maximum (or minimum) of the intensity-time trace, the refractive index of the film, n , and the wavelength of the monitoring beam, λ . It can be expressed as⁽³⁸⁻³⁹⁾.

$$r = \frac{\lambda}{2n} \cdot \frac{1}{\Delta t}$$

The etch rate calculated from the formula described above is only slightly different from the average etch rate determined from the known thickness of the film and the time it took for complete etching. Etch rates of the pure and Ag-doped As_2S_3 film are shown in Table 3.2 together with the comparison of the etch rates for different etching

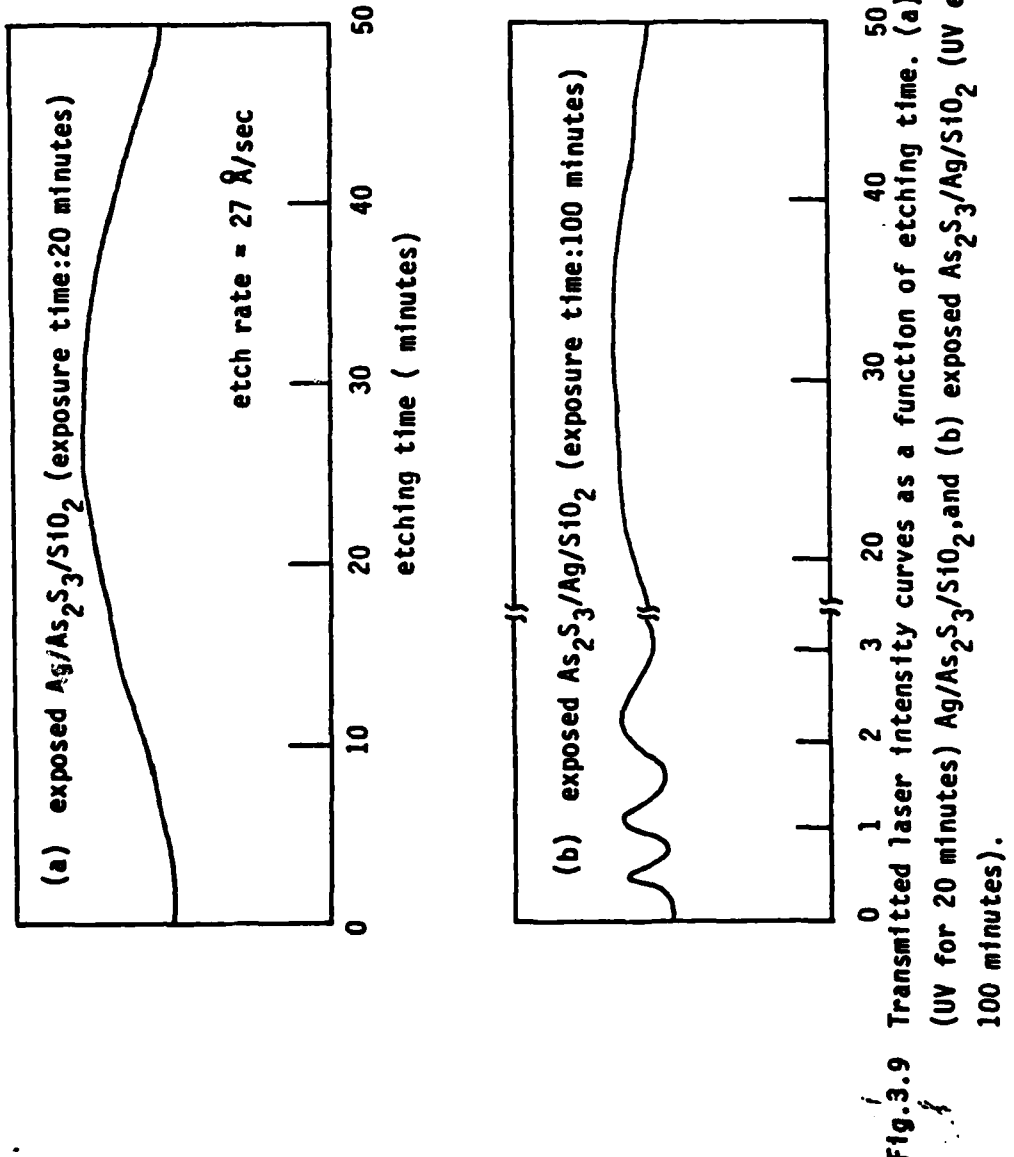


Fig.3.9 Transmitted laser intensity curves as a function of etching time. (a) exposed (UV for 20 minutes) $\text{Ag}/\text{As}_2\text{S}_3/\text{S}10_2$,and (b) exposed $\text{As}_2\text{S}_3/\text{Ag}/\text{S}10_2$ (UV exposure for 100 minutes).

the etching is run back to plasma etching (CE, no power
(0V) (0W)) (25 Watts)

current increased increased

Rate	11 A/sec	17 A/sec	17 A/sec
Rate	11 A/sec	17 A/min.	250 A/min.

techniques, wet and plasma etching processes.

The reaction gas flow rate was also varied to obtain a maximum etch rate ratio between the unexposed and exposed As_2S_3 films. The plasma reactor pressure was set at 0.36 torr as the CF_4 gas flow rate was varied. Fig. 3.10 shows the experimental results. It was found that the etch rate ratio depends strongly on the gas flow rate. The maximum ratio of 1.8 occurs at a rate of 12×10^{-3} SCCM with 25w rf power and the flow rate at the maximum ratio shifts to a smaller value as the rf power increases.

Grating patterns with a 6 μm linewidth were delineated by plasma etching under optimum conditions and are shown in Fig. 3.11. The corresponding first order diffraction efficiency continuously monitored as a function of etching time is shown in Fig. 3.12. The details were described previously in Chapter 2. These photomicrographs together with the numerical values of grating efficiencies of the various samples gives us qualitative information about the depth and edge definition of the grating patterns. The Ag overcoated sample gives the best result as anticipated. The electron micrograph of one of the Ag overcoated As_2S_3 films after CF_4 plasma etching is shown in Fig. 3.13. The edge profile is tapered as we expected because of the isotropic etching in the tube reactor. Additional efforts will be required to improve the final image quality. However, the basic principle of pattern delineation in inorganic resists by dry etching has been demonstrated in this work.

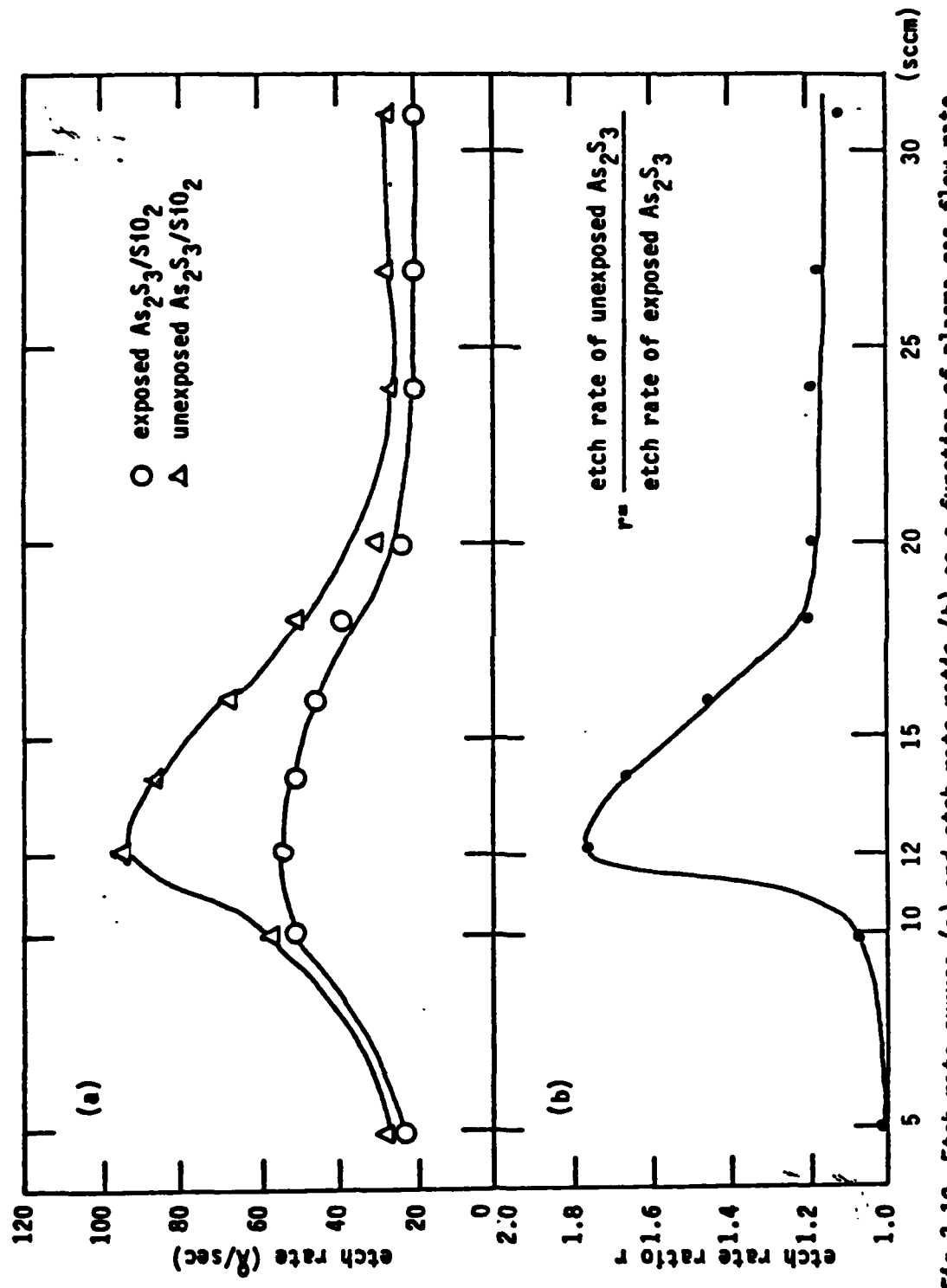


Fig.3.10 Etch rate curves (a) and etch rate ratio (b) as a function of plasma gas flow rate.

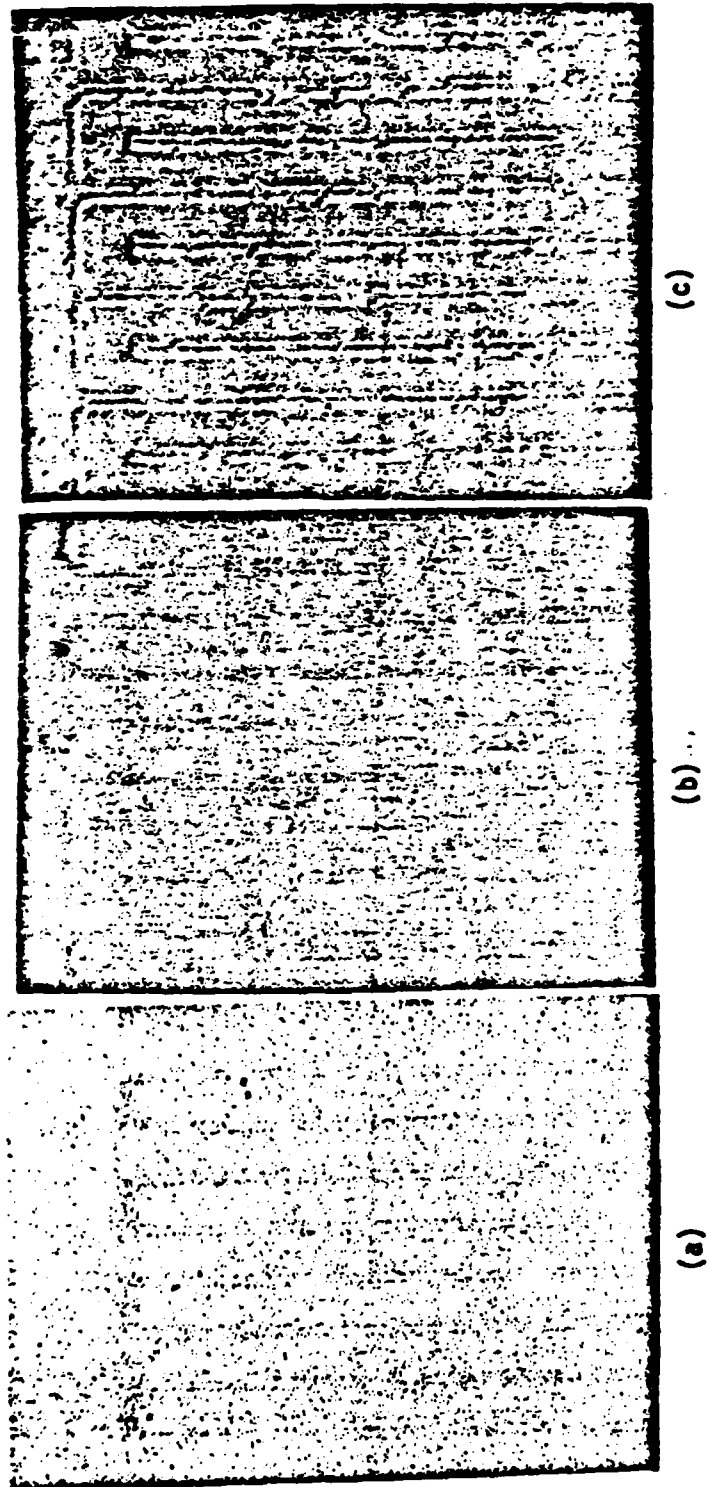


Fig. 3.11 CF₄ plasma delineated grating patterns with 1 line width of about 6 μm and their corresponding diffraction efficiency curves shown in the next figure. (a) As₂S₃/SiO₂, (b) Ag/As₂S₃/SiO₂, (c) As₂S₃/Ag/SiO₂.

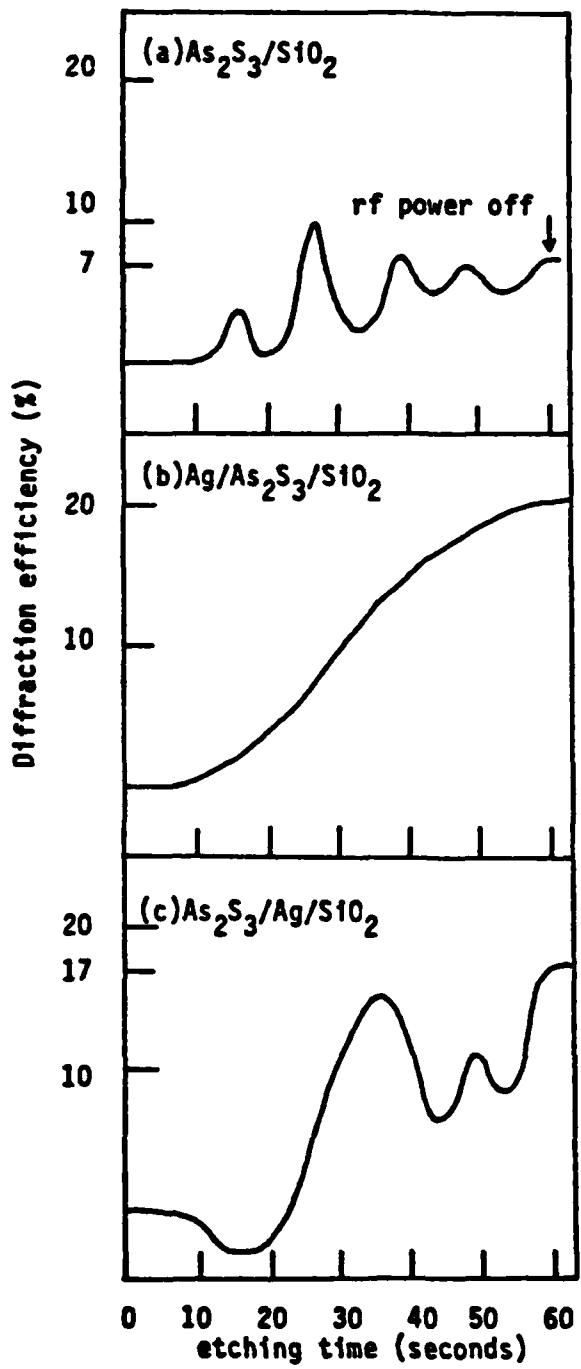


Fig.3.12 Diffraction efficiency curves are corresponding to the grating patterns shown in the previous figure.

(a)



(b)

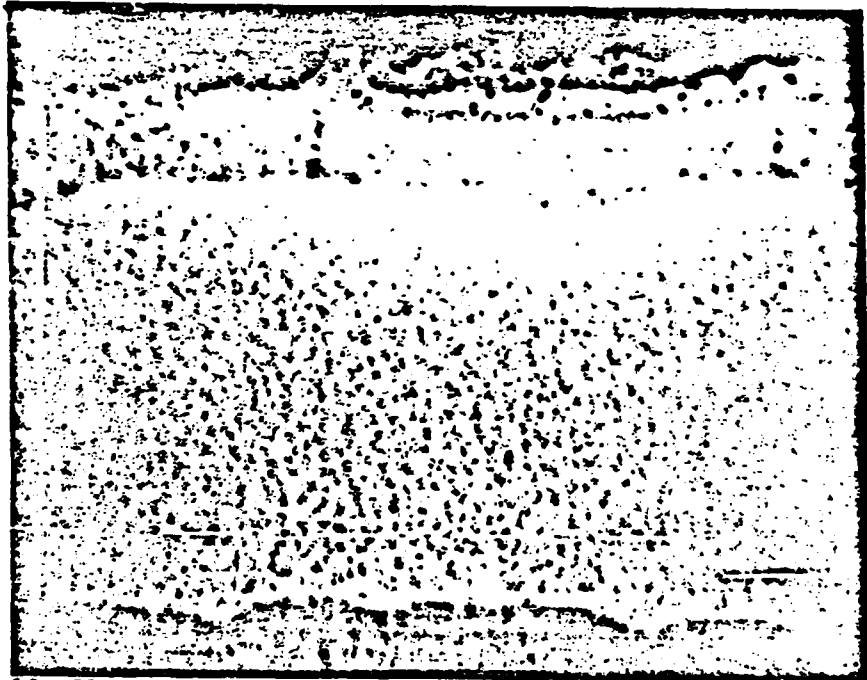


Fig.3.13 Electron micrographs of one of the Ag-overcoated As_2S_3 films after CF_4 plasma etching. (a)x5,000 (b)x10,000.
The edge profile is tapered as one expects. The residues
is due to incomplete etching.

3.5 FACTORS CONTROLLING PLASMA ETCH RATES

It is recognized that plasma etching, while conceptually simple, encompasses several rather complex processes which are poorly understood. The etching process depends not only on the complicated phenomena occurring in the discharge itself, but also on the kinetic details of the interaction of the solid with one or more active species adsorbed at the solid surface. A detailed analysis which could account for the influence of the many variables would be difficult to formulate. Alternatively, by employing reasonable assumptions, a phenomenological treatment is possible. The most important factors controlling plasma etching are given in this section.

3.5.1 Reactor Pressure and RF Power

For a given gas, both the pressure and power density affect the electron energy distribution which, in turn, determine the generation rates of active species.⁽⁴¹⁾ It was found that the value of E_e/p (E_e is the effective electric field and P is the reactor pressure) in a plasma plays an important role in determining the properties of the plasma and the rates at which chemical processes occurring in it proceed.⁽⁴²⁻⁴³⁾ In general, etch rates increase monotonically with applied rf power (Fig. 3.14). At constant pressure, the collision rate will be constant, under the assumption that the collision cross sectional area is independent of energy, but average electron energy will increase when the existing electric field intensity

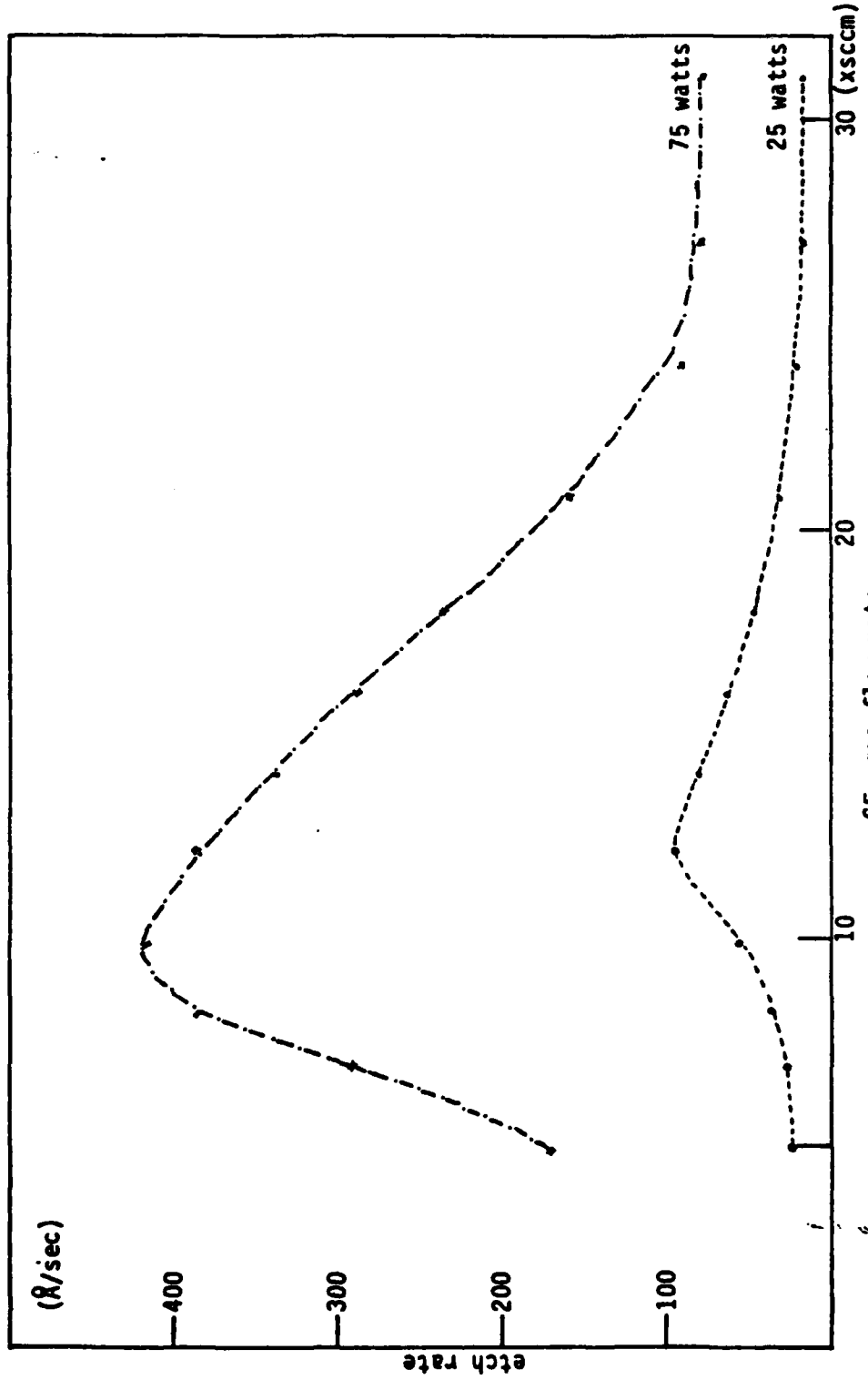


Fig.3.14 The As_2S_3 etch rate vs flow rate in the CF_4 plasma at two different rf powers, 25 and 75 W.

increases as applied rf power is increased. As a result, the generation rate of active species as well as the etch rate is increased. On the other hand, as pressure is increased at constant rf power density, the collision rate will increase but the average electron energy will decrease because the electric field will have less time to accelerate an electron between successive collisions. As a result, the etch rate decreases.

3.5.2. Flow Rate

Plasma etching is done under dynamic flow to replenish continually the reactant species from the gas reservoir and remove volatile products by the mechanical pump. Thus, a flow rate dependence for the etch rate is expected. The residence time τ_r of the molecule in the plasma is determined by the flow rate of the reaction gas, F, and reactor pressure, P. It can be expressed as⁽⁴⁴⁾

$$\tau_r = \frac{PV}{760F}$$

where V is the reactor volume. Since the residence time of a molecule is inversely proportional to the flow rate, the generation rate of active species as well as the etch rate will be decreased (Fig. 3.10). This phenomenon is called the pumping rate limited etching process.⁽⁴⁴⁾ In this limiting case, active species will be swept through the reactor too rapidly to accomplish etching. In the very low flow rate region,

the etch rate increases with the flow rate. This is simply due to an increase in the supply of reactant gas (see Fig. 3.10).

Effects of other important parameters, such as rf frequency (45) and substrate temperature, (46) in plasma etching are described elsewhere.

3.6 ETCHING MECHANISMS OF As_2S_3 FILMS IN A CF_4 PLASMA

Before discussing the mechanism, it is instructive to consider the steps which must occur during the etching of a surface with active gaseous species⁽²³⁾. A necessary first step is that the gas-phase species diffuse from the flow stream and reach the etchable surface. The next step is that the gas-phase species chemisorb on the surface. In the case of molecular gases, this chemisorption will often involve dissociation of the molecule. However, even in cases where chemisorption is nondissociative, the radiation present in the plasma will usually cause the adsorbed molecule to fragment. The next step is the formation of the volatile reaction product through various chemical reactions between the chemisorbed active species and the etchable material. The fourth step is the desorption of the reaction product from the surface and the last step is the diffusion of the desorbed materials into the flow stream. These steps are illustrated in Fig. 3.15, using the model for the etching of Si with molecular fluorine as an example. Any of these steps could be rate limiting in the etching process and if any one of them does not occur, then the surface will not be etched.

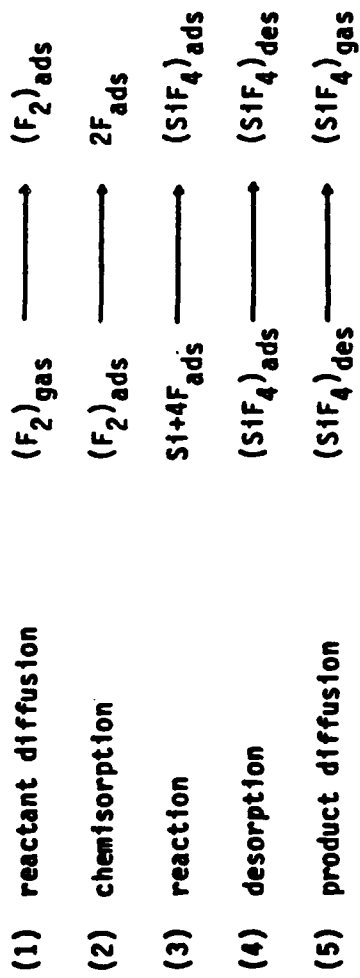
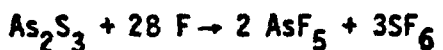


Fig.3.15 The steps which occur during the etching of a Si surface with active gaseous species. (53)

In this work, the CF_4 plasma was used to etch As_2S_3 films. The mechanism of the etching process is not understood at present. The rf power excites the CF_4 gas molecules and dissociates some of them into other species, such as ions, free radicals, and free electrons. It is believed that dissociative processes in a CF_4 plasma produce primarily positive ions, CF_3^+ , negative ions, F^- and CF_3^- , and free radicals, F and CF_3 .⁽⁹⁾ Since the plasma potential is more positive than the grounded or floating electrode (see Fig. 3.3) on which the samples are resting, the negative ions do not usually contribute to etching.⁽⁴⁷⁻⁴⁸⁾ The possible species responsible for As_2S_3 etching in a CF_4 plasma are the positive ions, CF_3^+ , and free radicals, CF_3 and F . For the CF_3^+ ion and CF_3 free radical, the etching action is impeded by the carbon residue resulting from dissociative chemisorption. The question of the role of carbon is discussed in detail by Coburn and Winters.⁽²³⁾ Their model could be also applied to the As_2S_3 etching process in a CF_4 plasma. For example, the system $\text{CF}_3 - \text{As}_2\text{S}_3$ is fluorine deficient with respect to the anticipated volatile products of AsF_5 , SF_6 and CF_4 , and, as a result, the CF_3 radical cannot be thought of as a viable source of etching species. In other words, fluorine from CF_3 will be used up to form AsF_5 and SF_6 at the As_2S_3 surface but the resulting carbon must also be removed by fluorine from another source in order for the etching process to continue. From the above considerations, fluorine atoms or molecules will be the best candidates for As_2S_3 etching in a CF_4 plasma. The

overall reaction is tentatively written as



Here the role of oxygen is excluded deliberately to simplify the problem. Fig. 3.16 illustrates the possible model for CF_4 plasma etching in the As_2S_3 film.

3.7 THE PLASMA OXIDATION OF AMORPHOUS As_2S_3 FILMS

During etching studies of thermally evaporated thin films of As_2S_3 using the plasma technique, As_2S_3 films were found to be susceptible to oxidation. The nature of the product and plasma conditions governing the reaction are studied in this section.

0.5 μm thick As_2S_3 films were used. The plasma chamber pressure was set at 0.1 torr and the O_2 gas flow rate maintained at 15×10^{-2} SCCM, and the rf power was set at 100 W. Under these conditions an appreciable oxidation of the As_2S_3 film occurred in 30 minutes.

The presence of crystalline material was noted by the appearance of several Bragg reflections on the x-ray diffraction pattern. These peaks were identified by position and relative intensity as being the (111) and (222) reflections from the cubic phase of As_2O_3 .⁽⁴⁹⁾ The (111) and (222) reflections, corresponding to lattice spacing of 6.394 and 3.195 \AA , respectively, gave the strongest intensities. In some cases weak (333), (444) and (555) reflections were also observed. No diffraction lines from crystalline sulfur were observed, though it

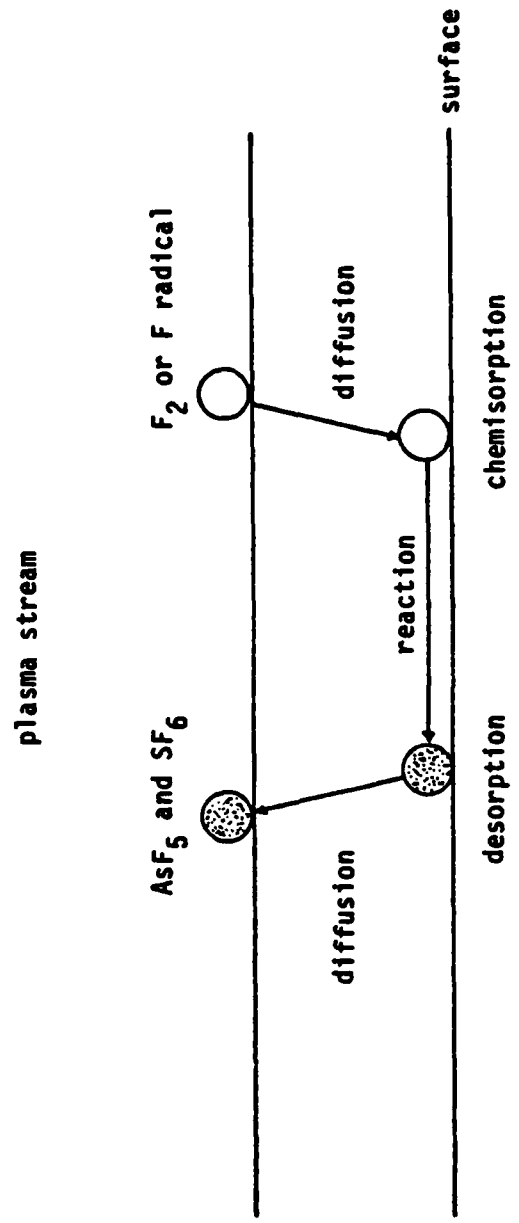


Fig.3.16 The possible process for CF_4 plasma etching in the As_2S_3 film.

has been established that prolonged photo-decomposition of As_2S_3 in an oxidizing atmosphere results in the presence of both As_2O_3 and sulfur crystals.⁽⁵⁰⁾ The x-ray diffraction pattern is shown in Fig. 3.17. The oxidized surface was also examined by SEM and an electron micrograph is displayed in Fig. 3.18. Most of the crystallites show clearly defined (111) growth faces, most probably due to the highly anisotropic As diffusion rate. In many cases these appear to be parallel to the glass surface. An apparently non-crystalline structure is also observed on the surface and it seems likely that these may be sulfur-rich phases produced by the oxidation. Also, specimens kept for a few days under normal atmospheric conditions either in the dark or in artificial light do not show any oxidation. Similar results were obtained by Berkes et. al.,⁽⁵¹⁾ Apling et. al.,⁽⁵²⁾ and Bowlt et. al.⁽⁵³⁾ using other oxidation techniques.

A phenomenological model was developed to describe the oxidation behavior of As_2S_3 . Although no direct evidence exists to identify the resultant species, all of the information available suggest that the following reaction occurs:⁽⁵⁴⁻⁵⁵⁾



where $0 < x < 2$. The optical property change is possibly caused by the growth of arsenic clusters. These clusters are very small in size since crystalline As could not be detected by electron diffraction. The liberated arsenic which appears in the above equation oxidized in

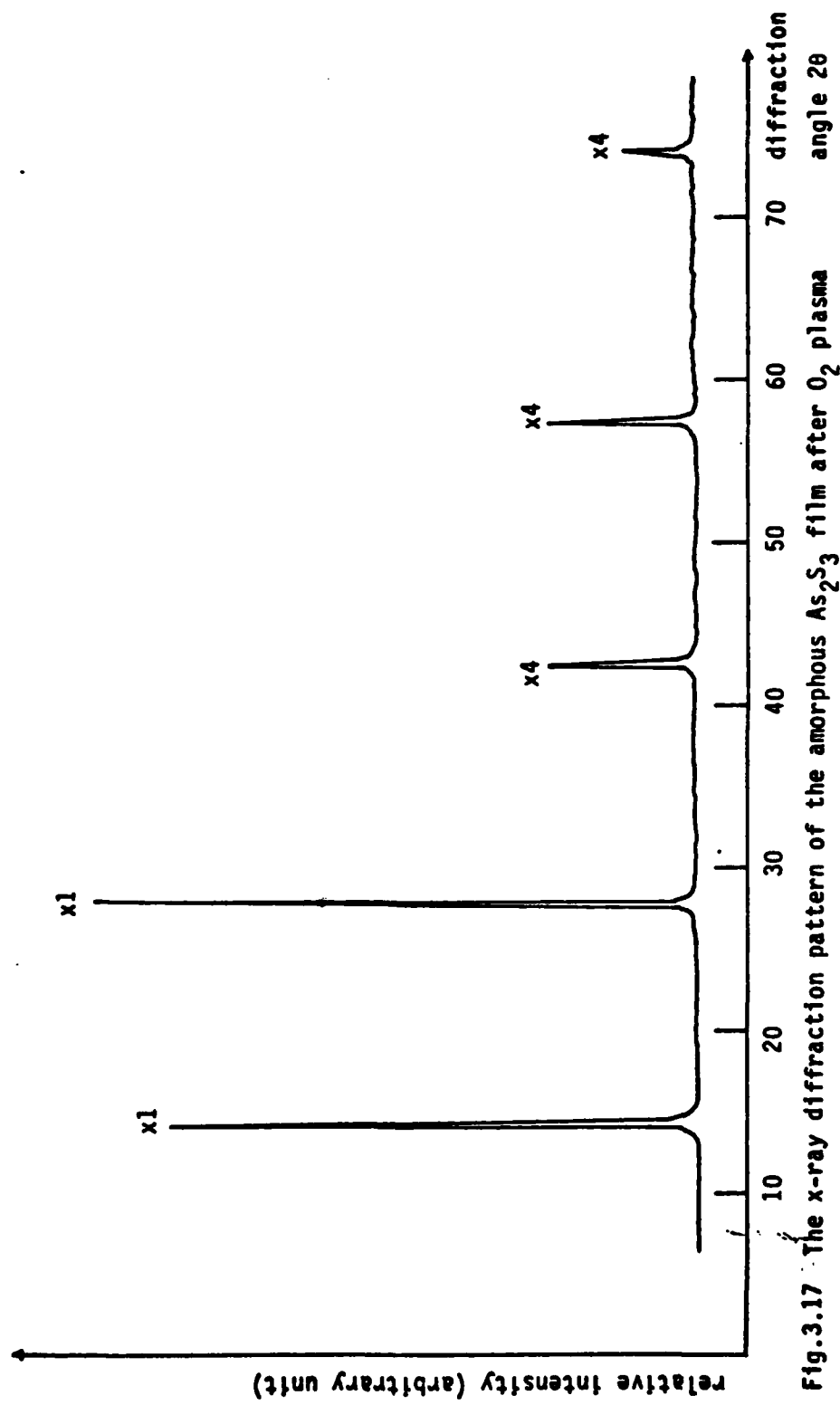


Fig.3.17 The x-ray diffraction pattern of the amorphous As_2S_3 film after O_2 plasma treatment. All the diffraction peaks are due to the cubic phase of As_2O_3 .

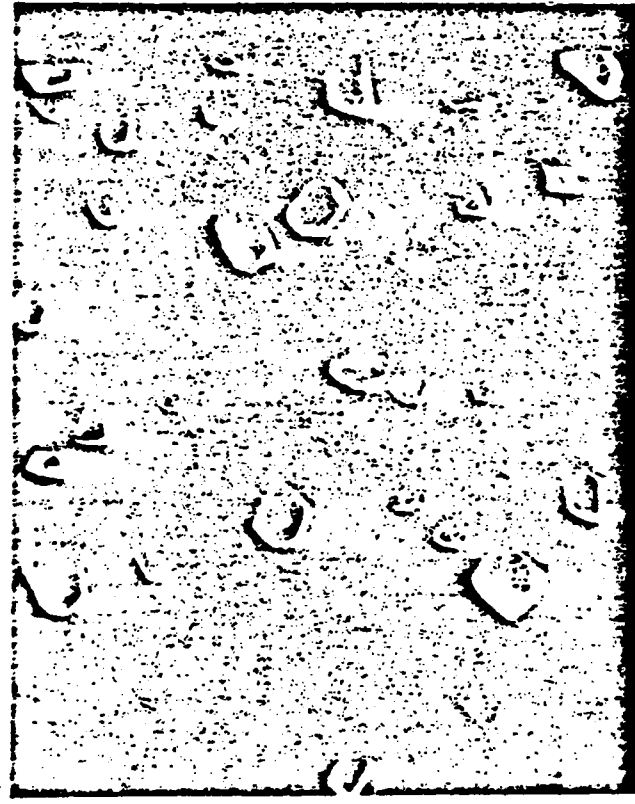
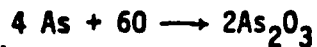


Fig. 3.18 The scanning electron micrograph (x5,000) of the oxidized surface of the As₂S₃ film after the O₂ plasma treatment. Most crystallites show clearly defined (111) growth faces, and in many cases these appear to be parallel to the substrate surface.

the O₂ plasma in the following manner.



Berkes suggests that water molecules appear to enter this reaction as a catalyst.⁽⁵⁵⁾ It is almost certain that there was a small amount of H₂O vapor in the plasma reactor that speeded up this reaction. Also, the oxidation process appeared to be confined to the surface of the As₂S₃ film where all the constituents necessary for the reaction are readily available.

References to Chapter 3

1. C.M. Melliar-Smith, C.J. Mogab, in "Thin Film Processes", ed. by J. L. Vossen and W. Kern, Academic Press, N.Y., (1978).
2. A.R. Reinberg, in "Etching For Pattern Definition", ed. by H.G. Hughes and M.J. Rand, Electrochem. Soc., Princeton, N.J., (1976).
3. A.J. Bondur, J. Vac. Sci. Technol., 13, 1023, (1976).
4. R.G. Poulsen, J. Vac. Sci. Technol., 14, 266, (1977).
5. L. Holland, J. Vac. Sci. Technol., 14, 5, (1977).
6. R.W. Kirk, in "Techniques and Applications of Plasma Chemistry", ed. by J.R. Holland and A.T. Bell, John Wiley & Sons, N.J.,(1974).
7. P.D. Parry, A.F. Rodde, Solid State Technol., 22, 125, (1979).
8. D.L. Flamm, Solid State Technol., 22, 109, (1979).
9. J.W. Coburn, H.F. Winters, T.J. Chuang, J. Appl. Phys., 48, 3532, (1977).
10. C.J. Mogab, A.C. Adams, D.L. Flamm, J. Appl. Phys., 49, 3796, (1978).
11. H.F. Winters, J. Appl. Phys., 49, 5165, (1978).
12. G.C. Schwartz, L.B. Zielinski, T. Schopen, in "Etching for Pattern Definition", ed. by H.G. Hughes and N.J. Rand, Electrochem. Soc., Princeton, N.J., (1976).
13. S. Takahashi, F. Murai, H. Kodera, IEEE on Electron Devices, ED-25, 1213, (1978).
14. K. Ukai, H. Hanazawa, J. Vac. Sci. Technol., 15, 338, (1978).
15. A.T. Bell, in "Techniques and Applications of Plasma Chemistry", ed. by J.R. Holland and A.T. Bell, John Wiley & Sons, N.J., (1974).
16. E.W. McDaniel, "Collisions Phenomena in Ionized Gases", Wiley, N.Y., (1964).
17. H.S.W. Massey, E.H.S. Burhop, H.B. Gilbody, "Electronic and Ionic Impact Phenomena", Oxford Press, N.Y., (1971).

18. L.J. Kieffer, "Bibliography of Low Energy Electron Collision Cross Section Data", N.B.S. Pub. 289, Washington, D.C., (1967).
19. E.W. McDaniel, V. Cermak, A. Dalgarno, E.E. Ferguson, L. Friedman, "Ion-Molecule Reactions", Wiley, N.Y., (1970).
20. V.N. Kondratieo, "Chemical Kinetics of Gas Reactions", Addison Wesley, Reading, Mass., (1964).
21. G. Carter, J.S. Colligan, "Ion Bombardment of Solids", American Elsevier, N.Y., (1969).
22. A.T. Bell, J. Vac. Sci. Technol., 16, 418, (1979).
23. J.W. Coburn, H.F. Winters, J. Vac. Sci. Technol., 16, 391, (1979).
24. F.F. Chen, in "Plasma Diagnostic Techniques", ed. by R.H. Huddleston and S.L. Leonard, Academic Press, N.Y., (1965).
25. H.R. Koenig, L.I. Maissel, IBM J. Res. Dev., 14, 276, (1970).
26. E.H. Snow, B.E. Deal, J. Electrochem. Soc., 113, 263, (1966).
27. D.R. Kerr, J.S. Logan, P.J. Burkhardt, W.A. Pliskin, IBM J. Res. Dev., 8, 376, (1964).
28. J.L. Lambert, K. Roy, M. Reese, Solid-State Electron, 10, 877, (1967).
29. R. Bersin, M. Singleton, U.S. Patent 3, 879,596 (1976).
30. Y. Horike, M. Shibagaki, Proc. of the 7th Conf. on Solid State Dev., Tokyo, (1975).
31. A.R. Reinberg, U.S. Patent 3, 757,733 (1975).
32. G.B. Bunyard, B.A. Raby, Solid State Technol., 20, 53, (1977).
33. R.G. Poulsen, G.M. Smith, in "Semiconductor Silicon, 1977", ed. by H.R. Huff and E. Sirtl, p. 1058, (1977).
34. J.E. Griffiths, E.D. Degenkolb, Appl. Spectrosc., 31, 134, (1977).
35. C.J. Mogab, J. Electrochem. Soc., 124, 1262, (1977).
36. B.A. Raby, J. Vac. Sci. Technol., 15, 205, (1978).
37. H.H. Busta, R.E. Lajos, D.A. Kiewit, Solid State Technol., 22, 61, (1979).

38. M.S. Chang, T.W. Hou, Opt. Commu., 24, 220, (1978).
39. M.S. Chang, T.W. Hou, Thin Solid Films, 55, 463, (1978).
40. M.S. Chang, J.T. Chen, Appl. Phys. Lett., 33, 892, (1978).
41. H. Dreicer, Phys. Rev., 117, 343, (1960).
42. A.T. Bell, I&EC Fund. Quart., 9, 160, 679, (1970).
43. A.T. Bell, I&EC Fund. Quart., 11, 209, (1972).
44. B.N. Chapman, V.J. Minkiewicz, J. Vac. Sci. Technol., 15, 329, (1978).
45. R.H. Bruce, A.R. Reinberg, in "International Conference on Microlithography", (1980).
46. R.G. Poulsen, M. Brochu, in "Etching for Pattern Definition", ed. by H.G. Hughes and N.J. Rand, Electrochem. Soc., Princeton, N.J. (1976).
47. J.W. Coburn, E. Kay, Solid State Technol., 22, 117, (1979).
48. W.F. Libby; J. Vac. Sci. Technol., 16, 414, (1979).
49. NBS Circular 539, Vol. 1, p. 51.
50. A.D. Pearson, B.G. Bagley; Mat. Res. Bull., 6, 1041, (1971).
51. J.S. Berkes, J.M. Short, K.J. Johnson; in "Proc. of the 5th Intern. Conf. of Amorphous and Liquid Semiconductors", ed. by J. Stuke and W. Brenig, Taylor and Francis, London, (1974).
52. A.J. Apling, M.F. Daniel, A.J. Leadbetter; Thin Solid Films, 27, L11, (1975).
53. C. Bowlt, B.N. Ghosh; Br. J. Appl. Phys., 16, 1762, (1965).
54. S.A. Keneman, J. Bordogna, J.N. Zemel; J. Appl. Phys., 49, 4663, (1978).
55. J.S. Berkes, S.W. Ing, Jr., W.J. Hillegas; J. Appl. Phys., 42, 4908, (1971).

Chapter 4

STRUCTURAL TRANSFORMATIONS IN AMORPHOUS As_2S_3 FILMS

In recent years, a renewed interest has developed in optical-storage effects in As_2S_3 and related chalcogenide materials, caused, in part, by the applicability of such materials to optical information storage systems, and new applications in microlithography and optical integrated circuits. All of these potential applications rely on the physio-chemical property changes upon light exposure to above band gap irradiation or heat treatment. The configurational changes so induced are characterized as photostructural or thermostructural, respectively. Photostructural transformations are additionally specified as reversible or irreversible.⁽¹⁻⁹⁾ The wide variety of photostructural (or photochromic, since the optical properties change accompanying these photostructural transformations) effects in amorphous chalcogenide glass systems have led to an array of complex and often contradictory mechanisms to account for them.⁽¹⁰⁻¹⁵⁾

In this chapter, emphasis has focused on the structural transformation of evaporated As_2S_3 films upon band gap illumination and the development of models for various anomalous structural transformations. The existing models proposed by Keneman⁽¹⁰⁻¹¹⁾ and Fritzsche⁽¹²⁾ are described first.

Keneman et. al.⁽¹⁰⁻¹¹⁾ presented a three-stage model to explain the effects of evaporation, heat-cycling, and light exposure. In their

AD-A113 148

PENNSYLVANIA UNIV PHILADELPHIA
SILVER-DOPING EFFECTS AND PHOTOSTRUCTURAL TRANSFORMATION IN EVA—ETC(U)
FEB 82 T J CHEN, J N ZEMEL, I LAUKS

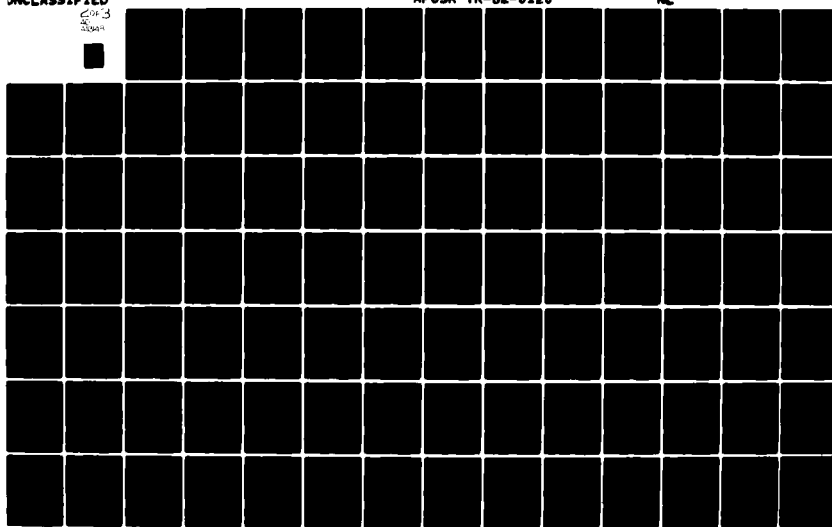
F/8 7/4

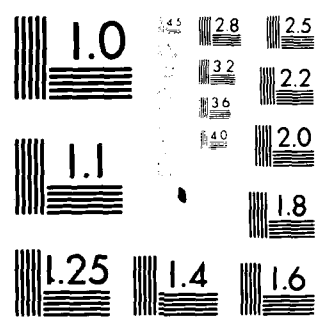
UNCLASSIFIED

AFOSR-TR-82-0120

ML

2013
20044





MICROCOPY RESOLUTION TEST CHART
NATIONAL BUREAU OF STANDARDS 1963 A

model, they assumed that As_2S_3 vapor consisted of at least three components: an arsenic-rich component (As_2S_2), As_4S_6 , and sulfur, S_2 . The evaporated film then contained As_2S_2 , S, and As_2S_3 . Heat cycling caused the As_2S_2 and S_2 to combine to form homogeneous As_2S_3 . Light exposure also enhanced the combination. A reversible change was observed under heat cycling which they ascribed to As clustering. A schematic diagram of the three-stages proposed is shown in Fig. 4.1.

Fritzsche⁽¹²⁾ proposed that the combination of relatively large band gaps and low coordination number in these materials accounted for the existence of photostructural phenomenon in sulfide and selenide glasses. Sulfur and selenium both are lone pair semiconductors as defined by Kastner⁽¹³⁾, meaning that the highest occupied valence band states derive their parentage from primarily non-bonding p-type electrons. The non-bonding S-states and the bonding P-states lie lower in the valence band while the antibonding P-states constitute the conduction band. Such atoms provide an especially structure sensitive contribution to the electronic band level energies of these phases in which they occur, because changes in bonding geometry can affect the degree of hybridization of the S and P lone pair and bonding states.⁽¹⁴⁻¹⁵⁾ Furthermore, such changes in bond geometry are relatively unrestricted topologically for a two-fold coordinated S or Se atom, so that structural perturbations are easily achieved.

4.1 THE STRUCTURES OF CRYSTALLINE AND GLASSY As-S COMPOUNDS

It is instructive to give a survey of the structures occurring

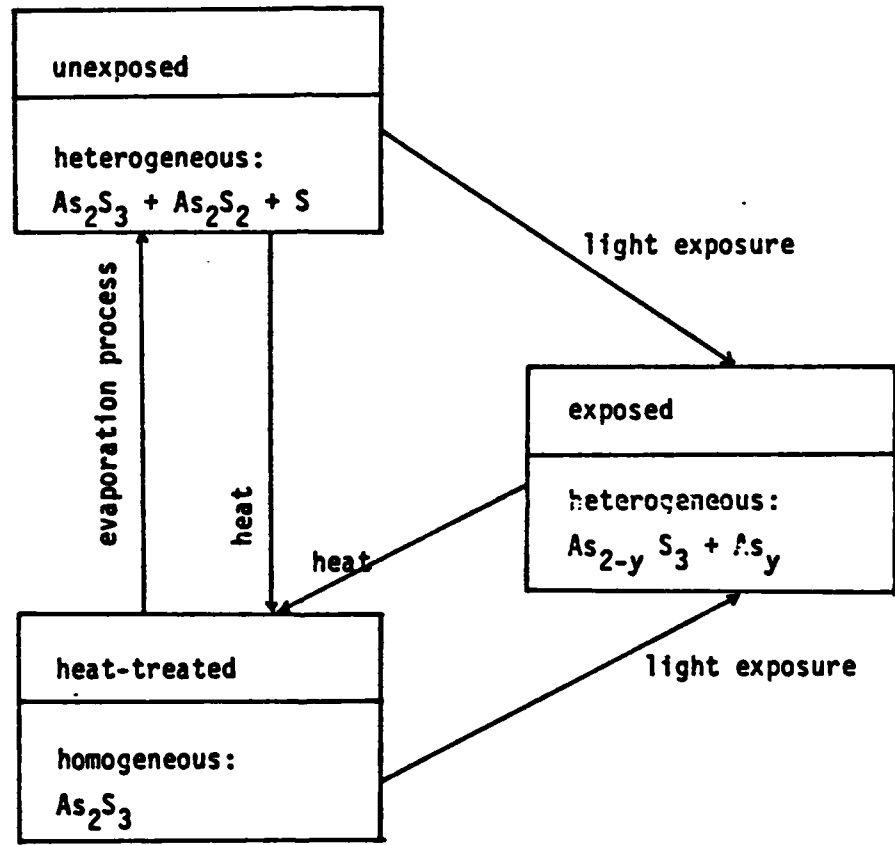


Fig.4.1 Three-state model of As_2S_3 optical-storage medium proposed by Kenemam et al.⁽¹¹⁾

in arsenic-group chalcogenides As_2X_3 (where X = S or Se). These compounds are semiconductors in their normal states. As_2X_3 usually crystallizes in layer structures.⁽¹⁶⁾ Single crystal As_2S_3 is known as orpiment. The monoclinic structure of orpiment As_2S_3 is shown in Fig. 4.2(a). The lattice constants are $a = 11.475 \text{ \AA}$, $b = 9.577 \text{ \AA}$, $c = 4.256 \text{ \AA}$ and $\beta = 90^\circ 41'$.⁽¹⁷⁾ Orpiment is in the crystal glass C_{2h}^5 ($P2_1/n$). ----As - S - As - S ---- spiral chains are linked by sulfur atoms to form corrugated layers perpendicular to the [010] direction. The As-S distances within the layers range from 2.243 \AA to 2.308 \AA . The shortest nonbonded contacts between the layers are S-S distances of 3.242 \AA and As-S distances of 3.475 \AA . The bond angle As-S-As of the sulfur atom bridging two parallel spiral chains is 87.9° , corresponding to covalent p^2 bonds, while the bond angles of the S atoms within the chains are 101.0° and 103.7° . The As bond angles range from 92.8° to 105° , reflecting the tendency to sp^3 bonding due to the s^2 lone pair.

Another distinct As-S compound known to exist is As_4S_4 . Single crystal As_4S_4 , known as realgar, is a molecular (non-layer) structure. It is also monoclinic with $a = 9.27 \text{ \AA}$, $b = 13.50 \text{ \AA}$, $c = 6.56 \text{ \AA}$, and $\beta = 106^\circ 37'$.⁽¹⁸⁾ Ito⁽¹⁸⁾ pointed out that there are similar -As-S-As-S- chains in both orpiment and realgar. These structures are illustrated in Fig. 4.2. Fig. 4.2(a) shows two different projections of the structure of orpiment As_2S_3 and (b) shows two orthogonal views of the As_4S_4 "cradle". The similar chains in both structures are noted by numbers: 1,2,3,4.

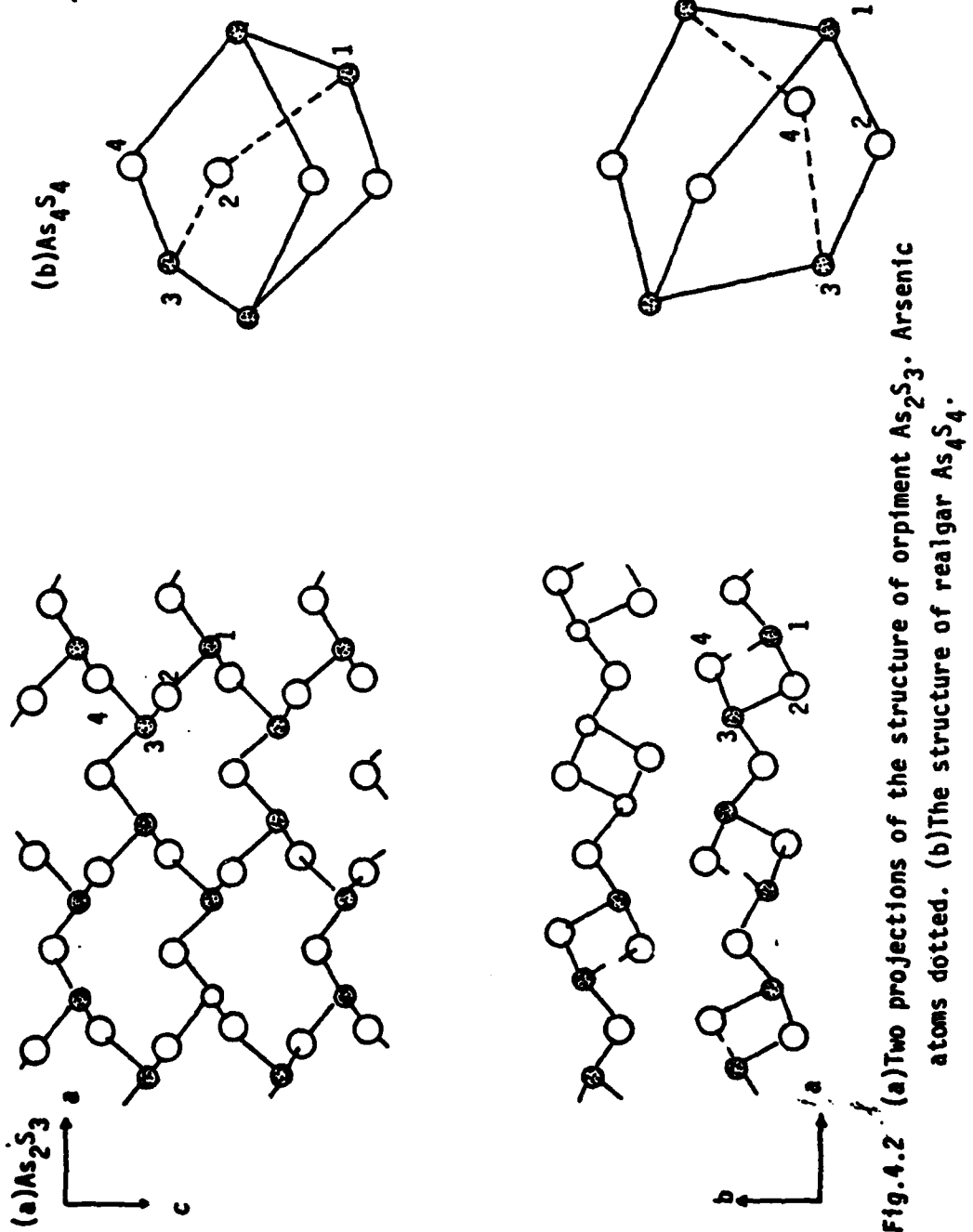


Fig. 4.2 (a) Two projections of the structure of orpiment As_2S_3 . Arsenic atoms dotted. (b) The structure of realgar As_4S_4 .

Numerous As-S compositions exist as homogeneous phases (Fig. 2.1). Structural models for the glasses and evaporated films have been suggested by Maruno, etc., and are summarized below: (19-22)

1. As_2S_3 glass is a layer structure similar to orpiment but with larger interlayer separation.
2. As_2S_x ($3 < x < 10$) contains S links between pairs of As atoms of As_2S_3 .
3. As_2S_x ($x > 10$) contains S_8 rings as well. There is no interlayer sulfur structure.
4. As_2S_x ($2.67 < x < 3$) contains As-As bonds where As-s-As existed in As_2S_3 . The layer structure is maintained with increased interlayer separation and no discrete As_4S_4 molecules exist.
5. As_2S_x ($x < 2.67$) a heterogeneous structure with As_4S_4 (or As_2S_2) groups exist.

4.2 EXPERIMENTAL

Films for the structural investigation were evaporated in a conventional vacuum system as described in Sec. 2.1. The structure of the As_2S_3 film was examined with x-ray diffraction, transmission electron microscope, infrared spectroscopy, near IR and visible spectroscopy, and electrochemical measurements. The effect of heat treatment of the As_2S_3 films was also studied. The chemical nature of the exposure was studied with differential etching in basic NaOH solution and CF_4 plasma as described in the previous chapter.

The x-ray intensity data were collected in the range $2\theta = 6^\circ$ to 90° with a Philips-Norelco diffractometer using copper radiation (40 kv, 30 mA) and a monochromator set on the Cu K α line. Variations in film thickness limited the usefulness of comparisons of absolute intensity from one set of experiments to another, so only relative intensity is used in this study. Transmission electron microscope examinations were performed on copper grids overcoated with about 500 Å of the As₂S₃ film using a Philips 300 TEM operated at 100 kv. The Gaussian image and the electron beam diffraction pattern were obtained for different samples. The refractive index change data are calculated by observing the wavelengths of the reflection maxima and minima in the transparent portion of the optical spectrum. The IR transmission of films was measured from 250 to 5000 cm⁻¹ with a Perkin-Elmer Model 457 Grating Infrared Spectrophotometer. In this double-beam IR spectroscope, the output signal is the difference between sample and reference signals. The As₂S₃ overcoated Si substrate and another identical Si substrate without any overcoating were placed in the sample and reference windows, respectively. The IR transmission data are the difference signal due to the As₂S₃ film only. One As₂S₃ film of about 2.5 μ m thickness was examined in the unexposed state, the exposed state and after heat treatment.

4.3 EXPERIMENTAL RESULTS

4.3.1 X-Ray Diffraction

Amorphous solids yield an x-ray diffraction pattern similar to that of a microcrystalline powder, i.e., broad rings vanishing rapidly with increasing diffraction angle without any evidence of spots or sharp rings which would indicate some degree of crystallinity. In this study no attempt was made to obtain the radial distribution function (RDF) in the As_2S_3 film. X-ray diffraction was used to obtain information on structural changes resulting from light exposure.

In this investigation, unexposed and exposed As_2S_3 films were examined by x-ray diffractometer to see if the As_2S_3 optical storage effect is caused by an amorphous-crystalline phase transition. Fig. 4.3 shows the x-ray diffraction spectra of the As_2S_3 film obtained with copper $\text{K}\alpha$ ($\lambda = 1.54 \text{ \AA}$) radiation. A relative sharp diffuse peak at about 17° and a broader diffuse peak near 30° are found for as-deposited As_2S_3 film. It was observed that the film examined is amorphous in the main before exposure. After UV exposure for 3 hours, the film is still amorphous in the main, however, crystalline As (not crystalline As_2O_3) is found on the surface which has a peak at about 57° . Also, even though the films are basically amorphous As_2S_3 in both states, comparison of x-ray diffraction traces revealed structural change due to the light exposure effect; for Cu $\text{K}\alpha$ radiation, the amorphous peaks shift from $2\theta = 16.5^\circ$ to 17.2° and from 29.8° to 30.1° and decrease in intensities which is in agreement with the results of DeNeufville et. al. (25) and Keneman et. al. (11). The same effect (see Fig. 4.4) is also observed for the samples annealed at 180°C in air for one hour.

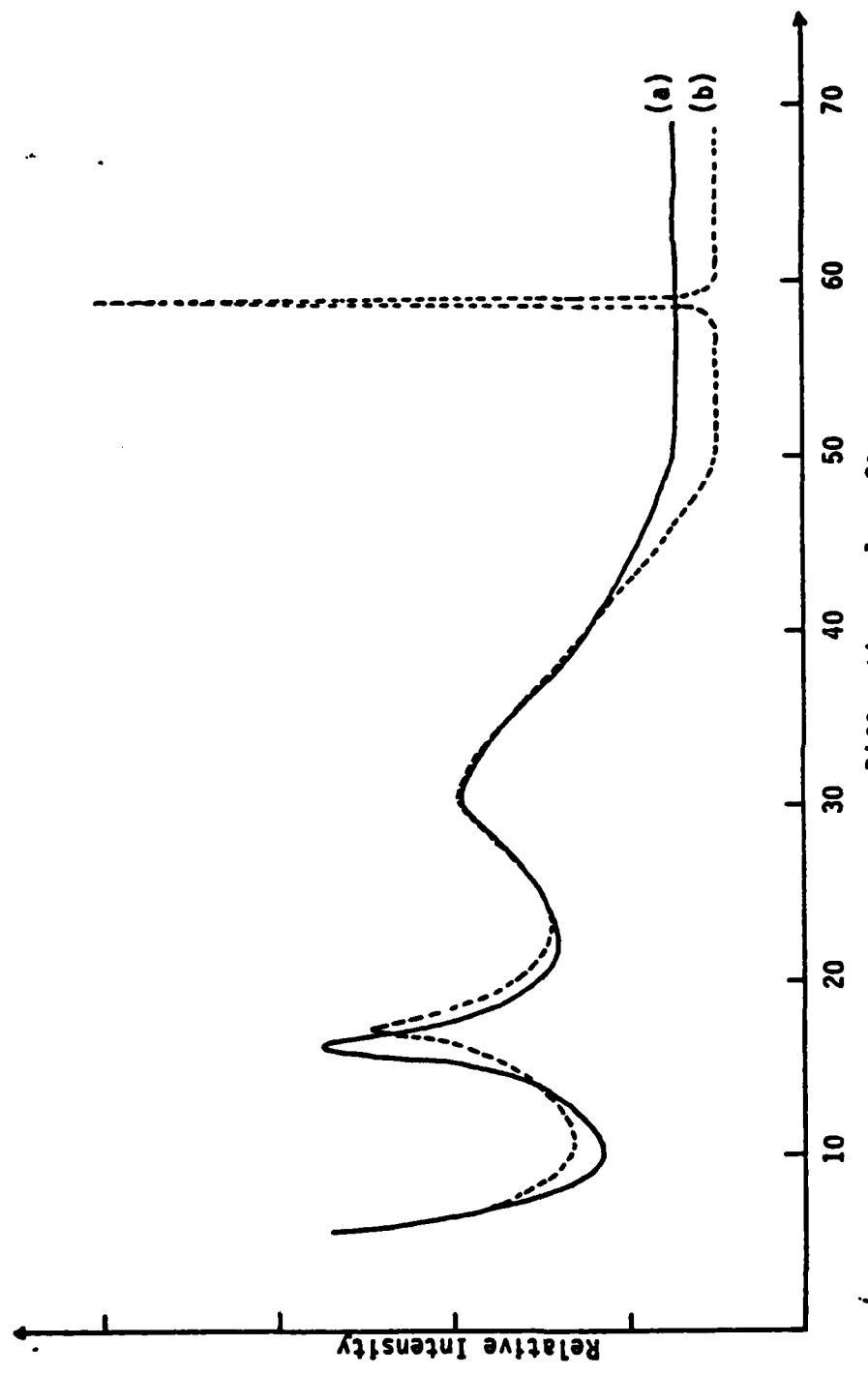


Fig.4.3 The x-ray diffraction spectra of the As_2S_3 film obtained with $\text{Cu K}\alpha$ ($\lambda=1.54 \text{ \AA}$) radiation. (a) the unexposed case; (b) after UV exposure for 3 hours.

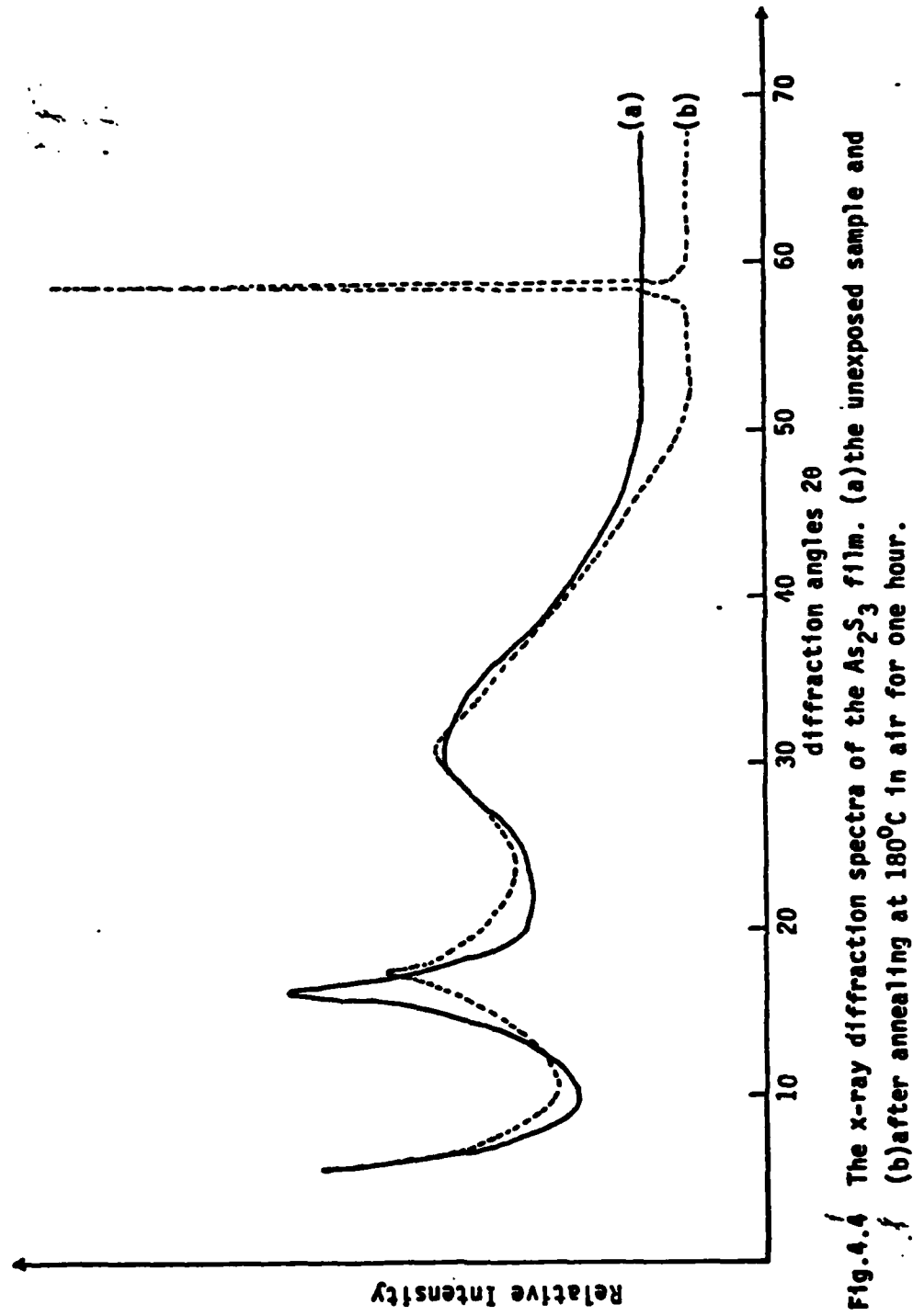


Fig. 4. The x-ray diffraction spectra of the Ag_2S film. (a) the unexposed sample and (b) after annealing at $180^\circ C$ in air for one hour.

It is concluded that heat treatment and band-gap light exposure lead to the same state with respect to x-ray diffraction.

Tanaka⁽²⁷⁻²⁸⁾ reported a difference in the x-ray diffraction spectra for what corresponds to our heated and exposed films and noted that the x-ray peak shifts in angles 2θ by $0.15 \pm 0.06^\circ$. This shift, not observed in this study, is quite small compared to the 0.7° shift associated with exposed or heated samples and unexposed films. Keneman et. al.⁽¹¹⁾ reported a shift in angle 2θ of 1.5° between exposed or heated samples and unexposed films. Crystalline As was not observed in their study. This is almost certainly due to differences in the composition of the initial films due to the different film evaporation conditions.

The principal point to be noted in Fig. 4.3 is the change in the entire x-ray scattering pattern under UV exposure or heat treatment. We observe that the first relative sharp diffuse peak is reduced by a factor of 1.5 in intensity and is broadened and shifted to a higher angle by 0.7° as a result of illumination or heat treatment; the minimum at $2\theta = 20^\circ$ is about the same, the second diffuse peak changes its shape and is shifted slightly to higher angle. What we observe in these two diffuse peaks is a structural alteration that cannot be attributed simply to phase separation and is not due to crystallization in As_2S_3 films.⁽²⁵⁾ Since it is difficult to obtain direct structural information from the x-ray scattering intensity function, other structural characterization techniques are needed to obtain more information.

Because the intensity profile of the first diffuse peak decreases, broadens, and shifts, it can be concluded that it is not merely a variation in nearest neighbor coordination but rather a much more dramatic alteration of the longer range structure since the x-ray intensity profile is very dependent on the long range structure. Another significant point is that voids do not normally form in deposited films as far as is known, thus Bishop et. al. (26), using small angle x-ray scattering with angles $2\theta = 0.29^\circ - 17.4^\circ$, found no evidence for their existence in several chalcogenides including evaporated As_2S_3 films. It is in contrast to the situation found in deposited films of Ge and Si where voids with radii between 5 and 40 Å can occupy about 5% of the total volume. (27) It is important to point out that for As_2S_3 films prepared by glow discharge decomposition of a gas mixture of As H₃ - H₂S, (28) the x-ray structural analysis shows that the peak near 30° is sharper than the peak near 17° and the broadening of the peak is not observed.

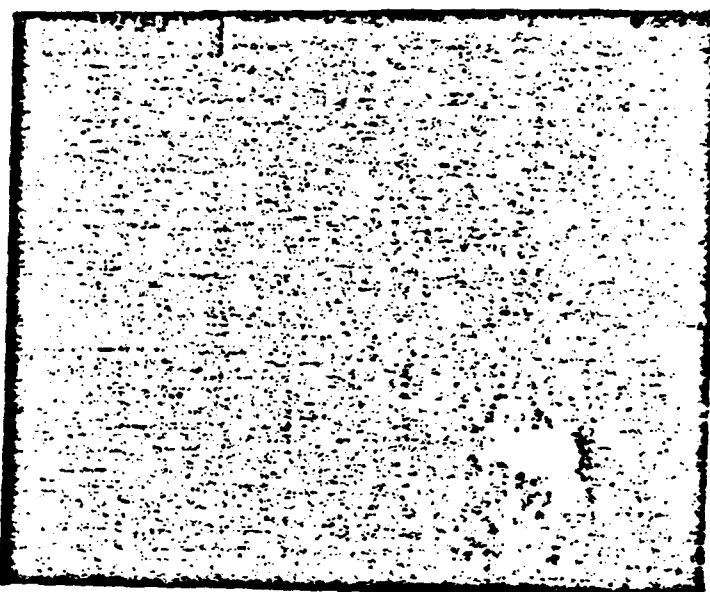
4.3.2 Transmission Electron Microscopy (TEM)⁽²⁹⁻³⁰⁾

Normal electron microscopy provides information about the geometrical aspects of thin films such as continuity, homogeneity, surface roughness and about the evolution of the crystallization process. Amorphous chalcogenide films have been found to be either continuous and homogeneous or to contain some phase separation morphology depending on the substrate, deposition conditions, annealing, and the

stoichiometry of the compound.

In this work, TEM was performed on 500 Å - 1000 Å films of As_2S_3 evaporated onto carbon coated grids which were examined both before and after illumination. Fig. 4.5 and 4.6 show the results. The first micrograph in Fig. 4.5 represents the unexposed As_2S_3 sample and the following micrograph shows the sample after illumination. Fig. 4.6 shows the corresponding selective area electron diffraction patterns. Fig. 4.6(a) contains only amorphous bands and no sharp crystalline rings. Fig. 4.6(b) contains some degree of crystalline rings which are probably due to arsenic crystallization or the oxidation of As_2S_3 films accompanying optical illumination in the ambient environment. The oxidation of As_2S_3 films seems unlikely since the x-ray diffraction pattern does not show the corresponding As_2O_3 peaks in the exposed sample. From this data, it is established that all the products in the as-deposited films are amorphous and arsenic crystallization produces some microcrystals on the exposed films which are identified by x-ray diffraction. Fig. 4.5(a) shows that the as-deposited As_2S_3 film is a continuous network and homogeneous film. It is important to point out that in this study the electron beam which produced continuous heating volatilized the film. This can easily be observed under the focussed electron beam. It is understandable because amorphous As_2S_3 films are electron-beam sensitive materials. A cold sample stage in the TEM is needed to avoid the electron-beam heating problem. Fig. 4.5(b) shows the small phase separations from the con-

(a)



(b)

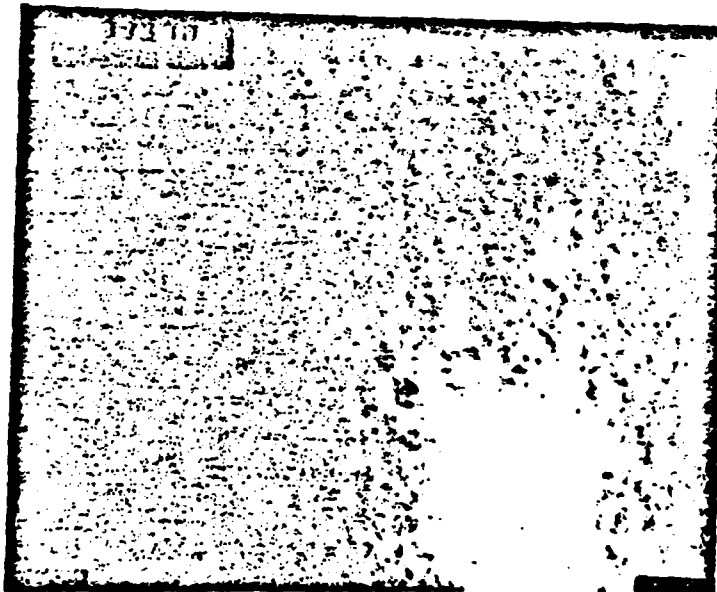


Fig.4.5 Bright field image of As_2S_3 films deposited on carbon coated grids taken before (a) and after (b) UV illumination.

(a)

(b)

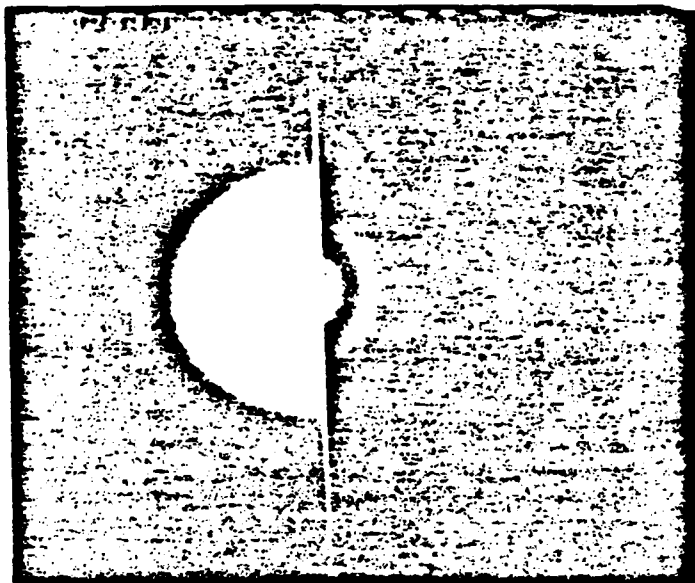


Fig.4.6 The Electron diffraction patterns of As_2S_3 films before (a) and after (b) prolonged UV illumination.

tinuous background should be arsenic-rich since a sulfur-rich phase would be the more likely to volatize under electron beam exposure.

From x-ray diffraction and electron-beam diffraction patterns, it is established that our films are richer in arsenic.

It is important to note that in this study the property changes in the As_2S_3 film is irreversible in the sense that a simple annealing treatment at a temperature higher than the illumination temperature cannot restore the initial structural state and optical properties. It is believed that the irreversible structural transformation resultant upon light exposure is due to the decomposition of the film and long range structural changes. On the other hand, the reversible photostructural change is due to the photoinduced change in the local order of the amorphous structure only.

4.3.3 Infrared Spectroscopy

The structure of most amorphous chalcogenides is not well characterized. For any binary system A_xB_{1-x} , analysis of the RDF obtained from x-ray diffraction is complicated by the difficulty of separating contributions from A-A, B-B and A-B bonds. In multicomponent systems identification is even more ambiguous. Several techniques, such as EXAFS (extended x-ray absorption fine structure)⁽³¹⁻³²⁾ or EDXD (energy dispersive x-ray diffraction),⁽³³⁻³⁴⁾ have the capability of making distinctions between bond types but problems associated with data acquisition and analysis have not allowed conclusive results to

be obtained except in a few cases. For several systems, complementary infrared and Raman spectroscopies have been found to be the most useful techniques in the study of local structural. Infrared spectra of crystalline solids reveal characteristic frequencies associated with different modes of atomic vibrations; the actual assignments being based on selection rules and calculated frequency values. These, in turn, involve force constants, atomic masses, and geometric configurations between nearest and higher order neighbors. A comparison of results from crystalline and amorphous materials enables recognition of modes associated with local molecular grouping of atoms. In this subsection, the optically and thermally induced irreversible changes of the IR vibrational spectra of evaporated As_2S_3 films will be examined.

Films with thickness about $2.5 - 3.0 \mu\text{m}$ are prepared by evaporating glassy As_2S_3 bulk onto high resistivity Si single crystal substrates in vacuum at a rate of $0.1 \mu\text{m}/\text{min}$. After deposition the samples are removed from the vacuum chamber and placed in a desiccator and stored in the dark until they are ready to use. IR transmission measurements are made between 250 cm^{-1} and 4000 cm^{-1} . A typical IR transmission spectrum of a $2.5 \mu\text{m}$ thick evaporated As_2S_3 film is shown in Fig. 4.7. The sinusoidal IR transmission curve between 400 cm^{-1} and 4000 cm^{-1} is due to multiple internal interferences. The difference in the spacing of the interference fringes between unexposed and exposed films indicates the increase of n_d (refractive

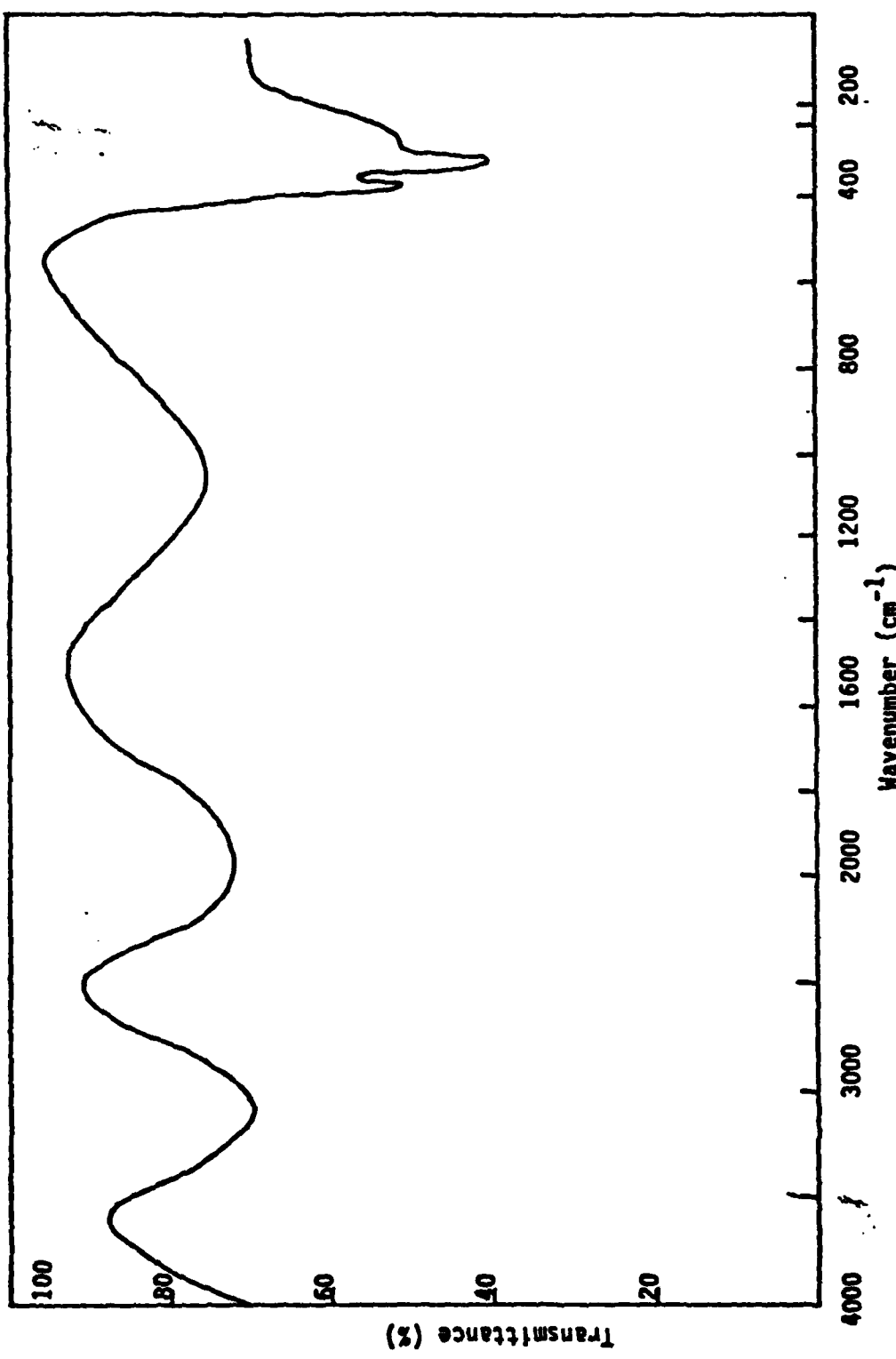


Fig.4.7 An IR transmission spectrum of a 3 μm thick evaporated As_2S_3 film.

index \times film thickness) with ultraviolet exposure. Transmission spectra for unexposed and exposed states are shown in Fig. 4.8(a) and (b), respectively. A freshly deposited film of As_2S_3 is also thermally annealed in the dark at $190^\circ C$ for one hour. The spectrum of the annealed sample is shown in Fig. 4.9(b) together with the spectrum of the as-deposited As_2S_3 film. It is found that UV exposure and heat treatment have the same effect on absorption band frequencies: a pair of bands at 374 cm^{-1} and 337 cm^{-1} is replaced by a single band at 311 cm^{-1} . However, in some cases the spectral features at 374 and 337 cm^{-1} after light exposure or an annealing process are still barely observed. It is concluded that the as-deposited film has features at 374 cm^{-1} and 337 cm^{-1} assigned to As_4S_4 as well as the 311 cm^{-1} absorption of glassy As_2S_3 . The broader shoulder centered at 311 cm^{-1} in the freshly deposited film can be identified with 310 cm^{-1} IR absorption peak observed in glassy As_2S_3 . This absorption peak at 310 cm^{-1} is associated with the As-S bond stretching in As_2S_3 glasses. (35-37) The IR spectra observed in this study are compared against the results of others in Table 4.1. (35-39) Table 4.1 may be interpreted as follows: Exposed and annealing affect the IR spectra in the same manner. Further it is noted that the dominant initial species is As_4S_4 (or As_2S_2) and the final species is As_2S_3 . One has also to note that As_4S_3 has vibrational frequencies similar to As_4S_4 in the spectra range considered.

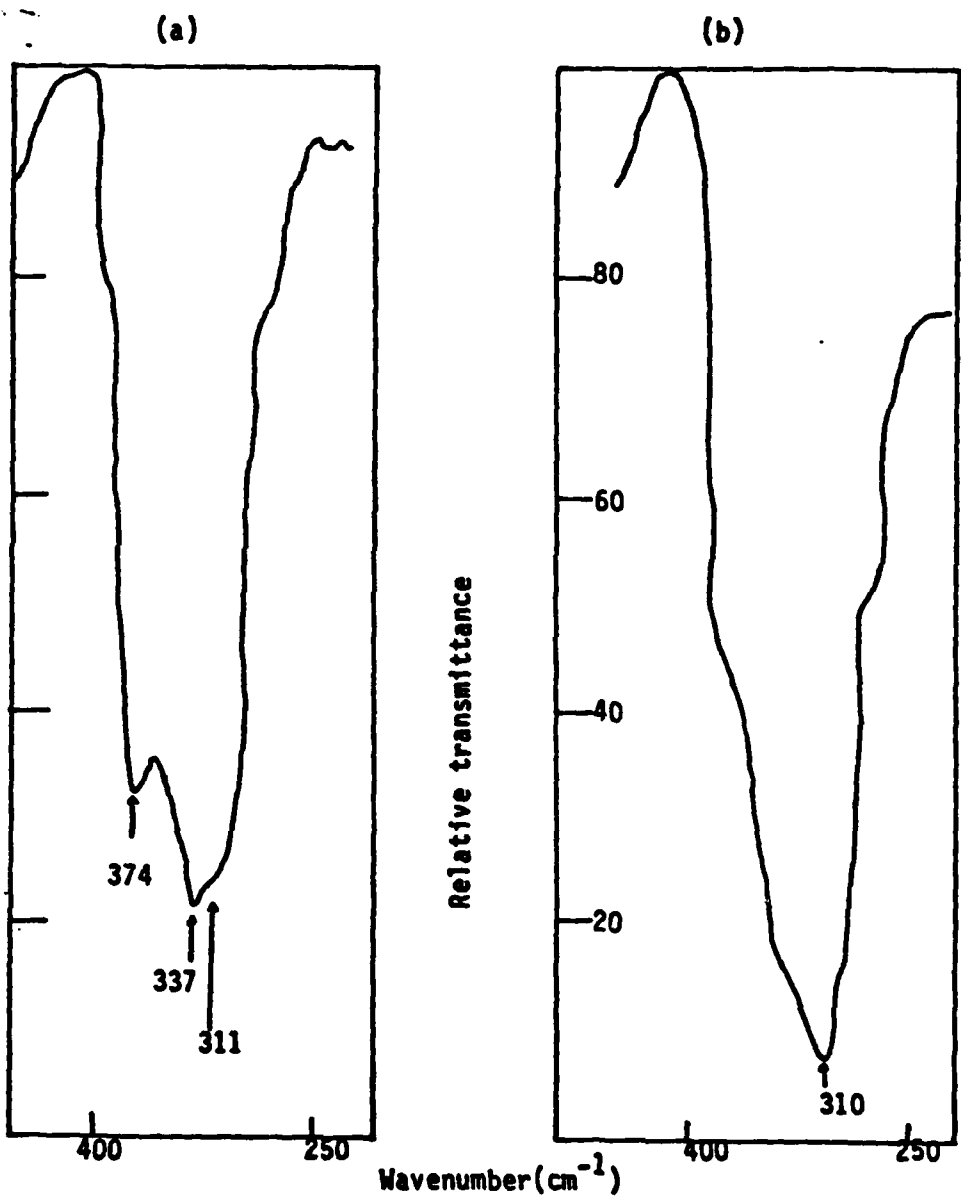


Fig.4.8 IR transmission spectra for unexposed (a) and UV-exposed (b) As_2S_3 films.

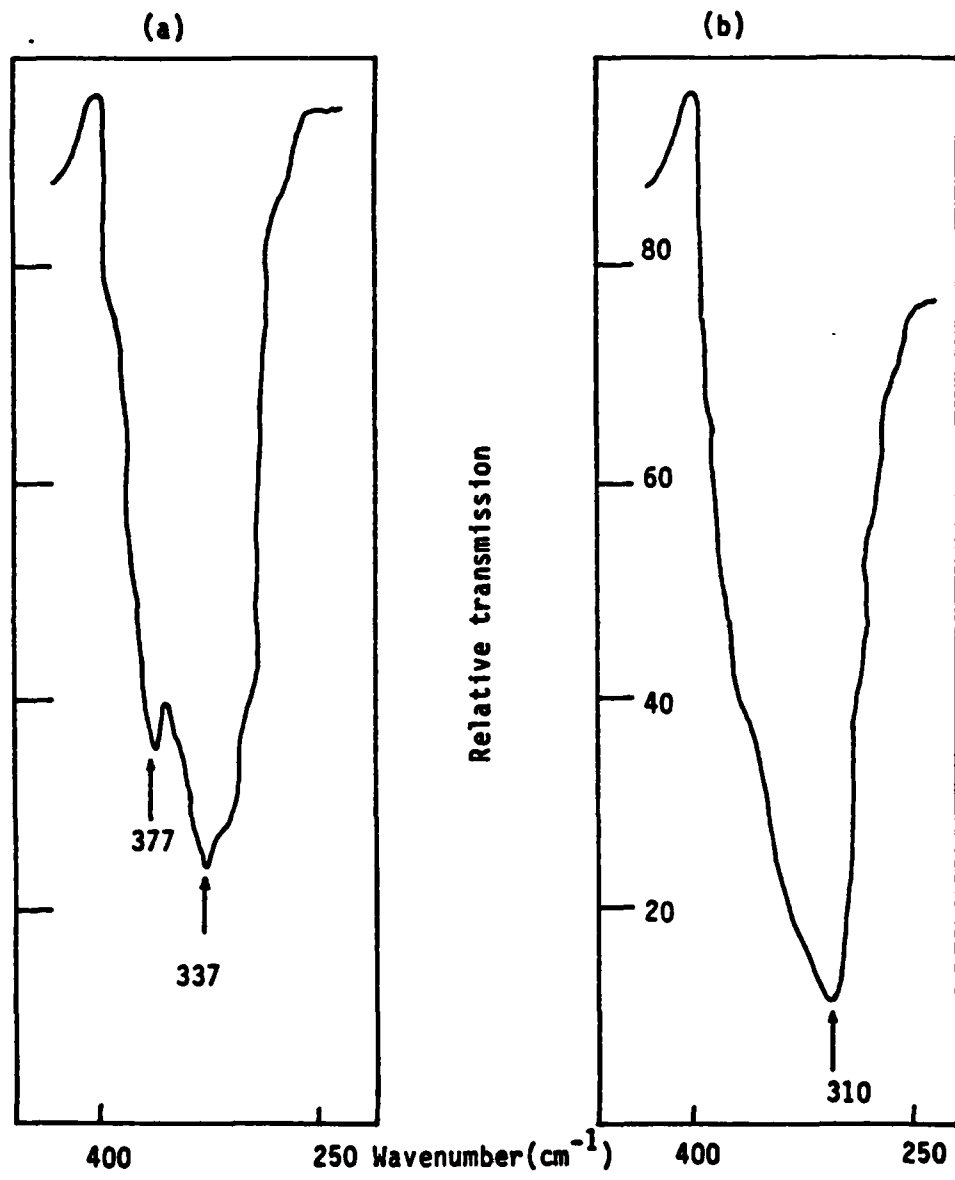


Fig.4.9 IR spectra for as-deposited and annealed states (b) of As_2S_3 films. Annealing temperature is 190°C .

IR (present work) evaporated film (as-deposited)	IR (37,39) As_2S_3 (illuminated)	IR (38) As_4S_4 α -crystal	IR (11) As_2S_3 evaporated film(as-deposited)
311 (weak)	310 (strong)	310 (strong)	315 (strong)
337 (strong)	338(weak)	340 (weak)	336 (strong)
374 (strong)	377(weak)	375 (weak)	378 (strong)

Table 4.1 Infrared absorption bands in As_2S_3 and related materials.

4.3.4 Summary

From our x-ray and electron-beam diffraction data together with the measurements of others,⁽⁴⁰⁻⁴²⁾ it can be concluded that the films are arsenic-rich and there are significantly more As-As bonds than required by stoichiometry. IR transmission spectra further indicate that As-As bonds exist primarily in As_4S_4 structural units. The remaining network consists of the usual As_2S_3 pyramidal units as well as S in chains of various lengths. This conclusion agrees very well with the Raman spectra of an as-deposited As_2S_3 film, one annealed at 180°C, and bulk As_2S_3 glass reported by Solin et. al.⁽³⁸⁾ They concluded that the sharp additional bands in the Raman spectrum for the as-deposited film suggested the presence of As_4S_4 molecular units which polymerized into the As_2S_3 network on annealing. DeNeufville et. al.⁽²⁵⁾ suggested that the structure of freshly deposited films of As_2S_3 could be described as a dense packing of As_4S_6 molecules. However, the Raman spectra imply the existence of a considerable extent of polymerization as well as the molecular As_4S_4 units. The same conclusion is also drawn in this study. Unfortunately, the ratio of the amounts of As_4S_4 and As_2S_3 in the as-deposited film is not known at the present time. However, Strom et. al.⁽⁴³⁾ indicate that the amounts of As_4S_4 and As_2S_3 in the freshly evaporated film are comparable.

4.4 PHOTODARKENING EFFECT IN AMORPHOUS AS₂S₃ FILMS

In general, absorption edges of amorphous chalcogenide semiconductors are often much more sensitive to the conditions of preparation, light exposure, thermal history, and purity than the broad features of the whole optical absorption band. This holds in particular for thin films. It is well known that irradiation of chalcogenide glasses with band-gap illumination can cause shifts of the fundamental absorption edge to lower photon energies which are often accompanied by changes in the x-ray diffraction patterns and infrared absorption spectra. It is also true for As₂S₃ films which has been presented in the previous subsection.

In this study the As₂S₃ film was 0.3 - 0.5 μm thick. Optical measurements were made over the photon energy range 1.0 - 2.0 eV. The reflection of films was measured with a PbS detector. The wavelength dependence of the index of refraction was calculated from extrema by wavelengths determined by

$$4n(\lambda_m)d = m\lambda_m \quad (4-1)$$

where m is the order of interference, the λ_m are the wavelengths of the corresponding extrema, and d is the film thickness. The conventional assumption of nominal constancy of n at long wavelengths is used to determine the order of the initial extremum. The result of nd in As₂S₃ films as a function of exposure time is shown in Fig.

4.10. The maximum 4.7% change of nd between as-deposited and exposed films is reached after 10 minutes UV exposure. Tanaka⁽⁴⁴⁾ reported

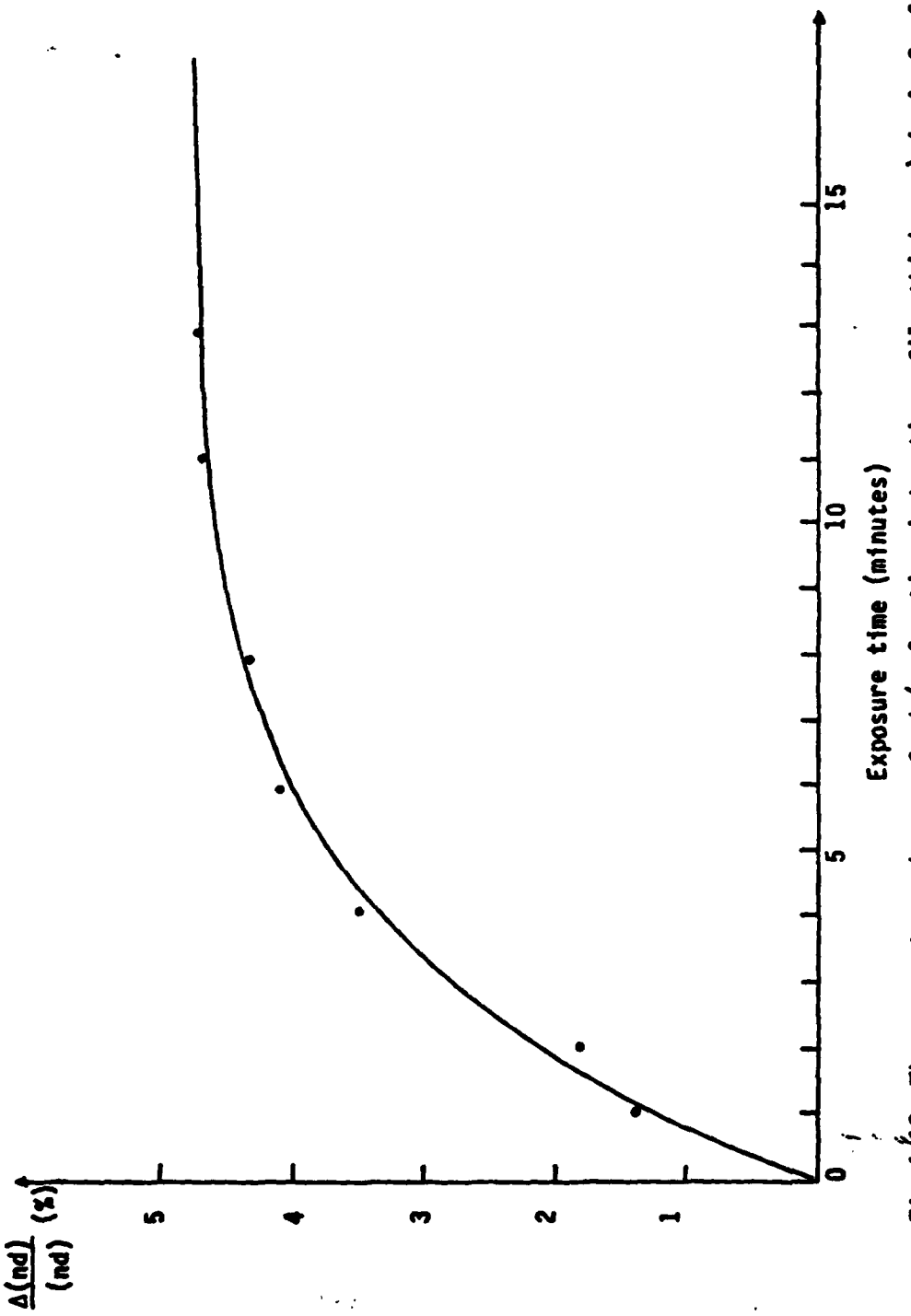


Fig.4.10 The percentage change of nd (refractive index times film thickness) in As_2S_3 films as a function of UV exposure time.

thickness change before and after exposure was only about 0.4%, so the refractive index change upon light exposure is much more sensitive than the change in thickness. The % changes of refractive index in As_2S_3 films in this study is larger than the results reported elsewhere⁽⁴⁵⁻⁴⁶⁾. Before discussing this discrepancy, the optical absorption edges of the chalcogenides will be briefly discussed.

The optical absorption edges are characterized by an absorption coefficient α that rises exponentially with increasing photon energy up to a value of α in the range $10^3 - 10^4 \text{ cm}^{-1}$. In chalcogenides and some compound glasses in the strong absorption region of the edge ($\alpha > 10^4 \text{ cm}^{-1}$), the absorption constant α can be described by Urbach's rule⁽⁴⁷⁾

$$\alpha\hbar\omega = B(\hbar\omega - E_0)^2 \quad (4-2)$$

where B lies in the range $10^5 - 10^6 \text{ cm}^{-1} \text{ eV}^{-1}$ and E_0 is the optical band-gap energy. In this region the absorption is due to transitions between valence band and conduction band states. Below $\alpha = 10^{-4} \text{ cm}^{-1}$, it has been observed in all compound semiconducting glasses so far studied that

$$\alpha = \exp(\hbar\omega/E_1) \quad (4-3)$$

where E_1 is in the range $0.05 - 0.08 \text{ eV}$. At very weak absorption levels ($\alpha < 1 \text{ cm}^{-1}$) one observes another exponential part of the absorption edge⁽⁴⁸⁾

$$\alpha \approx \exp(-\omega/E_t) \quad (4-4)$$

where E_t is always larger than E_1 . The exponential shape of the absorption edge suggests that the optical absorptions in this region are associated with localized states in the gap. The spectral dependence of the absorption coefficient and the refractive index is generally connected by the Kramers-Kronig relations. With the aid of these equations, the correspondence between changes in an absorption coefficient α and a refractive changes can be calculated.⁽¹⁰⁾ Since the refractive index changes in As_2S_3 films induced by band-gap illumination are positive, a red-shift of optical absorption edge is expected to occur. Indeed, the edge is shifted to lower photon energy by 0.04 eV after light exposure at room temperature.^(44,47)

The spectral dependence of optical property changes can be explained in terms of states in the gap. In evaporated As_2S_3 films, high defect concentrations are to be expected and it is assumed that these defects are responsible for states in the gap.^(49,52) According to this model, electrons are photoexcited out of the valence band and trapped by the states broadly located above the valence band. These trapped electrons can be re-excited and produce an absorption edge shift, increase the refractive index, and interact with the neighbor lattice to induce a local structural rearrangement. The details of this possible microscopic mechanisms by which local bonding configurations are optically changed and rearranged will be studied in the next section.

4.5 CHARGED DEFECT MODEL IN EVAPORATED As₂S₃ FILMS

The photo-induced absorption edge shift and recent measurements of photo-luminescence⁽⁵³⁾ and electron spin resonance⁽⁵⁴⁾ have demonstrated the presence of gap states in chalcogenide materials. Anderson⁽⁵⁵⁾ had previously proposed a model based on the idea that in amorphous materials the effective interaction between a pair of electrons in the same state can be attractive because of a strong electron-phonon coupling, and so an effective negative correlation energy results. Later Street and Mott⁽⁴⁹⁻⁵⁰⁾ applied this concept specifically to point defects by assuming a large density of dangling bonds ($10^{18} - 10^{19} \text{ cm}^{-3}$) in such materials that act both as acceptors and donors. These dangling bonds are point defects at which normal coordination (2 for chalcogenides, 3 for pnictides) cannot be satisfied because of constraints of local topography. The neutral dangling bonds therefore contain an unpaired electron. The authors further assume that a dangling bond may be occupied by zero, one or two electrons, and label these states D⁺, D⁰ and D⁻, respectively. These charged defects in turn give rise to states in the gap. This could also apply to the case of evaporated films of As₂S₃. They suggest that the process



is exothermic. Ovshinsky⁽⁵⁶⁾ suggested that the interactions between lone-pair electrons on different atoms, such as sulfur and

and arsenic atoms in As_2S_3 , and interactions with their local environment result in localized states in the gap of chalcogenide glasses. Kastner et. al. (13, 52, 57-58) used this concept to show that specific interactions between nonbonding orbitals give rise to unusual bonding configurations which they call valence alternative pairs (VAP's). They point out that the negative correlation energy is a result of this special chemical bonding of these materials and not a result of disorder. Therefore it is expected to arise in crystals as well. With this new model, they not only successfully explained the high density of defects but also the origin of the large negative correlation energy suggested by Street and Mott.

Band-gap illumination (2.4 eV for As_2S_3) removes an electron from the nonbonding, p like, orbital of the chalcogenide atom leaving a hole behind. According to the Anderson and Mott theory a large lattice distortion in the vicinity of the excited carriers will occur due to the immobility of the electron-hole pair and the presence of a strong electron-phonon interaction. These lattice distortions generally occur before any recombination of the exciton can take place. Under certain conditions, this strong electron-phonon coupling will involve the switching of bonds, leading to the formation of chalcogen atoms which are three-fold and singly coordinated, instead of the normal two-fold coordination in chalcogen atoms. These are designated D^+ and D^- (or C_3^+ and C_1^- according to Kastner's designation) charged defect centers in Mott's model, respectively. Furthermore, Street⁽⁵⁹⁾ suggests that a D^+D^- pair can be regarded as a self-trapped

exciton.

Mott and Stoneham⁽⁶⁰⁾ first used the configurational coordinate diagram of Fig. 4.11(a) which was modified later by Street⁽⁵⁹⁾ (Fig. 4.11(b)). They show that the exciton can exist either in state A (Fig. 4.11(a)) without the distortion of lattice, or in state B when strong distortion occurs and the exciton can be self-trapped. A potential barrier W separates these two states, A and B, which must be overcome for self-trapping to occur. Street⁽⁵⁹⁾ suggests that excitons in chalcogenides have a strong electron-phonon coupling such that the barrier to self-trapping is small enough to be overcome at all temperatures. Their modified configurational coordinate diagram (Fig. 4.11 (b)) applicable to chalcogenides shows two recombination paths, I and II. Since the electron-phonon coupling in amorphous materials is strong, path I, direct recombination to the ground state, is less likely than path II, thermal excitation to the ground state with the creation of a metastable D^+D^- pair. The same charged defect centers can also form in pnictides. Kastner labels them as P_4^+ and P_2^- (i.e., 4-fold and 2-fold), respectively. When both chalcogenides and pnictides are present in a glass, such as As_2S_3 , all the species P_4^+ , C_3^+ , P_2^- and C_1^- will be present.⁽⁵²⁾

The above model gives an explanation of the reversible photostructural transformation in arsenic chalcogenides. In Fig. 4.11(b) the self-trapped D^+D^- pair needs thermal excitation to return to the ground state. This is the origin of the reversible photostructural

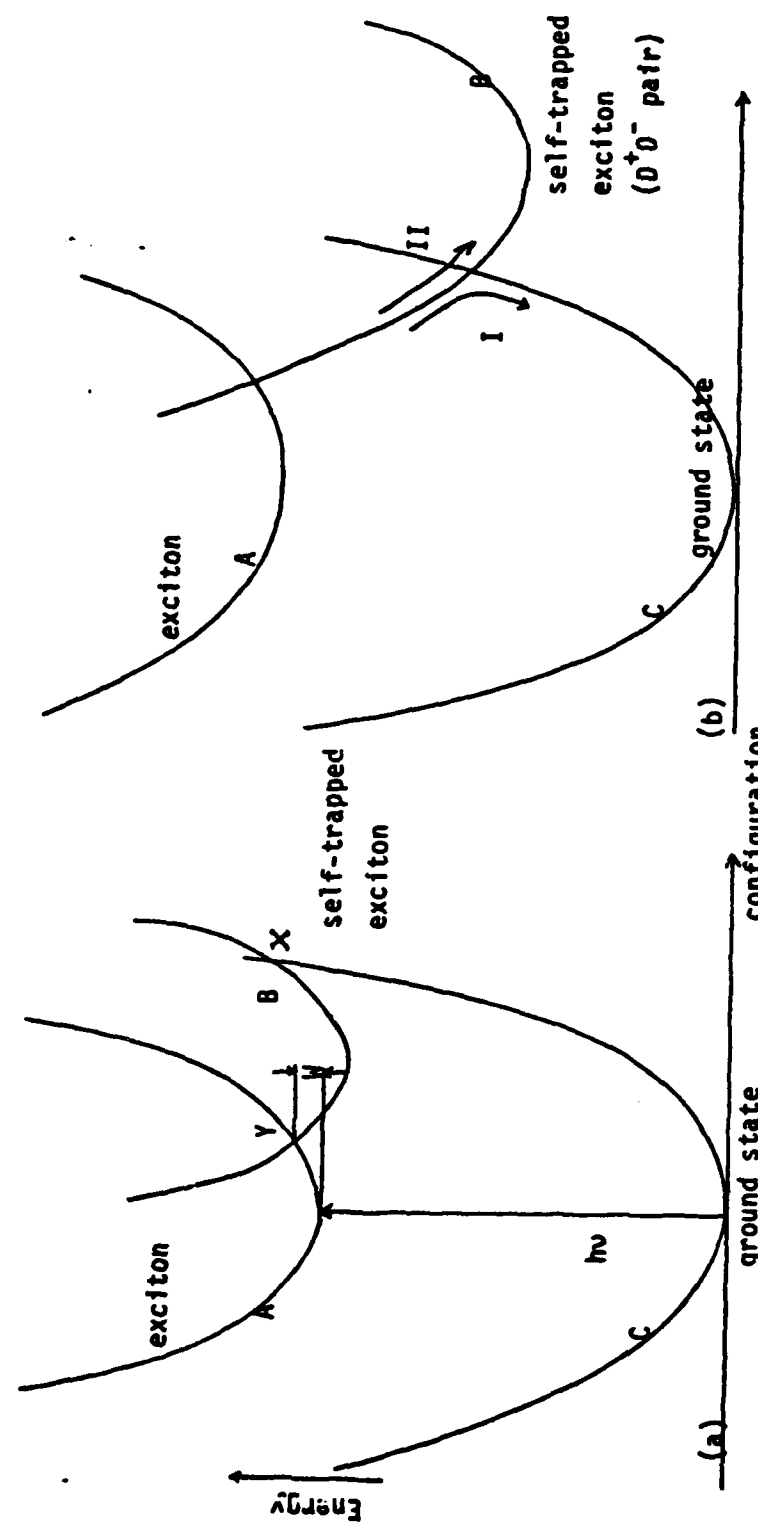


Fig. 4.11 (a) configurational coordinate diagram proposed by Matt and Stoneham. (60)
 (b) configurational diagram of evaporated As₂S₃ proposed by Street. (59) Curve A-
 electron-hole pair after excitation, curve B- self-trapped D⁺D⁻ pair, and curve C-
 ground states (As₄S₄ molecules and S chain).

change and the accompanying photodarkening in chalcogenides. Photodarkening occurs because the self-trapped exciton states lie above the initial ground state, and so the re-excitation of an electron-hole pair requires less energy. Although this model explains a variety of phenomena in chalcogenide materials, it cannot account for the irreversible photostructural transformation observed in this study. IR absorption spectra indicate that the ground state in evaporated As_2S_3 films consists of glassy As_2S_3 and As_4S_4 molecular units as well as S chains. After UV exposure the structure of the film changes to a continuous As_2S_3 network. Optical absorption data indicate that the bond energies of As-S bonds lie energetically lower than the bond energies associated with As-As and S-S homobonds.⁽⁵¹⁾ Thus, in the absence of other contributions, the energy of the final state after exposure should be lower than that of the initial state. Later Strom and Martin⁽⁴³⁾ propose a configurational coordinate diagram of photopolymerization of evaporated As_2S_3 films which is shown in Fig. 4.12. Curve A is the ground state, B is the exciton state but before structural relaxation, C is the self-trapped exciton state, and D is the final state which lies below curve A because the corresponding state in curve D has lower energy than the state in curve A.

According to the above model developed by Mott et. al., a plausible sequence of events leading to polymerization of As_4S_4 into a glassy As_2S_3 network is shown in Fig. 4.13.⁽⁴³⁾ In Fig. 4.13(a) is shown a possible structural arrangement in the evaporated As_2S_3

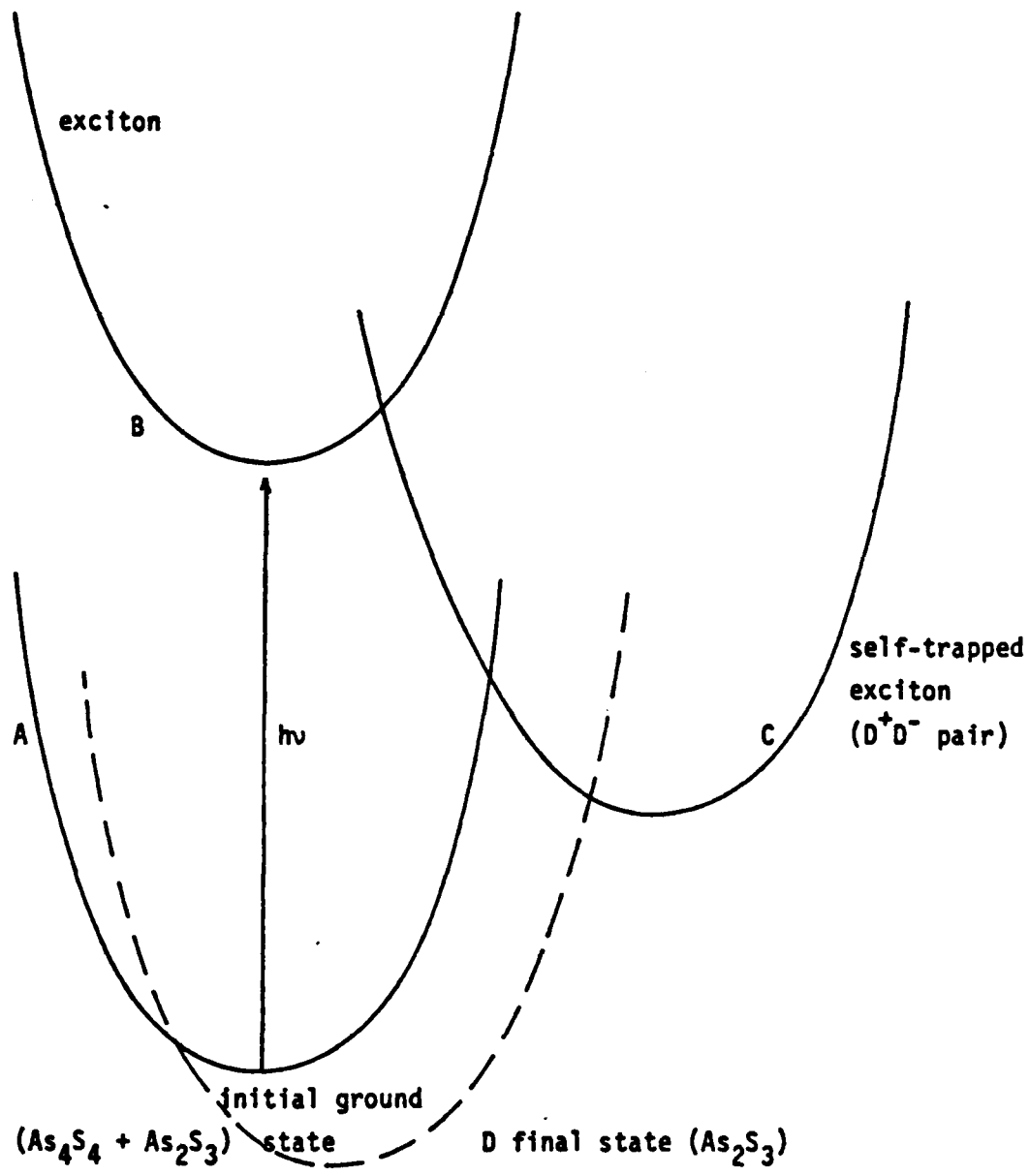


Fig.4.12 Configuration diagram of photo-polymerization of evaporated As_2S_3 film. Curve A- ground, curve B- electron-hole pair after optical excitation but before structural relaxation. curve C- self-trapped exciton D^+D^- pair; curve D-final state (glassy As_2S_3)

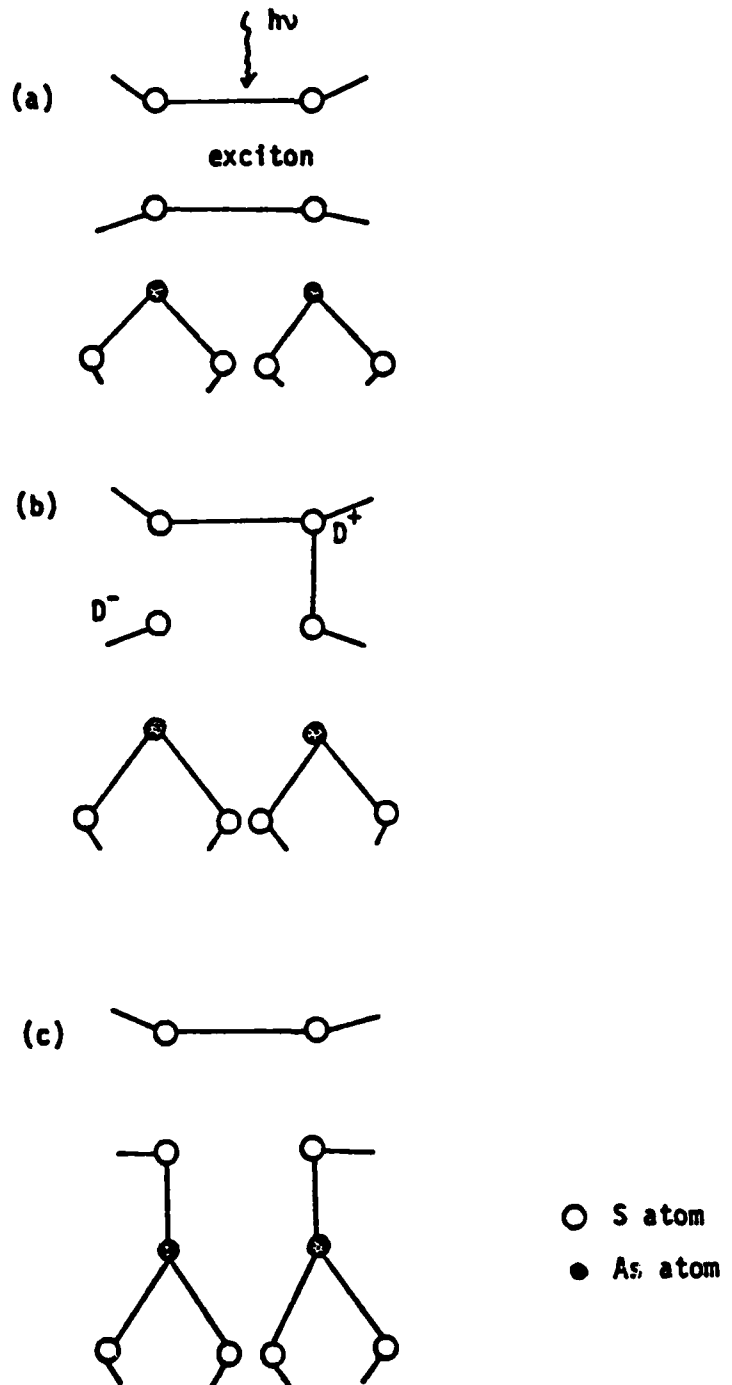
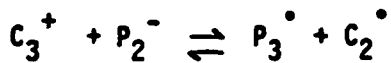
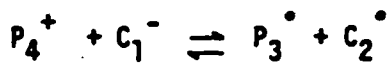


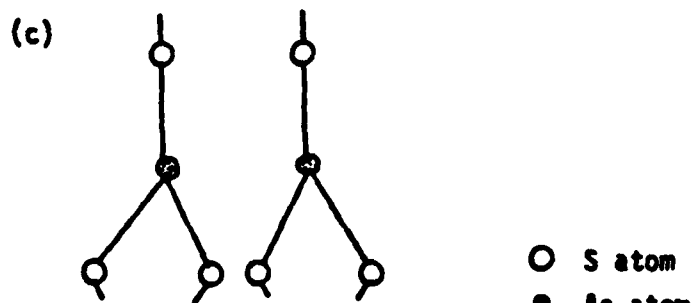
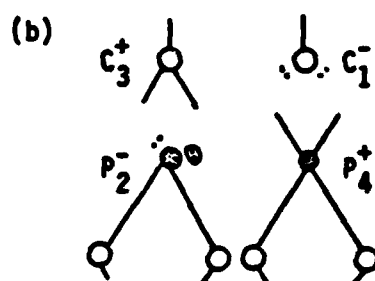
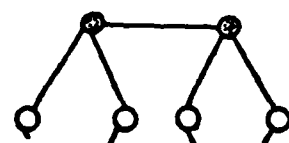
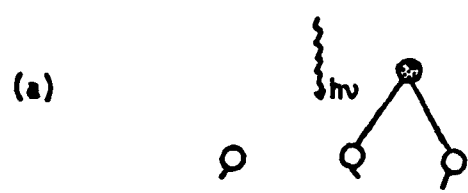
Fig.4.13 Proposed states in polymerization of As_4S_4 molecules by Strom et al.⁽⁴³⁾ (a) initial configuration, and after light absorption (b) structural rearrangement to form self-trapped D^+D^- pair, (c) bond switching between As-As and D^+D^- pair.

film, only one of the two As-As bonds in As_4S_4 molecules is displayed for simplicity. Adjacent to the As_4S_4 molecule are shown sulfur chains. Upon UV exposure, a D^+D^- pair is formed, it can be recombined by bond switching involving As atoms as indicated in Fig. 4.13(c), corresponding to the transition from curve C to curve D in Fig. 4.12. The polymerization process between As_4S_4 molecular units is also possible in the arsenic-rich film. Upon band-gap illumination the C_3^+ (or D^+), C_1^- (or D^-) charged defect centers can form in the chalcogenide centers and P_4^+ , P_2^- defects in the pnictide centers. Kastner and Fritzsch⁽⁵²⁾ suggest the following reactions can occur:



where P_3° , C_2° are the normal bonding states of pnictides and chalcogenides, respectively. The proposed possible bonding rearrangement between neighboring As_4S_4 molecules is shown in Fig. 4.14. This tentative model interpretation in which optically induced self-trapped excitons catalyze the structural changes is consistent with our observed IR vibrational spectra.

Bishop et. al.⁽⁶²⁻⁶³⁾ pointed out that the observation of optically induced electron spin resonance (ESR) spectra in glassy As_2S_3 , As_2Se_3 , Se, a-As, and GeS_2 can be well represented as the sum of a spectrum characteristic of a center localized primarily on an As p-like orbital and a spectrum characteristic of a hole center localized on



○ S atom
● As atom

Fig.4.14 Proposed stages in polymerization between As_4S_4 molecules.

: denotes the lone-pair p electrons and O denotes the lone-pair s electrons

a non-bonding chalcogen p-orbital. Also the density of the optically induced ESR centers in arsenic chalcogenide is increased proportionally to the atomic content of arsenic in the glass. It may be concluded that in the arsenic-rich As_2S_3 film a larger absorption edge shift can be expected due to a larger defect density around arsenic centers. That explains why in this study we observed a larger refractive index change than the results reported elsewhere, it is simply due to our arsenic-rich As_2S_3 films.

4.6 STRUCTURAL STUDIES OF Ag-DOPED As_2S_3 FILMS

In the previous sections the Ag photodissolution effect in As_2S_3 films and its applications to imaging technology have been discussed. In this section the structural changes in the Ag-doped As_2S_3 film will be examined.

Before describing our studies on the structure of Ag-doped As_2S_3 films, a special feature of the Ag-doped As_2S_3 film should be noted. The electrical conductivities of amorphous semiconductors are generally much less sensitive to nonstoichiometry and the presence of impurities than are those of crystalline semiconductors. However, several large conductivity increases can result from the addition of Cu, Ga, In, and Tl in As_2Se_3 (64-68) and Cu and Ag in As_2S_3 . (65-66) Mott⁽⁶⁸⁾ suggests that the insensitivity of the electrical conductivity of amorphous semiconductors to impurities is caused by the impurities being coordinated in keeping with the (8-N) rule, thereby satisfying their co-

valent bonding requirements. As a result, the impurities do not form donor or acceptor states and do not produce large changes in the conductivity. This structural picture does not seem applicable to the exceptions discussed above, because the conductivity changes are large. However, it is not clear how these impurities are incorporated into the amorphous network. No complete structural studies of the doped amorphous semiconductors has been reported so far.

It should be noted that the term "photodoping" may be a poor choice to describe these Ag insertion effects because the quantity of Ag which is transported is very large and the accompanying changes in film composition and structure are substantial. Also, because of the inherent complexity of this multi-layer phenomenon, the detailed mechanisms of Ag doping are not yet well understood.

Specimens were prepared as described in Section 2.1 on Si wafers or glass microslides. A layer of evaporated As_2S_3 of thickness 1.5 - 2.0 μm was deposited over a layer of evaporated Ag of different thickness ranging from 0.01 to 1 μm (or, conversely, the Ag may be deposited over the As_2S_3 layer), and the sandwich was then illuminated from the front side (opposite to the substrate) or annealed at 190°C to achieve the silver doping effect. Samples with different at. % of Ag denoted by x (up to 50%) were prepared for measurements.

4.6.1 Transmission Electron Microscope (TEM)

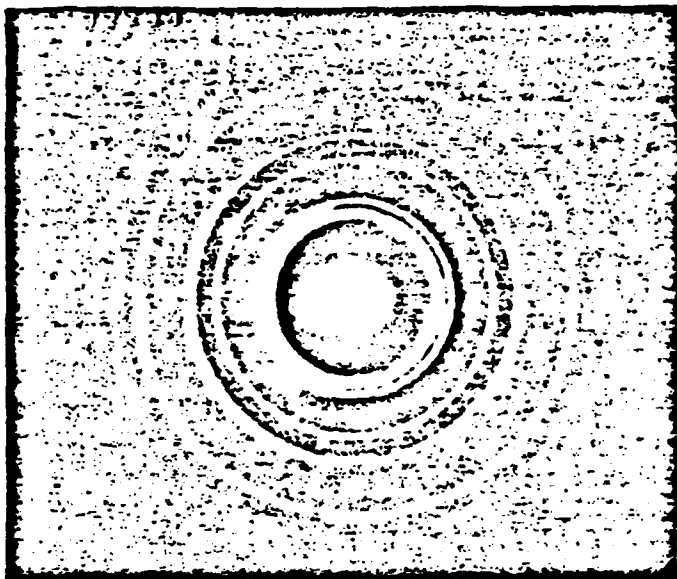
A 500 Å As_2S_3 , 150 Å Ag composite was deposited onto a

carbon coated grid. Fig. 4.15 shows the electron diffraction patterns of the sample before and after 15 minutes UV exposure. In Fig. 4.15(a) the structure of the unexposed $\text{As}_2\text{S}_3/\text{Ag}$ composite film can be observed to consist of polycrystalline Ag over amorphous As_2S_3 , with no evidence for "significant" inter-diffusion during evaporation. However, at least 10 Å of Ag-doped As_2S_3 in the $\text{Ag}/\text{As}_2\text{S}_3$ interface is believed to exist due to Ag thermal autodoping during Ag evaporation. This small amount of Ag-doped As_2S_3 is beyond the resolution of our TEM. In Fig. 4.15(b) the structure of the illuminated composite film shows a thicker amorphous layer in addition to a thin residual polycrystalline Ag layer. DeNeufville⁽⁶⁹⁾ also reported similar TEM results in Ag-doped As_2S_3 films. He points out that it is possible to diffuse 100 Å layer of Ag into a 200 Å film of As_2S_3 and entirely exhaust the Ag reservoir.

4.6.2 IR Spectroscopy

In order to obtain more information about the structure of Ag-doped As_2S_3 films, IR was employed to examine Ag-doped As_2S_3 samples. First, the IR absorption spectra for metallic Ag films of varying thickness on Si wafer were obtained. It was demonstrated that a 150 Å thick layer of Ag completely blocks the infrared transmission through the sample. For Ag films of 100 Å thickness only about 5% IR transmission was obtained. The IR transmission spectra of one sample with a 0.1 μm thick film of Ag and a 1.5 μm thick film of As_2S_3 , is shown

(a)



(b)

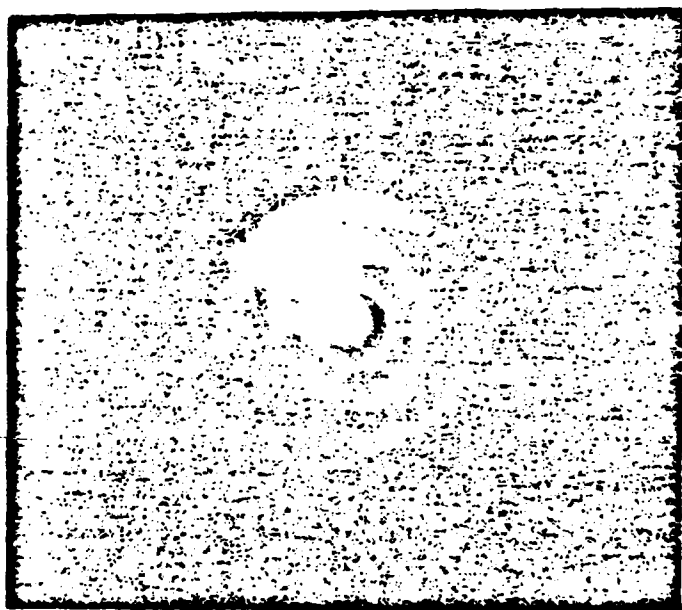


Fig.4.15 Electron diffraction patterns of (a) the unexposed $\text{As}_2\text{S}_3/\text{Ag}$ composite film and (b) the exposed composite film (25 seconds under UV exposure).

as a function of UV exposure time in Fig. 4.16. From Fig. 4.16 it is concluded that after ultraviolet exposure for 40 minutes almost all the Ag is consumed and incorporated into the As_2S_3 matrix. For any further UV exposure, the IR transmission spectra does not change. The fringe shifts in the Ag-doped As_2S_3 film are larger than the shifts in the undoped As_2S_3 film. This indicates that larger refractive index changes and related absorption edge shifts occur in the Ag-doped As_2S_3 samples. The IR absorption peak at 311 cm^{-1} which is due to the vibration of As-S bonds shows no difference from the undoped As_2S_3 films except that the IR transmittivity is smaller in the Ag-doped samples. The same results are observed in the annealed samples. Fig. 4.17 shows the final stable IR transmission spectra for different film thicknesses of Ag over-layers after UV exposure. In this study, a $0.4 \mu\text{m}$ thick film of Ag can be easily doped into $1.5 \mu\text{m}$ of As_2S_3 either by UV exposure or thermal anneal.

4.6.3 X-Ray Diffraction

X-ray diffraction experiments were also conducted on the specimens in which the Ag film has been entirely diffused into the As_2S_3 film. X-ray diffraction patterns of an exposed As_2S_3 and Ag-doped film are given in Fig. 4.18. As shown in Fig. 4.18(a), the exposed As_2S_3 film shows As_2S_3 is amorphous and also shows the As crystal peaks as before. On the other hand, Ag and probably Ag_2S having a peak at $2\theta = 38^\circ$ is observed with good reproducibility in

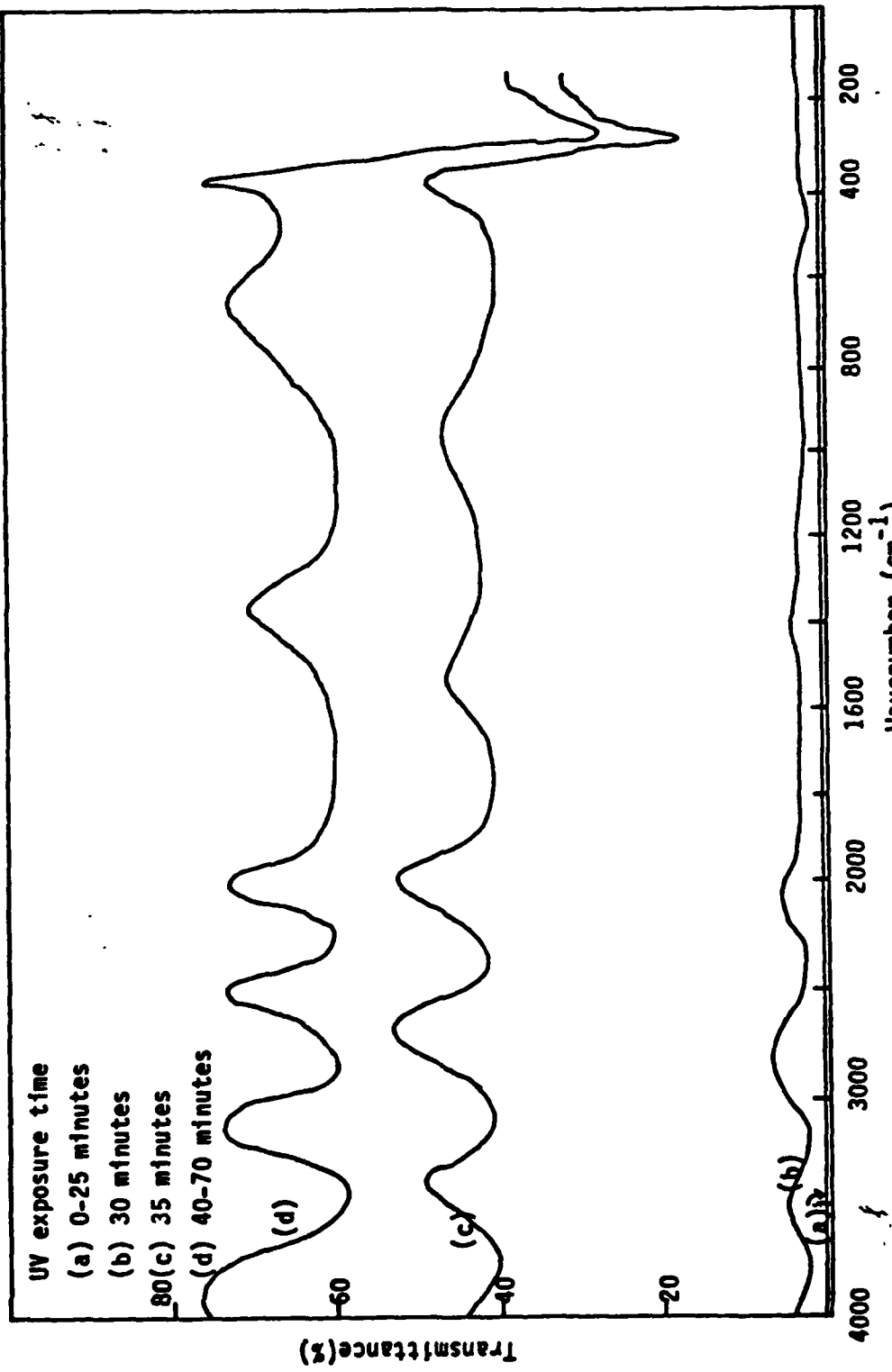


Fig.4.16 The IR transmission spectra of a Ag-overcoated As_2S_3 sample ($0.1 \mu\text{m}$ Ag/ $1.5 \mu\text{m}$ As_2S_3) as a function of UV exposure time.

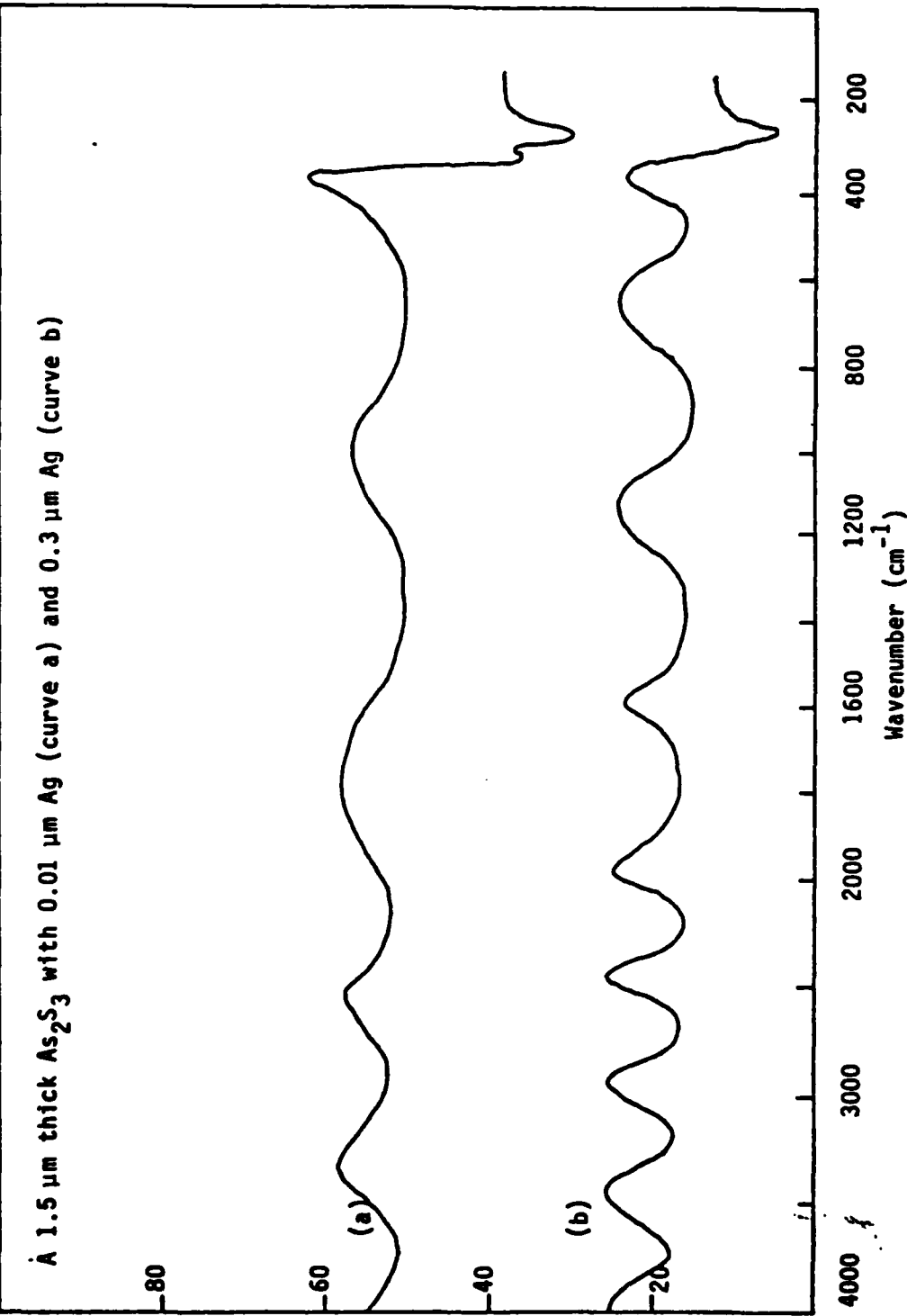


Fig.4.17 The IR transmission spectra for different film thickness of Ag overlayer after UV exposure. Exposure times are (a) 15 minutes and (b) 110 minutes, respectively.

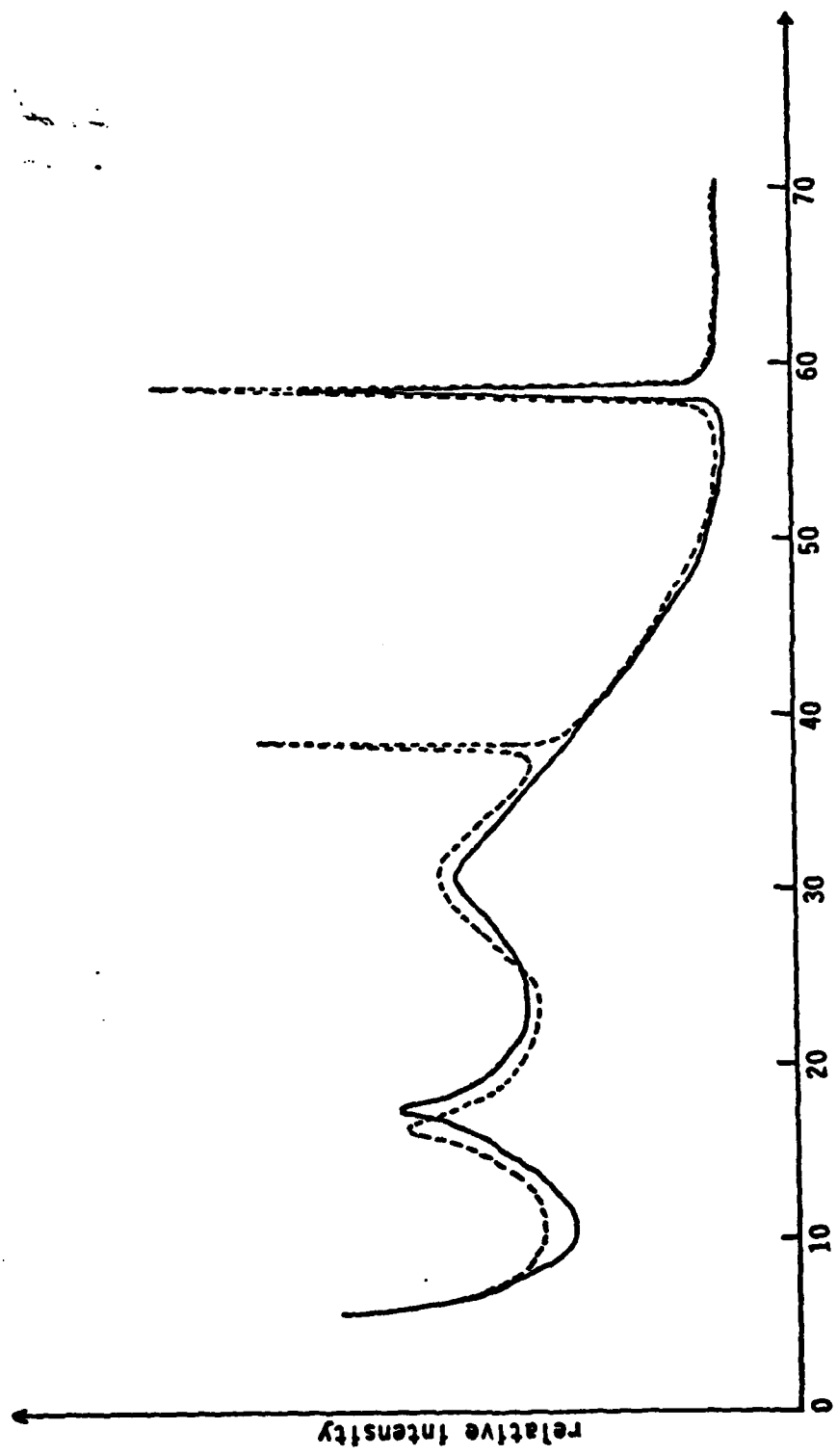


Fig. 4.18 X-ray diffraction spectra of exposed As_2S_3 film(2.0 μm)—solid line, and an Ag-doped As_2S_3 film(0.1 μm Ag and 2.0 μm As_2S_3)—dotted line. The exposed As_2S_3 film shows the As_2S_3 crystal peak as before and the Ag-doped As_2S_3 film shows another peak around 38° .

the photodoped films. Other diffraction peaks related to metallic Ag appear in the heavily Ag-doped films which are shown in Fig. 4.19. The corresponding IR transmission spectra showed 20% transmisitivity indicating the presence of Ag clusters dispersed through the entire As_2S_3 matrix. It can not be a continuous Ag film since the IR transmission would be much lower for that case. Ternary crystalline compounds which are known to be formed by these three elements (As, S, Ag), such as prousite Ag_3AsS_3 , are not observed in this study. At low silver doping levels neither the Ag peaks nor the Ag-related compound peaks were observed in the x-ray diffraction spectra.

4.7 MORPHOLOGY OF THE HEAVILY Ag-DOPED As_2S_3 FILM

One of the heavily Ag-doped As_2S_3 film was examined under the optical microscope and photomicrographs were taken. These are shown in Fig. 4.20. Fig. 4.20(a) shows several different phases in the heavily Ag-doped sample. From the above data, including x-ray diffraction, electron-beam diffraction and infrared absorption spectra, these different phases can be identified as: (1) uniform Ag-doped As_2S_3 , (2) Ag-rich As_2S_3 , (3) an Ag_2S phase (black color), and (4) the arsenic crystals. Fig. 4.20(b) is the same micrograph at higher magnification. Ring formation surrounding the As crystals is observed. The detailed mechanisms of this ring formation are not yet understood. Before presenting the possible microprocess of the Ag-doping phenomenon, a possible mechanism of the ring formation is proposed.

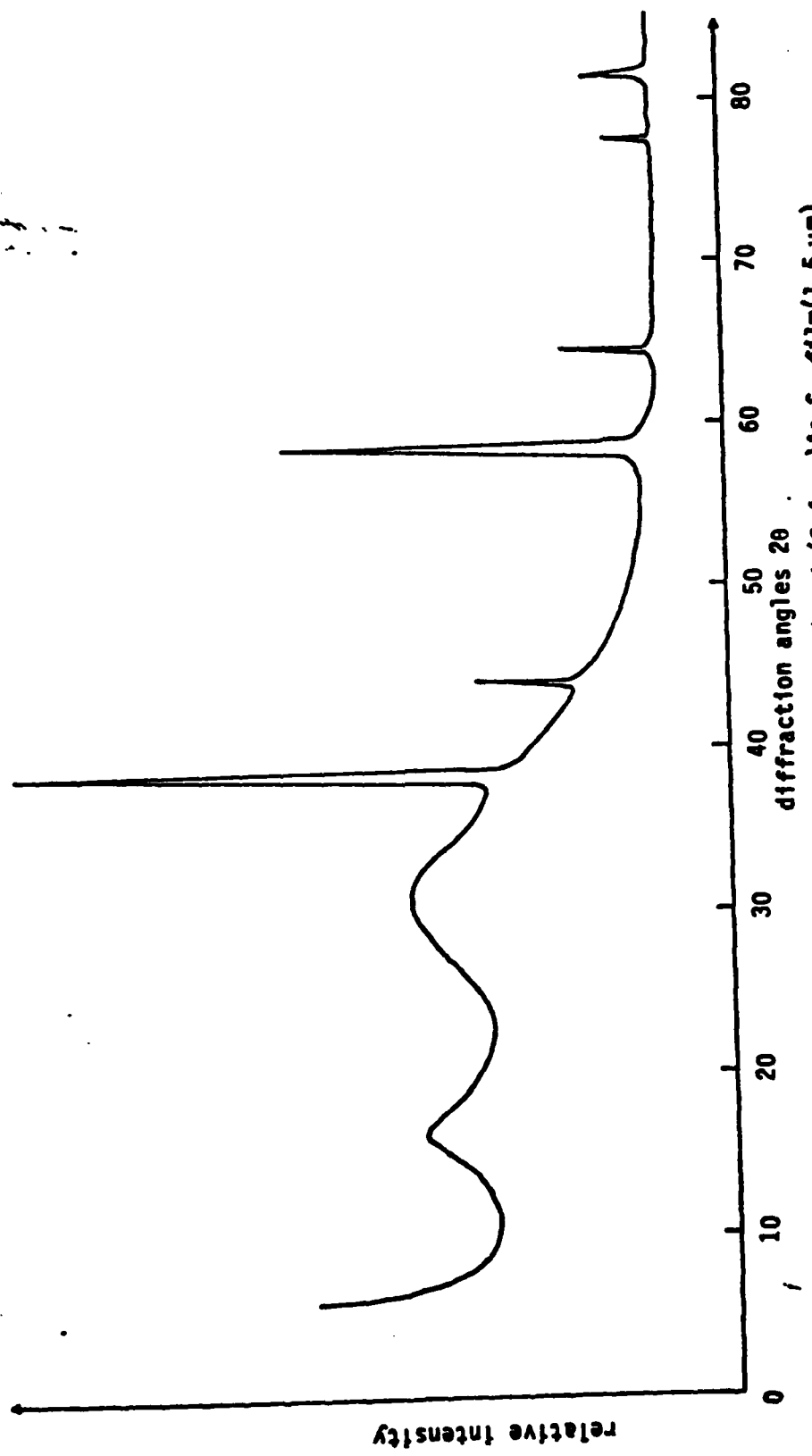
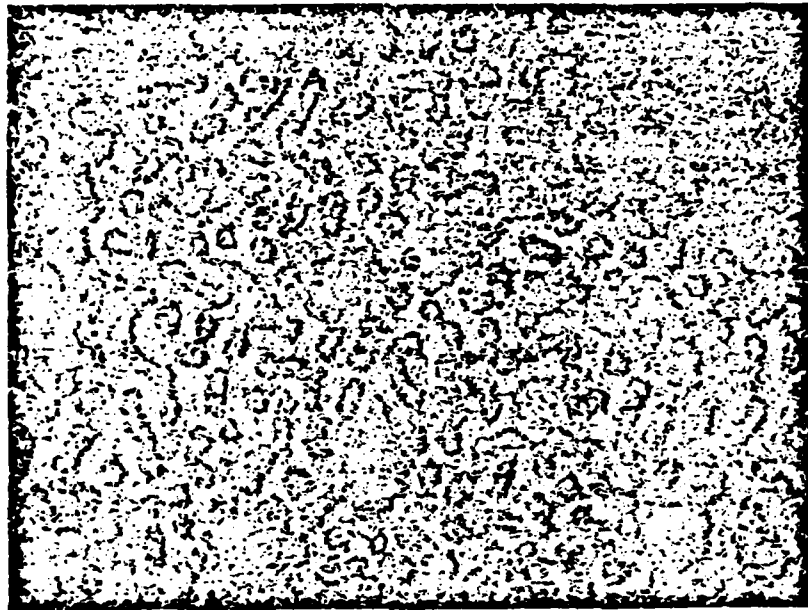


Fig. 4.19 / The x-ray diffraction pattern of the heavily Ag-doped ($0.4 \mu\text{m}$) As_2S_3 f11m($1.5 \mu\text{m}$).
The extra diffraction peaks are related to the metallic Ag.

(a)



(b)



Fig.4.20 Optical micrographs of the heavily Ag-doped As_2S_3 film.
(a) $\times 100$, $0.4 \mu\text{m}$ Ag + $1.5 \mu\text{m}$ As_2S_3 , 650 joules UV exposure.
(b) $\times 1,000$.

4.7.1 Spinodal Decomposition (70-71)

Nucleation processes often involve a composition change.

Consider the free energy of an isomorphous system which separates into A-rich and B-rich phases on cooling as shown in Fig. 4.21. (70) Assume a small concentration fluctuation occurring such that neighboring regions change from some initial homogeneous composition of C_0 to compositions of $C_0 + \Delta C$ and $C_0 - \Delta C$, respectively. Then the Gibbs free energy change per unit volume of these two regions during this process is obtained in the following way:

$$G(C_0 + \Delta C) = G(C_0) + \Delta C G'(C_0) + \frac{(\Delta C)^2}{2} G''(C_0) + \dots$$

$$G(C_0 - \Delta C) = G(C_0) - \Delta C G'(C_0) + \frac{(\Delta C)^2}{2} G''(C_0) + \dots$$

then $\Delta G = G(C_0 + \Delta C) + G(C_0 - \Delta C) - 2G(C_0)$

From above equations, one obtains

$$\Delta G = (\Delta C)^2 G''(C_0) \quad (4-5)$$

The free energy changes around C_0 is directly proportional to the second derivative of free energy at composition C_0 . In Fig. 4.21 there are several different categories. For compositions near pure A and pure B, i.e., region I and II, $G'' > 0$, the free energy of the system is increased by any small fluctuation in composition C. In region III and IV, $G'' < 0$, so any small fluctuation will increase the

- region I: $\Delta G > 0$ for all ΔC
 region II: $\Delta G > 0$ for small ΔC and $\Delta G < 0$ for large ΔC
 region III: $\Delta G < 0$ for all ΔC
 region IV: $\Delta G > 0$ for small ΔC and $\Delta G < 0$ for large ΔC
 region V : $\Delta G > 0$ for all ΔC

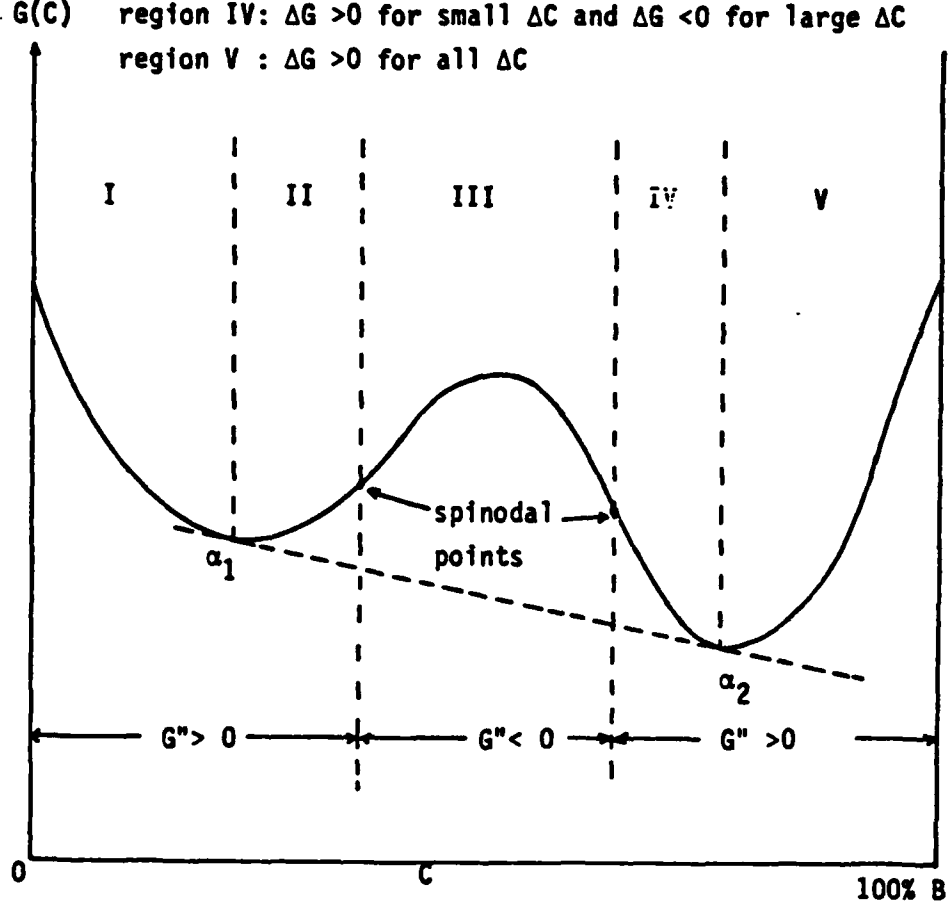


Fig.4.21 $G(C)$,Gibbs free energy,curve for system with a miscibility gap showing regions in which various types of fluctuation decrease G for the system,⁽⁷⁰⁾

free energy of the system even though a larger fluctuation will make $\Delta G < 0$. In these regions a nucleation barrier exists so that a composition fluctuation must become rather large before it will decrease the free energy of the system. But in region III the situation is entirely different because $G'' < 0$ in this region. The composition at which $G'' = 0$ is called the spinodal composition. The phase diagram of this system is shown in Fig. 4.22. The regions in Fig. 4.22 corresponding to the regions in Fig. 4.21 are also shown. In the composition range between the spinodal points any small fluctuation in composition is supercritical. The decomposition of this unstable solution inside the spinodal will be discussed below.⁽⁷¹⁾

Inside region III, not only is $\Delta G < 0$ for any small fluctuation ΔC , but also the magnitude of ΔG increases as ΔC increases according to Eq. (4-5). An increase in ΔC must occur by solute diffusing from the low concentration regions to the higher concentration region. Fig. 4.23⁽⁷¹⁾ shows the growth in amplitude of a sinusoidal fluctuation in composition resulting from such diffusion. Note that diffusion occurs up the concentration gradient instead of down it as one is used to seeing in the usual diffusion process. This is allowable only when $G'' < 0$. In this composition the ring formation is possible. In a stable solution G'' is always positive and the diffusion is always in the negative direction of concentration gradient since that is in the direction of decreasing free energy.

In the ternary As-S-Ag system, when the at. % of Ag impurity

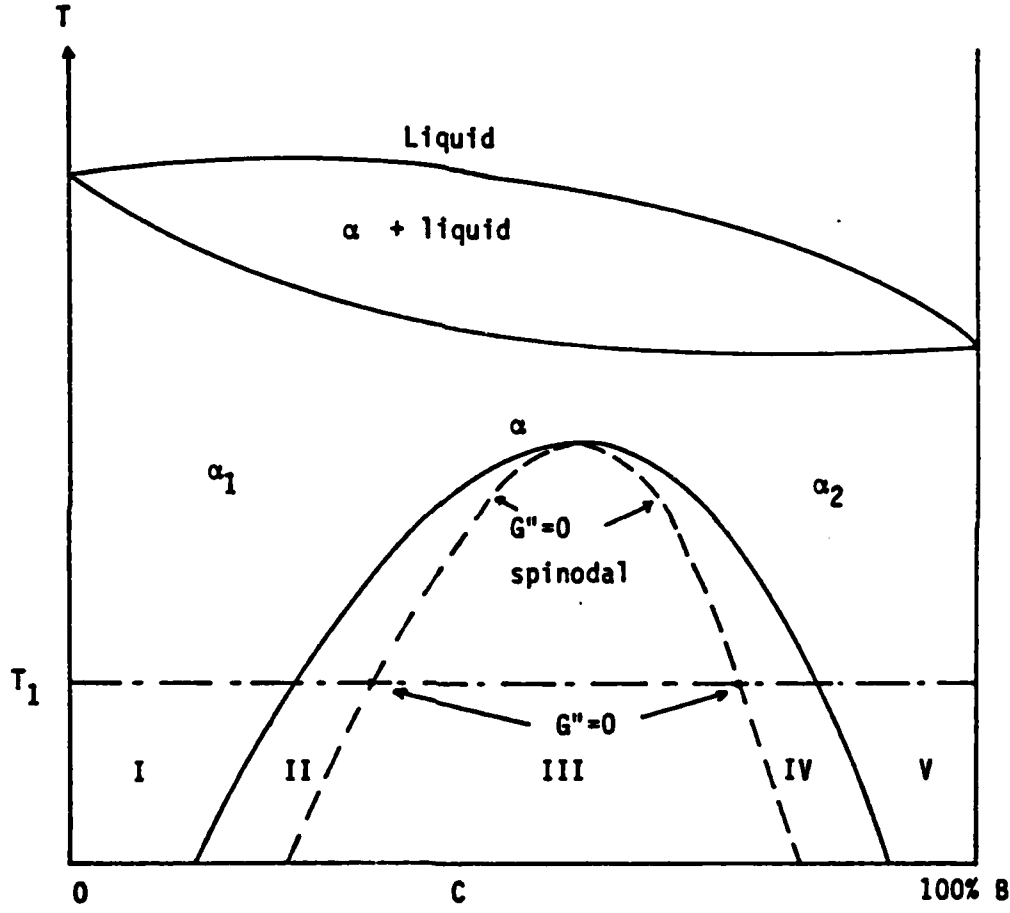


Fig.4.22 Coherent phase diagram and spinodal. In the composition range between the spinodal points any small fluctuation in composition is supercritical. (70-71)

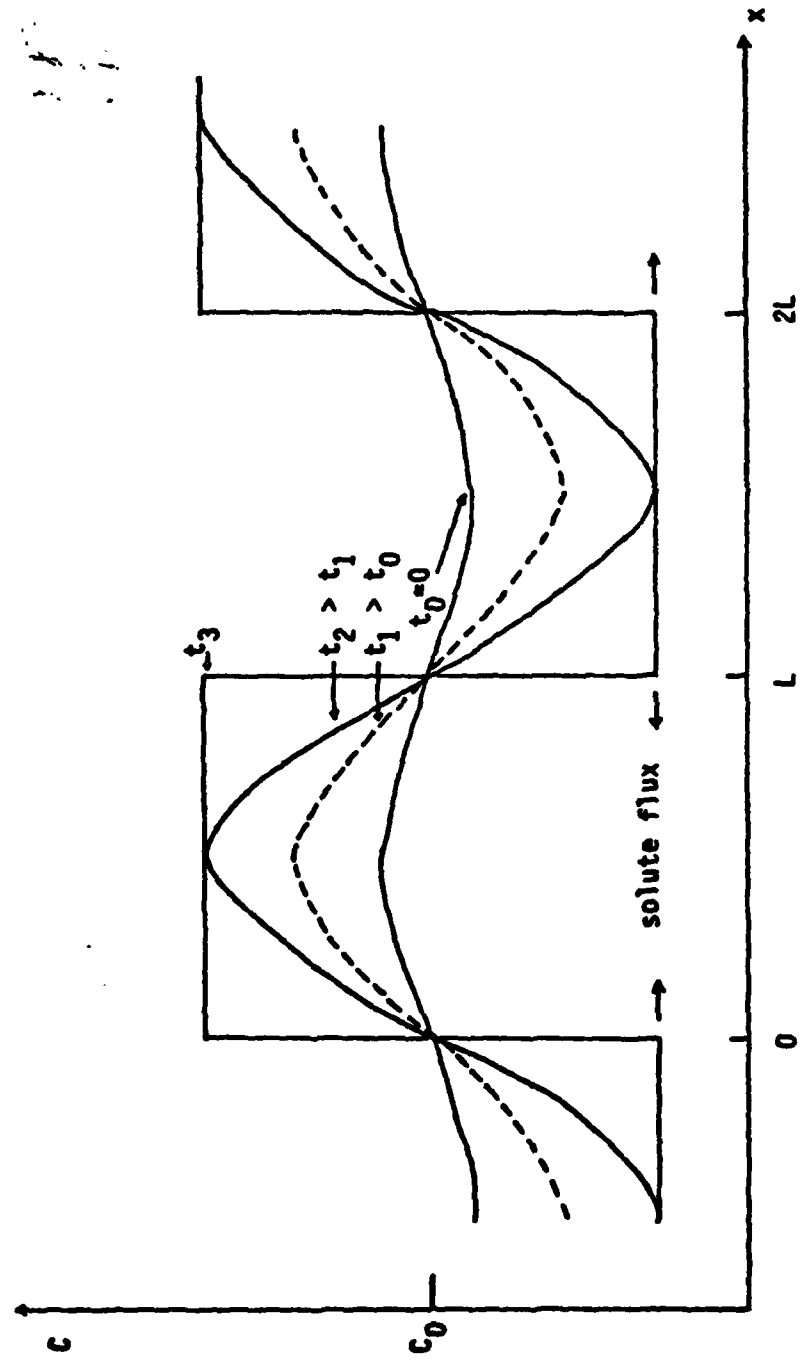


Fig.4.23 The growth in amplitude of a sinusoidal fluctuation in composition resulting from the diffusion discussed in the text. The rate of development of these fluctuations into zones is determined by the rate of diffusion of solute.

increases to a certain level, the solid solution is in a supercritical composition. The Ag-rich As_2S_3 regions will start to decompose into separate phases due to the instability of this heavily Ag-rich As_2S_3 solution. The Ag may react with sulfur and form Ag_2S . With these arguments the ring structure formation is possible. Owing to sulfur deficiency arsenic atoms will finally form crystallites. It was experimentally observed that all the arsenic crystals are formed at the center of these rings and the structure between these rings is more like the background As_2S_3 matrix which is consistent with the above model. It is an interesting phenomenon but more experiments are needed to fully understand the underlying mechanisms.

4.8 Ag IMPURITY STATES IN As_2S_3 FILMS

To explain the role of Ag in As_2S_3 , Mott and Davis⁽⁴⁷⁾ assume the existence of a significant band tail of localized states into the energy gap. The decrease of the band gap is then conjectured to be due to a decrease in the range of the localized states. That is the valence band mobility edge is assumed to move towards the band edge, leading to a decrease in the activation energy for electrical conduction. They suggest that the increased electrical conductivity arises not from the formation of impurity bands, but from structural changes due to Ag doping that reduce the disorder. They do not elaborate on the origin of the structural changes.

Goldschmidt and Rudman⁽⁷³⁾ reported that photoenhanced Ag-doping is a two-step process. Firstly, a critical radiation damage dose must be accumulated in the As_2S_3 layer. Secondly, the Ag atom is phon-assisted across the As_2S_3 -Ag interfacial activation barrier. Their experiments show that the Ag photodissolution in the As_2S_3 film exhibits an induction time and that there is a certain minimum damage required before the Ag can dissolve in the As_2S_3 layer. They do not know how this minimum damage affects the Ag-doping process and what the damage is. Recently Biegelsen and Street⁽⁷⁴⁾ showed that prolonged exposure to strongly absorbed light induces a large density of metastable defects in chalcogenide glasses as shown by light-induced ESR experiments. Their model is fully consistent with the model of D^+D^- pairs which was discussed earlier. Optical excitation of an electron-hole pair at a D^+D^- pair may cause one of the three possible transitions:⁽⁷⁴⁾

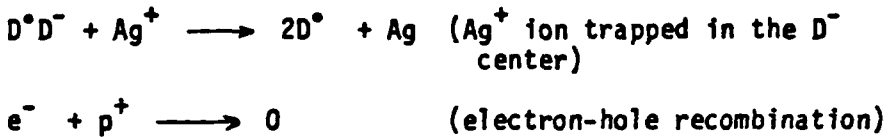


The process indicated by Eq. (4-8) is expected to result in a rapid non-radiative recombination to the ground state.⁽⁵⁹⁾

If one further assumes Ag atoms in contact with or incorporated into the As_2S_3 film may be ionized as



due to ultraviolet exposure. From Eqs. (4-6) and (4-9), the Ag^+ ions can be trapped in the D^- defect center by the following reaction,



The Ag^+ ion act as a D^- center killer and leaves a D^+ center intact. According to the law of mass action there are many D^+ centers remaining. In this case the pinning of Fermi level⁽⁷⁵⁾ by the charged defects D^+D^- pairs in the amorphous chalcogenide semiconductors would be changed, since the Ag atoms prevent the equilibration between the charged Ag^+ ions and the D^+D^- pairs. This can lead to much larger changes in the electrical properties because now the Ag^+ ions concentration can exceed the number of defect centers. The Fermi level becomes unpinned and moves closer to one of the band edges, this resulting in an increase in the electrical conductivity. The Ag impurities behave as electron donors in the As_2S_3 film which act similarly to a partially compensated semiconductor. Initially the Ag will be trapped in the defect center, but if the Ag impurity concentration increases gradually and exceeds the solubility in As_2S_3 , then Ag clusters will be formed and phase separation can be observed.

References to Chapter 4

1. M.T. Kostyshin, E.V. Mikhailovskaya, P.F. Romanenko, Sov. Phys.-Solid State, 8, 451, (1966).
2. M.T. Kostyshin, P.F. Romanenko, E.P. Krasnozhenov, Sov. Phys.-Semicond., 2, 973, (1969).
3. R.G. Brandes, F.P. Laming, A. D. Pearson, Appl. Opt., 9, 1712, (1970).
4. S.A. Keneman, Appl. Phys. Lett., 19, 205, (1971).
5. J.S. Berkes, S.W. Ing, Jr., W.J. Hillegas, J. Pall. Phys., 42, 4908, (1971).
6. J.S. Berkes, J.M. Short, K.J. Johnson in "Proc. 5th Intern. Conf. on Amorphous and Liquid Semiconductors, Garmisch-Partenkirchen", Taylor and Francis, London, (1974).
7. T. Igo, Y. Toyoshima, Jpn. J. Appl. Phys., 11, 117, (1972).
8. T. Igo, Y. Toyoshima, J. Non-Cryst. Solids., 11, 304, (1973).
9. Y. Ohmachi, T. Igo, Appl. Phys. Lett., 20, 506, (1972).
10. S.A. Keneman, J. Bordogna, J.N. Zemel, J. Opt. Soc. Am., 68, 32, (1978).
11. S.A. Keneman, J. Bordogna, J.N. Zemel, J. Appl. Phys., 49, 4663, (1978).
12. H. Fritzsche in "Electronic and Structural Properties of Amorphous Semiconductors", ed. by P.G. Lecombergn, J. Mort., Academic Press, London, (1973).
13. M. Kastner, Phys. Rev. Lett., 28, 355, (1972).
14. S.R. Oushinsky, K. Sapur in "Proc. 5th Intern. Conf. on Amorphous and Liquid Semiconductors, Garmisch-Partenkirchen", Taylor and Francis, London, (1974).
15. I. Chen, Phys. Rev., B7, 3672, (1973).
16. F. Hullinger, "Structural Chemistry of Layer-type Phases", ed. by F. Lévy, D. Keidel Pub. Co., Holland, (1976).

17. D.J.E. Mullen, W. Nowacki, Z. Krist., 136, 48, (1972).
18. T. Ito, N. Morimoto, R. Sadanaga, Acta Cryst., 5, 775, (1952).
19. M.B. Myers, E.J. Felty, Mat. Res. Bull., 2, 535, (1967).
20. S. Maruno, Jpn. J. Appl. Phys., 7, 1434, (1968).
21. S. Tsuchihashi, Y. Kawamoto, J. Non-cryst. Solids, 5, 286, (1971).
22. S. Maruno, M. Noda, J. Non-Cryst. Solids, 7, 1, (1972).
23. R. Grigorovici, in "Amorphous and Liquid Semiconductors" ed. by J. Tanc, p. 45, Plenum, New York, (1974).
24. A.J. Leadbetter, A.J. Apling, M.F. Daniel, J. Non-Cryst. Solids., 21, 47, (1976).
25. J.P. DeNeufville, S.C. Moss, S.R. Ovshinsky, J. Non-Cryst. Solids, 13, 191, (1973/74).
26. S.G. Bishop, N.J. Shevchik, Solid State Commun., 15, 629, (1974).
27. N.J. Shevchik, W.J. Paul, J. Non-Cryst. Solids, 8-10, 381, (1972).
28. V. Smid, M. Fritzsche, Solid State Commun., 33, 735, (1980).
29. W.M. Stobbs in "The Structure of Non-Crystalline Materials", ed. by P.H. Gaskell, p. 253, Taylor and Francis, London, (1977).
30. L.A. Freeman, A. Howie, A.B. Mistry, P.H. Gaskell, ibid., p. 245, (1977).
31. D.E. Sayers, E.A. Stern, F.W. Lytle, Phys. Rev. Lett., 35, 584, (1975).
32. E.A. Stern, Sci. Am., 234, 96, (1976).
33. T. Egami, J. Mat. Sci., 13, 2587, (1978).
34. T. Egami, in "Metallic Glasses" ed. by J.H. Güntherodt, Springer-Verlag, (to be published).
35. G. Lucovsky, R.M. Martin, J. Non-Cryst. Solids, 8-10, 185, (1971).
36. F.L. Galecner, G. Lucovsky, in "Proc. 6th Intern. Conf. on Liquid and Amorphous Semiconductors", p. 305, Leningrad, (1975).

37. P.B. Klein, P.C. Taylor, D.J. Treacy, Phys. Rev., B16, 4501, (1977).
38. S.A. Solin, G.N. Papatheodorou, Phys. Rev., B15, 2084, (1977).
39. A.T. Ward, J. Phys. Chem., 72, 4133, (1968).
40. K. Tanaka, M. Kikuchi, Solid State Commun., 11, 1311, (1972).
41. K. Tanaka, M. Kikuchi, in Proc. 5th Intern. Conf. on Amorphous and Liquid Semiconductors, p. 439, Garmisch-Partenkirchen, (1973).
42. P. DeNeufville, ibid, p. 1351, (1973).
43. U. Strom, T.P. Martin, Solid State Commun., 29, 527, (1979).
44. K. Tanaka, in "Structure and Excitations of Amorphous Solids", ed. by G. Lucovsky and F.L. Galeener, Williamsburg, VA., p. 148, (1976).
45. K. Tanaka, Y. Otsuka, Thin Solid Films, 48, 17, (1978).
46. K. Tanaka, Solid State Commun., 34, 201, (1980).
47. N.F. Mott, E.A. Davis, "Electronic Processes in Non-Crystalline Materials", 2nd ed., Clarendon Press, Oxford, (1979).
48. D.L. Wood, J. Tanc, Phys. Rev., 85, 3144, (1972).
49. R.A. Street, N.F. Mott, Phys. Rev. Lett., 35, 1293, (1975).
50. N.F. Mott, R.A. Street, Phil. Mag., 36, 33, (1977).
51. M. Kastner, in "Proc. of 7th Intern. Conf. on Amorphous and Liquid Semiconductors", ed. by W.E. Spear, Edinburgh, U.K. (1977).
52. M. Kastner, H. Fritzsche, Phil. Mag., 37, 199, (1978).
53. R.A. Street, Adv. Phys., 25, 397, (1976).
54. S.G. Bishop, W. Strom, P.C. Taylor, Phys. Rev. Lett., 36, 543, (1976).
55. P.W. Anderson, Phys. Rev. Lett., 34, 953, (1975).
56. S.R. Ovshinsky, H. Fritzsche, IEEE Trans. Electron Dev., 20, 91, (1973).
57. M. Kastner, J. Non-Cryst. Solids, 31, 223, (1978).

silver ions from an Ag-containing electrolyte into the As_2S_3 film at controlled potentials. The silver injection level can be exactly controlled electrochemically. The experimental set-up will be presented first followed by the experimental results. The modeling and analysis of experimental data will be given in the subsequent sections.

5.1 VOLTAMMETRY STUDIES OF THE As_2S_3 FILMS

5.1.1. Introduction - General Requirements ⁽⁵⁾

An electrochemical cell consists of an electrolyte or ionic conductor contacted by two electrodes. The electrodes themselves may consist of a variety of internal phases but are terminated by a metal. The potential difference between the metal ends of the cell is called the cell potential. It is composed of the potential differences at the boundaries of the phases making up the circuit. The potential differences arise as a result of the transfer of charges across the phase boundaries. ⁽⁶⁻⁷⁾

The potential of a single electrode or half-cell cannot be directly measured. At least two electrodes are needed to measure the cell potential. Because the potential of the second interface created by immersing the second electrode into the electrolyte may not be well defined, the potential of the working electrode or electrode of interest must be measured with respect to some reference electrode whose potential is stable and reproducible. Although the measurement of cell potential is conceptually simple, its interpretation can be complicated by IR drops in the cell in which a net current is flowing.

Chapter 5

THE ELECTROCHEMICAL STUDY OF THE SILVER INJECTION INTO As_2S_3 FILMS IN THE DARK

When a semiconductor surfaces come in contact with an electrolyte (e.g. aqueous solution of AgNO_3 or CuSO_4), charge transfer takes place until, at equilibrium, a potential difference (electrochemical potential) is established between the semiconductor and the bulk of the solution. It has been reported chalcogenide semiconductors, such as As_2S_3 , reduce silver nitrate in solution and adsorption of the metallic silver takes place on the semiconductor surface.⁽¹⁾ This author dipped the As_2S_3 film in a 0.001 N AgNO_3 aqueous solution followed by a rinse in deionized water resulting in what appears to be a thin layer of Ag-doped As_2S_3 formed on top of the As_2S_3 film. The sensitized film was then exposed to ultraviolet light through a mask with a grating pattern. In the illuminated region, silver ions migrated into the bulk of the As_2S_3 film. Excess silver on the surface was removed by dipping into a dilute aqua regia solution and then fixing in Kodak Rapid Fixer A. The film was then developed in 0.03 N NaOH solution and a grating pattern obtained. The same process was also applied to Se-Ge amorphous films by Tai et. al.,⁽²⁻⁴⁾ and a sub-1000 Å line was obtained. Although the chalcogenide glass film has been successfully used in lithographic imaging, the underlying mechanism is still not understood. In this chapter, a new approach utilizes the electrochemical injection of

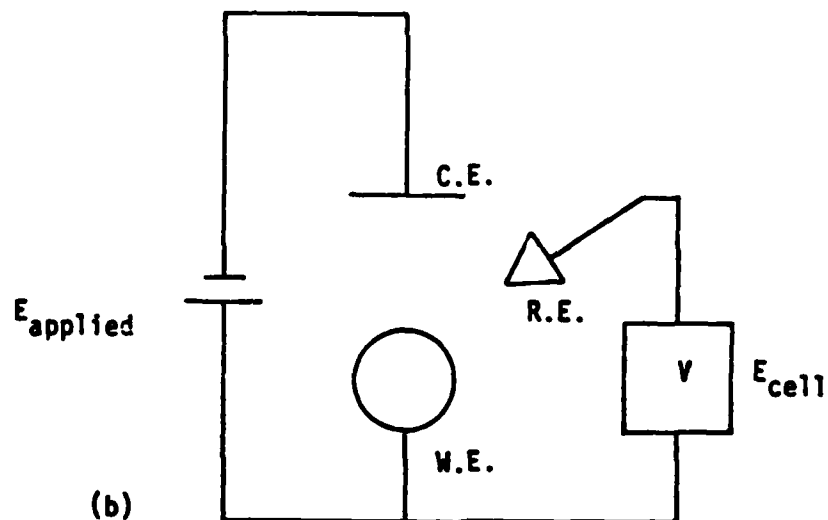
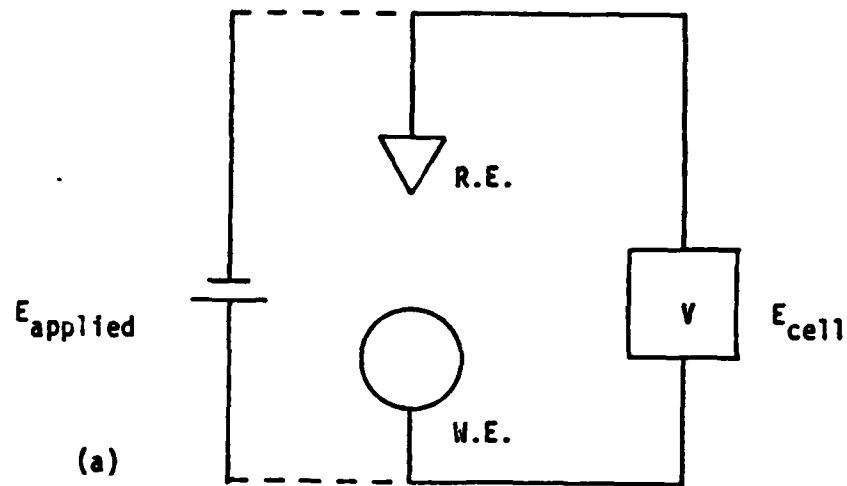


Fig.5.1 Circuits for the measurements of cell potentials.

(a) two-electrode system with current passing through both working and reference electrodes. (b) three-electrode system with current passing through the working and counter electrodes but not the reference electrode. (5)

and by internal polarization of the electrodes caused by net chemical changes caused by the passage of a current. Fig. 5.1(a) represents a two-electrode cell configuration in which the current passes through both the working electrode and the reference electrode. The IR drops in the electrolyte and the possible polarization of the reference electrode act to reduce the potential of the working electrode.

$$E_{W.E} = E_{cell} - IR_{cell} - E_{pol.}$$

In order to avoid these errors, a three-electrode configuration is commonly used (Fig. 5.1(b)). The cell current flows between the working electrode and counter or auxiliary electrode, while the potential of the working electrode is measured with respect to the reference electrode (through which no current passed), using a high impedance control device, such as a potentiostat. In the three-electrode configuration, the internal polarization of the reference electrode can be avoided because of the negligible current passing through the reference electrode and, as a result, compensation for the major portion of the IR drop in the cell is possible. When the working electrode impedance is much larger than the electrolyte resistance and reference electrode impedance a two electrode measurement is acceptable.

5.1.2 Description of the Cell for Voltammetry

The working electrode Cr|Au|As₂S₃ was prepared by sequential evaporation of Cr and Au films on a glass microslide. Films of

current through the reference electrode. A typical potentiostat is shown schematically in Fig. 5.2 (a). In this configuration, the reference electrode is incorporated into the negative feedback loop with the output from the control amplifier connected to the counter electrode. (Fig. 5.2 (b)) The working electrode is maintained at ground potential. Since it is desirable to vary only the potential drop across the working electrode/electrolyte interface, it is necessary to compensate for all the IR drops in the cell. The details of this IR compensation will be discussed in the next section.

The current output from the potentiostat and voltage function fed across the working electrode and the reference electrode using a x-y recorder.

5.3 EXPERIMENTAL RESULTS

Before taking the data, the electrochemical cell was cyclically scanned back and forth between -100 mv and +20 mv at a sweep rate of 2 mv/sec several times until a stable surface was reached.

First the As_2S_3 electrode was scanned anodically from zero potential down to about -100 mv and then cathodically scanned to a certain positive potential. The curve is shown in Fig. 5.3. The result shows that the relation of the current to the potential for freshly prepared As_2S_3 films is governed by the Butler-Volmer equation.^(7,21) The As_2S_3 - electrolyte (10^{-3} N AgNO_3 aqueous solution) interface shows rectification. In order to inject Ag^+ ions into the As_2S_3 electrode, the working electrode was biased cathodically at +35 mv for a certain period of time. The quantity of Ag^+ ions injected into the As_2S_3 electrode can be calculated from the charging curve I-t shown in Fig.

As_2S_3 with variable thickness from 0.3 - 2 μm were deposited on top of the Cr/Au metal contact. In this work, the active area of the working electrode was 0.16 cm^2 . Both the reference and counter electrodes are silver wire.

The electrolyte was a 10^{-3} N AgNO_3 aqueous solution. The cell temperature was kept constant at 25°C and the electrolyte stirred to make the solution homogeneous at all times.

5.2 EXPERIMENTAL

Measurements were carried out in the dark at room temperature. A triangular potential waveform was applied across the working and reference electrode. The silver was injected from the Ag^+ -ion containing electrolyte into the As_2S_3 electrode by biasing the As_2S_3 electrode cathodically. The amount of injected silver was controlled by the biasing voltage and time. At each Ag injection level, an anodic voltammogram at constant potential sweeping rate was obtained.

The experimental set-up used for carrying out these measurements consists of two major parts: the electrochemical cell and cell chamber, and the electrical measurement system. In order to maintain the potential between the working electrode and the reference electrode equal to some signal-generator potential (which may be a constant voltage or a time-varying signal), a potentiostat made by Electronischer Model 6251 TR was used. In its fundamental operation the controller reacts to the difference between these two potentials through a feedback circuit in such a way as to reduce the potential difference to zero. This potentiostatic control is achieved without drawing significant

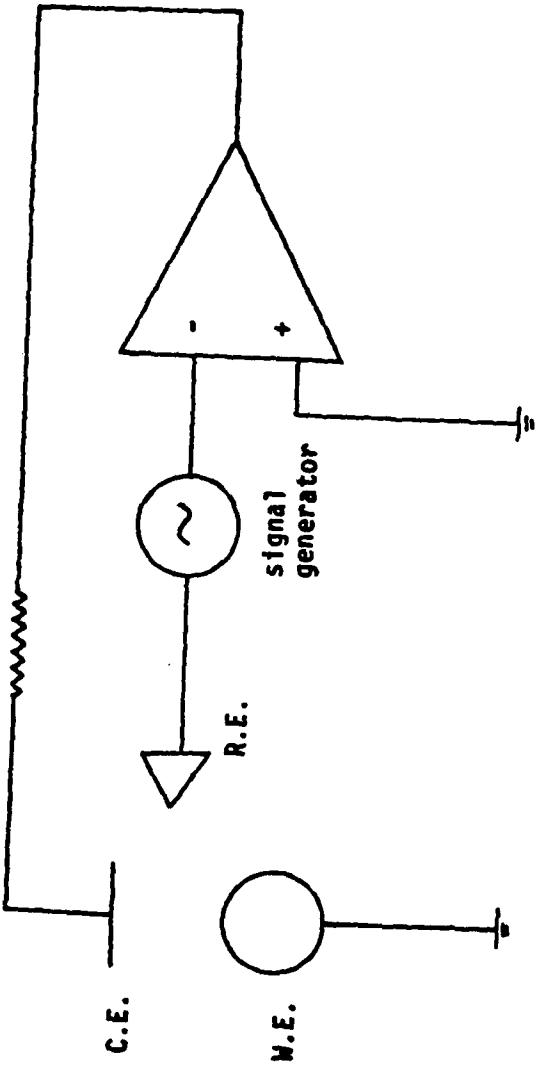


Fig. 5.2(b) The circuit schematics for the single-amplifier potentiostat which shows the principle of operation.

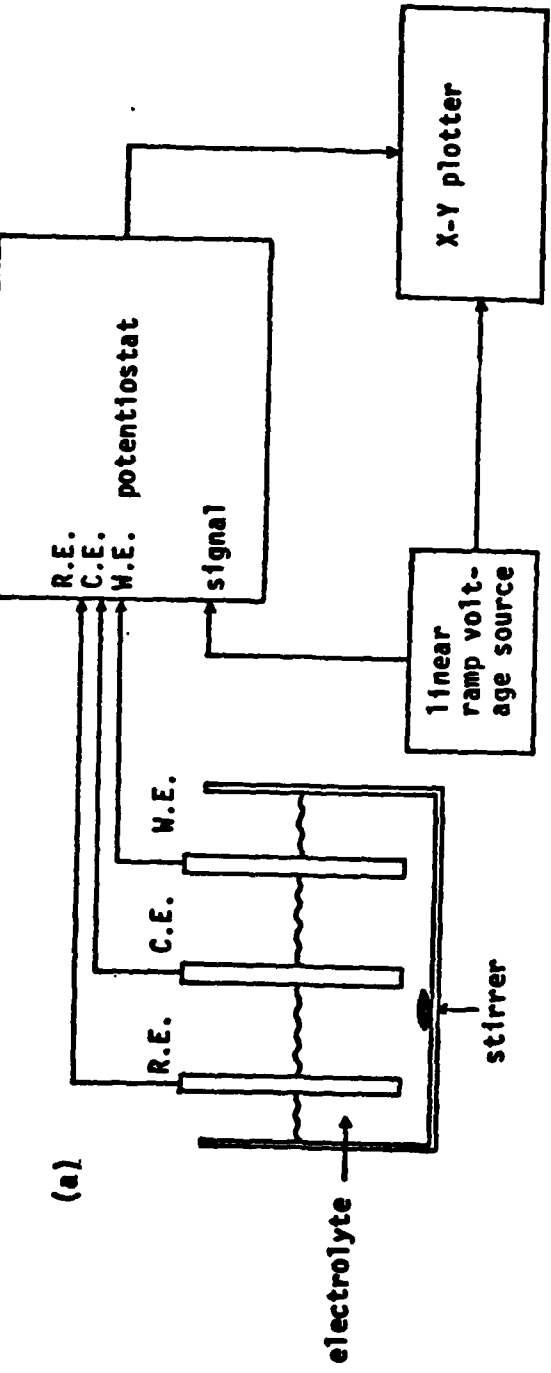


Fig. 5.2 The schematics of the electrical measurement system for the linear sweep potential voltammogram. (a)

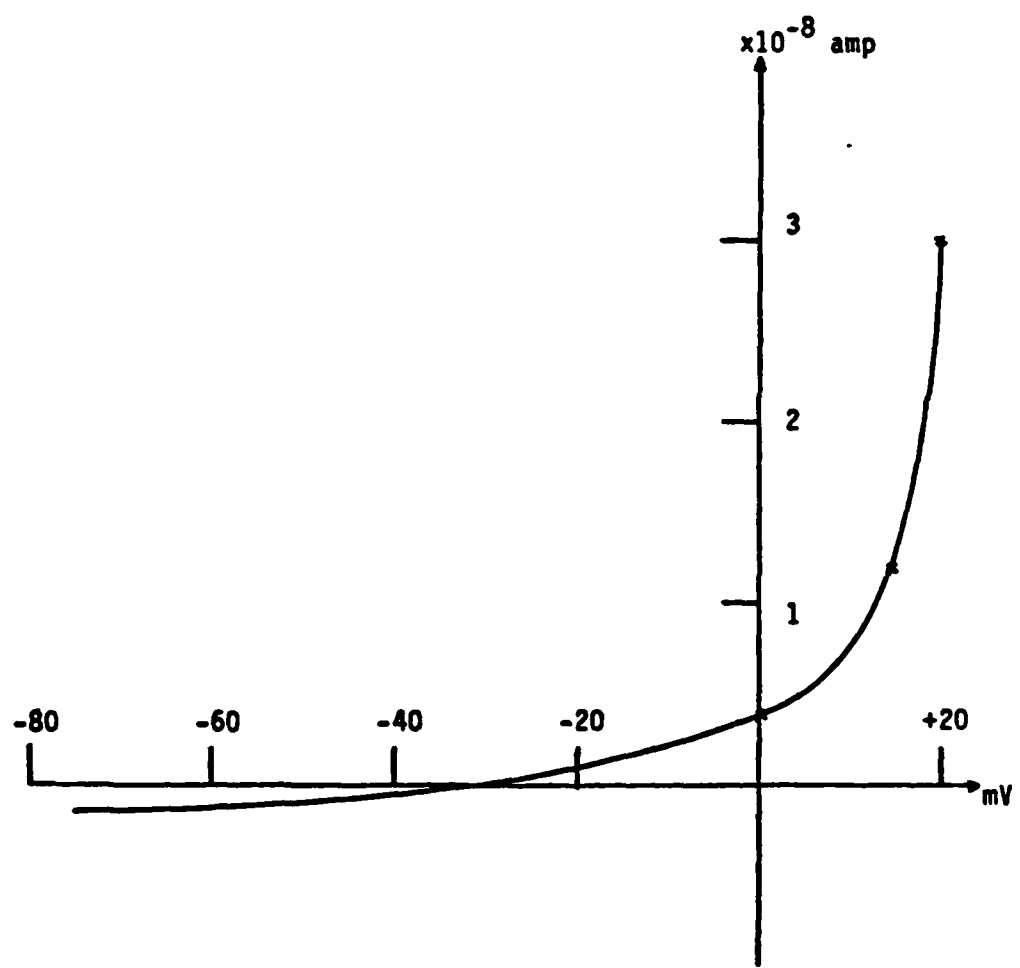


Fig.5.3 Voltage-current curve of the system $\text{As}_2\text{S}_3/\text{Ag}^+$ -electrolyte shows the rectification property in the as-deposited As_2S_3 electrode.

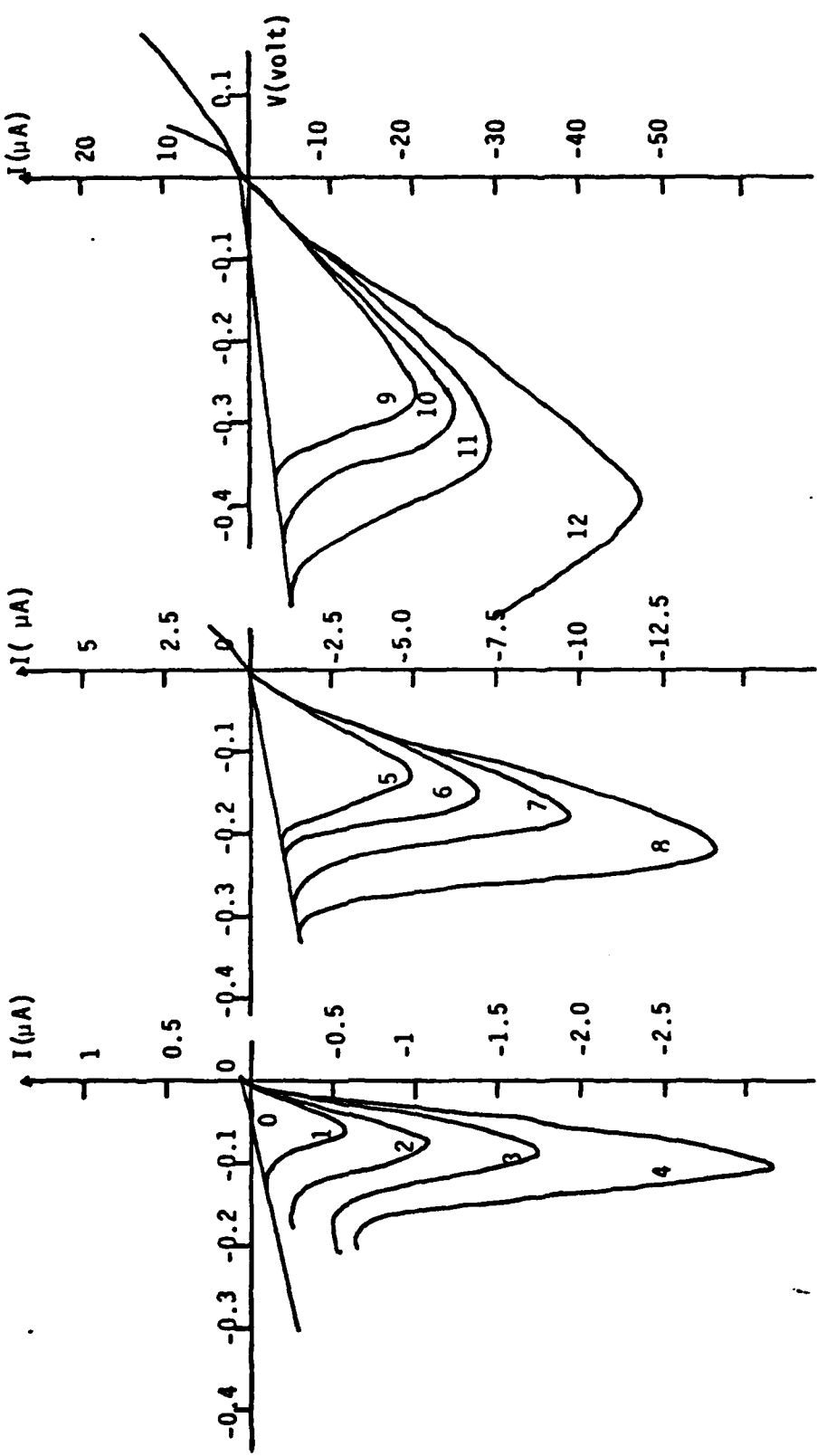


Fig. 5.5 This figure shows a set of voltammograms corresponding to the different silver doping levels. The voltammograms indicate a maximum peak in the anodic process. The voltage ramping rate is 2 mV/sec.

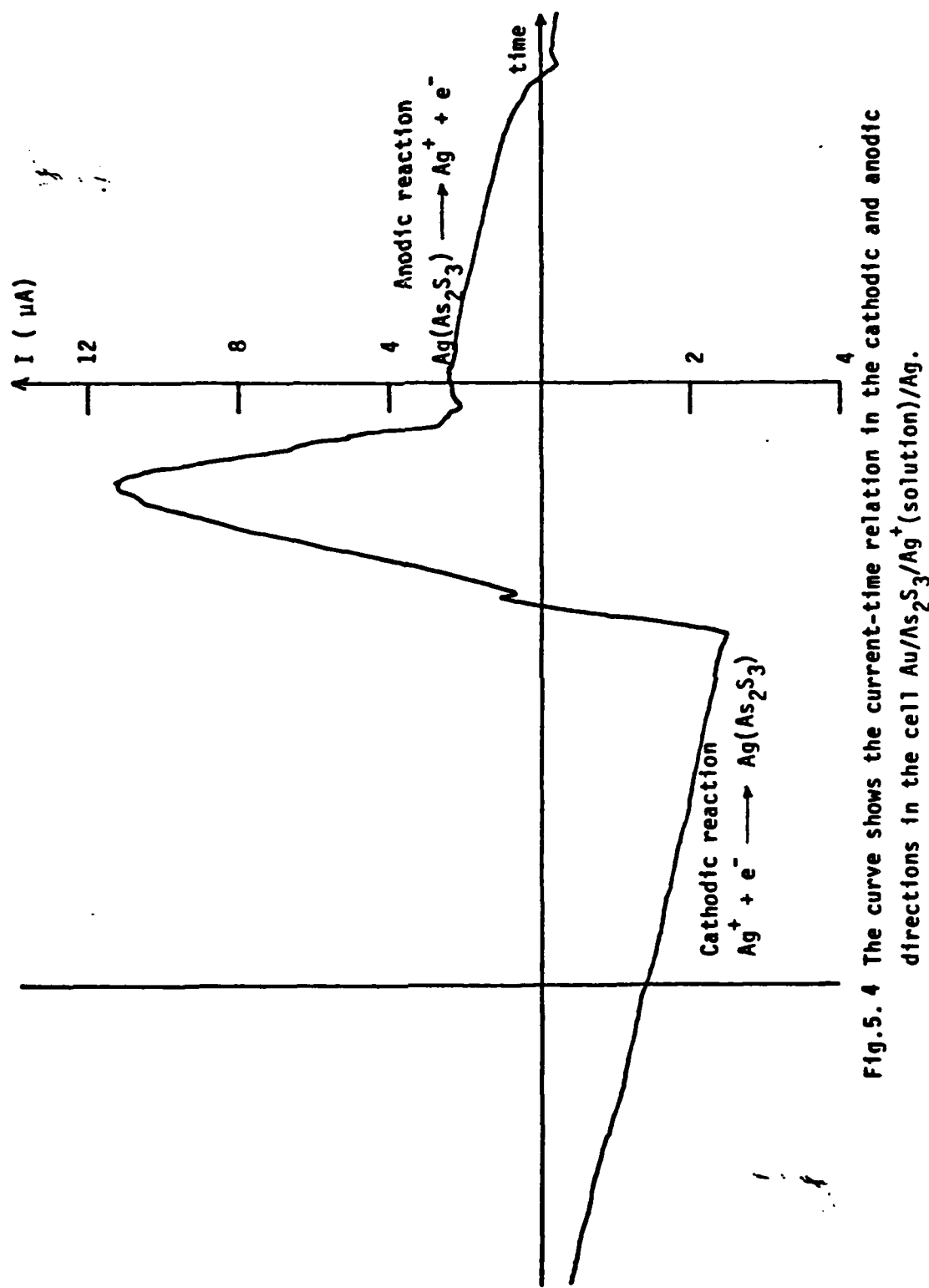


Fig. 5. 4 The curve shows the current-time relation in the cathodic and anodic directions in the cell $\text{Au}/\text{As}_2\text{S}_3/\text{Ag}^+$ (solution)/ Ag .

describing various reaction mechanisms, a brief survey of the potential distributions at the As_2S_3 electrode/electrolyte interface at equilibrium and non-equilibrium are given.

5.4.1. Electrical Properties of the As_2S_3 Electrode/Electrolyte Interface

Consider an electrochemical cell (shown in Fig. 5.6 (a)) with an As_2S_3 semiconductor as working electrode and a silver electrode as the reference electrode. The cell potential is composed of the potential differences at the boundaries of the phases making up the circuit. Every interface in the cell, but not necessarily the As_2S_3 -electrolyte interface, may be in equilibrium with one exchangable charge carrier. It can be shown that the cell potential is equivalent to the difference in free energy of electrons between the two ends of the cell.⁽¹¹⁾ Fig. 5.6 (b) shows the potential distribution of the As_2S_3 electrode in contact with an electrolyte in equilibrium condition (solid line in Fig. 5.6 (b)). In general, the potential difference at the As_2S_3 /electrolyte interface may distribute itself over three regions of the interface: (1) the space-charge layer in the As_2S_3 electrode; (2) the one or two atom-diameter region of the Helmholtz layer; (3) the diffuse Gouy-Chapman layer in the electrolyte.^(7,12-15) The potential differences over these different regions of the interface are denoted by $\Delta_0\Phi_s$, $\Delta_0\Phi_H$, and $\Delta_0\Phi_{GC}$, respectively.(see Fig. 5.6 (b)) In addition to these potential differences, there are also potential differences at the Au- As_2S_3 interface and the electrolyte/reference electrode interface, denoted by $\Delta_0\Phi_{Au}$ and $\Delta_0\Phi_{Sol-Ref}$, respectively. The subscript , denotes the potential difference at the equilibrium

by a sequence of steps involving not only the transfer of charges at an electrode/electrolyte interface but also the transport through the electrolyte and electrode phase. Though the overall electrochemical reaction may consist of several steps, it is usually possible to single out one step as a rate-determining step.⁽⁶⁾ In the case of the silver -ion injection process in the As_2S_3 electrode, at least four separate steps in the cathodic process occur:

- (1) Transport of the hydrated Ag^+ ion from the bulk electrolyte to the interface.
- (2) Adsorption of Ag^+ ions onto the As_2S_3 surface.
- (3) Charge transfer at the As_2S_3 electrode/electrolyte interface.
- (4) Transfer of Ag^+ ions from the interface into the bulk of the As_2S_3 electrode.

The reverse steps occur in the anodic process. Since these steps occur sequentially, any of these steps can be rate-determined. Steps (1) and (4) are known as mass transport processes. In this study, it is assumed that mass transport occurs only by diffusion. Steps (2) and (3) are referred to as the activation processes. This process involving not only the properties of the As_2S_3 electrode, but also the mechanism of charge transfer between the As_2S_3 electrode and Ag^+ ions in the electrolyte.

The evaporated As_2S_3 film is an amorphous semiconductor.⁽⁸⁻¹⁰⁾ Because of the lower carrier concentrations, semiconductor can not be treated electrostatically like a metallic conductor. The well-developed theory of the charge transfer process at the metal/electrolyte interface cannot be directly employed in this work. Before

condition. $\Delta_0\Phi$, the cell potential at equilibrium, is the sum over all potential differences at the interfaces,

$$\Delta_0\Phi = \Delta_0\Phi_{Au} + \Delta_0\Phi_s + \Delta_0\Phi_H + \Delta_0\Phi_{GC} + \Delta_0\Phi_{Sol-Ref} \quad (5-1)$$

If the cell is not at equilibrium, then the cell potential can be expressed as (dotted line in Fig. 5.6 (b)),

$$\Delta\Phi = \Delta\Phi_{Au} + \Delta\Phi_s + \Delta\Phi_H + \Delta\Phi_{GC} + \Delta\Phi_{Sol-Ref} + \Delta\Phi_\Omega \quad (5-2)$$

where $\Delta\Phi_\Omega$ is the ohmic potential drop in the bulk of the As_2S_3 electrode. Therefore,

$$\begin{aligned} (\Delta\Phi - \Delta_0\Phi) &= (\Delta\Phi_{Au} - \Delta_0\Phi_{Au}) + \Delta\Phi_\Omega + (\Delta\Phi_s - \Delta_0\Phi_s) + (\Delta\Phi_H - \Delta_0\Phi_H) \\ &\quad + (\Delta\Phi_{GC} - \Delta_0\Phi_{GC}) + (\Delta\Phi_{Sol-Ref} - \Delta_0\Phi_{Sol-Ref}) \end{aligned} \quad ----- (5-3)$$

Denoting the potential difference between the equilibrium and non-equilibrium condition at the interface i , $\Delta\eta_i - \Delta_0\Phi_i$, as the overpotential at the interface i , η_i , then

$$\eta = \eta_{Au} + \eta_s + \eta_H + \eta_{GC} + \eta_{Sol-Ref} + \eta_\Omega \quad (5-4)$$

Assuming that the interface between the electrolyte and the reference electrode is ideally unpolarizable,⁽⁵⁾ then $\eta_{Sol-Ref} = 0$. In this study, both experimental and theoretical treatments are restricted to conditions (i.e. high ionic concentration in the electrolyte) under which the overpotential across the Gouy-Chapman diffuse layer is negligible, i.e. $\eta_{GC} = 0$. The Au- As_2S_3 interface has been reported to form an ohmic barrier.⁽¹⁶⁾ It can be further assumed $\eta_{Au} = 0$. Under these assumptions, Eq (5-4) can be reduced to

$$\eta = \eta_s + \eta_H + \eta_\Omega \quad (5-5)$$

For the time being, the overpotential due to the ohmic drop in the bulk of As_2S_3 will be omitted for simplicity. It will be reconsidered later

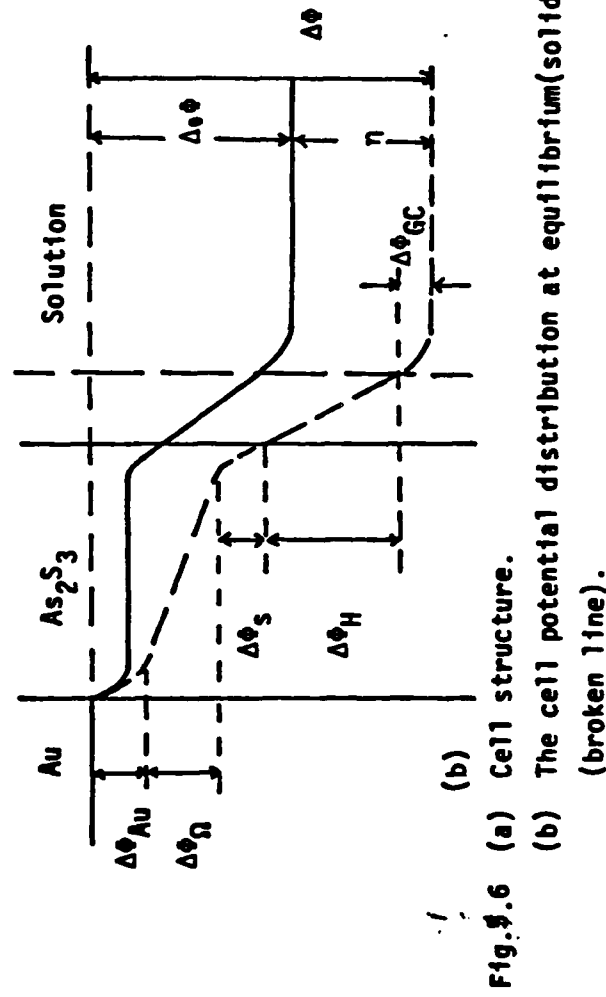
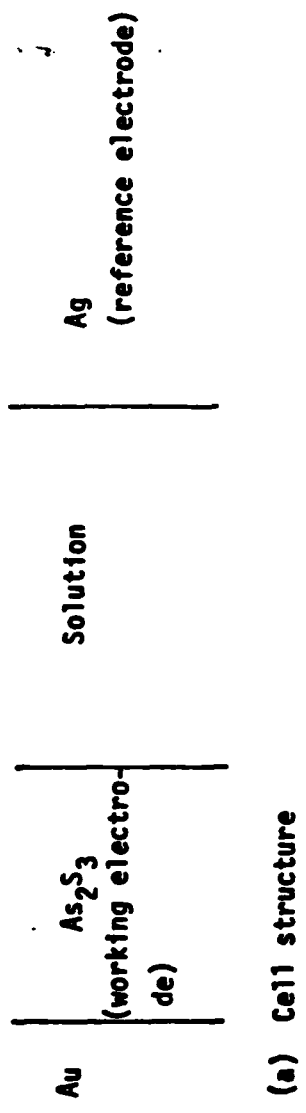
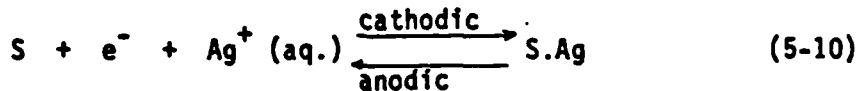


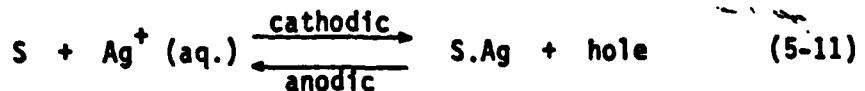
Fig. 3.6 (a) Cell structure.
 (b) The cell potential distribution at equilibrium (solid line) and non-equilibrium (broken line).

Since the silver ions passing the Helmholtz double layer are not a constituent of the As_2S_3 electrode but are chemically adsorbed to the electrode surface, the situation is very different from the usual metal-electrolyte interface.^(11,21-22) The electron quantum states which form the chemisorption bond can be represented in the bond model of the semiconductor as additional quantum states in the surface, which can have donor or acceptor properties according to their relation to the energy band.⁽²¹⁾ The probability of charge transfer through the Helmholtz layer will strongly depend on the probability of finding an electron in the surface which can occupy the new electron state formed by the approach of a particle to the surface (for example, Ag^+ ions) or on the probability of finding a hole in the surface if the approaching particle should bring its own binding electrons.

For the silver ion transporting through the Helmholtz double layer, it is assumed the following reaction occurs:



which describes the process of transfer of the hydrated Ag^+ ion at the outer Helmholtz plane (OHP) moving through the Helmholtz layer, losing its hydration shell and adsorbing at a surface site S as a neutral specie by reacting with a conduction band electron. A similar adsorption process could also result in transfer of a hole to valence band through the following reaction:



The kinetic equations for the above charge transfer reactions were derived by Gerischer.⁽¹¹⁾ The current density for the

as an IR correction term in the theoretical calculation. The cell overpotential is thus given as the sum of the overpotential at the As_2S_3 semiconductor surface and across the Helmholtz layer in the electrolyte.

$$\eta = \eta_H + \eta_s \quad (5-6)$$

The origin of this potential difference is described elsewhere. (17-20)

In general, η_s can be expressed as the sum of the overvoltage at equilibrium of electrons or holes in the semiconductor, η_s^0 , and the electron or hole transport overvoltage, η_T , which represents the contribution of electron or hole transport to the space-charge overvoltage.

Therefore, (11)

$$\eta_s = \eta_s^0 + \eta_T \quad (5-7)$$

where

$$\eta_s^0 = - \frac{k_B T}{q} \ln \left(\frac{n_s}{e n_s^0} \right) \quad \text{for electrons,} \quad (5-8a)$$

$$\eta_s^0 = - \frac{k_B T}{q} \ln \left(\frac{p_s}{e p_s^0} \right) \quad \text{for holes,} \quad (5-8b)$$

and

$$\eta_T \approx - \frac{j}{q} \ln \left(1 + \frac{j}{j_{,Sat}} \right) \quad (5-9)$$

where j is the electron or hole current density, i.e. j_c or j_v , in the electrode reaction,

$j_{,Sat}$ is the sum of the maximum electron or hole current density flowing from the bulk into the space-charge layer and the maximum surface generation current density of electron or hole, and $e n_s^0$ and n_s are the concentrations of free electrons at the surface at equilibrium and non-equilibrium condition, respectively.

5.4.2. Electrode Reactions With Charge Transfer By Ag-ion at the $\text{As}_2\text{S}_3/\text{Electrolyte}$ Interface

$$j = \alpha j_C \left[\frac{C_{Ag}}{\alpha C_{Ag}} \times e^{\alpha_c q \eta_H / k_B T} - \frac{n_s}{\alpha n_s} \times \frac{(C_{Ag}^\infty - C_{Ag})}{(C_{Ag}^\infty - \alpha C_{Ag})} \times e^{-(1-\alpha_c)q\eta_H / k_B T} \right] \\ + \alpha j_V \left[\frac{C_{Ag}}{\alpha C_{Ag}} \times \frac{p_s}{\alpha p_s} \times e^{\alpha_v q \eta_H / k_B T} - \frac{(C_{Ag}^\infty - C_{Ag})}{(C_{Ag}^\infty - \alpha C_{Ag})} \times e^{-(1-\alpha_v)q\eta_H / k_B T} \right]$$

--- (5-14)

This is the most general expression for obtaining the j vs η characteristics. The Butler-Volmer equation,

$$j = \alpha j \left[e^{\alpha_c q \eta_H / k_B T} - e^{-(1-\alpha_c) q \eta_H / k_B T} \right]$$

, for the metal electrode, can be easily obtained from Eq. (5-14) under certain conditions.

Considering the special case where the current density αj_V is so small in comparison with αj_C that it is possible to neglect reactions involving the valence band. In this special case, the total current density in accordance with relation Eq. (5-14) is determined by the expression:

$$j = j_C \\ = \alpha j_C \left[\frac{C_{Ag}}{\alpha C_{Ag}} \times e^{\alpha_c q \eta_H / k_B T} - \frac{n_s}{\alpha n_s} \times \frac{(C_{Ag}^\infty - C_{Ag})}{(C_{Ag}^\infty - \alpha C_{Ag})} \times e^{-(1-\alpha_c)q\eta_H / k_B T} \right]$$

---- (5-15)

conduction band process (Eq.(5-10)) is given by

$$j_c = \eta j_c \left[\frac{C_{Ag}}{\eta C_{Ag}} \times e^{\alpha_c q n_H / k_B T} - \frac{n_s}{\eta n_s} \times \frac{C_{Ag}^+}{\eta C_{Ag}^+} \times \frac{(C_{Ag}^\infty - C_{Ag})}{(C_{Ag}^\infty - \eta C_{Ag})} \times e^{-(1-\alpha_c)q n_H / k_B T} \right] \quad (5-12)$$

where C_{Ag} is the concentration of the adsorbed silver, C_{Ag}^∞ is the maximum adsorbed coverage, C_{Ag}^+ is the concentration of the hydrated silver ion, Ag^+ (aq.), at the OHP, α_c is the transfer coefficient for the conduction band process, and ηj_c is the electron exchange current density at equilibrium. For the valence band process (Eq.(5-11)), it is given by

$$j_v = \eta j_v \left[\frac{C_{Ag}}{\eta C_{Ag}} \times \frac{p_s}{\eta p_s} \times e^{\alpha_v q n_H / k_B T} - \frac{C_{Ag}^+}{\eta C_{Ag}^+} \times \frac{(C_{Ag}^\infty - C_{Ag})}{(C_{Ag}^\infty - \eta C_{Ag})} \times e^{-(1-\alpha_v)q n_H / k_B T} \right] \quad (5-13)$$

where ηj_v is the hole exchange current density at equilibrium, α_v is the transfer coefficient for the valence band process, and p_s is the hole concentration on the semiconductor surface. Since $n_{GC} = 0$ is assumed, then $C_{Ag}^+ = \eta C_{Ag}^+$. The total current density $j = j_c + j_v$ is now given

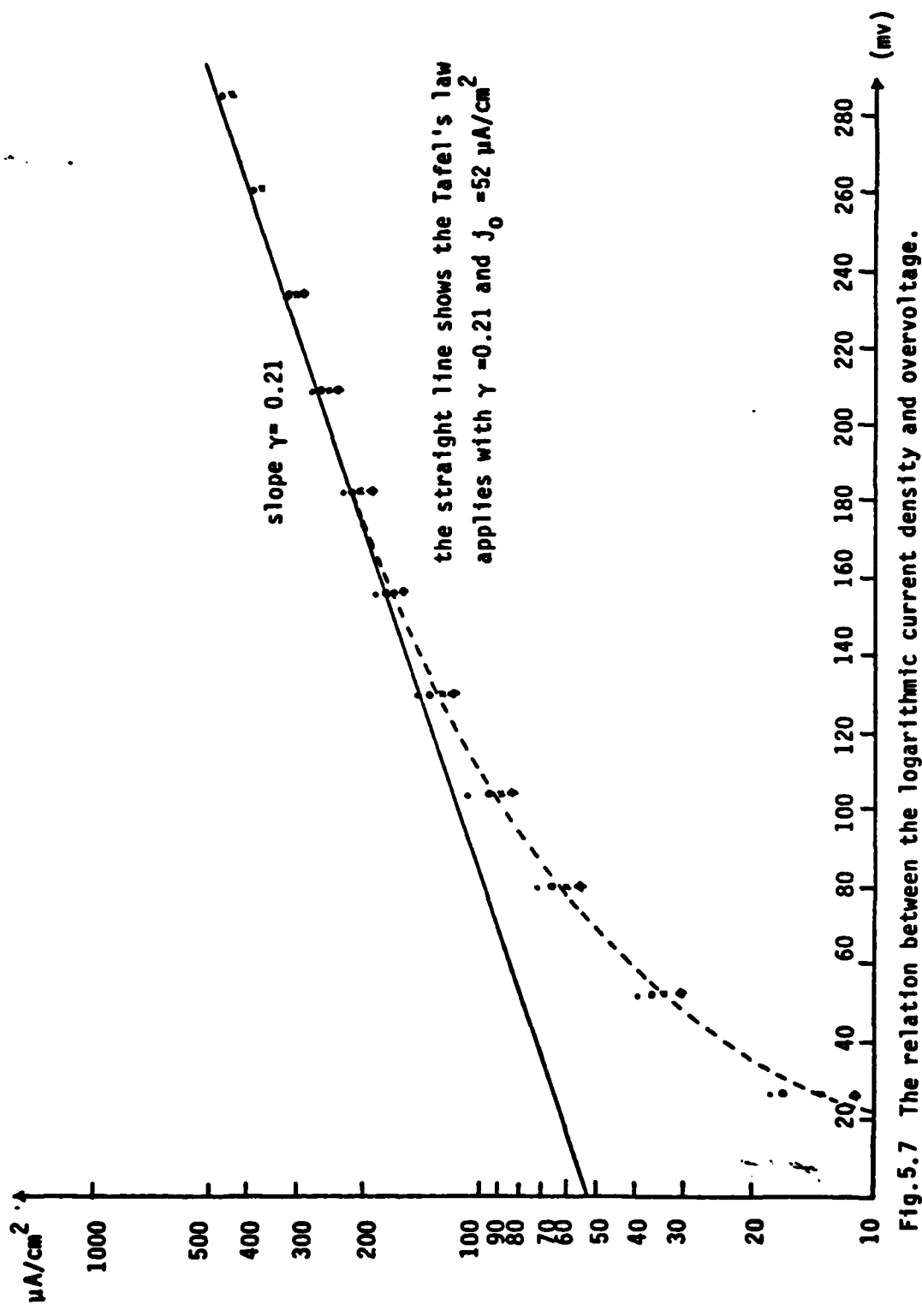


Fig. 5.7 The relation between the logarithmic current density and overvoltage.

For the anodic reaction, the current- overvoltage relation derived from Eq.(5-15) is

$$J_c = \alpha j_c \left[\frac{C_{Ag}}{\alpha C_{Ag}} \times e^{\alpha_c q n_H / k_B T} - 1 \right] \quad (5-16)$$

Let $n_H = \beta n$, where $0 < \beta < 1$. Therefore,

$$J_c = \alpha j_c \left[\frac{C_{Ag}}{\alpha C_{Ag}} \times e^{\gamma q n / k_B T} - 1 \right] \quad (5-17)$$

where $\gamma = \alpha_c \beta$. The transport coefficient is generally about $\frac{1}{2}$, but it may differ from $\frac{1}{2}$ if certain conditions do not hold.⁽⁷⁾ From more detailed consideration, it is found that αj_c is proportional to αC_{Ag} , the concentration of adsorbed silver on the As_2S_3 electrode at equilibrium.⁽⁷⁾ From Eq.(5-17), at overvoltage greater than several $k_B T/q$, it is possible to neglect the second term in Eq.(5-17) and write Eq. (5-17) in the form

$$\ln J_c \approx \ln \alpha j_c + \gamma q n / k_B T \quad (5-18)$$

i.e., Tafel's law applies.^(7,21) The coefficient γ may have various values. Fig. 5.7 shows the relation between the overvoltage n and the logarithmic current density $\ln J_c$ for the As_2S_3 /electrolyte (10^{-3} N $AgNO_3$ aqueous solution) interface studied in this work. It is found from this curve that the coefficient γ in the Tafel relation is about 0.2 and the exchange current αj_c about $50 \mu A/cm^2$. From theory it follows that the coefficient γ have shown values from 0 to 1.⁽⁷⁾ Our experimental data may be explained by assuming that the values of α_c and β are both comparable to $\frac{1}{2}$. It implies that the overvoltage is

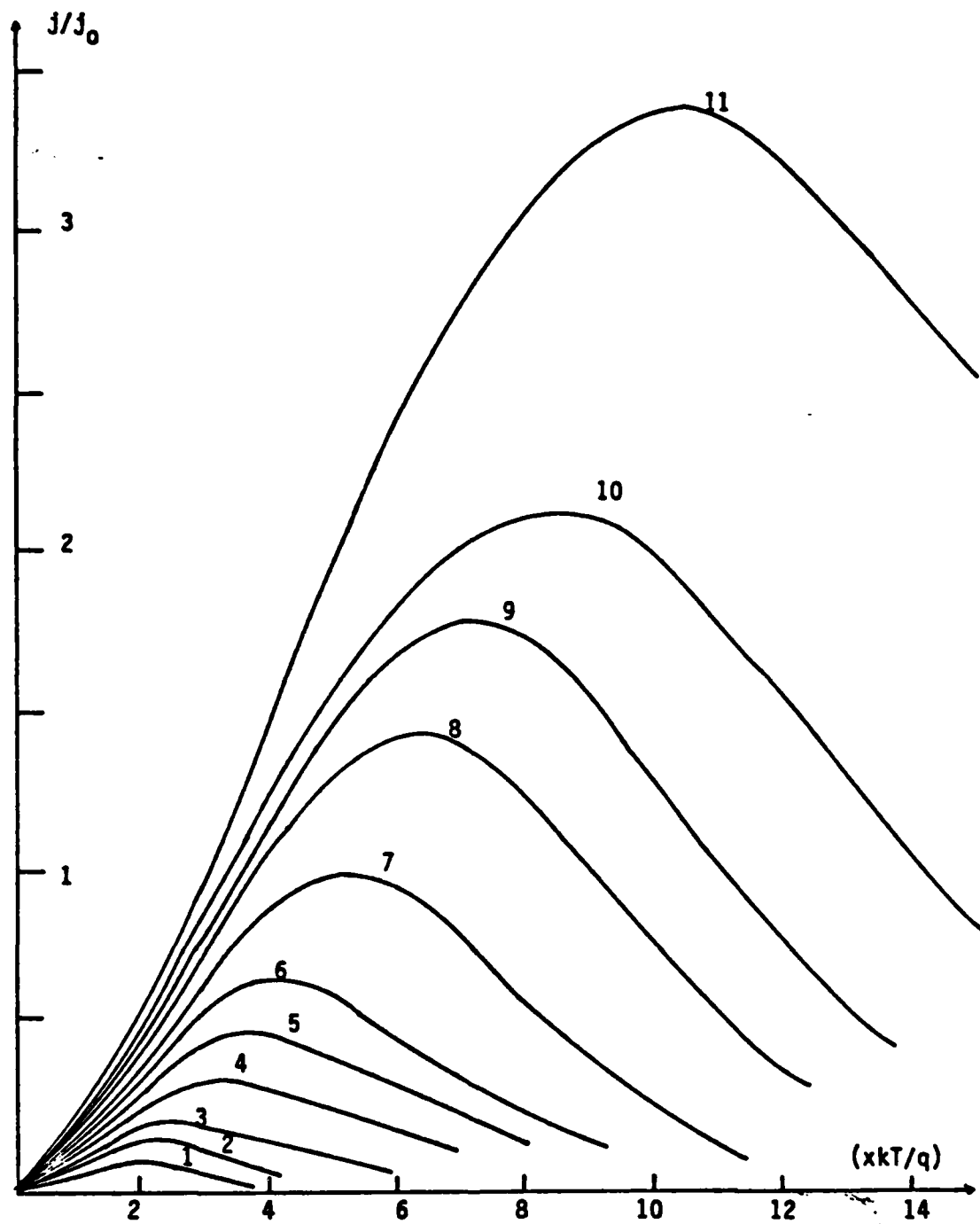


Fig. 5.8 The anodic characteristics after IR correction. The bulk resistances used in the correction are given in Table 5.1.

distributed approximately equally between the space charge region in the As_2S_3 electrode and the Helmholtz layer in the electrolyte. Since thin films of amorphous chalcogenide semiconductors provide surfaces with a very high density of defect states,⁽²³⁻²⁴⁾ the linearity of the logarithmic current density-overvoltage curves may be lost and the curves become rather complex as we observed in this work.

Fig. 5.5 shows the kinetics of silver injection into amorphous As_2S_3 films. It can be seen that the amount of silver injection increases rapidly toward a saturation. It also shows that the bulk resistance of As_2S_3 electrode is changing during the injection process. From Fig. 5.5 and 5.7, one can calculate the bulk resistance of the As_2S_3 electrode for each injection process. The modified anodic characteristics of the As_2S_3 / electrolyte interface is then replotted in Fig. 5.8. The bulk resistances of As_2S_3 film used in Fig. 5.8 are given in Table 5.1. To model our experimental results, a detail numerical analysis has been done by Lauks.⁽²⁵⁾ His results are shown in Figs. 5.9 and 5.10. The curves shown in Fig. 5.9 were obtained by assuming the As_2S_3 /electrolyte interface is at equilibrium (i.e., the transport of the hydrated Ag^+ ion from the bulk electrolyte to the interface is the rate-determining step). Fig. 5.10 was obtained by assuming the As_2S_3 /electrolyte interfacial reaction is the rate-determining step. It is clearly shown, by comparing the numerical curves (Figs. 5.9 and 5.10) with the experimental curves (Fig. 5.8), that the reaction between the As_2S_3 electrode and the aqueous electrolyte is the rate-determining step in the silver-ion injection process.

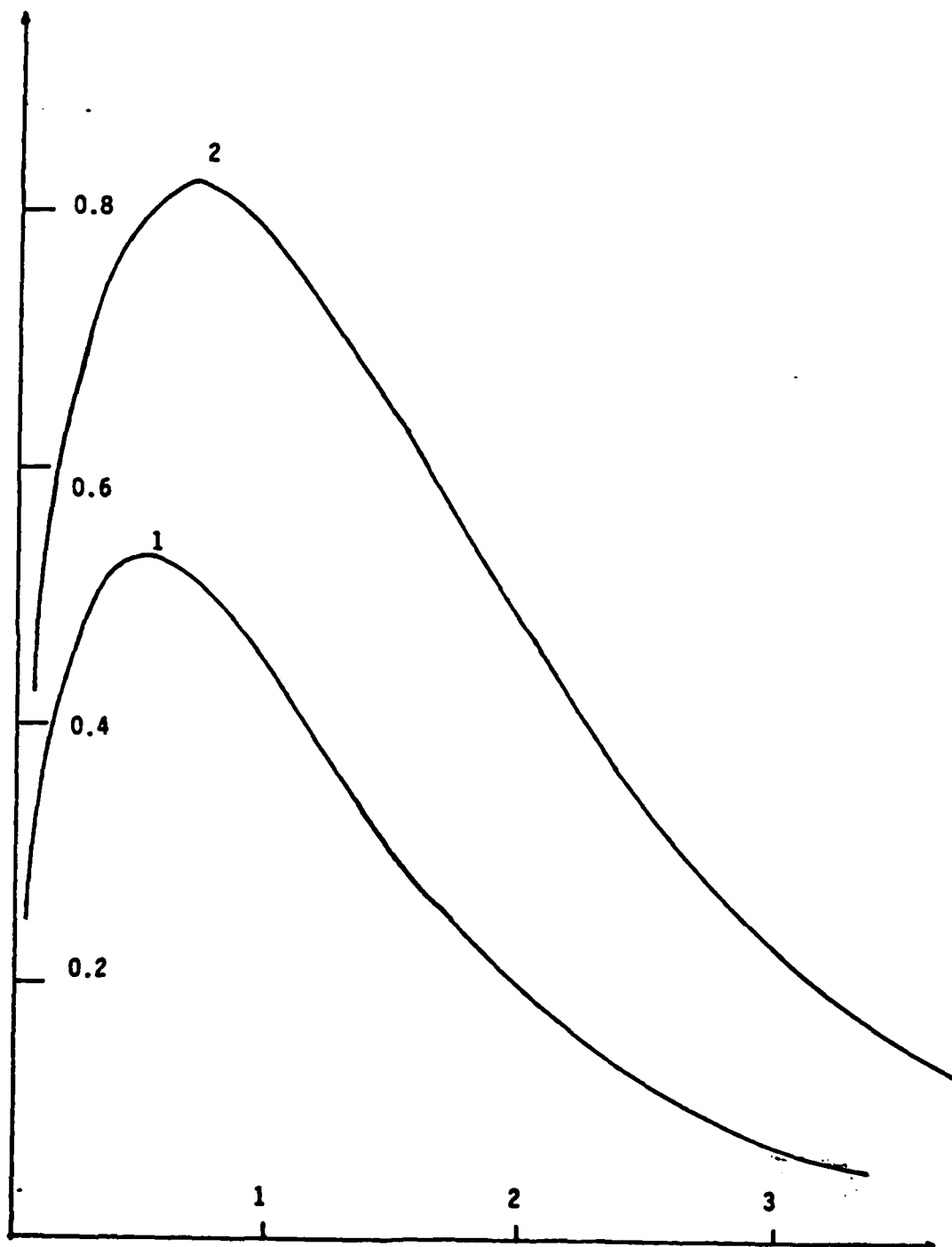


Fig.5.9 The numerical data obtained by assuming the As_2S_3 /electrolyte interface is at equilibrium.
(25)

Run number	R_{bulk}^*
1	3.7×10^4
2	2.9×10^4
3	2.3×10^4
4	2.0×10^4
5	1.2×10^4
6	9.4×10^3
7	7.5×10^3
8	6.0×10^3
9	4.9×10^3
10	4.3×10^3
11	3.5×10^3
12	3.0×10^3

$$*R_{bulk} = V/I \text{ and } V = 15 \times 10^{-3} \text{ volt.}$$

Table 5.1 The bulk resistance of As_2S_3 film calculated from Fig.5.5.

5.5 THE AC RESPONSES OF As₂S₃ FILMS

5.5.1. The Cell for AC Impedance Measurements

The two-electrode system was used for the ac impedance measurements. The cell current passes through both the working electrode and the reference electrode. In order to minimize the IR drop through the electrolyte, the working electrode and the reference electrode were held as close as possible to each other. In addition, the current passing through the reference electrode may cause its potential to deviate from its equilibrium (zero current) value due to changes in concentration of the electroactive species at the reference electrode/solution interface. To avoid serious errors, the cell current and in turn the applied voltage must be kept as small as possible.

The working electrode was the same as the one described previously except the thickness of the As₂S₃ film was in the range 1.5 to 2 μm . The choice of the reference electrodes depends on the type of electrolytes. The AgCl/Ag reference electrode was used in the potassium chloride solution and the Ag reference electrode in the silver nitrate aqueous solution. The AgCl/Ag reference electrode was made by electroplating a silver wire in 0.1 M HCl solution against a platinum cathode. By applying a potential of 250 mv to these silver and platinum electrodes for about half an hour, the silver wire was coated with a thin layer of AgCl. This AgCl/Ag electrode will establish a well-defined surface potential across the electrolyte/reference electrode interface if the chlorine ion in the aqueous solution is constant. The electrolyte was agitated by a stirrer to make the solution homogeneous at all times. All the measurements were performed at room temperature.

Run number	R_{bulk}^*
1	3.7×10^4
2	2.9×10^4
3	2.3×10^4
4	2.0×10^4
5	1.2×10^4
6	9.4×10^3
7	7.5×10^3
8	6.0×10^3
9	4.9×10^3
10	4.3×10^3
11	3.5×10^3
12	3.0×10^3

$$*R_{bulk} = V/I \text{ and } V = 15 \times 10^{-3} \text{ volt.}$$

Table 5.1 The bulk resistance of As_2S_3 film calculated from Fig.5.5.

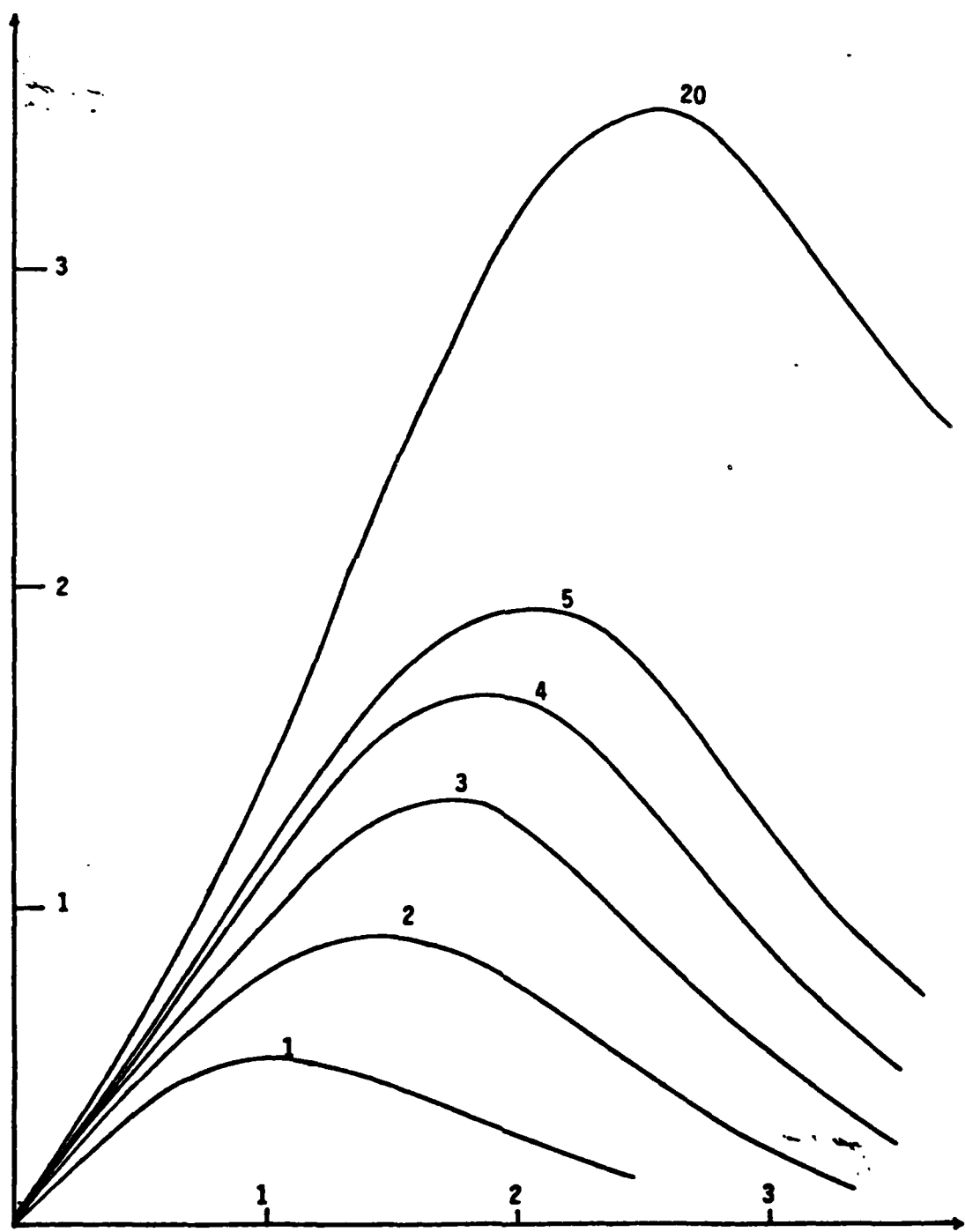


Fig.5.10 The numerical data obtained by assuming the As_2S_3 /electrolyte interfacial reaction is the rate-determining step. (25)

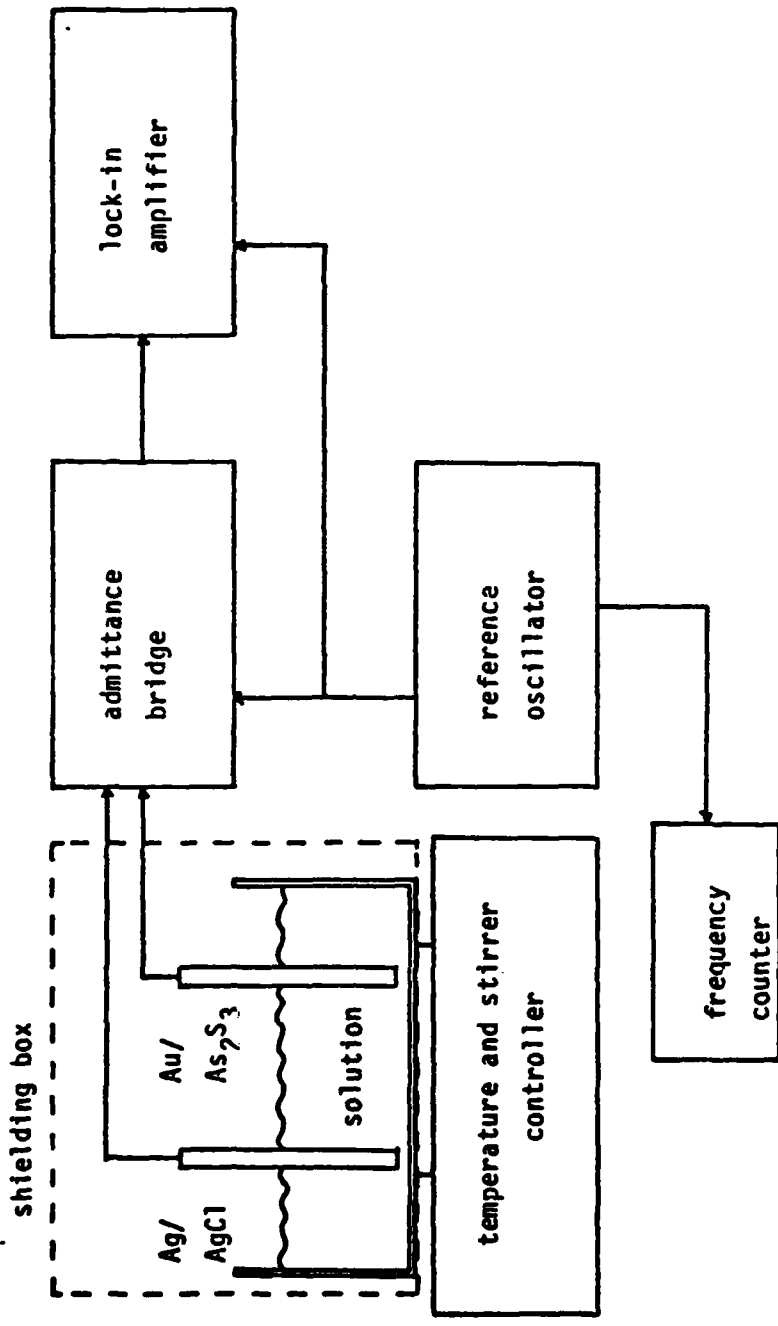


Fig. 5.11 The schematics of the ac impedance measurement for the bridge method.

5.5.2 AC Impedance Measurement Systems

Two experimental methods were used in this study to investigate the ac response of an electrochemical system: (i) the AC bridge method, and (ii) the direct impedance measurement. In these two methods, the components of impedance are obtained, which provide information about the electrochemical processes involved. The basic principles of the ac response of the electrochemical cell^(12,23) will be discussed in the next section. Since the sensitivity and the accuracy are different in these two measurement techniques, they will be discussed separately.

(i) AC Bridge Method

A simple schematic representation of an ac bridge is shown in Fig. 5.11. The circuit shown includes a PAR 124 lock-in amplifier as a detector, a Boonton admittance bridge, an ac signal generator, and a frequency counter. The working and reference electrodes were connected to the input terminals of the capacitance bridge. A signal with adjustable frequency ranging from 1 KHz to 100 KHz was used as an excitation source for the bridge. This bridge measurement is operated on the principle that the output signal is nulled by appropriately adjusting the bridge capacitance and conductance value. Under the null condition, the capacitance C and conductance G can be directly read from the dial scale. In order to increase the sensitivity and accuracy of admittance bridge, the lock-in amplifier was used as a detector. The reference signal for the lock-in amplifier comes from the same

concentration electrolyte. As a result Z_{ref} can be neglected and the impedance of the working electrode can be rewritten as

$$Z_w = Z_{cell} - R_{sol}$$

where R_{sol} is usually determined from the cell impedance extrapolated to infinite frequency.

(ii) Direct Impedance Measurement

The minimum working frequency for the admittance bridge is about 300 Hz. For lower frequency measurements an alternative measurement had to be used and is described below.

From the definition of the impedance of the cell, $Z_{cell} = V/I$ where V, I are complex numbers. A simple approach is to measure the ac current I by means of a small resistor R_g and the voltage V of the cell with the lock-in amplifier. To minimize the error of measurements, the resistor R_g must be small enough to avoid changing the cell current and the input impedance of the lock-in amplifier must be larger than R_g in the measuring frequency region. The measurement scheme is shown in Fig. 5.12. The cell current is calculated from $I = V_b/R_g$. V_{ab} and V_b are directly obtained from the lock-in amplifier. From this definition,

$$Z = V/I$$

the real component Z' and imaginary component Z'' of the cell impedance can be easily calculated through the following equations.

oscillator used to drive the bridge. The lock-in amplifier can accurately measure the in-phase and quadrature-phase components of the input signal with respect to the phase adjusted reference signal. By appropriately adjusting the phase shift of the reference signal in the lock-in amplifier, the output signal from the admittance bridge can be resolved into two independent components. One is the capacitance and the other is the conductance.

The driving signal level for the admittance bridge, in principle, should be smaller than the thermal energy, $k_B T$, 25 mv at room temperature to ensure the current-voltage relationship can be linearized. For practical applications, a 5 mv peak-to-peak sinusoidal driving signal is appropriate. The voltage level for the reference signal of the lock-in amplifier, on the other hand, is not so critical, so long as it is not too small. The manufacturer suggests that 2 volts peak-to-peak signal be used.

The impedance of the electrochemical cell may be regarded as a series combination of the working electrode impedance, Z_w , ohmic resistance in the electrolyte, R_{sol} , and the reference electrode impedance, Z_{ref} . Therefore,^(12,23)

$$Z_{cell} = Z_w + R_{sol} + Z_{ref}$$

In this work, the resistance of Ag reference electrode is much less than both the working electrode and solution resistance in the high

$$Z' = |Z| \cos \Psi$$

$$Z'' = |Z| \sin \Psi$$

where Ψ is the phase angle between V and I measured with a lock-in amplifier.

5.5.3. AC Impedance Responses

The ac impedance measurement techniques previously described in Section 5.5.2. were the ac bridge method and the direct impedance method, above and below 1 KHz, respectively. The frequency dependence of the impedance in the KCl and AgNO_3 electrolytes are shown in Figs. 5.13 and 5.14(a), respectively, for $3 \text{ Hz} < f < 100\text{KHz}$. Fig. 5.14(b) shows the impedance after the silver injection. At high frequency, the impedance follows one semicircle while below 1 KHz it appears to follow another semicircle with a larger radius.

Note also the difference between ac responses on the As_2S_3 electrode in the potassium chloride and silver nitrate aqueous solutions (see Figs. 5.13 and 5.14(a)). At high frequency, the difference is due to the different ionic conductivity in the aqueous solution. On the other hand, at low frequency, it is due to the different electrode/electrolyte interfacial reaction. (12)

5.6 THE EQUIVALENT CIRCUIT OF THE As_2S_3 ELECTROCHEMICAL CELL

The complex impedance plots (or Nyquist plots), Figs. 5.13 and 5.14, of the As_2S_3 electrode in the potassium chloride and silver nitrate aqueous solutions are quite different. In this section, we will develop an equivalent circuit to explain our experimental results.

In general, the overall electrochemical reaction involves several

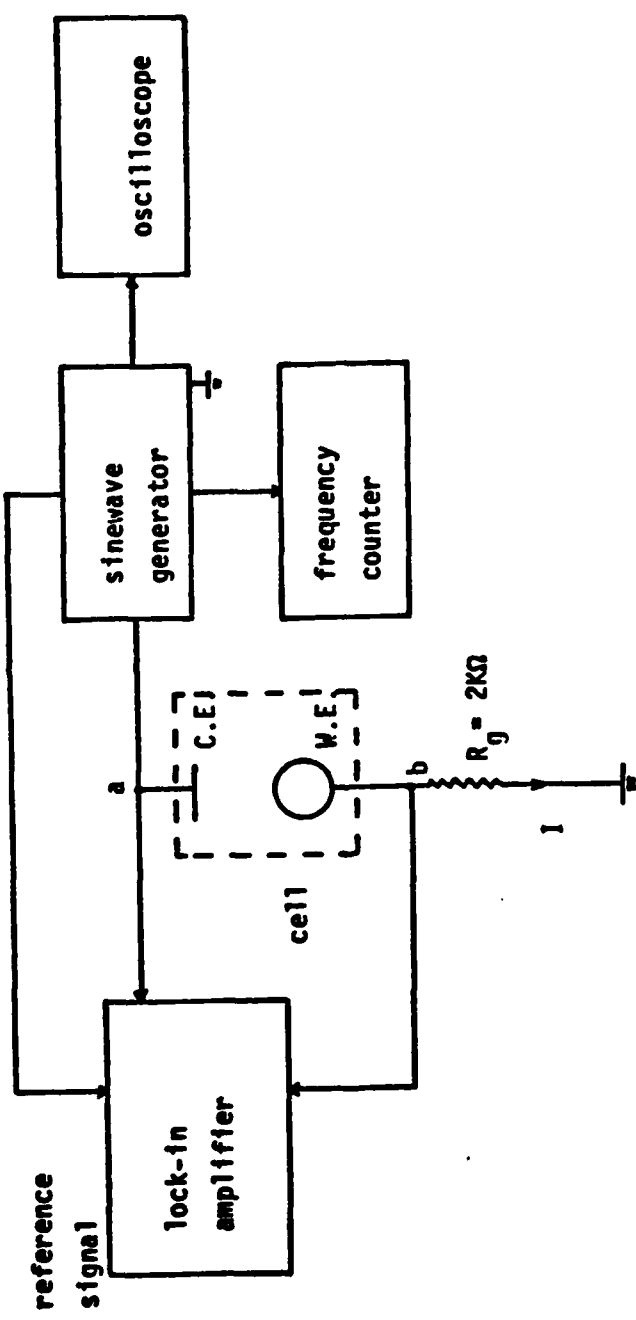


Fig.5.12 The schematics of the ac impedance measurement for the "direct" method.

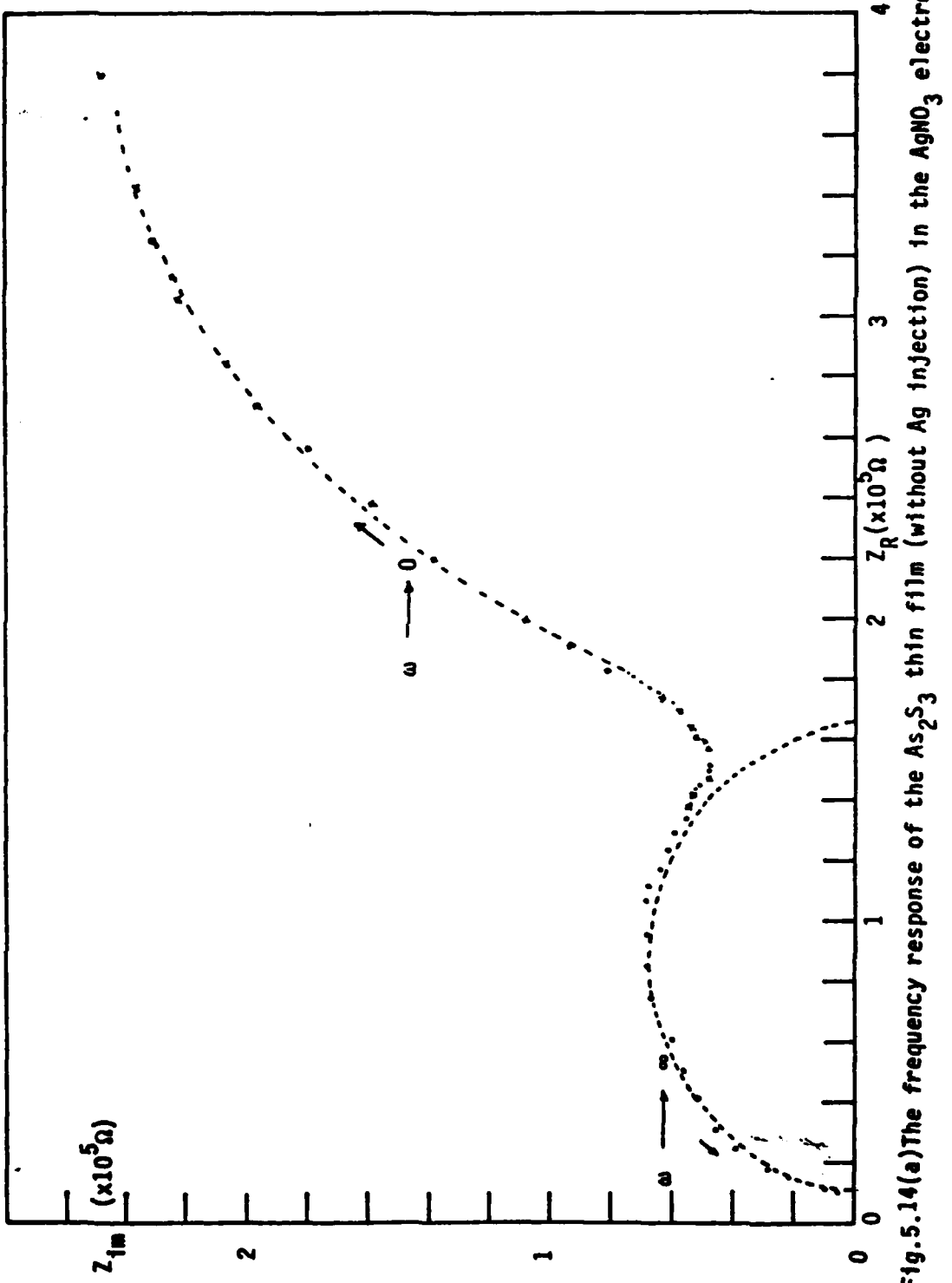


Fig. 5.14(a) The frequency response of the As_2S_3 thin film (without Ag injection) in the AgNO_3 electrolyte.

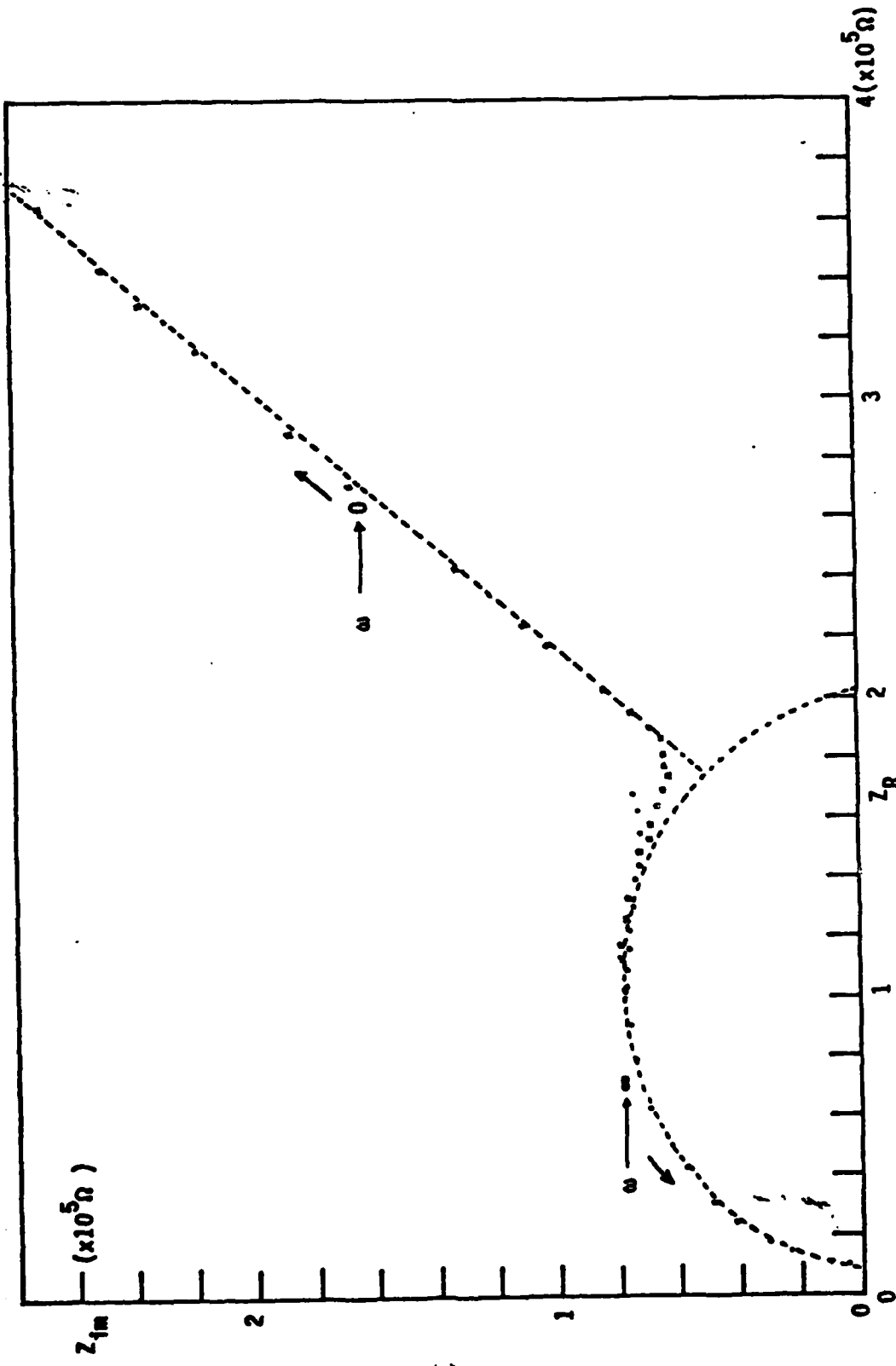


Fig.5.13 The frequency response of the As_2S_3 film in the KCl aqueous solution.

steps sequentially. If each of the main processes which lead to the electrical response considered separately produces one of the parallel RC branches, then the ac response of the electrochemical cell can be simulated by an equivalent circuit with several parallel RC sections in series. For the present homogeneous model, at least in the limit of very loosely coupled processes, each parallel RC section is associated with a separate process or physical region. (26-28)

In this work, the following equivalent circuit, shown in Fig. 5.15 (a), is proposed. It consists of three separate RC branches: the left-hand section corresponding to the bulk of solution, the middle section to the bulk of electrode, and the righthand section to the interfacial reaction. The capacitance of the electrolyte is usually very large compared with the other capacitances considered in the electrochemical system. Therefore, the capacitance of the electrolyte, C_{sol} , is neglected. The resulting equivalent circuit is shown in Fig. 5.15(b).

Consider first one parallel $R_b C_b$ section in series with R_{sol} . The impedance $Z = Z' + j Z''$ is given by

$$Z' = \frac{R_b}{1 + (\omega \tau)^2} + R_{sol} \quad (5-19a)$$

and

$$Z'' = \frac{-\omega \tau R_b}{1 + (\omega \tau)^2} \quad (5-19b)$$

where $\tau = R_b C_b$ = relaxation time constant of the bulk electrode and ω is the signal frequency. Eliminating $\omega \tau$ yields

$$(Z' - R_{sol} - \frac{R_b}{2})^2 + Z''^2 = \frac{R_b^2}{4}; \quad Z'' < 0 \quad (5-20)$$

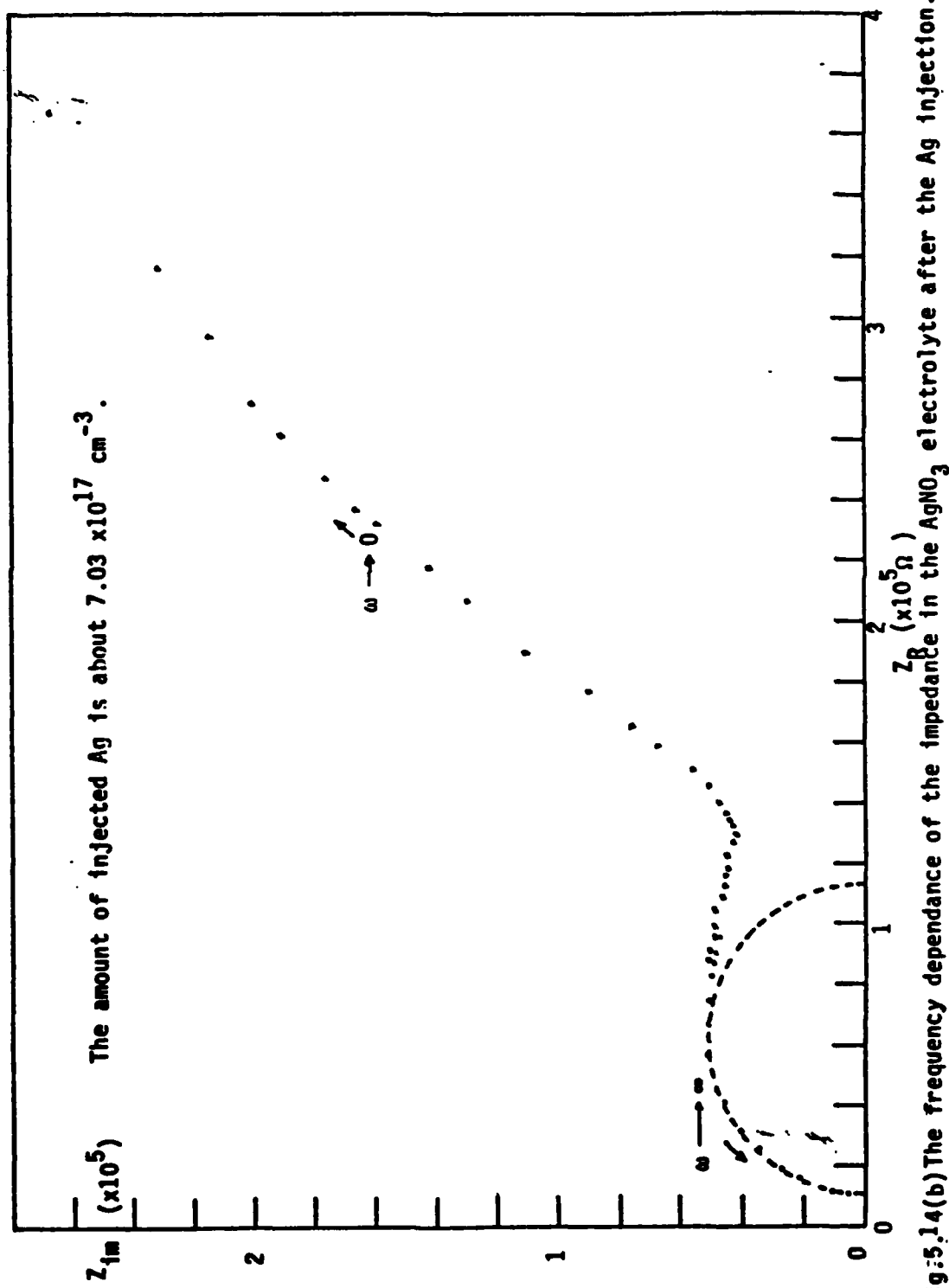


Fig.5.14(b) The frequency dependance of the impedance in the AgNO_3 electrolyte after the Ag injection.

and which is equation of a semicircle in the complex plane (Fig. 5.16) with a center at $(R_{sol} + R_b/2, 0)$ and radius $R_b/2$.

If the sequential steps in the overall electrochemical reaction are loosely coupled, then the different RC branch will be differentiated by varying the signal frequency. It is expected that the ac responses plotted as parametric functions of frequency in the complex plane will consist of a series of semicircles. In this study, it is observed that at high frequency the impedance is dominated by the bulk impedance of the As_2S_3 electrode. On the other hand, at low frequency it is dominated by the interfacial reaction between the As_2S_3 film and electrolyte. It is also observed that the experimental semicircle (Figs. 5.13 and 5.14) is depressed (i.e., less than a semicircle), possibly arising from a continuous distribution in one or more of the elements of the given process.⁽²⁷⁾ The lowest applied frequency is limited by the frequency responses of the capacitance bridge and PAR lock-in amplifier.

5.7 CONCLUSION

From the experimental data and the numerical analysis developed by Lauks,⁽²⁵⁾ it appears that the kinetics of the silver injection process is limited by the interfacial reaction rather than the bulk diffusion. The model also indicates the existence of two phases, one is silver-doped As_2S_3 and the other undoped, in the As_2S_3 film. The boundary between these two different phases moves with the extent of silver injection.

AD-A113 148

PENNSYLVANIA UNIV PHILADELPHIA
SILVER-DOPING EFFECTS AND PHOTOSTRUCTURAL TRANSFORMATION IN EVA--ETC(IU)
FEB 82 T J CHEN, J N ZEMEL, I LAUKS

F/0 7/4

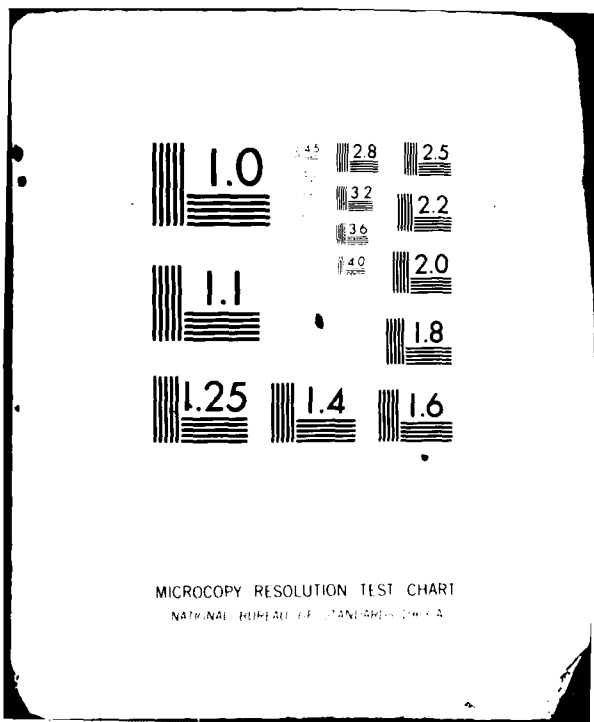
UNCLASSIFIED

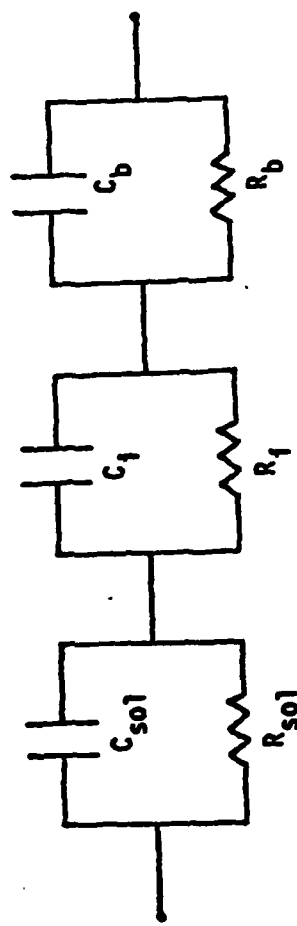
3013
20
200019

AFOSR-TR-82-0120

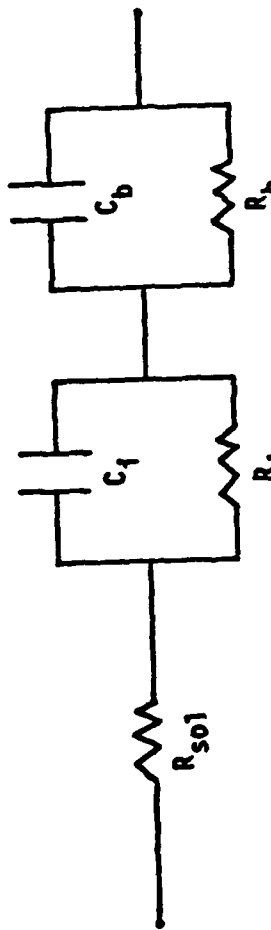
NL

END
DATE
FILED
4-29-82
RTIC





(a) The subscripts sol , i , b are corresponding to solution, interface and bulk of electrolyte, respectively.



(b) The capacitance of solution is much larger than the other capacitances considered and can be ignored.

Fig. 5.15 The equivalent circuit of an electrochemical cell.

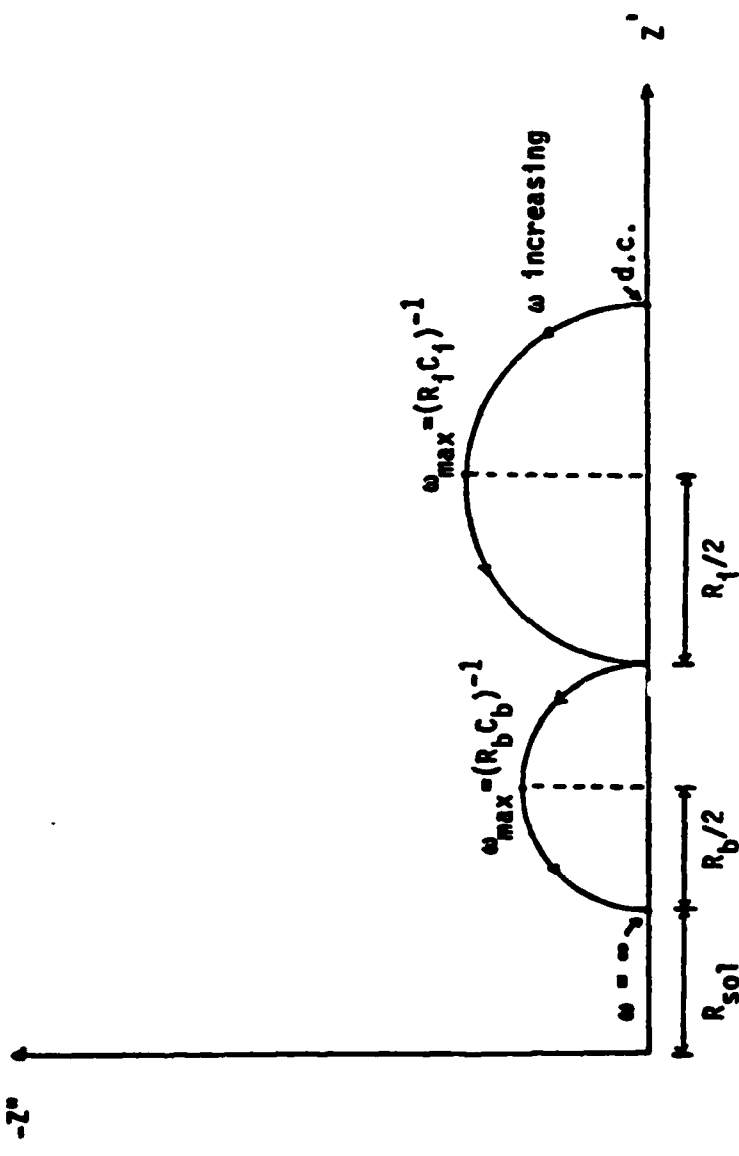


Fig. 5.16 The ac response of the equivalent circuit (Fig. 5.17b)). The physical meanings of various parameters are given in Ref. 26-28.

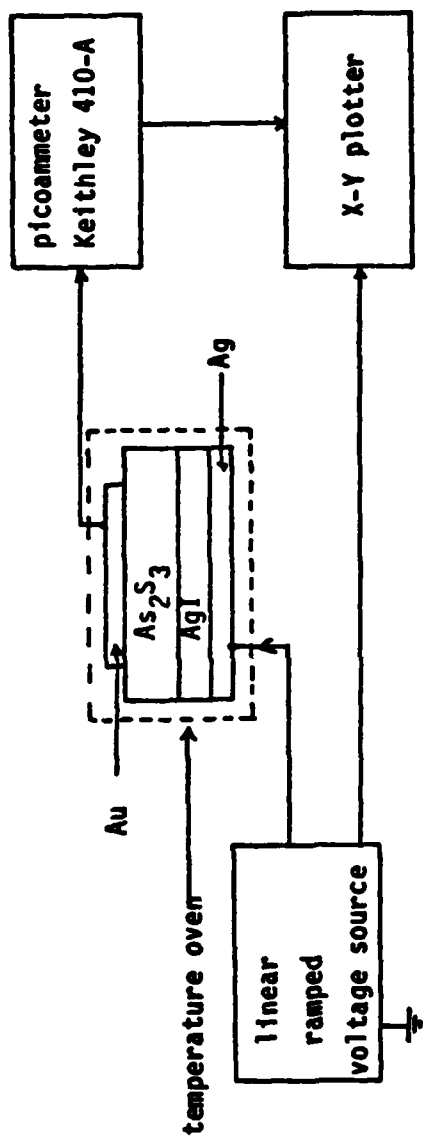
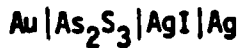


Fig. 5.17 The I-V measurement system in the two-electrode configuration for the solid electrolyte cell Au/As₂S₃/AgI/Ag.

5.8.1 The Transport Mechanism of Silver Ions in the Solid Electrolyte

In the cell,



, silver iodide is an ionic conductor and As_2S_3 is nominally an insulator. Under steady state condition, the measured cell current will be equal to the ionic current in the AgI electrolyte. On applying a positive potential to the silver electrode, silver ions (which are replenished by the silver electrode) are transported through the AgI electrolyte and injected into the As_2S_3 film due to the charge transfer reaction at the $\text{As}_2\text{S}_3|\text{AgI}$ interface. On the other hand, if a positive potential is applied to the Au electrode, then the injected silver ion will be displaced from the As_2S_3 film through the $\text{As}_2\text{S}_3|\text{AgI}$ interface, the AgI electrolyte, and redeposited on the Ag electrode. One expects that a reversible Ag injection process will occur at the $\text{As}_2\text{S}_3|\text{AgI}$ interface.

5.8.2 Experimental Techniques and Results

The details of the preparation of the different thin films were described in the previous sections. The thickness of the silver iodide film is about $0.5 \mu\text{m}$. The I-V measurement in the two-electrode configuration is schematically shown in Fig. 5.17. The current was measured with a Keithley 410A Picoammeter. A linear sweep potential was directly applied to the reference electrode (i.e., Ag electrode).

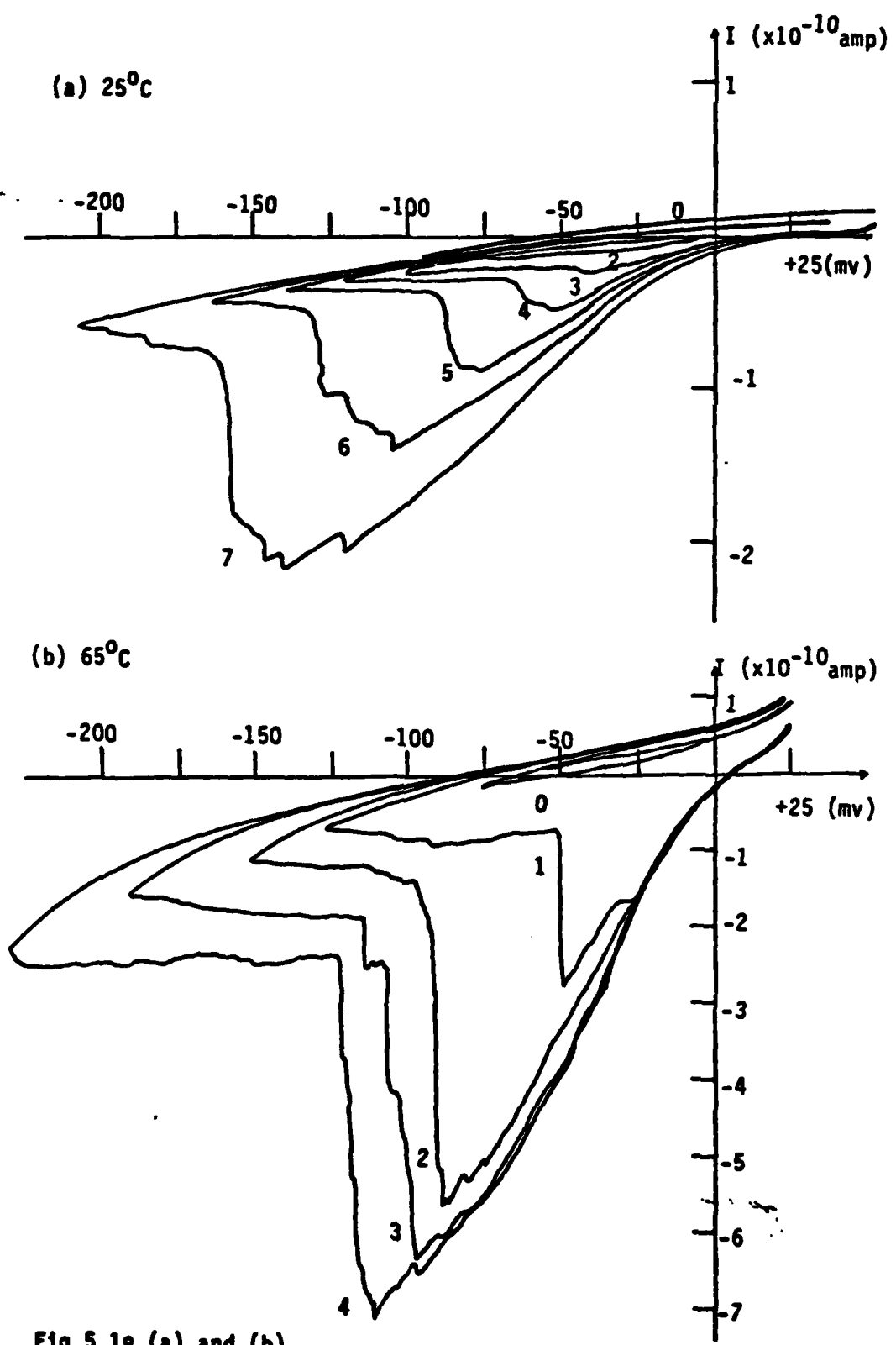


Fig.5.18 (a) and (b)

The details of the measurement techniques were given in Section 5.3. The voltammograms at different cell temperatures (25°, 60°, and 90°C) are shown in Fig. 5.18 (a)-(c), respectively. The increasing area of the voltammograms corresponds to increasing initial Ag injection levels. The voltammograms in the solid electrolyte cell are similar to those in the aqueous electrolyte cell. However, this does not necessarily imply that the mechanisms of charge transfer across the As_2S_3 and electrolyte interface are the same for the aqueous and solid cases.

The observed sudden change in the voltammogram is believed to be due to the formation of local highly conductive paths in the nonuniformly silver-doped As_2S_3 film. More experiments are needed to clarify the underlying mechanism in this case.

5.9 ETCHING BEHAVIOR IN NaOH AQUEOUS SOLUTION AND MORPHOLOGY OF THE CHEMICALLY PROCESSED As_2S_3 FILM

5.9.1 Etching Behavior of the Chemically Processed As_2S_3 Film

The chemically sensitized As_2S_3 thin film used as an UV sensitive resist was demonstrated earlier in this chapter. The etch resistance to the NaOH aqueous solution is not only dependent on the time in the silver-ion bath, but also on the UV exposure time. The results suggest that a critical concentration of silver is needed in the As_2S_3 film in order for it to be totally resistant to the chemical etching solution. The sensitivity of the sensitized As_2S_3 film is slightly poorer than the $\text{AgCl}|\text{As}_2\text{S}_3$ composite resist.

The electrochemically treated As_2S_3 film, is totally resistant to the NaOH etch. This is understandable because the As_2S_3 film can be heavily Ag-doped with the assistance of the externally applied electric field in the electrochemical treatment.

5.9.2 Morphology of the Chemically Processed As_2S_3 Film

The electrochemical injection of silver atoms represents a powerful method for investigating the process of silver injection. This is because the silver injection level, given by the current i , can be exactly controlled by the current magnitude and duration. Simultaneously, morphological observation gives additional advantages in directing and controlling the overall process of silver-injection. Fig. 5.19 shows the morphologies of the sensitized As_2S_3 film (a) and the electrochemically treated As_2S_3 film (b). In the sensitized film, i.e., only a thin photosensitive surface layer on top of the surface, the surface was smooth and basically structureless. On the other hand, the ring-like structure was observed in the electrochemically silver-doped sample which cannot be etched in NaOH aqueous solution. The photomicrograph (Fig. 5.19 (b)) shows different phases in the electrochemically doped sample and is very similar to that of the heavily photo-doped As_2S_3 film. (See Section 4.7). Further structural experiments in the electrochemically doped sample are needed to identify these separate phases.

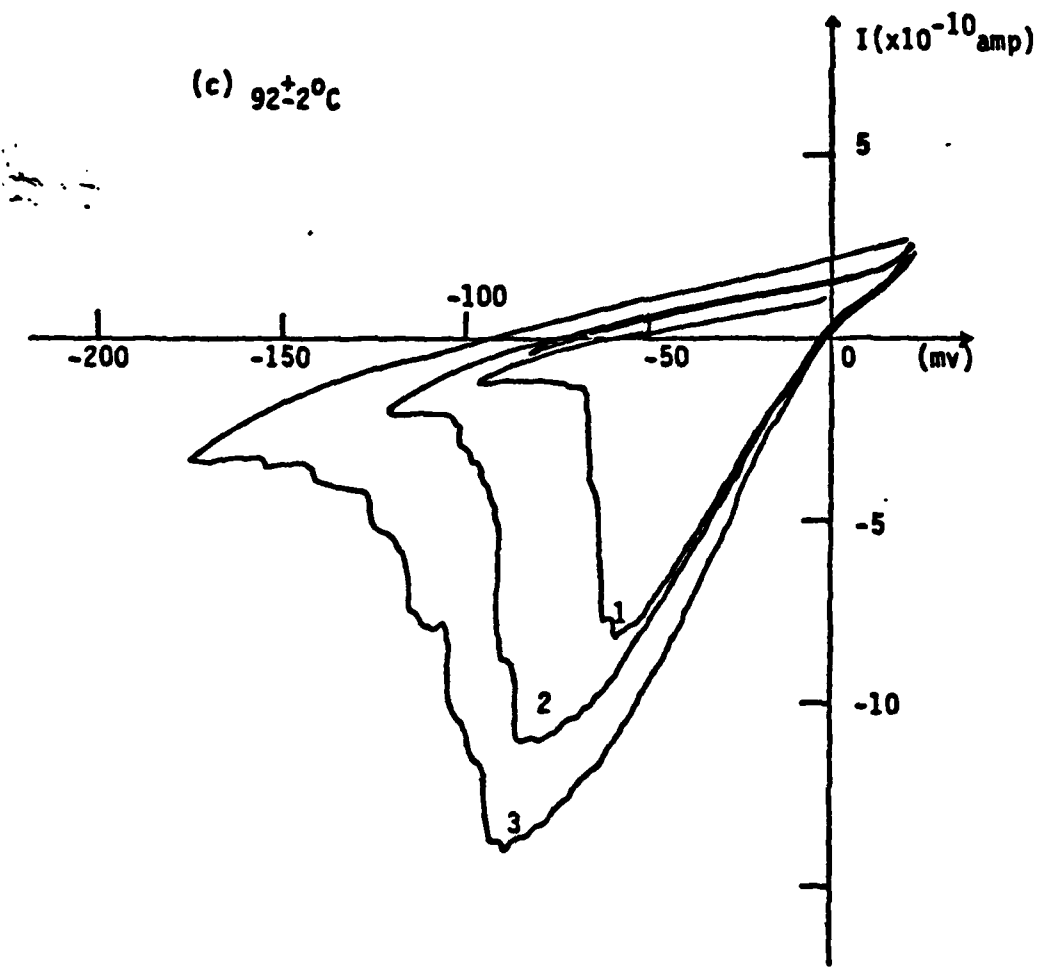
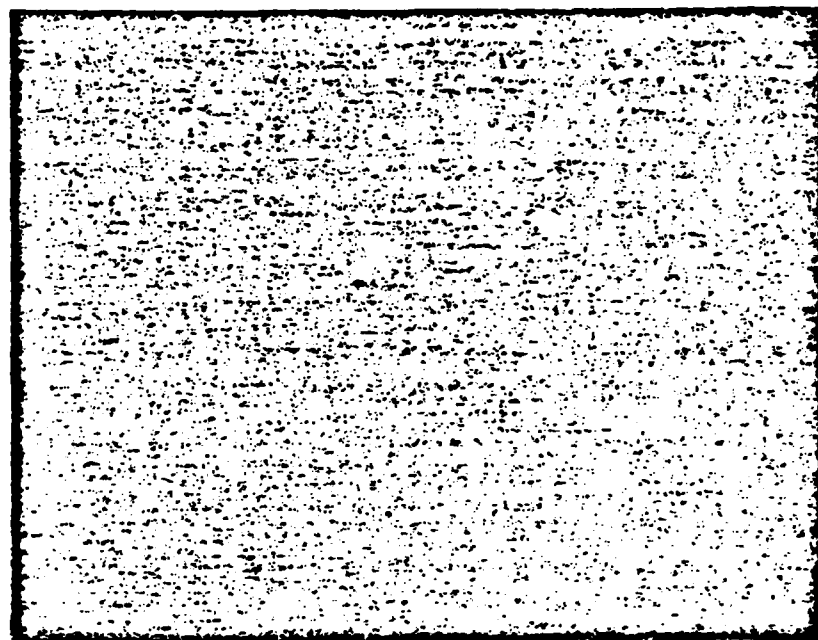


Fig.5.18 The voltammograms of the solid electrochemical cell $\text{Au}/\text{As}_2\text{S}_3/\text{AgI}/\text{Ag}$ at different cell temperatures:
 (a) 25°C , (b) 65°C and (c) 92°C . The voltammograms in the solid electrolyte cell are similar to those in the aqueous electrolyte cell. The observed sudden change in the voltammogram is believed to be due to the formation of local highly conductive paths in the nonuniformly Ag-doped As_2S_3 film.

References to Chapter 5

1. A. Buroff, P. Simidchieva, K. Koley, R. Stoycheya; in "Proc. of the 1978 Intern. Conf. on Photographic Science", P. 243, (1978).
2. K.L. Tai, L.F. Johnson, D.W. Murphy, M.S.C. Chung; Extended Abst., No. 94, The Electrochem. Soc., Spring Meeting, Boston, Mass., (1979).
3. K.L. Tai, R.G. Vadimsky, C.T. Kemmerer, J.S. Wagner, V.E. Lamberti, A.G. Tinko; J. Vac. Sci. Technol., 17 (5), Sept/Oct., (1980).
4. K.L. Tai, W.R. Sinclair, R.G. Vadimsky, J.M. Moran; J. Vac. Sci. Technol., 16, 1977, (1979).
5. D.T. Sawyer, J.L. Roberts, Jr.; "Experimental Electrochemistry for Chemists", John Wiley & Sons, New York, (1974).
6. J.O'M. Bockris, A.K.N. Reddy; "Modern Electrochemistry", Vol. 1 & 2, Plenum, New York, (1970).
7. V.A. Myamlin, Y.V. Pleskov; "Electrochemistry of Semiconductors", Plenum, New York, (1967).
8. E.A. Davis; in "Amorphous Semiconductors", ed. by M.H. Brodsky, Springer-Verlag, New York, (1979).
9. R.A. Street, N.F. Mott; Phys. Rev. Lett., 35, 1293, (1975).
10. M. Kastner, D. Adler, H. Fritzsche; Phys. Rev. Lett., 37, 1504, (1976).
11. H. Gerischer; in "Advances in Electrochemistry and Electrochemical Engineering", ed. by P. Delahay and C.W. Tobias, Vol. 1, p.139, Wiley-Interscience, New York, (1961).
12. D.D. MacDonald; "Transient Techniques in Electrochemistry", Plenum, New York, (1977).
13. K.J. Vetter; "Electrochemical Kinetics", Academic Press, New York, (1967).
14. B.E. Conway; "Theory and Principles of Electrode Processes", Roland Press, New York, (1965).
15. J.F. Dewald; "Semiconductor Electrochemistry" in "Semiconductors", ed. by N.B. Hannay, Reinhold Publishing Corp., New York, (1959).
16. H. Kokado, I. Shimizu, T. Tatsuno, E. Inoue; J. of Non-crystal. Solids, 21, 225, (1976).

(a)



(b)

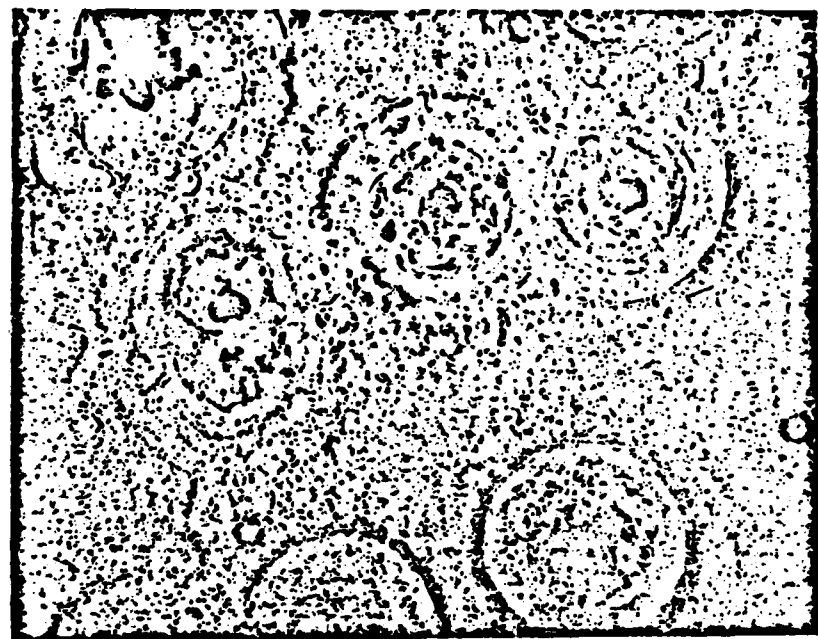


Fig.5.19 Optical micrographs of the sensitized As_2S_3 thin film (a) and the electrochemically treated As_2S_3 thin film (b). The magnification is 500. The Ag concentration in the electrochemically treated sample is about $2 \times 10^{20} \text{ cm}^{-3}$.

CHAPTER 6

CONCLUSIONS AND RECOMMENDATIONS FOR FURTHER RESEARCH

The subject of this dissertation is the study of the feasibility of using amorphous As_2S_3 as an inorganic photoresist for micro-structure fabrication. As a result of this study, the underlying mechanisms of photostructural changes in films of As_2S_3 with or without silver doping has been gained. The results may prove useful for the design of practical devices and as a basis for future research programs.

6.1 SUMMARY OF RESULTS

The as-deposited As_2S_3 films undergo photostructural transformations upon band-gap illumination, resulting in a shift of the absorption edge which in turn causes an increase in the refractive index of the exposed area. This process is known as the photodarkening effect. The exposed region becomes less soluble in an alkaline hydroxide aqueous solution. Using this differential etching property a pattern may be delineated. For a 300 nm thick As_2S_3 resist film, an ultraviolet exposure energy of 30 J/cm^2 is required to insure that a maximum of 40% of the initial film thickness remains. A maximum etch rate ratio of 1.7:1 between the unexposed and exposure-saturated As_2S_3 films is obtainable in a 0.03 N NaOH aqueous solution at 21° C .

17. W.H. Brattain, J. Bardeen; BSTJ., 32, 1, (1953).
18. M. Green; J. Chem. Phys., 31, 200, (1959).
19. R.H. Kingston, S.F. Neustadter; J. Appl. Phys., 26, 718, (1955).
20. R. Seiwatz, M. Green; J. Appl. Phys., 29, 1034, (1958).
21. H. Gerischer; in "Solar Energy Conversion", ed. by B.O. Seraphin, Topics in Applied Physics, Vol. 31, p.115, Springer-Verlag, Berlin, (1979).
22. H. Gerscher; in "Physical Chemistry: An Advanced Treatise" ed. by Henry Eyring, A. Henderson, W. Jost, Vol. IX A, p.463, Academic Press, New York, (1970).
23. M. Sluyters-Rehbach, J.H. Sluyters; in "Electroanalytical Chemistry", ed. by A.J. Bard, Vol. 4, Marcel Dekker, New York, (1970).
24. B.P. Lemke, D. Haneman; Phys. Rev., B17, 1893, (1978).
25. I. Lauks; Private Communication, (1980).
26. R.D. Armstrong, M.F. Bell, A.A. Metcalfe; in "Electrochemistry", A Special Periodical Report, ed. by H.R. Thirsk, Vol. 6, The Chem. Soc., Burlington House, London, (1978).
27. J.R. Macdonald; in "Superionic Conductors", ed. by G.D. Mahan and W.L. Roth, Plenum, New York, (1976).
28. P.H. Bollerberghs; in "Solid Electrolytes: General Principles, Characterization, Materials, Applications", ed. by P. Hagenmuller and W. Van Gool, Academic Press, New York, (1978).

cluding organic polymer resists are also demonstrated for the first time. The plasma etching mechanism for a CF_4 discharge that is proposed consists of an attack by the atomic fluorine free radicals on the As_2S_3 film.

Volatile reaction products such as AsF_5 and SF_6 are assumed to form and are then pumped out through the vacuum system. The developed As_2S_3 pattern can then be converted into an As_2O_3 pattern with an oxygen plasma treatment. The resulting patterned layer contains the arsenic dopant which can be used as a diffusion source subsequently. Thus a considerable simplification in the overall device processing is expected, and a complete dry process for device fabrication is then conceivable. A phenomenological model is also proposed to describe the plasma oxidation process in As_2S_3 films. The results suggest the following reaction sequence;



The oxidation process appears to be confined to the surface of As_2S_3 films. The As and S appear to diffuse to the surface where they react to form the As_2O_3 and volatile SO_2 . Ag-photodoped As_2S_3 samples are found to have a much slower etch rate in a CF_4 plasma. It is also noted that a thin cap of a silver-doped layer is sufficient for protection during etching. This fact would require an anisotropic

X-ray and electron-beam exposure of the As_2S_3 films result in the same differential etching characteristics in NaOH aqueous solution. For electron-beam exposure, an electron dosage of about 5×10^{-5} coul/cm² is needed in order that a maximum of 50% of the initial film thickness remains after etching in the same solution. In this electron-beam exposure experiment, the optimal electron dosage for PMMA is about 1×10^{-4} coul/cm². This study shows that the ultraviolet light and x-ray sensitivity of As_2S_3 films is poorer than that of conventional organic polymer resists, but that electron-beam exposure sensitivity is better than the typical PMMA resist. However, the contrast in the As_2S_3 films is poorer than that of PMMA resist. The ultraviolet, x-ray, and electron-beam sensitivity of a modified $\text{AgCl}-\text{As}_2\text{S}_3$ composite resist was also studied. Not only can the sensitivity be enhanced at least by one order of magnitude, but the contrast in this novel composite resists is also improved.

A complete dry processing technique was developed and the results are summarized below. After ultraviolet, x-ray, or electron-beam exposure, the resist pattern was developed in a CF_4 plasma. A barrel-type plasma reactor was used initially. This configuration allows an in-situ monitoring of the etching. The dependence of etch rate on the rf power and reactive gas flow rate were examined. It is found that the etch rate ratio depends strongly on the gas flow rate. The maximum etch rate ratio of 1.8 occurs at a rate of 12×10^{-3} SCCM with 25 W rf power. Patterns delineated by dry processing in resists in-

changed into the exposed state being composed of a glassy As_2S_3 network and arsenic in the form of clusters. A wide variety of amorphous chalcogenide systems show similar structural transformations upon band-gap illumination. An array of complex and often contradictory mechanisms have been proposed to account for them. In this study a model developed by Anderson et al is employed to explain the microscopic structural transformations in As_2S_3 and a plausible sequence of events leading to the polymerization of As_4S_4 molecules into glassy As_2S_3 network is proposed.

According to the Mott's model an amorphous As_2S_3 film upon band-gap illumination can produce D^+D^- (or C_3^+C_1^- according to Kastner designation) charged defect centers in the vicinity of chalcogen atoms. Under certain conditions strong electron-phonon coupling will involve the switching of bonds, leading to the formation of chalcogen atoms which are three-fold and singly coordinated, instead of the normal two-fold coordination in chalcogen atoms. In the pnictide centers such as arsenic atoms, P_4^+ and P_2^- charged defect centers can also be formed under the same condition. Upon band-gap illumination when both chalcogenides and pnictides are present in a glass such as evaporated As_2S_3 films, all the species P_4^+ , C_3^+ , P_2^- and C_1^- can be present. The polymerization process between As_4S_4 itself or As_4S_4 and S-chains can proceed because of the strong electron-phonon coupling in the vicinities of the charged defect centers which in turn causes the switching of local bonds. The rearrangements of local structure

etching to avoid undercutting. Therefore, a home-made parallel-plate plasma reactor was used. For heavily silver-doped As_2S_3 films, the plasma etching can be continued for subsequent pattern transfer to the underlying SiO_2 layer without breaking vacuum.

It is known that the physical and chemical properties of amorphous chalcogenide films including As_2S_3 are strongly dependent on the methods of film preparation. The differential etching characteristics between the unexposed and exposed As_2S_3 films also indicate that a structural transformation is induced upon band-gap light exposure. The structural characterization of As_2S_3 film before and after band-gap illumination was needed in order to understand the underlying mechanisms. X-ray and electron-beam diffraction experiments indicate that the as-deposited As_2S_3 films are in an amorphous state, and IR absorption experiments show the existence of an As_4S_4 component as well as As_2S_3 in the unexposed films. The results suggest the as-deposited state of As_2S_3 film is a heterogeneous system of As_2S_3 , As_4S_4 and S. After intense ultraviolet light exposure, IR spectroscopy shows the absorption features at 374 and 337 cm^{-1} assigned to As_4S_4 disappear and only an absorption peak around 310 cm^{-1} associating with As-S bond stretching in As_2S_3 is observed. X-ray diffraction experiments not only show the formation of arsenic clusters, but also show the shifts of the relatively diffuse peaks from 16.5° and 29.8° to 17.2° and 30.1° , respectively. It may be concluded that after band-gap exposure the as-deposited state is

compounds prousite Ag_3AsS_3 , are not observed in this work. However, the formation of Ag_2S cannot be excluded here and its existence is reported elsewhere. The morphology of Ag-doped As_2S_3 samples was also studied. The photomicrographs show several different phases are present in the heavily Ag-doped As_2S_3 film. These phases may be identified as uniformly Ag-doped As_2S_3 matrix, Ag-riched As_2S_3 , Ag_2S , and As crystallites. A ring formation surrounding arsenic crystallites was observed. The detailed mechanism of this ring-formation is not yet understood. One of the reasons is that the phase diagram of the Ag-As-S system, to the author's knowledge, has not been reported. However, a plausible model based on spinodal decomposition has been proposed. The properties of As_2S_3 can be changed both structurally and physically as a result of silver photodoping. The silver states and their effects on physical property in doped As_2S_3 are elaborated below in terms of the charged defects model described before.

If silver atoms in contact with or incorporated in the As_2S_3 films are already ionized due to ultraviolet light exposure, and one further assumes the layer structure does exist to some degree in the exposed film, then silver ions can easily pass between the layers of the As_2S_3 network due to its small ionic radius (1.26 \AA) compared with the S-S distance of 3.242 \AA and As-S distance of 3.475 \AA between layers in the crystal structure. Eventually the silver ions would be trapped at the C_1^- or P_2^- charged defect center. The silver ions behave as a negative charged defect killer. So the pinned Fermi level due to the

will reduce the system energy to a minimum. Optical absorption data indicate that the bond energies of As-S bonds lie energetically lower than the bond energies associated with As-As and S-S homobonds. The density of As-As and S-S homobonds can then be reduced by the band-gap illumination, and the structure of the exposed film can reach a more continuous glassy As_2S_3 network. Arsenic clusters can also be formed.

The $\text{AgCl}-\text{As}_2\text{S}_3$ composite resist has been proved to be promising and attractive for microstructure pattern fabrication. In order to improve the design rules for practical devices, more experiments on the structural changes and silver doping process in As_2S_3 films are needed. For the sample - $0.1\mu\text{m}$ of metallic silver coated with $1.5\mu\text{m}$ of As_2S_3 , it is concluded that ultraviolet exposure for 40 minutes causes all the silver to be incorporated into the As_2S_3 matrix. IR spectra indicate a refractive index change, and the only absorption peak observed is around 310 cm^{-1} corresponding to the As-S bond stretching in the As_2S_3 . However, x-ray diffraction experiments show several strong peaks associating with silver clusters dispersed through the As_2S_3 matrix especially in the highly Ag-doped sample. In this study it is possible to diffuse as much as $0.4\mu\text{m}$ layer of silver into a $1.5\mu\text{m}$ film of As_2S_3 under a prolonged ultraviolet light exposure and entirely exhaust the silver reservoir. It is later confirmed that the ternary Ag-As-S system can contain as much as 35 at. % as a result of photodoping. It is found that such ternary crystalline

As_2S_3 film and a grating pattern with $6 \mu\text{m}$ line width was successfully achieved. In order to obtain more control over the silver dopant concentration electrochemical injection methods were employed. The silver doping level is controlled by varying the current density through the electrochemical cell. The results show the relation of the current to the potential for freshly prepared As_2S_3 films is governed by the Butler-Volmer equation. The As_2S_3 -electrolyte (10^{-3} N AgNO_3 aqueous solution) interface shows rectification. The current increase in the cathodic process is less than 60 mV per decade, i.e., less than an exponential increase. The cyclic voltammograms indicate a maximum peak in the anodic process, i.e., As_2S_3 electrode is at positive potential with respect to the bulk of the electrolyte. The peak current and voltage vary as a function of potential sweep rate and silver doping level in the As_2S_3 film. The deviation from an exponential law in the cathodic reaction suggests that it may be due to the electron transport overvoltage in the As_2S_3 electrode or the saturation of the silver-adsorption sites on the surface of the As_2S_3 electrode. It is still an open question at this stage. On the other hand, the peak in the anodical process indicates that the silver injection process is highly reversible. It also suggests that the kinetics is limited by the interface reaction rather than by the bulk diffusion. Finally, the existence of two phases, one is silver-doped and another is undoped, in the As_2S_3 electrode is strongly supported by the experimental data and the boundary between these two different phases moves with the extent of silver injection.

charged defect centers in an amorphous chalcogenide material will become unpinned after heavy silver doping, and dramatic changes in the physical and structural properties can be expected. For instance, the large increase of electrical conductivity in the thermally quenched silver-doped As_2S_3 has been reported and may be explained according to this model.

The high sensitivity and high contrast available in the $\text{AgCl}-\text{As}_2\text{S}_3$ composite resists makes it potentially attractive for lithographic applications. However, the mechanism responsible for the silver dissolution in the chalcogenide films is by no means well characterized. Also the Ag-doped As_2S_3 is not suitable as a dopant material since Ag is a life-time killer in silicon devices. It could become useful if a suitable method can be found to selectively remove the photodoped Ag from As_2S_3 film and resulting dopant source. These questions are examined below.

It is known that some chalcogenide semiconductors can reduce silver nitrate from aqueous solution resulting in the deposition of metallic silver on the surface. In this work it was found that Ag can be incorporated into the As_2S_3 matrix both optically and chemically. Firstly the As_2S_3 film is dipped into a silver-containing aqueous solution for a few minutes, followed by rinsing in deionized water. It is believed that a thin layer of Ag-doped As_2S_3 is formed on the surface of the film. Then the film is exposed under ultraviolet light. In the exposed area silver ions migrate into the bulk of the

1. The As_2S_3 thin films are shown to be negative inorganic resists with a poor sensitivity to ultraviolet light or x-ray exposure but with a promising sensitivity to electron-beam exposure. Modified $\text{AgCl}-\text{As}_2\text{S}_3$ composite resists were studied and their sensitivity and exposure characteristics were evaluated.
2. Differential etching of As_2S_3 in a CF_4 plasma has been demonstrated. Pattern delineated by dry processing in resists, including organic polymer resists, is reported for the first time. A model is proposed to describe the etching characteristics of As_2S_3 films in a CF_4 plasma. The factors controlling plasma etch rate are discussed in detail.
3. The oxidation of As_2S_3 film into As_2O_3 crystallites with an oxygen plasma treatment is reported. A phenomenological model is proposed to describe the plasma oxidation process in the As_2S_3 thin film. A complete dry process for device fabrication has been proposed and demonstrated.
4. A physical model is proposed to describe the structural changes associated with the effects of band-gap illumination on As_2S_3 films. The theory developed by Anderson et al is included in the analysis and the results are used to explain the irreversible structural changes of As_2S_3 films upon a prolonged ultraviolet light exposure. Physical measurements have been performed. They support many aspects of the model

The cyclic voltammograms of the solid cell Au | As₂S₃ | A_gI | Ag also show a maximum in the anodic process. The silver electrode can be dissolved cathodically and silver ions are transported through the silver iodide and injected into the As₂S₃ film. On the other hand, in the anodic process silver ions migrate from the bulk of the As₂S₃ film and deposit back on the silver electrode through the ionic conductor. The mechanisms of charge transfer across As₂S₃ and electrolyte interface are not necessarily the same for the aqueous and solid cases. Though the kinetics of charge transfer reactions on As₂S₃ electrode are not yet well characterized, the reversibility of the silver injection process from either aqueous or solid silver electrolyte has been demonstrated for the first time.

The ac impedance response of the As₂S₃ film in different aqueous solution was measured. At high frequency, atom or ion diffusion effect can be ignored and the ac response of the cell is determined by the geometric capacitance and resistance of the bulk As₂S₃ electrode. At low frequency (less than 1 KHZ), atom or ion diffusion process and desorption-adsorption on the electrode surface are more significant. Further evidence is obtained from the difference between ac responses on the As₂S₃ electrode in the potassium chloride and silver nitrate aqueous solutions.

6.2 CONTRIBUTIONS

The major contributions of this Dissertation are summarized in the following:

arsenic if As_2O_3 is used) in the silicon substrate as well as in the plasma-overcoated SiO_2 or Si_3N_4 films.

2. The model suggested in this work has clarified the observed structural changes on As_2S_3 films upon band-gap illumination. However, it also points out that further structural experiments have to be performed. The structure of amorphous As_2S_3 chalcogenides is not well characterized. The radial distribution function (RDF) obtained from x-ray diffraction is complicated by the difficulty of separating contributions from homo- and heterobonds. A recent development on the extended x-ray absorption fine structure (EXAFS) is capable of making the distinction between bond types. Then the local structural changes induced by band-gap illumination can be studied in terms of the local configuration number changes for each kind of atom. Also the complimentary technique to infrared spectroscopy, i.e. Raman spectroscopy ought to give useful information in the study of local structure.
3. The kinetics of silver doping in the As_2S_3 film should be studied further. Most important is the determination of the phase diagram of the Ag-As-S system. The transport mechanism of silver ions in the As_2S_3 film should be examined in detail. It is particularly important to understand whether the silver ions in the As_2S_3 film are transported by hopping between

described. Phase separation and ring formation surrounding arsenic crystallites are reported in the Ag-As-S system for the first time.

5. A structural study of silver-doped As_2S_3 films was performed. It was shown that clusters of silver are formed and dispersed through the entire As_2S_3 matrix. It was found that the ternary Ag-As-S system can contain as much as 35 at. % of silver as a result of photodoping. The silver states in the As_2S_3 films are also discussed.
6. Electrochemical measurements were performed to study the behavior of the As_2S_3 -electrolyte interface. Reversible electrochemical injection of silver into As_2S_3 was demonstrated. A model is proposed to describe the current-over-voltage characteristic of the As_2S_3 -aqueous electrolyte interface. The ac response of As_2S_3 electrodes was studied.

6.3 RECOMMENDATIONS FOR FURTHER RESEARCH

1. A preliminary study on direct device fabrication methods demonstrated that the idea is feasible and attractive, but questions concerning the diffusion mechanism remain to be answered. Auger electron spectroscopy together with sputtering etching or secondary ion mass spectroscopy (SIMS) should give the information about the impurity profiles (arsenic and sulfur if As_2S_3 is used as a dopant source or

than was employed in this study, particularly to characterize long time constant effects.

It is felt that the research suggested above could extend further our understanding of the structural changes and silver photodoping induced by band-gap illumination.

**DATE
FILMED**

8